Development and Evaluation of Magnetic, Photocatalytic and Photothermal Nanoparticles and their Application to Cancer Therapy

（磁性、光触媒および光熱ナノ粒子の開発と評価
およびがん治療への応用）

By

Md. Shariful Islam

March 2012

Development and Evaluation of Magnetic, Photocatalytic and Photothermal Nanoparticles and their Application to Cancer Therapy

（磁性、光触媒および光熱ナノ粒子の開発と評価およびがん治療への応用）

By

MD. SHARIFUL ISLAM

*A thesis submitted to **Kagoshima University** in Partial Fulfillment of the Requirements for the degree of Doctor of Philosophy in Engineering*

March 2012

Department of System Information Science
Graduate School of Science and Engineering
Kagoshima University
Japan

Development and Evaluation of Magnetic, Photocatalytic and Photothermal Nanoparticles and their Application to Cancer Therapy

A Thesis

By

MD. SHARIFUL ISLAM

Approved as to the style and contents by

…….	……...
(Junichi Kurawaki) Prof. & Dr. Sci. (PhD)	**(Yuji Horie) Prof. & Dr. Sci. (PhD)**
Supervisor	**Co-supervisor**
Department of Chemistry and Bioscience	*Department of Electrical and Electronics Engineering*

……

(Toshifumi Yoshidome) Prof. & Dr. Sci. (PhD).
Co-supervisor
Department of Chemistry, Biotechnology and Chemical Engineering

Graduate School of Science and Engineering
1-21-35 Korimoto, Kagoshima 890-0065
Kagoshima University
Japan

Date of approved: March, 2012

DEDICATED TO MY BELOVED PARENTS

AND

Late:
SHAFIKUR RAHMAN

MST. SUFIA BEGUM

ABSTRACT

In this thesis, we present a series of different novel experimental techniques for the synthesis of various magnetic, photocatalytic and photothermal nanoparticles with the aim of using them to cancer therapy. We adopted HeLa cells as a model to investigate the thermal-photocatalytic cancer cell killing efficiency of as-synthesized nanomaterials. Furthermore, for the first time we assembled and used combined instrumentation modeling of AC (alternating current) magnetic-field induction and photoexcitation.

Nanosized neck-structured and rose type nanoplates of three types of iron oxides (Fe_3O_4, γ-Fe_2O_3 and α-Fe_2O_3) were successfully synthesized by a simple hydrothermal decomposition. Furthermore, Fe_3O_4@TiO_2 core-shell nanocomposites were successfully prepared and their thermal-photocatalytic cell killing efficiency was observed. We also synthesized mixed α and γ-Fe_2O_3 nanoparticles and their synergistic toxic effect against HeLa cells were investigated under AC (alternating current) magnetic-fields induction and photoirradiation conditions at room temperature. Besides we prepared three types of iron oxides (Fe_3O_4, γ-Fe_2O_3 and α-Fe_2O_3) by a co-precipitation method and a comparative study was followed in respects of shape, size, structure and other morphological and magnetic properties.

We successfully prepared Cu-TiO_2 nanocomposites. The catalytic activity of the Cu-TiO_2 nanocomposites was evaluated by the application to the photocatalytic cancer (HeLa) cell-killing under UV-visible light irradiation. The Cu-TiO_2 nanocomposites showed higher photocatalytic activity than commercial TiO_2 (P25) under the similar experimental conditions.

The Ag metal core-TiO_2 shell ($Ag@TiO_2$) composite nanoclusters with uniform size, shape and core-shell structures were successfully synthesized by a new simple citrate reduction method. The photocatalytic and photothermal cell killing efficiency of colloidal $Ag@TiO_2$ core-shell nanoclusters was evaluated against cancer (HeLa) cells under UV–vis irradiation. It was found that the $Ag@TiO_2$ nanoclusters with an adequate Ag ratio to TiO_2 killed more malignant (HeLa) cells by 80% compared to TiO_2 nanoparticles alone.

Finally, from the thorough observations during this research tenure it can be concluded that our synthesized various kinds of nanomaterials whether magnetic, photocatalytic or photothermal showed the great potential use in cancer therapy.

Acknowledgments

First of all the author would like to offer innumerable thanks and admiration to the only Sustainer of the whole universe, Allah Subhanahu Wa-Ta A`la with Drood and Salam to His prophet Rasullulah Sallallahu Alaihi Wassalam because He has enable him to pursue this research and to carry out the hard job like higher study.

Distinctly, the author is glad and very much grateful to necessarily express his deepest sense of immense indebtedness and profound regards to the Ministry of Education, Culture, Sports, Science and Technology (MONBUKAGAKUSHO) of the Japanese Government for the Scholarship grant and financial supports.

The author feels immense proud to express his heart felt respect and deepest sense of gratitude and indebtedness to his former research supervisor Prof. Yoshihumi Kusumoto for giving him the valuable opportunity to come to Kagoshima University as a PhD student to his laboratory. Further, the author is cordially grateful to Prof. Yoshihumi Kusumoto, Department of Chemistry and Bioscience, Kagoshima University, Japan, for his cordial guidance, scholastic supervision, valuable suggestions and inspiration, constant incitement, affectionate feelings and constructive criticisms throughout the course of research work and successful completion of the research tenure.

The author is cordially grateful and express his heart felt respect and deepest sense of gratitude to his research supervisor Prof. Junichi Kurawaki, Department of Chemistry and Bioscience, Kagoshima University, Japan, for his cordial guidance, responsible supervision, valuable suggestions and inspiration, constant incitement, affectionate feelings and anticipated help and co-operation throughout the course of research work and successful completion of this manuscript.

The author would like express his sincere and cordial gratefulness to his co-supervisor Prof. Yuji Horie, Department of Electronics and Electrical Engineering, Kagoshima University, Japan, for his anticipated help and co-operation, valuable suggestions and inspiration, useful discussions and assembling of the hyperthermia instruments and others during the research tenure.

It's also pleasure of the author to express his sincere, heartfelt and cordial gratefulness to his co-supervisor Prof. Toshifumi Yoshidome, Department of Chemistry, Biotechnology and Chemical Engineering, Kagoshima University, Japan, for his anticipated help and co-operation, valuable suggestions and inspiration, useful discussions and criticisms during the research tenure as well as preparation on this manuscript.

The author is also very much thankful to entire staff of the Department of Chemistry and Bioscience, especially Mr. Yoshihisa Ozono and Mr. Terumi Kakoi of Frontier Science Research Center for measurement of XPS, EDAX and FE-SEM, TEM etc.. The author would like to offer special thanks to staff of the Japanese Language Center in Kagoshima University, for their contribution to learn Japanese Language and Culture and to understand the Japanese Society.

The author would like to thank former and present co-workers of our laboratory, especially Dr. Md. Abdulla-Al-Mamun, Dr. Bashir Ahmmad, Dr. M. Muruganandham, Miss. Chiyo Okamoto and Miss. Aki Mihata for their kind help and supports.

The author gratefully acknowledges his sincere application and warmest gratitude to his honorable community members here in Kagoshima (BAK-Japan) for their kind comments, inspiration and supports during his research tenure and in writing this manuscript.

Diction is not enough to express the author profound gratitude and deepest appreciation to his beloved mother, brother, brother-in-law, sister, nephews and cousins for their never ending prayer, encouragement, sacrifice and dedicated efforts to educate him to this level and to pursue his research work in aboard.

It is the great pleasure of the author to express his sincere acknowledge and warmest gratitude to his cousin Mr. Md. Riazul Haque Sarker and his family for their valuable support, affection and endless encouragement from his childhood till to date.

Finally, the author express his heart felt love and heart squeezed gratitude to his beloved wife, Tohura Khatun, father-in-law, mother-in-law and brother-in-laws for their endless prayer, encouragement, sacrifice and dedicated efforts for carrying out this research work in aboard.

The Author

TABLE OF CONTENTS

EXPERIMENTAL DETAILS AND INSTRUMENTS SET UP

HYPERTHERMIA SUITABLE NANOPARTICLES PREPARED BY CO-PRECIPITATION AND HYDROTHERMAL METHOD

CYTOXICITY AND CANCER (HeLa) CELL KILLING EFFICACY OF AQUEOUS GARLIC (*Allium sativum*) EXTRACT

CHAPTER 1

INTRODUCTION

Over the past few years, a little word with big potential has been rapidly insinuating itself into the world's consciousness. That word is "nano." It has conjured up speculation about a seismic shift in almost every aspect of science and engineering with implications for ethics, economics, international relations, day-to-day life, and even humanity's conception of its place in the universe.

The term 'nanoparticle' is used to describe a particle with size in the range of 1 to 100 nm, at least in one of the three possible dimensions. In this size range, the physical, chemical and biological properties of the nanoparticles change in fundamental ways from the properties of both individual atoms/molecules and of the corresponding bulk material. Nanoparticles can be made of materials of diverse chemical nature, the most common being metals, metal oxides, silicates, non-oxide ceramics, polymers, organics, carbon and biomolecules. Nanoparticles exist in several different morphologies such as spheres, cylinders, platelets, tubes, etc. Generally, they are designed with surface modifications tailored to meet the needs of specific applications they are going to be used for [1].

Research on nanomaterials has evinced keen interest in recent years because of the new opportunities they present in nanocomposites, catalysis, environmental remediation and sensing [2–6]. Metal nanoparticles have potential applications in catalysis because of their large surface to volume ratio and unusual chemical reactivity [7]. Metal nanoparticles of different shapes could catalyze the reactions with different efficiencies because nanocrystals of different shapes represent various facets. Nanoparticles of silver, gold, copper, iron and its oxides, palladium and

platinum have found applications in catalyzing reactions [8–12] which offer immense scope for green chemistry. Iron and its oxide nanoparticles are excellent materials for environmental remediation [5]. Nanoscale materials are used as sorbents for contaminants, in nanofiltration and in reactive membranes [13]. The use of metal nanoparticles in sensing could bring about a revolution in biology, healthcare, military and day-to-day life [14].

The most significant consequences of the nanoscale are the presence of a high fraction of atoms/molecules constituting the nanoparticle on the particle surface rather than in the particle interior and the immense surface area available per unit volume of the material. Both of these properties increase in magnitude with a decreasing particle size. The unique physical, chemical and biological properties of nanomaterials originate from these two features. In some nanoscale materials quantum effects are exhibited allowing for a number of interesting applications. The small particle size leads to many unique properties of nanoparticles. Nanoparticles display interesting optical properties since the absorption and/or emission wavelengths can be controlled by particle size and surface functionalization. If the nanoparticle size is below the critical wavelength of light, then transparency can be attained. The chemical nature and the size of the nanoparticle control the ionic potential or the electron affinity and thereby the electron transport properties. For metals, with decreasing size of nanoparticles, the sintering and melting temperatures decrease. Nanoparticles may be incorporated into a solid matrix to provide better thermal conduction. For some metals and metal oxides, the decrease of the particle size results in improved magnetic behavior. Individual metallic magnetic nanoparticles can exhibit superparamagnetic behavior [1].

1.1 Facts of Nanoparticle, Nanoscience and Nanotechnology

The prefix "nano" means one billionth. One nanometer (abbreviated as 1 nm) is 1/1,000,000,000 of a meter, which is close to 1/1,000,000,000 of a yard. To get a sense of the nano scale, a human hair measures 50,000 nanometers across, a bacterial cell measures a few hundred nanometers across, and the smallest features that are commonly etched on a commercial microchip as of February 2002 are around 130 nanometers across. The smallest things seeable with the unaided human eye are 10,000 nanometers across. Just ten hydrogen atoms in a line make up one nanometer. It's really very small indeed [15] and understable by the diagram below [16].

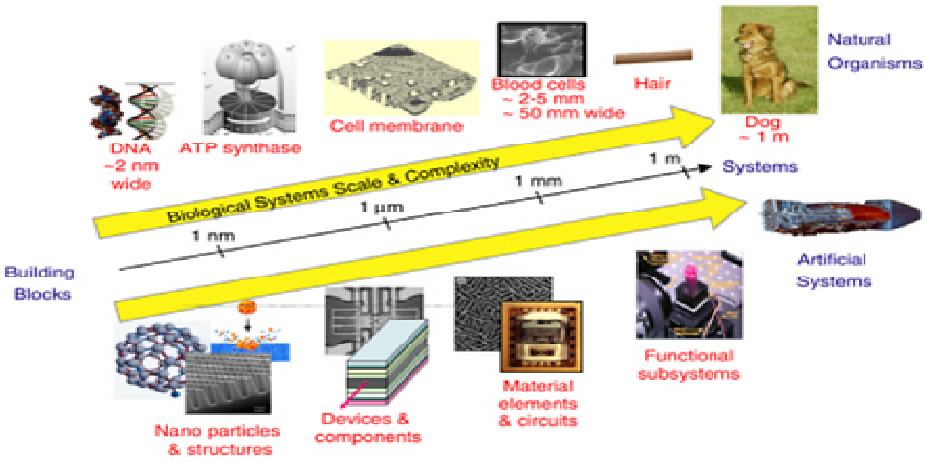

Fig. 1-1: Dimensional scale of nano

Nanoscience and nanotechnology are two of the hottest fields in science, business, and the news today. Since the 1980s, there has been a rapid expansion in the field now known as nanoscience [17]. The research area encompasses physics, chemistry, biology, engineering, medicine and materials science, and impacts on other disciplines as well. Nanoscience addresses a large number of important issues, with many of these having the potential for novel technical

applications. When the focus moves from the basic science towards the applications, the term nanotechnology is more commonly used. Nanoscience is generally defined as the study of phenomena on the scale of 1–100 nm, although it is often convenient to extend the range a little at either end.

Nanotechnology is the study of the control of matter on an atomic and molecular scale. Nanotechnology has promised to be one of the important growth areas in the twenty first century: it has the potential to create many new materials and devices with wide-ranging applications in medicine, electronics, energy production and so on. Nanotechnology is the ability to measure, design, and manipulate at the atomic, molecular and supramolecular levels on a scale of about 1 to 100 nm in an effort to understand, create, and use material structures, devices, and systems with fundamentally new properties and functions attributable to their small structures.

Nanotechnology for cancer research (also known as cancer nanotechnology) has been attracted as their effective size and shape structure of the nanoparticles. Nanotechnology is a multidisciplinary field, which covers a vast and diverse array of devices derived from engineering, biology, physics and chemistry. These nanoscale devices are somewhere from one hundred to ten thousand times smaller than human cells. They are similar in size to large biological molecules (biomolecules) such as enzyme and receptors. As an example, hemoglobin, the molecule that carries oxygen in red blood cells, is approximately 5 nanometers in diameter. Nanoscale devices smaller than 50 nm can easily enter most cells, while those smaller than 20 nm can move out of blood vessels as they circulate through the body [18-20].

1.2 Prospects and Application of Nanoparticles

It is evident that nanoparticles are going to have significant impacts on our daily life, ranging from fabrication of new construction materials to applications in biomedicine and

pharmaceuticals. Nanotechnology is already found in minute particles used in everyday products such as sunscreens. Many sunscreens today contain zinc oxide or titanium oxide nanoparticles that allow the creams to be absorbed into the skin, leaving no whitish residue behind. Nanoparticles are also used in scratch-resistant glass, wrinkle-resistant clothes, and stronger but lighter tennis rackets. Many scientists believe that nanotechnology is going to be as pervasive and revolutionary in the 21st century as plastics had been in the last century. By manipulating material properties at atomic level, researchers are expected to develop various promising systems and devices. Ranging from clean manufacturing techniques to amazing advancements in biomedical sciences, nanomaterials are predicted to have a profound impact on human society. Recent research on biosystems at the nanoscale has created one of the most dynamic interdisciplinary research and application domains for human discovery and innovation (Fig. 1-2).

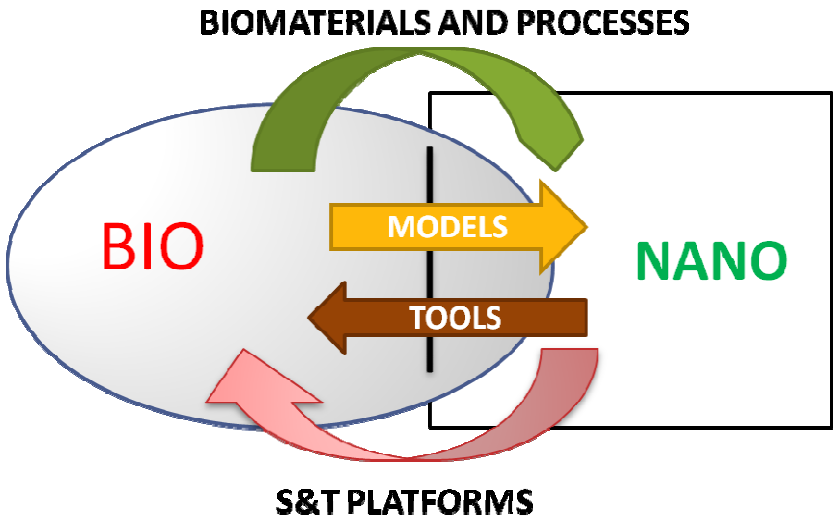

Fig.1-2: Interactions of Biology and Nanotechnology

Table.1-1 Types and Uses of Nanoparticles

Composition						
Structure	**Carbon**		**Metal**		**Ceramic/Silica**	
	Nanoparticle	**Examples of Uses**	**Nanoparticle**	**Examples of Uses**	**Nanoparticle**	**Examples of Uses**
Particle	Carbon black	Pigment; reinforcement of rubber products	Titanium dioxide (TiO_2)	Cosmetics; environmental remediation	Ceramic. nano-.particles	Coating on photo paper
	Nano-sized Wax particles	Car wax	Zero-valent iron; nanomagnetite (Fe_3O_4)	Environmental remediation		
			Silver	Antibacterial agent in wound care, athletic clothing, washing machines		
			Zinc oxide	Cosmetics		
			Cerium oxide	Diesel additive to decrease emissions		
Tube/wire	Carbon nanotubes	Electronics; sporting goods	Nanowire			
Dendrimer	G5 dendrimer	Targeted drug delivery	Iron sulfide clusters immobilized in dendrimers	Environmental remediation		
Other	Fullerene	Cosmetics	Quantum dots	Semi-conductors	Functionalized Ceramic, nano-porous sorbents	Water treatment

Applications based on nanotechnology offer many promising current and long term benefits in several areas of technology [21]. The technology is currently being employed to improve existing products and processes such as creating stain and water repellent clothing, strengthening the materials used in golf clubs and bicycle frames and producing wear resistant paints and coatings. In the long term scenario, nanotechnology promises to make revolutionary advances in a variety of fields. Possible uses of nanomaterials may include the cleaning of heavily polluted

sites, more effective diagnosis and treatment of cancer, cleaner manufacturing methods and much smaller and more powerful computers. Research shows that nanotechnology even may help create an alternative automotive fuel.

In the area of health and medicine, nanotechnology is expected to revolutionize the detection, prevention and treatment of various diseases. For instance, using buckyballs, scientists may be able to create nanodevices that can enter cells or even travel easily throughout the bloodstream. These devices may thus facilitate access to parts of the body that were previously not easily accessible. Additionally, it is hoped that buckyballs may be effective in the targeted delivery of medications directly to infected regions of the body. By placing the medication inside an array of buckyballs and injecting them into the bloodstream, the buckyballs can find their way to the diseased site and release the drug at specific target [22].

1.3 Magnetic Nanoparticles

Magnetic nanosized particles have already been known for over 50 years, but research into their potential use in medicine and pharmaceutics is now the hot topic in this domain. In bulk materials, magnetism occurs in a limited range of the periodic table. Iron, cobalt and nickel exhibit ferromagnetism due to the unfilled 3d electron bands, while their neighbours chromium and manganese display antiferromagnetism of various degrees of complexity. The rare earths, with unfilled 4f shells, exhibit complex magnetic order. At the atomic level, on the other hand, the majority of elements show a non-zero magnetic moment in the ground state. Nanoparticles are intermediate between atoms and bulk and an enhanced magnetic moment is observed for Fe, Co and Ni clusters up to several hundred atoms in size. An essential feature in a description of magnetic behaviour is the anisotropy energy. This arises from dipolar interactions or the spin–orbit interaction and leads to a preferred axis (or axes) along which the moment tends to align

(easy axis). Below the Curie temperature, the strong exchange interaction between spins on different atoms aligns them parallel (in the case of ferromagnetism). If a magnetic field is applied to reverse the spin direction, the anisotropy barrier has to be overcome; the strength of field required to do this is known as the coercivity and is a factor in determining the shape of the hysteresis loop [23].

In the past decade, the synthesis of superparamagnetic nanoparticles has been intensively developed not only for its fundamental scientific interest but also for many technological applications: among others, magnetic storage media, [24] biosensing applications, [25] medical applications, such as targeted drug delivery, [26, 27] contrast agents in magnetic resonance imaging (MRI), [28-35] and magnetic inks for jet printing [36]. Superparamagnetic iron oxide nanoparticles with appropriate surface chemistry can be used for numerous *in vivo* applications, such as MRI contrast enhancement, tissue repair, immunoassay, detoxification of biological fluids, hyperthermia, drug delivery, and cell separation [37]. All of these biomedical applications require that the nanoparticles have high magnetization values, a size smaller than 100 nm, and a narrow particle size distribution. Iron oxides exist in many forms in nature, with magnetite (Fe_3O_4), maghemite (γ-Fe_2O_3), and hematite (α-Fe_2O_3) being probably the most common [38]. These three oxides are also very important technologically and some of their physical and magnetic properties are summarized in Table. 1-2.

Table.1-2 Physical and magnetic properties of iron oxides [38]

Property	Oxides		
	Magnetite	**Maghemite**	**Hematite**
Molecular formula	*Fe_3O_4*	*γ-Fe_2O_3*	*α–Fe_2O_3*
Density (g/cm^3)	*5.18*	*4.87*	*5.26*
Melting point (°C)	*1583-1597*	-	*1350*
Hardness	*5.5*	*5*	*6.5*
Type of magnetism	*Ferromagnetic*	*Ferrimagnetic*	*Weakly ferromagnetic or antiferromagnetic*
Curie temperature (k)	*850*	820-986	*956*
*M*s at 300k (A-m^2/kg)	*92-100*	60-80	*0.3*
Standard free energy of formation $\Delta G_f°$ (kJ/mol)	*-1012.6*	-71.1	*-742.7*
Crystallographic system	*Cubic*	Cubic or tetrahedral	*Rhombohedral, hexagonal*
Structure type	*Inverse spinel*	Deflect spinel	*Corundum*
Space group	*Fd3m*	$P4_332$ (cubic); $P4_12_12$ (tetragonal)	*R3c (hexagonal)*
Lattice parameter (nm)	*a = 0.8396*	a = 0.83474 (cubic); a = 8347, c = 2.501 (tetragonal)	*a = 0.5034, c = 1.375 (hexagonal)* a_{Rh} *= 0.5427, α = 55.3°* (rhombohedral)

1.3.1 Synthesis Methods

Magnetic nanoparticles have been synthesized with a number of different compositions and phases, including iron oxides, such as Fe_3O_4 and γ-Fe_2O_3, [39- 41] pure metals, such as Fe and Co, [42, 43] spinel-type ferromagnets, such as $MgFe_2O_4$, $MnFe_2O_4$, and $CoFe_2O_4$, [44, 45] as well as alloys, such as $CoPt_3$ and FePt [24, 46]. In the last decades, much research has been devoted to the synthesis of magnetic nanoparticles. Especially during the last few years, many publications have described efficient synthetic routes to shape-controlled, highly stable, and monodisperse magnetic nanoparticles. Several popular methods including co-precipitation, thermal decomposition and/or reduction, micelle synthesis, hydrothermal synthesis, and laser pyrolysis techniques can all be directed at the synthesis of high-quality magnetic nanoparticles.

Co-Precipitation

Co-precipitation is a facile and convenient way to synthesize iron oxides (either Fe_3O_4 or γ-Fe_2O_3) from aqueous Fe^{2+}/Fe^{3+} salt solutions by the addition of a base under inert atmosphere at room temperature or at elevated temperature.

Thermal Decomposition

Inspired by the synthesis of high-quality semiconductor nanocrystals and oxides in non-aqueous media by thermal decomposition, similar methods for the synthesis of magnetic particles with control over size and shape have been developed. Monodispersed magnetic nanocrystals with smaller size can essentially be synthesized through the thermal decomposition of organometallic compounds in high-boiling organic solvents containing stabilizing surfactants [47].

Microemulsion

A microemulsion is a thermodynamically stable isotropic dispersion of two immiscible liquids, where the microdomain of either or both liquids is stabilized by an interfacial film of surfactant molecules [48]. In water-in-oil microemulsion, the aqueous phase is dispersed as microdroplets (typically 1–50 nm in diameter) surrounded by a monolayer of surfactant molecules in the continuous hydrocarbon phase. The size of the reverse micelle is determined by the molar ratio of water to surfactant [49]. By mixing two identical water-in-oil microemulsions containing the desired reactants, the microdroplets will continuously collide, coalesce, and break again, and finally a precipitate forms in the micelles [37]. By the addition of solvent, such as acetone or ethanol, to the microemulsion, the precipitate can be extracted by filtering or centrifuging the mixture. In this sense, a microemulsion can be used as a nanoreactor for the formation of nanoparticles.

Hydrothermal Synthesis

Under hydrothermal conditions a broad range of nanostructured materials can be formed. Li et al. reported a generalized hydrothermal method for synthesizing a variety of different nanocrystals by a liquid–solid–solution reaction. The system consists of metal linoleate (solid), an ethanol–linoleic acid liquid phase, and a water–ethanol solution at different reaction temperatures under hydrothermal conditions [50].

Sol-gel process

The sol-gel process involves the hydrolysis, condensation and thermal decomposition of metal alkoxides or metal precursors in solution [51]. In this process, the metal alkoxides or precursors form a stable solution with all necessary reagents, which is referred to as the sol. Then, the sol would undergo hydrolysis and condensation to form a networked structure (gel), resulting in a marked increase in the viscosity. Water, alcohol, acid or base can be used to control the kinetics of the reactions. The change in precursor concentration, temperature and pH values enables the particle size to be tuned. After the gel formation, an aging step is required to enable the formation of a solid mass. The aging step may take up to several days in which the expulsion of solvent, Ostwald ripening and phase transformation could occur. Finally, the gel would be subjected to a high-temperature treatment to decompose the organic precursors and remove the volatile reagents to yield the nanoparticles.

1.3.2 Applications in Catalysis and Biotechnology

Magnetic nanoparticles with good stability will be of great interest in catalysis and in biotechnology/biomedicine applications. Such magnetic nanoparticles can be very useful to assist an effective separation of catalysts, nuclear waste, biochemical products, and cells [52–54].

In biotechnology and biomedicine, magnetic separation can be used as a quick and simple method for the efficient and reliable capture of specific proteins or other biomolecules. Most particles currently used are superparamagnetic, meaning that they can be magnetized with an external magnetic field and immediately redispersed once the magnet is removed. Magnetic iron oxide nanoparticles grafted with dopamine have been used for protein separation [55]. The dopamine molecule has bidentate enediol ligands which can convert the coordinatively unsaturated iron surface sites back into a bulk-like lattice structure with an octahedral geometry for the oxygen-coordinated iron centers, resulting in tight binding of dopamine to iron oxide [56]. The resulting nanostructure can act as an anchor to further immobilize nitrilotriacetic acid molecules. This new material exhibits high specificity for protein separation and exceptional stability to heating and high salt concentrations. Magnetic nanoparticles are ideal molecular carriers for gene separation owing to their high separation efficiency [57]. The collection and then the separation of rare DNA/mRNA targets which have single-base mismatches in a complex matrix are critically important in human disease diagnostics, gene expression studies, and gene profiling. Tan et al. have synthesized a geomagnetic nanocapturer (GMNC) for the collection, separation, and detection of trace amounts of DNA/RNA molecules with one single-base difference [58]. GMNC was fabricated with a magnetic nanoparticle as core, silica coating as a protecting and biocompatible layer, and avidin-biotin molecules as linkers for bioconjugating a molecular beacon as the DNA probe. It was demonstrated that GMNC shows highly efficient collection of trace amounts of DNA/mRNA samples down to femtomolar concentrations and is able to real-time monitor and confirm the collected gene products. Avery promising application of magnetic nanoparticles is in drug delivery as drug carriers, that is, so called “magnetic drug delivery” proposed in the 1970s by Widder *et al.* [59]. The concept of magnetic targeting is to

inject magnetic nanoparticles to which drug molecules are attached, to guide these particles to a chosen site under the localized magnetic field gradients, hold them there until the therapy is complete, and then to remove them. The magnetic drug carriers have the potential to carry a large dose of drug to achieve high local concentration, and avoid toxicity and other adverse side effects arising from high drug doses in other parts of the organism. Although considerable achievements have been reached in *in vivo* applications, to date, actual clinical studies are still problematic.

Another interesting application of magnetic nanoparticles is in hyperthermia treatment which is considered as a supplementary treatment to chemotherapy, radiotherapy, and surgery in cancer therapy [60, 61]. The idea of using magnetic induction hyperthermia is based on the fact that when magnetic nanoparticles are exposed to a varying magnetic field, heat is generated by the magnetic hysteresis loss, Neel-relaxation, and Brown-relaxation [62, 63]. The amount of heat generated by magnetic nanoparticles depends strongly on the structural properties of the particles (e.g., size, shape) and should be as high as possible to reduce the dose to a minimum level. However, the following **Table.1-3** and **Table.1-4** indicate some important usages of magnetic nanoparticles in biological systems [64].

Table.1-3 List of the most commonly used biodegradable magnetic particles

Matrix of magnetic particles	Biomedical application
Erythrocytes	Drug targeting Cell separation
Liposomes	Drug targeting
Phospholipids	Immobilization of membrane bound enzymes
Albumin	Drug targeting Cell separation
Starch	Drug targeting MRI Radiotherapy
Poly(lactic acid)	Radiotherapy
Dextran	Cell separation Enzyme immobilization MRT Local hyperthermia Drug targeting Immunoenzyme assay
Chitosan	Drug targeting
Polyalkylcyanoacrylate	Drug targeting
Polyethylene imine	Drug targeting

Table.1-4 List of the most commonly used non-biodegradable magnetic particles

Matrix of magnetic particles	Biomedical application
Ethyl-cellulose	Arterial chemo-embolization
Synthetic polymers (e.g., polystyrene, polymethylmetacrylate parasites	Magnetic separation of bacteria, virus, mRNA-purification Isolation of specific gene sequences Immunomagnetic assays

1.3.3 Application to Cancer Therapy

The magnetic properties of iron oxides have been exploited in a broad range of applications including magnetic seals and inks, magnetic recording media, catalysts, and ferrofluids , as well

as in contrast agents for magnetic resonance imaging and therapeutic agents for cancer treatment. These applications demand nanomaterials of specific sizes, shapes, surface characteristics, and magnetic properties [65]. Magnetic nanoparticles have been investigated for biomedical applications for more than 30 years. In medicine they are used for several approaches such as magnetic cell separation or magnetic resonance imaging (MRI). The development of biocompatible nanosized drug delivery systems for specific targeting of therapeutics is the focus of medical research, especially for the treatment of cancer and diseases of the vascular system [66]. Superparamagnetic iron oxide nanoparticles (SPION), especially Fe_3O_4 (Magnetite) and γ-Fe_2O_3 (Maghemite) have been tested for its efficacy in cancer therapy. But still there is a great opportunity for progressive researchers to find out the cancer cell killing potentiality of superparamagnetic nanoparticles. Several possibilities for use of SPION in vitro and in vivo are outlined below.

a) In vitro use of SPION

SPION have proven to be very useful tools for magnetic separation techniques in clinical use and have replaced other separation technologies. This is true for Immunomagnetic cell separation and purification, as solid phase for immunoassays for isolation, purification and recognition of proteins. In addition they are used for molecular biology, where they were shown to be useful for the isolation, purification, hybridization, synthesis and as markers for DNA/ RNA [67]. The isolation and detection of microorganisms is easily possible using SPION [67], as well as efficient gene transfer of nucleotides or gene sequences into cells [68]. In medical and clinical diagnostics, the interaction of antigens and antibodies is routinely used to measure concentrations of biological markers. Traditionally, antibodies and/or antigens are immobilized as solid phases on filters, tubular structures, plastic spheres or plates. The use of SPION as solid

phases for these separation techniques has revolutionized and simplified this field of clinical chemistry through the development of more sensitive, highly efficient and automated immunoassays [69]. SPION have also demonstrated their efficiency as non-viral gene vectors that facilitate the introduction of plasmids into the nucleus multifold compared to routinely available standard technologies. As in cell separation, the applied magnetic field allows transporting the genes selectively to the desired local cells within cell cultures. This is possible for the investigation of cell differentiating factors in non-gene manipulated neighboring cells within the same cell culture [68].

b) In vivo application of SPION

Magnetic resonance imaging: Clinical diagnostics with MRI has become a popular non-invasive method for diagnosing mainly soft tissue or recent cartilage pathologies, because of the different relaxation times of hydrogen atoms. SPION were developed as contrast agents for MRI and increase the diagnostic sensitivity and specificity due to modifications of the relaxation time of the protons [69]. The first dextran coated SPION were already 10 years ago officially registered as contrast agents for MRI of the liver in Europe [70]. The efficacy of the SPION as contrast agent in various tissues depends on their physicochemical properties, such as size, charge and coating [71], and can be increased through surface modifications by biologically active substances (antibodies, receptor ligands, polysaccharides, proteins, etc.) [69].

c) Magnetic drug targeting (MDT)

One of the major problems in pharmacotherapy is the delivery of drugs to a specific location and maintenance of its location for the desired length of time. The total concentration of drugs could be reduced drastically and side effects could be avoided. Using an external magnetic field, SPION functionalized with reversibly bound drugs could be delivered to specific locations and

localized in place [72, 73]. The method of MDT is not only dependent on the physical properties, concentration and amount of applied particles, but also on the type of binding of the drugs. But also in vivo SPION were successfully applied intravenously and accumulated at specific locations by means of external magnets [68, 72, 73]. This is especially attractive for use in cancer therapy, where chemo- or radiotherapy is demonstrating serious, extensive side effects while only having a small therapeutic margin. Different methods were investigated such as thermo- and pH sensitive liposomes containing encapsulated chemotherapeutical agents or tumor specific antibodies [72]. MDT with SPION was also successfully used in gene therapy (magnetofection) in first experiments [68]. The transfect ion efficiency of commonly used viral vectors could be increased up to 100-fold through coupling of these vectors to SPION and application of an external magnetic field. The duration of the gene transport could be reduced to a few minutes, the tropism of adenoviral vectors could be enforced and the low titer of retroviral vectors compensated. The efficiency of this system could be reproducibly proven in vitro and in vivo in gene transport to cells of the gastrointestinal tract in rodents as well as in blood vessels of pigs.

d) Hyperthermia with magnetic ferrofluids

Hyperthermia is a cancer treatment modality that destroys tumors by elevating the temperature of the cancerous tissue to approximately 43 °C for 20–60 min [74]. The temperature in tumor tissues rises much easier than in normal tissues because the tumor tissues have higher heat sensitivity and a smaller cooling effect due to their blood flow. Hyperthermia is a therapeutic technique that is used against tumors for a small percentage of patients in the conjunction with other techniques such as surgical operation, chemotherapy and radiotherapy. However, the hyperthermia is expected in the future to be one of the most important treatments

for many kinds of cancer. Considering the method of heating, hyperthermia can be divided into three broad categories: whole body hyperthermia, regional hyperthermia and local hyperthermia. In the first two methods, a rising temperature is induced over a general volume containing the tumor. In local hyperthermia a focused heating is performed. The latter mentioned method is often preferred, since the capability of heating only the desired volume (tumor) without affecting the surrounding tissue is more ideal [75]. One of the most promising methods of localized hyperthermia is locating exothermic ferrite particles at the tumor site and then radiating this volume with AC magnetic fields. The cornerstone for the broad and reliable clinical use of hyperthermia in cancer treatment is a heat delivery technique that must provide a controlled, local thermal effect within the whole mass of the cancerous tissue while leaving normal tissues unaffected. Moreover, the technique as well must deliver the heat systemically to a tumor deep within the body.

1.4 Cancer Facts

Cancer (medical term: malignant neoplasm) is a large, heterogeneous class of diseases in which a group of cells display uncontrolled growth, invasion that intrudes upon and destroys adjacent tissues, and often metastasizes, wherein the tumor cells spread to other locations in the body via the lymphatic system or through the bloodstream. These three malignant properties of cancer differentiate malignant tumors from benign tumors, which do not grow uncontrollably, directly invade locally, or metastasize to regional lymph nodes or distant body sites like brain, bone, liver, or other organs [76]. Cancer is a clonal origin. It is a multi-gen, multi-step diseases originating from a single abnormal cell.

Researchers divide the causes of cancer into two groups: those with an environmental cause, and those with a hereditary genetic cause. Cancer is primarily an environmental disease, though genetics influence the risk of some cancers [77].

World Cancer Day 2011 is promoting ways to prevent cancer, particularly through being physically active. Physical inactivity is linked to breast and colon cancers. Almost 460,000 females died from breast cancer in 2008, while close to 610,000 males and females died from colorectal cancer [78]. Prostate cancer incidence is prominence in male whereas breast cancer incidence major in female worldwide. But liver and lung cancer incidence is also somewhat prominence in case of both sexes from whole over the world (Fig. 1-2 and Fig. 1-3) [79].

Cancer is a leading cause of death worldwide: it accounted for 7.9 million deaths (around 13% of all deaths) in 2007 and the total number of cases globally is increasing.

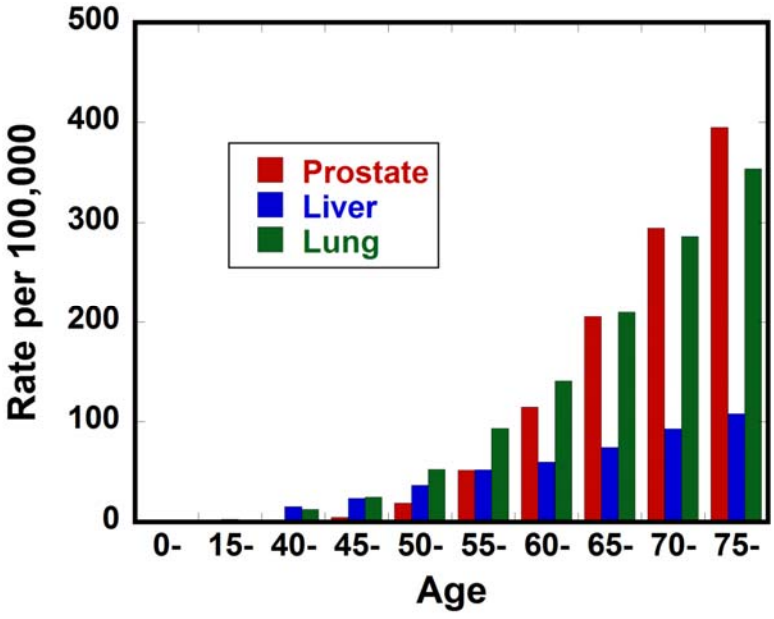

Fig.1-2: Worldwide cancer incidence for male.

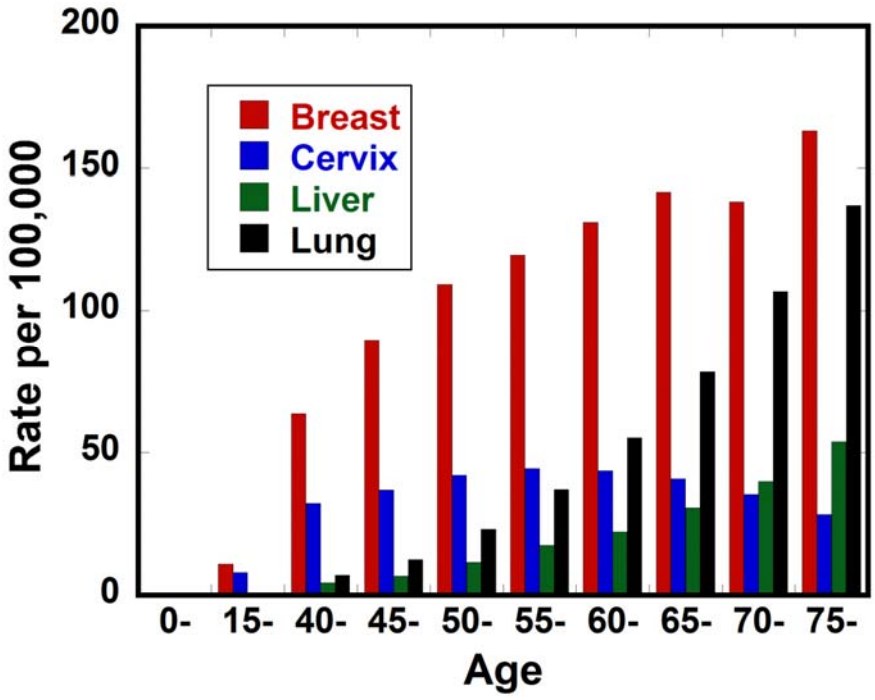

Fig.1-3: Worldwide cancer incidence for female.

Lung, stomach, liver, colon and breast cancer cause the most cancer deaths each year (Fig.1-4). The number of global cancer deaths is projected to increase 45% from 2007 to 2030 (from 7.9 million to 11.5 million deaths), influenced in part by an increasing and aging global population. The estimated rise takes into account expected slight declines in death rates for some cancers in high resource countries.

New cases of cancer in the same period are estimated to jump from 11.3 million in 2007 to 15.5 million in 2030. In most developed countries, cancer is the second largest cause of death after cardiovascular disease, and epidemiological evidence points to this trend emerging in the less developed world. This is particularly true in countries in "transition" or middle-income countries, such as in South America and Asia. Already more than half of all cancer cases occur in developing countries. Lung cancer kills more people than any other cancer - a trend that is expected to continue until 2030, unless efforts for global tobacco control are greatly intensified.

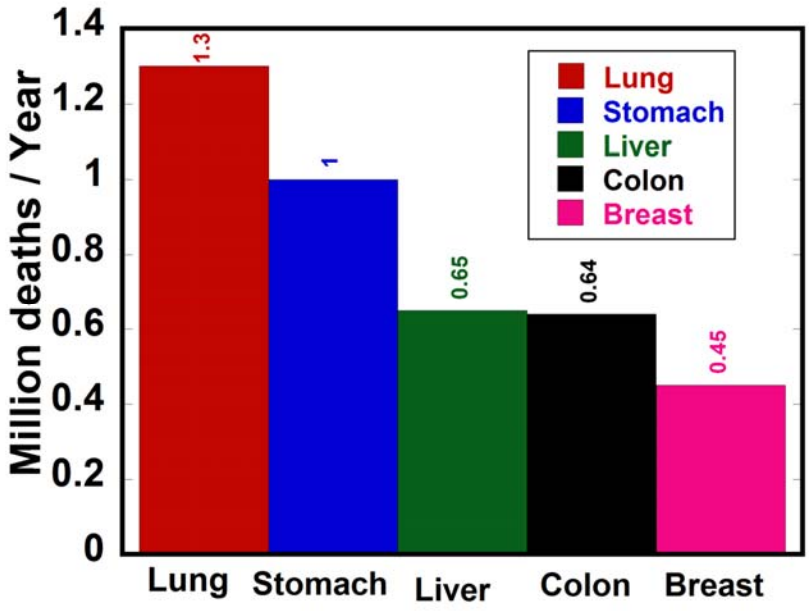

Fig. 1-4: Cancer fact in worldwide.

Some cancers are more common in developed countries: prostate, breast and colon where as Liver, stomach and cervical cancer is more common in developing countries. A number of common risk factors have been linked to the development of cancer: an unhealthy lifestyle (including tobacco and alcohol use, inadequate diet, physical inactivity), and exposure to occupational (e.g. asbestos) or environmental carcinogens, (e.g. indoor air pollution), radiation (e.g. ultraviolet and ionizing radiation), and some infections (such as hepatitis B or human papilloma virus infection) [80].

1.4.1 Definition of Cancer

Cancer is a group of diseases characterized by uncontrolled growth and spread of abnormal cells. If the spread is not controlled, it can result in death [81].

Cancer is an abnormal growth of cells caused by multiple changes in gene expression leading to deregulated balance of cell proliferation and cell death and ultimately evolving into a population of cells that can invade tissues and metastasize to distant sites, causing significant morbidity and, if untreated, death of the host. Cancer usually forms as a tumor. Some cancer, like leukemia, does not form tumors. Instead, these cancer cells involve the blood and blood-forming organs and circulate through other tissues where they grow. Often, not all tumors are cancerous. Benign (noncancerous) tumors do not spread (metastasize) to other parts of the body and, with very rare exceptions, are not life threatening [82].

Cancer develops when cells in a part of the body begin to grow out of control. Although there are many kinds of cancer, they all start because of out-of-control growth of abnormal cells. Under normal conditions, the cells in the human body divide and grow in an orderly, controlled manner. Cancer occurs when cells grow in an uncontrolled manner. Instead of dying, they outlive normal cells and continue to form new abnormal cells (Fig. 1-5) [76, 83]. The cancer cell is profoundly abnormal cells which can be observed under simple optical microscope. Cancer cell's morphology is different from that of a normal cell. Its nucleus is larger and irregular.

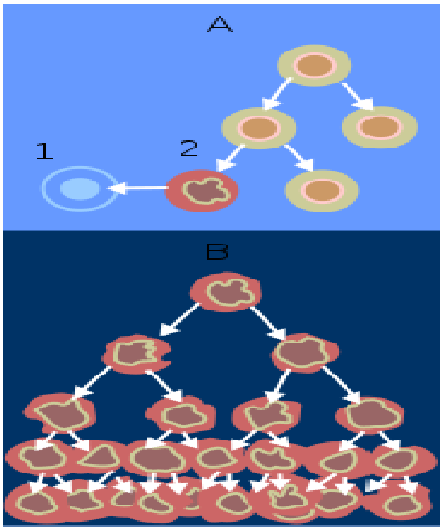

Fig.1-5: Normal and Cancer Cell Division. When normal cells are damaged beyond repair, they are eliminated by apoptosis (A). Cancer cells avoid apoptosis and continue to multiply in an unregulated manner (B).

1.4.2 Causes of cancer

Perhaps the most important question in cancer biology is what causes the cellular alterations that produce a cancer. The answer to this question has been elusive. If the actual cause of these alterations were known, the elimination of factors that produce cancer and the development of better treatment modalities would likely follow. Cancer prevention might become a reality. A cancerous growth has a number of predictable properties. The incidence rates of various cancers are strongly related to environmental factors and lifestyle, and cancers have certain growth characteristics, among which are the abilities to grow in an uncontrolled manner, invade surrounding tissues, and metastasize. Also, when viewed microscopically, cancer cells appear to be less well differentiated than their normal counterparts and to have certain distinguishing features, such as large nuclei and nucleoli. Most cancers arise from a single clone of cells, whose precursor may have been altered by insult with a carcinogen. In most cases cancer is a disease of aging.

It is almost always impossible to prove exactly what caused a cancer in any individual, because most cancers have multiple possible causes. For example, if a person who uses tobacco heavily develops lung cancer, then it was very probably caused by the tobacco use, but since everyone has a small chance of developing lung cancer as a result of air pollution or radiation, then there is a tiny chance that the smoker's lung cancer actually developed because of air pollution or radiation [76].

Cancers are primarily an environmental disease with 90-95% of cases attributed to environmental factors and 5-10% due to genetics. *Environmental*, as used by cancer researchers, means any cause that is not genetic, not merely pollution. Common environmental factors that

contribute to cancer death include *tobacco* (25-30%), diet and *obesity* (30-35%), *infections* (15-20%), *radiation* (both ionizing and non-ionizing, up to 10%), stress, lack of *physical activity*, and *environmental pollutants* [77]. A brief discussion of the main cancer causes are presented here.

Chemicals

Cancer pathogenesis is traceable back to DNA mutations that impact cell growth and metastasis. Substances that cause DNA mutations are known as mutagens, and mutagens that cause cancers are known as carcinogens. Particular substances have been linked to specific types of cancer. Tobacco smoking is associated with many forms of cancer [84], and causes 90% of lung cancer [85].

Diet and exercise

Diet, physical inactivity, and obesity are related to approximately 30–35% of cancer cases [77, 86]. In the United States excess body weight is associated with the development of many types of cancer and is a factor in 14–20% of all cancer deaths [86]. Physical inactivity is believed to contribute to cancer risk not only through its effect on body weight but also through negative effects on immune system and endocrine system [86].

Infection

Worldwide approximately 18% of cancers are related to infectious diseases [77]. This proportion varies in different regions of the world from a high of 25% in Africa to less than 10% in the developed world [77]. Viruses are usual infectious agents that cause cancer but bacteria and parasites may also have an effect.

Radiation

Up to 10% of invasive cancers are related to radiation exposure, including both ionizing radiation and non-ionizing radiation [77]. Additionally, the vast majority of non-invasive cancers are non-melanoma skin cancers caused by non-ionizing radiation from ultraviolet radiation. Sources of ionizing radiation include medical imaging, and radon gas. Radiation can cause cancer in most parts of the body, in all animals, and at any age, although radiation-induced solid tumors usually take 10–15 years, and can take up to 40 years, to become clinically manifest, and radiation-induced leukemias typically require 2–10 years to appear [87].

Heredity

The vast majority of cancers are non-hereditary, which are called *sporadic cancers*. Hereditary cancers are cancers that are primarily caused by an inherited genetic defect. Less than 0.3% of the population is carriers of a genetic mutation which has a large effect on cancer risk [88]. They cause less than 3–10% of all cancer [88].

Physical agents

Some substances cause cancer primarily through their physical, rather than chemical, effects on cells [89]. A prominent example of this is prolonged exposure to asbestos, naturally occurring mineral fibers which are a major cause of mesothelioma, a type of lung cancer [89]. Other substances in this category include both naturally occurring and synthetic asbestos-like fibers, such as wollastonite, attapulgite, glass wool, and rock wool, are believed to have similar effects [89].

Physical trauma and inflammation

Physical trauma resulting in cancer is relatively rare [90]. Claims that breaking bone resulted in bone cancer, for example, have never been proven [90]. Similarly, physical trauma is not accepted as a cause for cervical cancer, breast cancer, or brain cancer [90].

Hormones

Some hormones factor in the development of cancer by promoting cell proliferation [91]. Hormones are important agents in sex-related cancers such as cancer of the breast, endometrium, prostate, ovary, and testis, and also of thyroid cancer and bone cancer [91]. An individual's hormone levels are mostly determined genetically, so this may at least partly explains the presence of some cancers that run in families that do not seem to have any cancer-causing genes [91].

Others

Excepting the rare transmissions that occur with pregnancies and only a marginal few organ donors, cancer is generally not a transmissible disease. The main reason for this is tissue graft rejection caused by MHC incompatibility [92]. In humans and other vertebrates, the immune system uses MHC antigens to differentiate between "self" and "non-self" cells because these antigens are different from person to person.

1.4.3 Cancer Scenarios in Japan

In Japan one in every three people dies of cancer. According to statistics compiled by the Ministry of Health, Labor and Welfare, 336,290 people died of cancer in 2007, accounting for

one in every three deaths. Heart diseases, the second biggest killer, accounted for only about half of the number of cancer deaths [93].

Cancer deaths in Japan are surveyed by vital statistics, with 100% coverage. The number of cancer deaths in 2009 in Japan was approximately 344,000. The number of male cancer deaths was 1.5 times greater than that of female cancer deaths. In terms of cancer sites, lung was the leading site (24%) for males, followed by stomach (16%), liver (10.5%), colon (7%; 3rd when colon and rectum are combined: 11%), and pancreas (7%). The leading site for females was lung (13%; Note that colon and rectum was the leading cancer death site when combined: 14%), followed by stomach (12.5%), colon (10%), pancreas (9%), and breast (8.7%) [94].

Cancer mortality rate (annual number of deaths per 100,000 population) in Japan in 2009 was approximately 336 for males and 214 for females. The mortality rates were higher among males than females for many cancer sites, especially oropharynx, esophagus, liver, larynx, lung, bladder, and kidney (over twice). On the other hand, female mortality rates were higher than male for gallbladder and thyroid. The cancer sites with the highest mortality rate in 2009 were lung, stomach, liver (same rank for colon and rectum combined), colon, and pancreas for males, lung (Note that colon/rectum was higher than stomach when combined.), stomach, colon, pancreas, and breast, for females [95]. However, Fig. 1-6 illustrates all cancer mortality for both genders in Japan in 2008 [79].

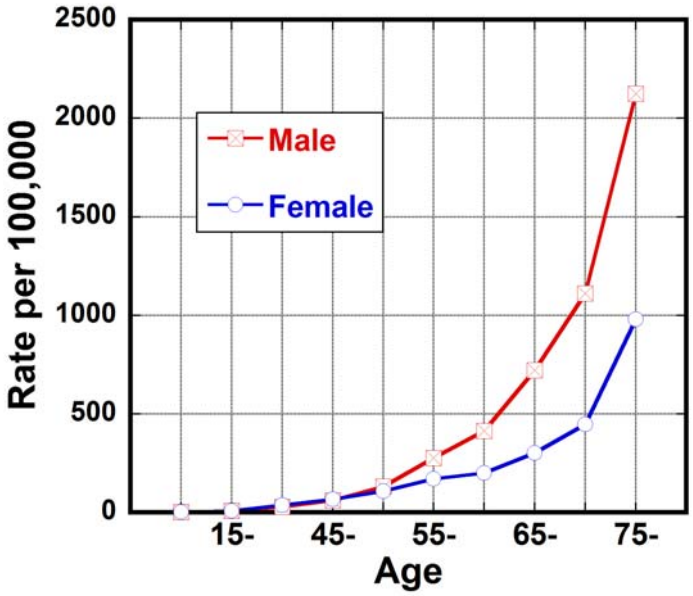

Fig.1-6: All cancer mortality in Japan (excluding non-melanoma skin cancer)

Cancer has been the leading cause of death in Japan since 1981. The Japanese government implemented the Comprehensive 10-year Strategy for Cancer Control (1984-1993) and the New 10-year Strategy to Overcome Cancer (1994-2003) to tackle cancer. Since 2004, the 3rd-term Comprehensive 10-year Strategy for Cancer Control has been implemented in order to promote cancer research and disseminate high-quality cancer medical services, with the slogan "Drastic reduction in cancer morbidity and mortality". In May 2005, the Japanese Ministry of Health, Labour and Welfare (MHLW) developed the Headquarters of Cancer Control. In July 2009, the Japanese MHLW developed the Headquarters of 50% Cancer Screening Rate to promote multidisciplinary activity for cancer screening [96].

1.4.4 Cancer Scenarios in Bangladesh

With the increase of the incidence of Cancer in the country, it has become a matter of serious concern for Bangladesh. It is estimated that there are around 800,000 cancer patients in the country of the 130 million people and about 200,000 new cases are being added every year.

Around 150,000 cancer patients die annually [97]. Cancer incidence and mortality for all cancer excluding non-melanoma skin cancer can be found for both genders in Fig. 1-7 and Fig. 1-8, respectively [79].

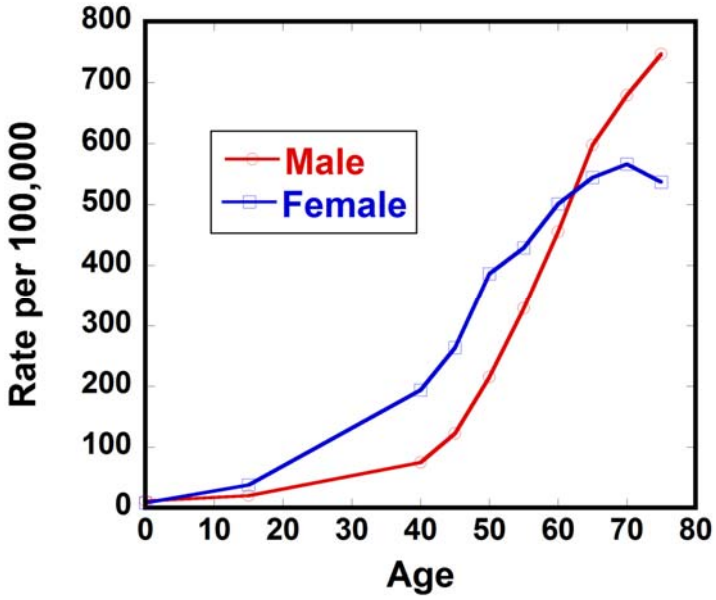

Fig. 1-7: Cancer incidence in Bangladesh (all cancer excluding non-melanoma skin cancer)

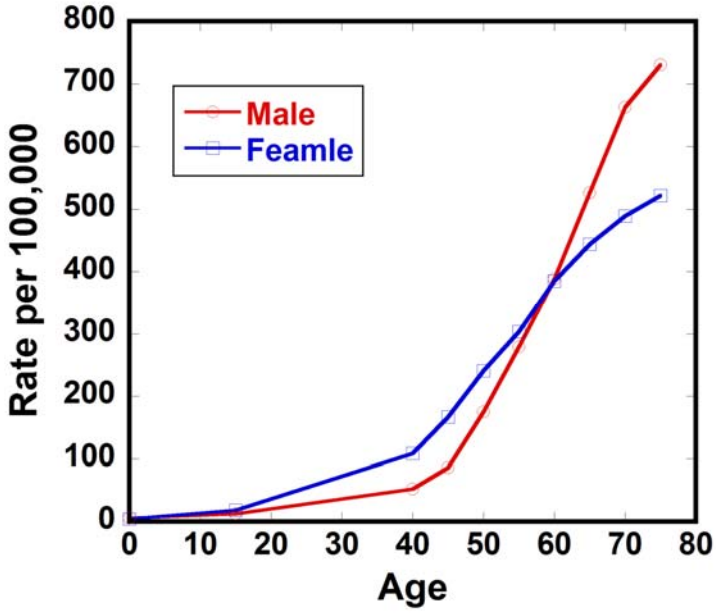

Fig. 1-8: Cancer mortality in Bangladesh (all cancer excluding non-melanoma skin cancer)

Both the cancer incidence and mortality is prominent in male than female because smoking is more common in male than female. Smoking is an increasingly prevalent habit in Bangladesh, particularly among men. In the past 10-15 years cigarette consumption has more than doubled [98].

1.4.5 Cancer Management and Therapy

Many management options for cancer exist including chemotherapy, radiation therapy, surgery, immunotherapy, monoclonal antibody therapy and other methods. Which are used depends upon the location and grade of the tumor and the stage of the disease, as well as the general state of a person's health. *Experimental cancer treatments* are also under development. It is well know that the tradition cancer treatment includes surgery, radiation, hormone therapy and more recently chemotherapy, immunotherapy and combines strategies [99].

Surgery

Surgery is the oldest form of treatment for cancer. It offers the greatest chance for cure for many types of cancer, especially those that have not yet spread to other parts of the body but not for cancers at late phase. It will continue to be an extremely important weapon against cancer. Complete removal of the cancer without damage to the rest of the body is the goal of treatment. Sometimes this can be accomplished by surgery, but the propensity of cancers to invade adjacent tissue or to spread to distant sites by microscopic metastasis often limits its effectiveness. Surgery often required the removal of a wide surgical margin or a free margin. The width of the free margin depends on the type of the cancer, the method of removal.

Radiation therapy

Radiation is the second weapon against cancer. Radiation therapy involves treating cancer with beams of high-energy particles, or waves (radiation), such as X-rays, gamma rays, neutrons or pimesons [100]. Radiotherapists often implant radioactive materials or radioisotopes into tumors. The particles transfer their energy into electrons which ionize the matter they reach such as water and/or the solid constituents of cytoplasm, RNA and DNA. This ionization damages the molecules and leads the free radicals to recombine with oxygen available in the environment.

Thus changes the biological properties of the biomolecules such as causing the cell to die or make it impossible to divide. Radiation is much more harmful to cancer cells than it is to normal cells. This is because cancer cells divide more rapidly than do healthy cells. Cells are more vulnerable to damage when they're dividing, making cancer cells to be more susceptible to radiation than normal cells. In addition, normal cells can recover from the effects of radiation more easily than cancer cells. But still it is nonetheless true that it is impossible to kill a tumor without harming the surrounding healthy cells. Radiation can also cause damage to normal tissue [101].

Hormone therapy

Hormone therapy changes the internal environment and prevents the growth of cancers that are hormone-dependent such as breast and prostate cancers. It is usually called androgen deprivation therapy (ADT) or androgen suppression therapy. Controlling cancer of the prostate is the triumph of hormone therapy. Androgens, produced mainly in the testicles, can actually stimulate prostate cancer cells to grow. Hormone therapy is to lower androgen levels (either by surgery or drugs such as pituitary down-regulators and antiandrogens) can usually make prostate

cancers shrink or grow more slowly. A large body of evidence indicates that hormones have an important role in the causation of cancer in women and men. For example, female hormones have been linked to the development of cancers of the breast, uterine endometrium, and ovary. Male hormones are implicated in the cause of prostate cancer. This type of hormone induced carcinogenesis appears to result from the ability of hormones to stimulate cell division in hormone target organs. This may in turn lead to an increased probability of accumulating genetic errors over time. It is estimated that hormone-related cancers account for at least 20% of all male and 40% of all female cancers in the United States [102]. Thus, chemoprevention of cancer by the manipulation of hormone levels or by the use of ‘‘antihormones’’ is a legitimate strategy. Several hormonal chemopreventive agents have been shown to be effective as chemopreventive agents and others are under intense clinical study.

Chemotherapy

Chemotherapy is a major therapeutic approach for the treatment of localized and metastasized cancers. The selective increase in tumor tissue uptake of anticancer agents would be of great interest in cancer chemotherapy since anticancer drugs are not specific to cancer cells. Routes of administration, biodistribution and elimination of available chemotherapeutic agents can be modified by drug delivery systems to optimize drug therapy [103]. It is most often used to mean taking medicines, or drugs, to treat cancer, especially suitable for those cancers that have been spread out and cannot be used by the local methods such as surgery and radiation. Normal cells grow and die in a controlled way. Cancer cells keep dividing and forming more cells without control. Anticancer drugs destroy cancer cells by stopping them from growing or multiplying. They also go after and damage any healthy cells that are quickly dividing, whether it's a cancer cell or not. Lately emerged photothermal therapy have greatly improved the therapy efficiency

by injecting contrast agents such as weak emitting dyes [104, 105] into the tumor sites which convert the photoengergy into thermal energy and thus kill the cancer cells. Photosensitizers are also been reported for photodynamic therapy which use photoexcited molecules to transfer their energy to oxygen forming excited singlet oxygen which injures cancer cells [106, 107]. The effectiveness of chemotherapy is often limited by toxicity to other tissues in the body.

Immunotherapy

With the development of immunology, immunotherapy (also known as biologic therapy) is emerged as a more specific cancer treatment method. Immunotherapy is a treatment that uses certain parts of the immune system to fight diseases, including cancer. This can be done by stimulating your own immune system to work harder or by using an outside source, such as manmade immune system proteins [108]. Compared to other forms of cancer treatment, such as surgery, radiation therapy, or chemotherapy, immunotherapy is relatively new. One of the immunotherapy is to use monoclonal antibody which specifically target the cancer cells and then block the cancer cell activation or cure the cancer cells by attaching radioactive chemicals on the antibodies [109]. Some monoclonal antibodies that react with specific antigens on certain types of cancer cells have been used in clinical trials [110]. Compared with side effects of standard chemotherapy, the side effects of naked MAbs are usually relatively mild and are often related to an "allergic" reaction.

1.4.6 Hyperthermia with magnetic ferrofluids under AC (alternating current) magnetic-field

Hyperthermia is a cancer treatment modality that destroys tumors by elevating the temperature of the cancerous tissue to approximately 43 °C for 20–60 min [74]. The temperature

in tumor tissues rises much easier than in normal tissues because the tumor tissues have higher heat sensitivity and a smaller cooling effect due to their blood flow. Hyperthermia is a therapeutic technique that is used against tumors for a small percentage of patients in the conjunction with other techniques such as surgical operation, chemotherapy and radiotherapy. However, the hyperthermia is expected in the future to be one of the most important treatments for many kinds of cancer. Considering the method of heating, hyperthermia can be divided into three broad categories: whole body hyperthermia, regional hyperthermia and local hyperthermia. In the first two methods, a rising temperature is induced over a general volume containing the tumor. In local hyperthermia a focused heating is performed. The latter mentioned method is often preferred, since the capability of heating only the desired volume (tumor) without affecting the surrounding tissue is more ideal [75]. One of the most promising methods of localized hyperthermia is locating exothermic ferrite particles at the tumor site and then radiating this volume with AC magnetic fields. The cornerstone for the broad and reliable clinical use of hyperthermia in cancer treatment is a heat delivery technique that must provide a controlled, local thermal effect within the whole mass of the cancerous tissue while leaving normal tissues unaffected. Moreover, the technique as well must deliver the heat systemically to a tumor deep within the body.

According to heat delivery techniques, hyperthermia can be classified into 3 categories [111]:

a) Whole body hyperthermia

Thermal energy is introduced into the body either non-invasively by use of hot wax, hot air, infra–red or RF radiation, or invasively by heating the extracorporeal blood. Thermal losses are minimized by using insulating blankets. It is not suitable for heating deep seated tumors.

b) Regional hyperthermia

Tumors within a large portion of the body (trunk or whole limbs) are heated with either non-invasive techniques including non-ionizing electromagnetic waves or ultrasound, or invasive techniques using interstitial implants.

c) Localized hyperthermia

Localized hyperthermia is heating a smaller volume of superficial tumor at a depth up to 4 cm by nonionizing electromagnetic waves, ultrasound or interstitial implants.

Basic principles of hyperthermia

Heating of certain organs or tissues to temperatures between 41 °C and 46 °C preferentially for cancer therapy is called “Hyperthermia”. Higher temperatures up to 56 °C, which yield widespread necrosis, coagulation or carbonization (depending on temperature) is called “thermo-ablation'. Both mechanisms act completely deferent concerning biological response and application technique. The ‘classical' hyperthermia induces almost reversible damage to cells and tissues, but as an adjunct it enhances radiation injury of tumor cells and chemotherapeutic efficacy. Modern clinical hyperthermia trials focus mainly on the optimization of thermal homogeneity at moderate temperatures (42-43 °C) in the target volume [112].

The essential feature of magnetic hyperthermia is that energy is absorbed from the alternating magnetic field and transformed into heat by means of one or combination of the following mechanisms [113].

1. Generation of eddy currents in a material of low electrical resistivity
2. Reversal of the magnetization inside a magnetic material
3. Rotation of the magnetic material relative to its surroundings

There are three issues that have to optimize to encourage more widespread clinical applications of hyperthermia [113].

(a) The generation of the temperature increase only within the target region (tumors) leaving all other regions unaffected.

(b) The temperature control within as well as outside the target region.

(c) The optimization of thermal homogeneity in the target volume.

To date, all magnetic nanoparticles intended to be used in vivo are composed of magnetic iron oxides. The main reason for this is their low toxicity and the known pathways of metabolism. The only two clinically relevant materials used are magnetite (Fe_3O_4) and maghemite (γ-Fe_2O_3). The crystal structures of both oxides are based on a cubic dense packing of oxide atoms, but they differ in the distribution of Fe ions in the crystal lattice [114].

1.4.7 Hyperthermia (Cancer) Research

Hyperthermia is a therapeutic procedure that promotes the increase of temperature in body tissues in order to change the functionality of the cellular structures. Its activity is based on the fact that a temperature increase of between 41 °C and 42 °C can induce tumor cell death, as the tumor cells are less resistant to sudden increases in temperature than the normal surrounding cells [115]. The rise in temperature changes the functioning of many enzymatic and structural proteins in the cells, in turn altering cell growth and differentiation, which can induce apoptosis [116, 117]. Changes triggered by hyperthermia in the cell membrane lead to a reduction in transmembrane transport and destabilize its potential [118,119]. It is also known that the rise in temperature can affect the synthesis of nucleic acids and inhibition of repair enzymes, and promote changes in the conformation of DNA [120]. The temperature increase required by hyperthermia can be achieved via different heat sources, such as electromagnetic radiation waves (hyperthermia by radiofrequency or microwave), ultrasound waves or electrically induced

hyperthermia [121-126]. These techniques have shown good results, however, the major problem with present conventional methods is reaching a heat homogenous distribution and therapeutic temperatures in the deep region of the tumor to be treated. In this sense, treatment failure results from an insufficient temperature rise in some parts of the tumor, allowing the tumor to recur. What also must be avoided is the excessive increase in temperature which would cause peritumoral tissue damage. The magnetic hyperthermia (MHT) technique has partly solved these problems. Studies on the application of magnetic materials to promote hyperthermia began with Gilchrist *et al*. in the late 1950s [127]. After this work, many empirical studies have been carried out to evaluate the therapeutic expression in different tumor types. However, the results of these preliminary studies had their widespread use in academic circles only in the early 1990s, and today there are a small number of clinical studies in this area [128-131]. Thus, more detailed studies on the physical limitations, degree of toxicity, and efficiency that would allow a better applicability of the method to humans are needed.

Silva *et al.* identified 71 publications by electronic search. Considering the inclusion criteria, they selected 15 articles: 3 in vitro studies, 10 animal model studies and 2 clinical studies [132]. Although there are different centers around the world that study magnetic hyperthermia as a cancer therapy, still there are huge scopes to use hyperthermia as a prominent tool to cancer therapy as well as welfare of human beings.

1.5 Aims and Objectives

The synthesis of nanostructured magnetic materials has become a particularly important area of research and is attracting a growing interest because of the potential applications such as drug delivery ,cell labeling and sorting, magnetic resonance imaging, sensing as well as therapeutic applications such as AC magnetic field-assisted cancer therapy. In this sense, the research work

presented in this Ph.D. thesis is also concerned with development, fabrication and application of magnetic nanoparticles to cancer therapy under AC magnetic-field induced and photoirradiation conditions.

The overall aim of this thesis was to develop magnetic, photocatalytic and photothermal nanoparticles with various novel shapes and sizes using wet synthesis methods and studying their cytotoxic effects in various aspects. Specific aims include:

(i) Developing of reproducible novel shaped superparamagnetic magnetite (Fe_3O_4) nanoparticles and transferred it to α-Fe_2O_3, γ-Fe_2O_3 or mixed α and γ-Fe_2O_3 nanoparticles [133, 134].

(ii) Characterizing the physical and chemical properties of the prepared samples

(iii) Preparing a modified stable photocatalyst by coating the photoactive titanium dioxide layer onto a protected magnetic core, e.g.; Fe_3O_4@TiO_2 [135].

(iv) Assembling combined AC magnetic-field induced and photoexcited instrumentations.

(v) Finally, application of prepared nanomaterials to cancer therapy under AC magnetic-field induced and photoirradiation conditions at room temperature.

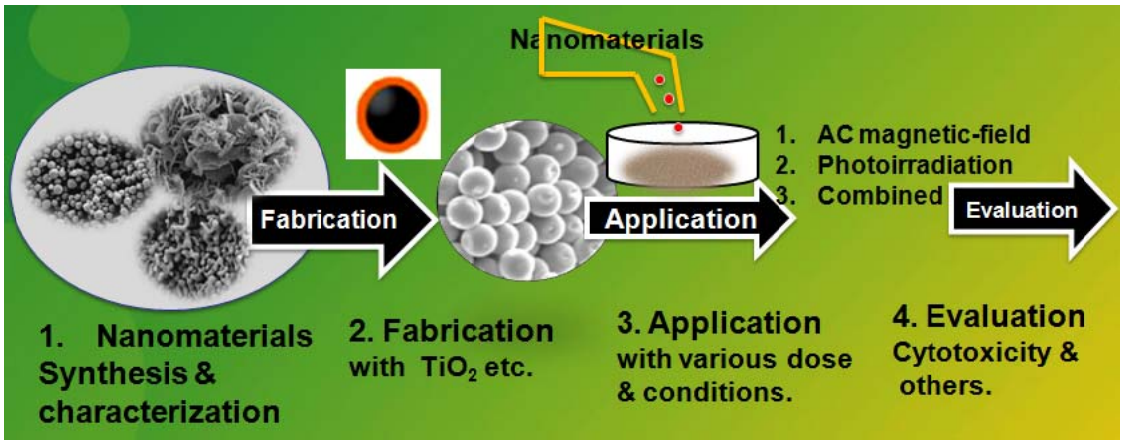

Fig. 1-9: Schematic presentation of research outline.

References

[1] Nagarajan. R, *ACS Symposium Series 996*, **2008,** Chapter 1, p 11**.**

[2] Lu Y and Liu J, *Acc Chem, Res.* **2007,** *40*, 315.

[3] Lee BI, Qi L and Copeland T, *J Ceram Process Res.* **2005***, 6*, 31.

[4] Daniel MC and Astruc D, *Chem Rev.* **2004***, 104*, 293.

[5] Zhang WX, *J Nanopart Res.* **2003***, 5,* 323.

[6] Fan J and Gao Y, *J Exp Nanosci.* ***2006****, 1*,457.

[7] Mayer ABR, *Polym Adv Technol.* **2001***, 12*, 96.

[8] Son S, Park IK, Park J and Hyeon T, *Chem Commun.* **2004**, 778.

[9] Crooks RM, Zhao M, Sun L, Chechik V and Yeung LK, *Acc Chem Res,* **2001***, 34*,181.

[10] Rahim EH, Kamounah FS, Frederiksen J and Christensen JB, *Nano Lett.***2001,** *1*, 499.

[11] Moreno-Manas M and Pleixats R, *Acc Chem Res.***2003***, 36*, 638.

[12] Stevens PD, Fan J, Gardimalla HMR, Yen M and Gao Y, *Org Lett.* **2005***, 7,* 2085.

[13] Savage N and Diallo MS, *J Nanopart Res.***2005***, 7,* 331.

[14] Coyle S, Wu SY, Lau KT, Rossi DD, Wallace G and Diamond D, *Mater Res Bullt.* **2007,** *32*, 434.

[15] Rita Colwell, Nanotechnology: A Gentle Introduction to the Next Big Idea, **2002,** Chapter 1, p 10**.**

[16] Barbara Wilson, AFRL Nano Science and Technology Initiative, National Academy of Sciences, Irvine, Calif. **2008**.

[17] HS. Nalwa (Ed.), Encyclopedia of Nanoscience and Nanotechnology, American Scientific Publishers, New York, **2004**.

[18] Johnson, NP, Butour, JL, Villani, G, Wimmer, FL, Defais, M, Pierson, V, et al., *Prog.*

Biochem. Med. **1989**, *10*, 1.

[19] BD Chithrani, A A. Ghazani and Warren CW Chan, *Nano Lett.* **2006,** *6*, 662.

[20] Scott E. McNeil, *J. Leukocyte Biol.* **2005**, *78*, 10.

[21] Kathleen Sellers, Nanotechnology and the environment, CRC press, Taylor & Francis Group, **2008**, Chapter 2, P-14.

[22] Guy Carpenter & Company, Inc. and Dr. Robert Blaunstein, Nanotechnology, the Plastics of 21st Century-Report, **2006**.

[23] JA Blackman and C Binns, Handbook of Metal Physics, Metallic Nanoparticles, Elsevier, **2009**, Chapter 1, p 12.

[24] S Sun, CB Murray, D Weller, L Folks, A Moser, *Science* **2000**, *287*, 1989.

[25] MM Miller, GA Prinz, SF Cheng, S Bounnak, *Appl. Phys. Lett.* **2002**, *81*, 2211.

[26] TK Jain, MA Morales, SK Sahoo, DL Leslie-Pelecky, V Labhasetwar, *Mol. Pharm.* **2005**, *2*, 194.

[27] I Chourpa, L Douziech-Eyrolles, L Ngaboni-Okassa, JF Fouquenet, S Cohen-Jonathan, M Souce, HMarchais, P Dubois, *Analyst* **2005**, *130* , 1395.

[28] JW Bulte´, Methods *Mol. Med.* **2006**, *124*, 419.

[29] M Modo, JW Bulte´, *Mol. Imaging* **2005**, *4*, 143.

[30] C Burtea, S Laurent, A Roch, L Vander Elst, RN Muller, *J. Inorg. Biochem.* **2005**, *99* (5), 1135.

[31] S Boutry, S Laurent, L Vander Elst, RN Muller, *Contrast Med. Mol. Imaging* **2006**, *1* (1), 15.

[32] L Babes, B Denizot, G Tanguy, JJ Le Jeune, P Jallet, *J. Colloid Interface Sci.* **1999**, *212* (2), 474.

[33] F Sonvico, C Dubernet, P Colombo, P Couvreur, *Curr. Pharm. Des.* **2005**, *11*, 2091.

[34] C Corot, P Robert, JM Idee, M Port, *Ad*V. *Drug Deli*V*ery Re*V. **2006**, *58* (14), 1471.

[35] MMJ Modo, JWM Bulte´, *Molecular and Cellular MR Imaging*; CRC Press: Boca Raton, FL, **2007**.

[36] S W Charles, J Popplewell, *Endea*V*our* **1982**, *6*, 153.

[37] AK Gupta, M Gupta, *Biomaterials* **2005**, *26* (18), 3995.

[38] RM Cornell, U Schwertmann, The Iron Oxides: Structure, Properties, Reactions, Occurrences and Uses, second ed. Wiley-VCH, Weinheim, **2003**.

[39] S Neveu, A Bee, M Robineau, D Talbot, *J. Colloid Interface Sci.* **2002**, *255*, 293.

[40] F Grasset, N Labhsetwar, D Li, DC Park, N Saito, H Haneda, O Cador, T Roisnel, S Mornet, E Duguet, J Portier, J Etourneau, *Langmuir* **2002**, *18*, 8209.

[41] S Sun, H Zeng, *J. Am. Chem. Soc*. **2002**, *124*, 8204.

[42] SJ Park, S Kim, S Lee, Z Khim, K Char, T Hyeon, *J. Am. Chem. Soc.* **2000**, *122*, 8581.

[43] V F Puntes, KM Krishan, A P Alivisatos, *Science* **2001**, *291*, 2115.

[44] Q Chen, AJ Rondinone, BC Chakoumakos, ZJ Zhang, *J. Magn. Magn. Mater.* **1999**, *194*, 1.

[45] J Park, K An, Y Hwang, JG Park, HJ Noh, JY Kim, JH Park, NM Hwang, T Hyeon, *Nat. Mater.* **2004**, *3*, 891.

[46] EV Shevchenko, D V Talapin, A L Rogach, A Kornowski, M Haase, H Weller, *J. Am. Chem. Soc.* **2002**, *124*, 11480.

[47] An-Hui Lu, EL Salabas, F Schüth, *Angew. Chem. Int. Ed.* **2007**, *46*, 1222.

[48] D Langevin, *Annu. Rev. Phys. Chem.* **1992**, *43*, 341.

[49] BK Paul, SP Moulik, *Curr. Sci.* **2001**, *80*, 990.

[50] X Wang, J Zhuang, Q Peng, Y Li, *Nature* **2005**, *437*, 121

[51] C Burda, XB Chen, R Narayanan, MA El-Sayed, *Chem. Rev.* **2005**, *105*, 1025.

[52] S Giri, BG Trewyn, MP Stellmaker, VSY Lin, *Angew. Chem.* **2005**, *117*, 5166.

[53] C Bergemann, D Muller-Schulte, J Oster, L Brassard, AS Lubbe, *J. Magn. Magn. Mater.* **1999**, *194*, 45.

[54] L Nunez, MD Kaminski, *J. Magn. Magn. Mater.* **1999**, *194*, 102.

[55] C Xu, K Xu, H Gu, R Zheng, H Liu, X Zhang, Z Guo, B Xu, *J. Am. Chem. Soc.* **2004**, 126, 9938.

[56] L X Chen, T Li, MC Thurnauer, R Csencsits, T Rajh, *J. Phys. Chem. B* **2002**, *106*, 8539.

[57] I Safarik, M Safarikova, *J. Chromatogr. B* **1999**, *722*, 33.

[58] X Zhao, R Tapec-Dytioco, K Wang, W Tan, *Anal. Chem.* **2003**, *75*, 3476.

[59] KJ Widder, AE Senyei, DG Scarpelli, *Proc. Soc. Exp. Biol. Med.* **1978**,*58*, 141.

[60] C C Berry, ASG Curtis, *J. Phys. D* **2003**, *36*, R198.

[61] SMornet, S Vasseur, F Grasset, E Duguet, *J. Mater. Chem.***2004**, *14*, 2116.

[62] R Hiergeist, W AndrS, N Buske, R Hergt, I Hilger, U Richter, W Kaiser, *J. Magn. Magn. Mater.* **1999**, *201*, 420.

[63] S Mornet, S Vasseur, F Grasset, P Verveka, G Goglio, A Demourgues, J Portier, E Pollert, E Duguet, *Prog. Solid State. Chem.* **2006,** *34*, 237

[64] T Neuberger, B Schöpf, H Hofmann, M Hofmann, BV Rechenberg, *J. Magn. Magn. Mater.* **2005**, *293,* 483.

[65] AS Teja, PY Koh, *Prog. Cryst. Growth Charact. Mater.* **2009**, *55*, 22.

[66] R Jurgons *et al*., *J. Phys.: Condens. Matter*, **2006**, *18***,** S2893.

[67] O Olsvik, T Popovic, E Skjerve, *et al*., *Microbiol. Rev.* **1994**, *7*, 43.

[68] F Scherer, M Anton, U Schillinger, *et al*., *Gene Therapy,* **2002**, *9,* 102.

[69] W Schutt, C Gruttner, U Häfeli, *et al*., *Hybridoma* **1997***, 16*,109.

[70] M Kresse, S Wagner, M Taupitz, in: U. Häfeli, *et al*. (Eds.), Scientific and Clinical Applications of Magnetic Carriers, Plenum Press, New York, **1997**, p. 545.

[71] C Chouly, D Polyquen, I Lucet, *et al*., *J. Microencapsulation* **1996**, *13,* 245.

[72] AS Lubbe, C Bergmann, H Riess, *et al*., *Cancer Res.* **1996**, *56,* 4686.

[73] V Strom, K Hultenby, C Gruttner, *et al*., *Nanotechnology* **2004**, *15*, 457.

[74] A Jordan, R Wust, H Faehling, *et al*., in: U. Häfeli, *et al*. (Eds.), Scientific and Clinical Applications of Magnetic Carriers, Plenum Press, New York, **1997**.p.569.

[75] YH Mier, AV Hernandez, LL Salas, *Proceedings of the Second Join EMBS/BMES Conference,* **2002**.

[76] Wikipedia , http://en.wikipedia.org/wiki/Cancer#Causes

[77] P Anand, AB Kunnumakkara, *et al., Pharm. Res.* **2008,** *25 (9)*, 2097.

[78] WHO, http://www.who.int/cancer/en/

[79] GLOBOCAN **2008** (IARC), 150 Cours Albert Thomas, France, http://globocan.iarc.fr/

[80] WORLD HEALTH ORGANIGATION (WHO) "The faces of cancer"

[81] Cancer Facts & Figures, Atlanta: American Cancer Society; **2010**.

[82] Oncologie [electronic resource], **2004,** Paris; New York: Springer.

[83] Released news*,* **6/6/05**, National Cancer Institute.

[84] AJ Sasco, MB Secretan, K Straif, "Tobacco smoking and cancer: a brief review of recent epidemiological evidence". *Lung cancer (Amsterdam, Netherlands),* **2004**, *45* **Suppl 2**: S3.

[85] HK Biesalski, B Bueno de Mesquita, A Chesson, *et al.*, *CA: a cancer journal for clinicians,* **1998**, *48 (3)*, 167–76; discussion 164–6.

[86] LH Kushi, T Byers, C Doyle, *et al.*, *CA Cancer J Clin.* **2006**, *56 (5)*, 254.

[87] Little, John B (2000). "Chapter 14: Ionizing Radiation". In Bast RC, Kufe DW, Pollock RE, *et al. Holland-Frei Cancer Medicine* (5th ed.). Hamilton, Ontario: B.C. Decker. Retrieved 31 January 2011.

[88] DH Roukos, *Expert review of anticancer therapy,* **2009**, *9 (4),* 389. http://www.expert-reviews.com/doi/pdfplus/10.1586/era.09.12.

[89] Maltoni, C F Minardi, J F Holland (2000). "Chapter 16: Physical Carcinogens". In Bast RC, Kufe DW, Pollock RE, *et al*., Holland-*Frei Cancer Medicine* (5th Ed.). Hamilton, Ontario: B.C. Decker, Retrieved 31 January 2011.

[90] JF Gaeta, (2000). "Chapter 17: Trauma and Inflammation". In Bast RC, Kufe DW, Pollock RE, *et al.*, *Holland-Frei Cancer Medicine* (5th Ed.). Hamilton, Ontario: B.C. Decker, Retrieved 27 January 2011.

[91] Henderson, E Brian, L Bernstein, RK Ross (2000). "Chapter 13: Hormones and the Etiology of Cancer". In Bast RC, Kufe DW, Pollock RE, *et al.*, *Holland-Frei Cancer Medicine* (5th ed.). Hamilton, Ontario: B.C. Decker, Retrieved 27 January 2011.

[92] J Tolar, JP Neglia, *J Pediatr Hematol Oncol.* **2003**, *25 (6):* 430.

[93] Japan Cancer Society, Cancer in Japan,

[94] National Cancer Center, Cancer Statistic in Japan 2010.

[95] Cancer statistics in Japan`10,http://ganjoho.jp/public/statistics/backnumber/2010_en.html

[96] Office for Cancer Control, Health Services Bureau, Ministry of Health, Labor and Welfare, Japan.

[97] Cancer: A Bangladesh Perspective, Mohd. Shamim Iqbal, M2 Graduate Student, Department of Bio-Signal Analysis, Yamaguchi University Graduate School of Medicine, Japan.

[98] Nicholas Cohen, THE LANCET, **1981**, *317(8229)*, 1090.

[99] AB Miller, B Hoogstraten, M Staquet, A Winkler, *Cancer* **1981**, *47(1),* 207.

[100] Lucien Israel, *Conquering Cancer*, Random House, New York, **1978**.

[101] M. Abdulla-Al-Mamun, PhD Thesis, Development, Evaluation and Application of Metal Nanoparticles, Nanophotocatalysts and Nanocomposites, 2010.

[102] BE Henderson, RK Ross, MC Pike, *Science* **1993***, 259*,633.

[103] Challa SSR Kumar, Nanotechnologies for the Life Sciences Vol. 6 Nanomaterials for Cancer Therapy, WILEY-VCH, Weinheim, **2006**, Chapter 1, p 1.

[104] WR Chen, RL Adamsc, R Carubellic, RE Nordquist, *Cancer Letters* **1997**, *115*, 25.

[105] WR Chen, R L Adamsc, AK Higginsb, KE Bartefsd, RE Nordquistc, *Cancer Letters* **1996**, *98*, 169.

[106] AK D'Cruz, MH Robinson, MA Biel, *Head & Neck* **2004**, *3*, 232.

[107] GJ McBride, *Nat. Cancer Inst.* **2002**, *94*, 1740.

[108] SA Rosenberg, *Immunity* **1999**, *10(3),* 281.

[109] LM Weiner, *Semin Oncol.* **1999,** *26(4 Suppl 12)*, 41.

[110] PM Harari, *Endocrine-Related Cancer* **2004**, *11*, 689.

[111] DF Chan, DB Kirpotin, P A Bunn, Jr, "Physical Chemistry and In Vivo Tissue Heating Properties of Colloidal Magnetic Iron Oxides with Increased Power Absorption Rates", in Scientific and Clinical Applications of Magnetic Carriers, edited by U. Hafeli, W. Schütt, J. Teller and M.Zborowski (Plenum Press, NY, **1997**) p. 607

[112] A Jordan, R Scholz, P Wust, H Faühling, R Felix. *J. Magn. Magn. Mater.* **1999**, *201*, 413.

[113] FK Fuss, SL Chia, SS Venkatraman, SM Krishnan, B Schmidt, *Proc. First Intl. Bioengg. Conf* (eds.), Singapore, **2004**, p.69.

[114] Challa SSR Kumar, Nanotechnologies for the Life Sciences Vol. 6 Nanomaterials for

Cancer Therapy, WILEY-VCH, Weinheim, **2006**, Chapter 8, p 243.

[115] R Cavaliere, EC Ciocatto, BC Giovanella, *et al*., *Cancer*. **1967**, *20(9),* 1351.

[116] KS Sellins, JJ Cohen, *Rad Res*. **1991**, *126(1),* 88.

[117] C Christophi, A Winkworth, V Muralihdaran, E Evans, *Surgical Oncology-Oxford*. **1998**, *7(1–2)*, 83.

[118] RA Coss, WA Linnemans, *Int J Hyperthermia*. **1996**, *12*, 173.

[119] JR Lepock, *Int J Hyperthermia*. **2003**, *19*, 252.

[120] RSL Wong, LN Kapp, G Krishnaswamy, WC Dewey, *Radiat Res*. **2003**, *133*, 52.

[121] PK Sneed, PR Stauffer, MW McDermott, *et al*., *Int J Radiat Oncol Biol Phys*. **1998**, *40*, 287.

[122] H Stahl, P Wust, K Maier-Hauff, M Seebass, *et al*., *Strahlenther Onkol*. **1995**, *171*, 510.

[123] M Mitsumori, M Hiraoka, Y Okuno, *et al*., *Int J Radiat Oncol Biol Phys*. **1996**, *36*, 1169.

[124] AN Guthkelch, LP Carter, JR Cassady, *et al*., *J Neurooncol*. **1991**, *10(3)*, 271.

[125] E Guilhon, P Voisin, JA de Zwart, *et al*., *J Gene Med*. **2003**, *5(4)*, 333.

[126] C Wismeth, C Dudel, C Pascher, *et al*., *J Neurooncol*. **2010**, *98(3)*, 395.

[127] RK Gilchrist, R Medal, WD Shorey, RC Hanselman, JC Parrott, CB Taylor, *Ann Surg*. **1957**, *146*, 596.

[128] NA Brusentsov, LV Nikitin, TN Brusentsova, *et al*., *J Magn Magn Mater*. **2002**, *252(1–3)*, 378.

[129] M Johannsen, U Gneveckow, L Eckelt, *et al., Int J Hyperthermia*. **2005,** *21(7)*, 637.

[130] A Jordan, R Scholz, K Maier-Hauff, *et al*., *J Neurooncol*. **2006**, *78*, 7.

[131] B Thiesen, A Jordan, *Int J Hyperthermia*. **2008**, *24(6)*, 467.

[132] AC Silva, TR Oliveira, JB Mamani, SMF Malheiros, L Malavolta, LF Pavon, TT Sibov, E Amaro Jr, A Tannús, E LG Vidoto, MJ Martins, RS Santos, LF Gamarra, *Int. J. Nanomedicine,* **2011**, *6*, 591.

[133] MS Islam**,** Y Kusumoto, M Abdulla-Al-Mamun, *Mat. Lett.* **2001**, *66(1)*, 165.

[134] MS Islam, Y Kusumoto, M Abdulla-Al-Mamun, Y Horie, *Chem. Lett.* **2011**, *40(7)*, 773.

[135] MS Islam, Y Kusumoto, M Abdulla-Al-Mamun, Y Horie, *Cat. Comm.* **2001,** *16*, 39.

CHAPTER 2

EXPERIMENTAL DETAILS AND INSTRUMENTS SET UP

2.1 Preparation of Distilled and Millipore Water

Distilled and Millipore water are prerequisite in any laboratory from the beginning of the research. In our lab, we prepared distilled and Millipore water ourselves according to requirements. First of all, 70% ion-exchanged water was taken into the boiling flask. After that 8-10 boiling stone was added and 5 ml NaOH of 6N and 2 ml KMnO4 of 0.1N was added subsequently. First drop-line was set up and gas line, cool water line was running subsequently. After about 30-40 min almost 200 ml first drop of water was accumulated in a beaker and then distilled water was collected in another green label container. This distilled water was again redistilled for further use.

Certain amount of distilled water was further converted to Millipore water by suing Millipore water filter 18.2 MΩ·cm at 25 °C.

2.2 Preparation of novel rose-type magnetic nanomaterials

Typical synthesis of rose type magnetite (Fe_3O_4) nanoplates was carried out in a hydrothermal system by modified reduction reactions between $FeCl_2$ and ethylene glycol. In this experiment chemicals used were iron chloride tetrahydrate ($FeCl_2 \cdot 4H_2O$, Wako Pure chemical industries Ltd., Japan), ethylene glycol (99.5%, Wako Pure chemical industries Ltd., Japan), polyethylene glycol 4000 (Tokyo Kasei Kogyo Co. Ltd, Japan) and sodium acetate, anhydrous (NaAc, 98%,

Nacalai Tesque Ltd., Japan). All chemicals were of analytical grade and used without any further purification.

$FeCl_2$•$4H_2O$ (1.98 g,10 mmol) was dissolved in ethylene glycol (100 mL) to form a clear solution, followed by the addition of NaAc (7.2 g) and polyethylene glycol (2.0 g). The mixture was stirred vigorously at 90 °C to get a clear solution and then sealed in a teflonlined stainless-steel autoclave (200 ml capacity). The autoclave was heated to and maintained at 200 °C for 5 h and allowed to cool to room temperature. After cooling, decantation was done by a permanent magnet to get the sedimented black products. The black products were washed several times with ethanol and dried at 70 °C for 3 h. Finally, we obtained 1.62g (82% of precursor) of Fe_3O_4 nanoplates (Fig. 2-1). The magnetite nanoplates were oxidized into maghemite and hematite at 250 °C for 6 h in the presence of oxygen and at 500 °C for 1 h in the presence of Ar gas, respectively [1].

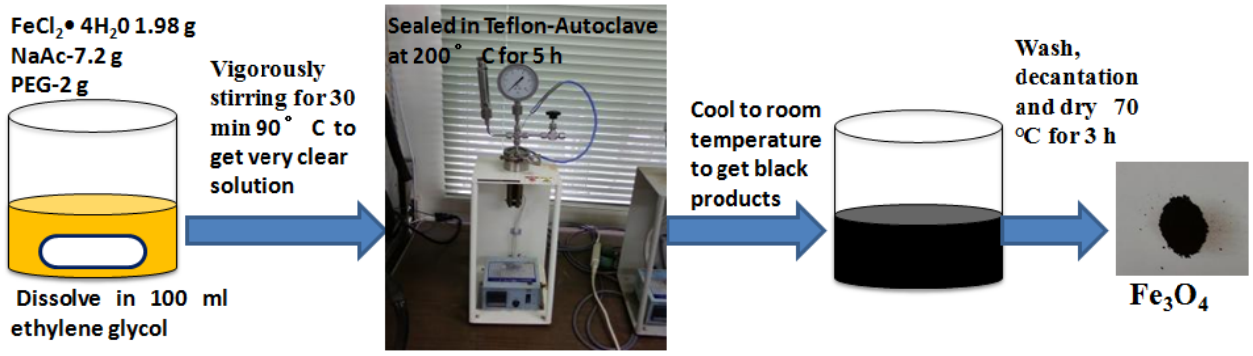

Fig. 2-1: Schematic representation of synthesis of rose-type Fe_3O_4 nanoplates.

2.3 Preparation of novel neck-structured magnetic nanomaterials

We synthesized neck-structured Fe_3O_4 nanoparticles by a modified hydrothermal method. Deng *et al.* prepared magnetic microspheres using $FeCl_3 \cdot 6H_2O$ as a precursor and autoclaved the mixture at 200 °C for 8-72 h [2]. However, we used $FeCl_2 \cdot 4H_2O$ as a precursor and the mixture was autoclaved at 190 °C for 5 h with air pressure 0.2 MPa to synthesize Fe_3O_4 magnetic nanoparticles. $FeCl_2 \cdot 4H_2O$ (0.99 g, 5 mmol) was dissolved in ethylene glycol (40 mL) to form a clear solution, followed by the addition of NaAc (3.6 g) and polyethylene glycol (1.0 g). The mixture was stirred vigorously for 45 min until getting a clear solution and then sealed in a teflonlined stainless-steel autoclave (50 mL capacity). The autoclave was heated to and maintained at 190 °C for 5 h and allowed to cool to room temperature. After cooling, decantation was done by a permanent magnet to get the sedimented black products. The black products were washed several times with ethanol and dried at 70 °C for 3 h. Finally, we obtained 0.81 g of Fe_3O_4 nanoparticles.

In this experiment chemicals used were iron chloride tetrahydrate ($FeCl_2 \cdot 4H_2O$, Wako Pure chemical industries Ltd., Japan), ethylene glycol (99.5%, Wako Pure chemical industries Ltd., Japan), polyethylene glycol 4000 (Tokyo Kasei Kogyo Co. Ltd, Japan) and sodium acetate, anhydrous (NaAc, 98%, Nacalai Tesque Ltd., Japan). All chemicals were of analytical grade and used without any further purification.

It is well known that Fe_3O_4 can be oxidized to γ-Fe_2O_3, which can be further transformed into α-Fe_2O_3 at higher temperatures [1]. However, magnetite (Fe_3O_4) is not very stable and is sensitive to oxidation. Magnetite is transformed into maghemite (γ-Fe_2O_3) in the presence of oxygen [3]. First, as-synthesized Fe_3O_4 was oxidized into γ-Fe_2O_3 at 250 °C for 8 h in the

presence of oxygen and then γ-Fe_2O_3 was calcinated at 500 °C for 3 h in the presence of Ar gas to get α-Fe_2O_3.

2.4 Preparation of spherical Fe_3O_4 and fabrication with TiO_2

Fe_3O_4 nanoparticles with diameter of ca. 20 nm were first synthesized via the co-precipitation method. In the next step, Fe_3O_4@C and finally, Fe_3O_4@TiO_2 core-shell NCs were synthesized by modifying (see supplemental material) the synthesis method of Li *et al*. [4]

2.4.1 Preparation of spherical Fe_3O_4 by Co-precipitation method

In a typical co-precipitation method, $FeCl_3$ (2.6 g) and $FeCl_2$ (1.3 g) were dissolved in nitrogen gas (N_2) purged 2.0 M hydrochloric acid solution and magnetically stirred under a continuous flow of N_2. The mixture was heated at 70 °C for 30 min and then the mixture was heated for another 5 min under a blanket of N_2. Ammonia was added drop by drop to precipitate the magnetic nanoparticles and the black product formed was treated hydrothermally at 70 °C for 30 min. All aqueous solutions and suspensions were made using nanopure water (18 MΩ cm resistivity). The resulting nanoparticles were subsequently separated from the reaction media under a magnetic field and washed three times with nanopure water before drying. Finally the MNPs were oven dried at 70 °C for 3 h to get Fe_3O_4 (Fig. 2-2).

In this experiment chemicals used for the synthesis of MNPs were $FeCl_3$, HCl, 25% NH_3 solution (Wako Pure Chemical Industries Ltd., Japan) and $FeCl_2$ (Strem Chemicals, Newburyport).

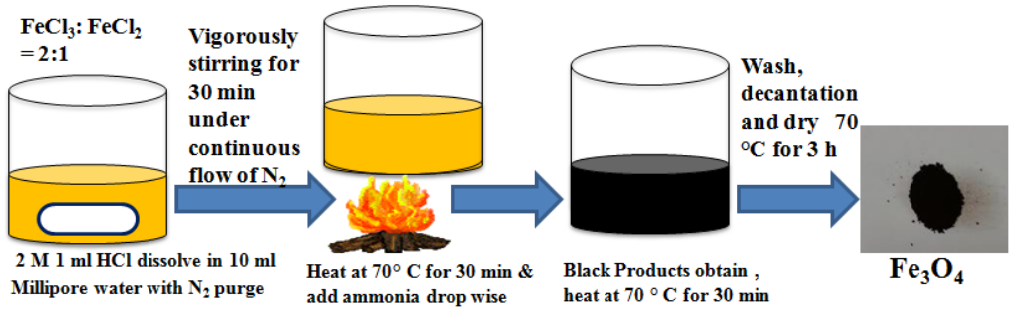

Fig. 2-2: Schematic representation of synthesis of Fe_3O_4 spherical nanoparticles by Co-precipitation method.

2.4.2. Synthesis of Fe_3O_4@C magnetic nanocomposites

Fe_3O_4 nanoparticles with diameter of ca. 20 nm were first synthesized *via* the co-precipitation method. In the next step, 0.05 g nanoparticles were ultrasonicated for 10 min in 0.1 M HNO_3, followed by washing with deionized water. Then, the treated Fe_3O_4 nanoparticles were redispersed in 0.5 M aqueous glucose solution. After vigorous stirring for 10 min, the suspension was transferred to an autoclave and kept at 190 °C for 4 h. After the reaction, the autoclave was cooled naturally in air and the suspension was isolated with the help of a magnet and washed with deionized water and alcohol three times, respectively. The final sample was obtained after oven-drying at 90 °C for more than 5 h.

2.4.3 Synthesis of Fe_3O_4@TiO_2 core-shell nanocomposite

Tetrabutyltitanate (5 mL) was dissolved in ethanol (35 mL) to form a clear solution. Fe_3O_4@C magnetic nanocomposites (~100 mg) were then dispersed in the freshly prepared solution with the aid of ultrasonication for 5 min. A 1:5 (v/v) mixture of water and ethanol was added drop wise to the suspension of Fe_3O_4@C magnetic nanocomposites with vigorous magnetic stirring over a period of approximately 15 min. Thereafter, the suspension was stirred for further 1 h before separation and washed with ethanol. After five cycles of

separation/washing/redispersion with ethanol, the powder obtained was oven-dried and calcined at 500 °C under nitrogen gas (Fig.2-3).

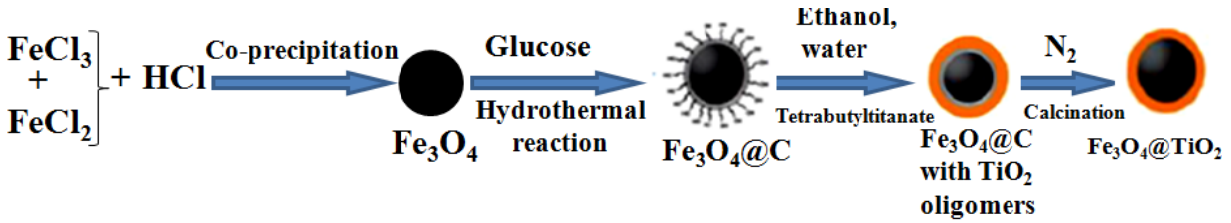

Fig.2-3: Diagrammatic representation of the overall synthetic routes of Fe_3O_4@TiO_2 core-shell nanocomposites.

2.5 Preparation mixed α and γ-Fe_2O_3 superparamagnetic nanoparticles

Typical syntheses of magnetic nanoparticles (MNPs) were carried out using the reaction between Fe^{2+} and Fe^{3+} in a co-precipitation method and then transferred Fe_3O_4 to mixed α and γ-Fe_2O_3 superparamagnetic nanoparticles. It is well known that Fe_3O_4 can be oxidized to γ-Fe_2O_3, which can be further transformed into α-Fe_2O_3 at higher temperature [1]. Magnetite (Fe_3O_4) is not very stable and is sensitive to oxidation. Magnetite is transformed into maghemite (γ-Fe_2O_3) in the presence of oxygen [5]. However, as-synthesized Fe_3O_4 was oxidized into γ-Fe_2O_3 at 250 °C for 8 h in the presence of oxygen and then γ-Fe_2O_3 was calcinated at 500 °C for 3 h in the presence of Ar gas to get α-Fe_2O_3 [6]. In this report, we simply transferred Fe_3O_4 to mixed α- and γ-Fe_2O_3 superparamagnetic nanoparticles by annealing it at 400 °C for 6 h in the presence of oxygen (Fig. 2-4).

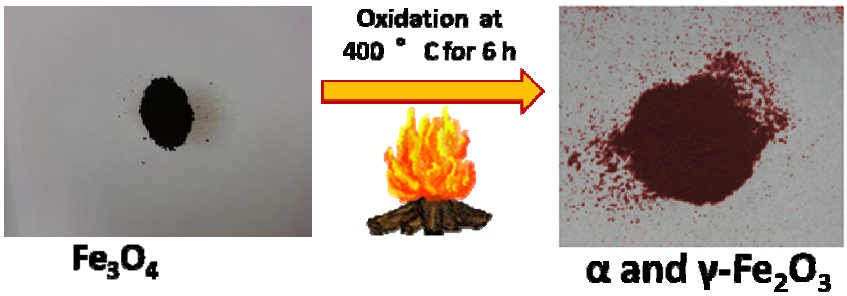

Fig.2-4: Phase transfer of Fe_3O_4 to mixed α and γ-Fe_2O_3 superparamagnetic nanoparticles.

2.6 Assembling of AC (alternating current) magnetic-field induction and photoirradiation instruments

Because of our interest in the enhanced toxic effect of AC magnetic-field induction and chemical reactions of as-prepared various nanomaterials produced by photoirradiation , for the first time we assembled and used combined instrumentation modeling of AC magnetic-field and photoexcitation (Fig. 2-5) with magnetic field intensity and frequency 5.0 kA/m and 560 kHz, respectively and a Xenon lamp (CERMAX 300-W LX300F, USA, ILC) with heat cut-off and band-pass filters (350–600 nm) with an average intensity of 30 mW cm^{-2} was used for the light irradiation on HeLa cells. The entire instrument set up was accomplished by the kind assistance of Professor Dr. Yuji Horie, Department of Electrical and Electronics Engineering, Graduate School of Science and Engineering, Kagoshima University, Japan.

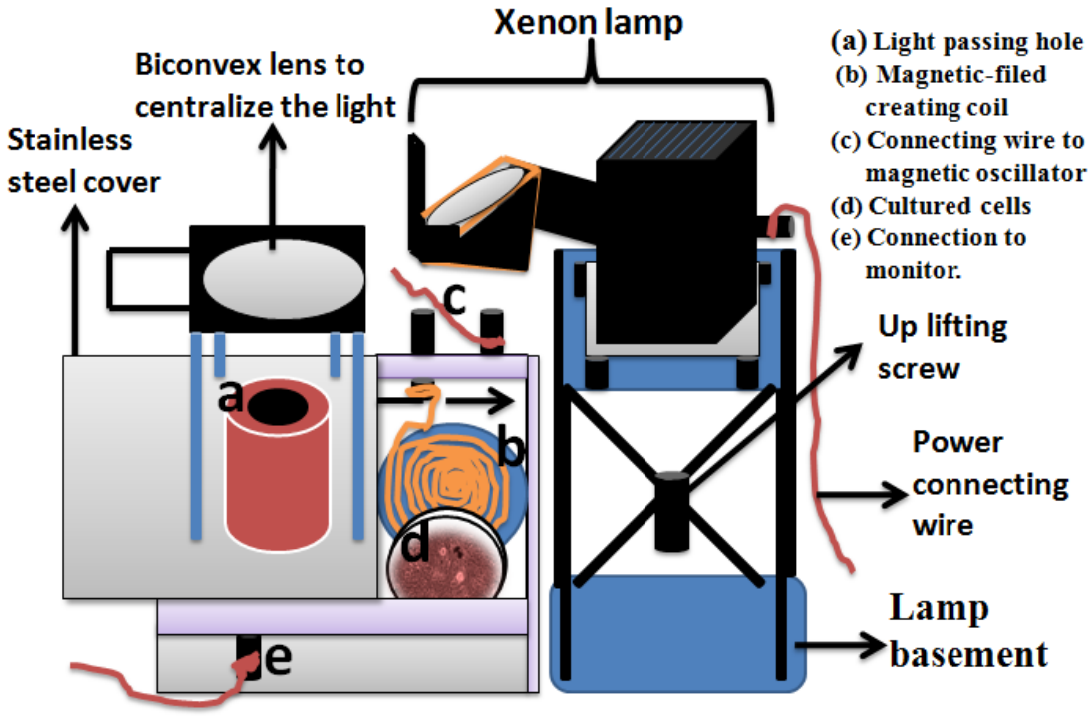

Fig.2-5: Combined assembles of AC magnetic-fields induction and photoirradiation instruments.

2.7 Cell culture

Malignant epithelial cell line, HeLa (human cervix epithelial-like cell line) are brought from Cell Bank, RIKEN BioResource Center, 3-1-1 Koyadai, Tsukuba, Ibaraki, 305-0074, Japan. The frozen cells were shipped in dry ice by Yamato Transport Co., LTD, Japan. Some facts about HeLa cell [7-10].

- A HeLa cell is a cell type in an immortal cell line used in scientific research. It is the oldest and most commonly used human cell line.
- The line was derived from cervical cancer cells taken on February 8, 1951 from Henrietta Lacks, a patient who eventually died of her cancer on October 4, 1951.
- The cell line was found to be remarkably durable and prolific as illustrated by its contamination of many other cell lines used in research.

Any way after received, the cells were stored in liquid nitrogen Cryogenic can. After every week about 5 L liquid nitrogen was added to the Cryogenic can to keep the HeLa cells in a standard condition. The chemicals and reagents used during the cell culture are listed below in Table 2-1.

2.7.1 Preparation of medium for cancer cells

- Before preparation of the medium, the culture hood (clean bench) was cleaned-up through wiping by alcoholic cotton and prepared all the necessary pipette and utensils by maintaining all the hygienic requirements.
- Then 10 ml of newborn calf serum (NBS) was taken in a bottle and 90 ml of minimum essential medium (MEM) was added to that bottle and was preserved in refrigerator for further use.

Table 2-1: The chemicals and reagents used during the cell culture and cancer research.

Name of the Chemical/Reagent	Company & other specifications
Minimum Essential Medium (MEM) Eagle	Liquid, Sterile filtered, Endotoxin tested, With Earle`s salts, L-glutamine and $NaHCO_3$, SIGMA-ALDRICH COMPANY LTD. Cat. No: M4655
NBS: Newborn Calf Serum	GIBCO, Invitrogen Corporation, Cat. No: 16010-167
PBS: Phosphate Buffered Saline	pH 7.2, [-] Calcium Chloride, [-] Magnesium Chloride, 1x solution, REF 20012-027 500 mL & 20012-050 10x500 mL, GIBCO, Invitrogen, Cat. No: 20012.
Trypsin-EDTA	0.25% Trysin-EDTA, 1x solution, GIBCO, Invitrogen, Cat. No: 25200.
Trypan Blue	0.5%- Trypan Blue Stain Solution, NACALAI TESQUE, INC. Cat. No: 35552-84.35
15 ml Centrifuge Tubes	External dimensions 120 x 17 mm, Nunc, Nagle Nunc International, Cat. No: 366060
60 mm Cell Culture Petri Dish	Culture area, 21.5 cm², Max. External dimensions, 60 x 15 mm, Max. External diameter bottom, 53.5 mm, Nunc, Nagle Nunc International, Cat. No: 150288.
Millipore water filter	18.2 MΩ·cm at 25 °C ultrapure water, Reverse osmosis or deionized water, Electrical, Ratings: 100 V 50/60 Hz 30 A, MILLIPORE, Cat. No: SIMS70000, Consumables Cat. No: SIMPAKKRJ.
Pipette	1 ml pipette, IWAKI, (IK-PAS-99) soda-lime-glass 10 ml pipette, IWAKI, Asahi Glass Co., LTD 20 ml pipette, IWAKI, Asahi Glass Co., LTD 50 ml pipette, IWAKI, Asahi Glass Co., LTD
Cover slips	Hemacytometer Cover Glass, Size 22x 24 mm, thick 0.4 mm, SLGC, A209
Cell Counter microscale slide	Depth 0.100 mm, 1/400 & 1/25 sqmm, No. B2018, Burker-Turk, SLGC, Japan

2.7.2 HeLa Cell Culture

- The culture hood (clean bench) was cleaned-up thoroughly wiping by alcoholic cotton and prepared all the necessary pipette and utensils by maintaining all the hygienic requirements.

- The frozen HeLa cell vial was collected from the Cryogenic can, sterilized with alcoholic cotton and was liquefied by warming into the palm at about 40°C.
- Then the liquid HeLa cells were collected through the micro pipette and were poured in to the centrifuge tube. It was then centrifuged at room temperature at 1200 rpm for 3 min to sediment the liquid cells.
- After centrifuge, the liquid of the tube was taken out without disturbances the sedimented cells and 2 mL culture medium was added and cells were diluted gently.
- Then 5 ml culture medium was taken into two Petri dishes, date and other marking was written down and finally 3-5 drops of diluted HeLa cell suspension was added to those of Petri dishes.
- Finally, the Petri dishes were kept into the incubator (5% CO_2, 37 °C) to incubation and allowed to grow for 3 days.

2.7.3 Medium exchange or washing procedure

- The culture hood (clean bench) was cleaned-up thoroughly wiping by alcoholic cotton and prepared all the necessary pipette and utensils by maintaining all the hygienic requirements.
- After 3days of incubation the cells were taken out from the incubator and old culture medium was taken out with the help of 1 mL micro pipette.
- Then 1mL PBS buffer was added to the Petri dishes and cells were thoroughly washed and repeated at least 3 times.
- After washed properly 5 mL of culture medium was added to the Petri dishes and date and other necessary information was written. Finally, the Petri dishes were kept into the incubator for further growth of the cells.

- This exchange procedure was continued every alternate day throughout the experimental period.

2.7.4 Phase or passage procedure

- The culture hood (clean bench) was cleaned-up through wiping by alcoholic cotton and prepared all the necessary pipette and utensils by maintaining all the hygienic requirements.
- The Petri dishes with cultured cells were first gently taken out from the incubator and washed with PBS buffer several times.
- Then the confluence was checked under the microscope. After finding 80% confluency, we went for the further process, otherwise just followed the exchange procedure.
- After checking the confluence, 1 mL Trypsin-EDTA (enzyme) was added to the dishes and incubated the dish in the incubator for 3 minutes.
- Then the dishes were taken out from the incubator, rinsed the dish with PBS buffer properly and all the cell suspension was collected to a centrifuge tube. The dishes were washed with 1mL medium and added this with pervious cell suspension of the centrifuge tube.
- The cell suspension was then centrifuged for about 5 min at 1200 rpm.
- After centrifugation (cell were precipitated on the bottom of the tube) the medium was collected from the tube carefully keeping the cell intact and undisturbed.
- Then 1.5~2 mL culture medium was added to the tube and the cells were diluted properly by rotating the pipette.
- After that 5 mL culture medium was taken in a new 60x15 mm Petri dish and 3-4 drops of diluted cells were added to that dish and was labeled accordingly. Note that we made the

new cell dishes as we needed.

- Lastly the dishes were kept into the incubator for further culture.

2.7.5 Experimental Treatment of Cancer Cells with desire nanomaterials

- In our experiments such as photothermal and photocatalytic experiments, we grow the cells in 60 mm Petri dishes. HeLa cells were cultured in a minimum essential medium (MEM) solution with 10% newborn calf serum (NBS) in a humidified incubator with an atmosphere of 5% CO_2 in air at 37 °C. The HeLa cells were plated at a concentration of about 3 x 10^5 in 60mm Petri dishes and allowed to grow for 3 days.
- After 3 days cultured cells were taken out from the incubator and washed with 1 mL PBS buffer. After properly wash 5 mL culture medium was added into the Petri dishes and the HeLa cell viability was examined by treating with desired nanomaterials using desired concentration and doses.
- The Petri dishes were labeled and kept into the 5% CO_2 incubator at 37°c for 24 hours.
- After passing 24 hours the Petri dishes were taken out from the incubator one by one and examined the cell growth state under microscope and were exposed under the AC magnetic-field or photoirradiation condition. Temperature increments and other data were recorded at that time.
- After light treatment the colloidal solution was removed and washed with the phosphate buffer saline (PBS, Invitrogen Corporation, Gibco). Then the cells were cleaved by Trypsin-EDTA (Gibco) solution and were stained with trypan blue (Nacalai Tesque, Inc., Kyoto, Japan).
- Finally, the living cells were counted and calculated as the percentage of the number of the cells against the control dish cells under a 10x in-bright-field microscope. A 40x

objective was used to collect the sample images.

2.8 List of Major Instruments Used

Name of the instrument	Company and other specifications
Cryogenic equipment	Liquid N_2 container
High Pressure Steam Sterilizer (Auto clave)	Tommy, BS-245
Electric drying oven	DRA430DA
Water Jacket Type CO_2 incubator	Astec
Centrifuge mechine	Himac CT4-Hitachi, 4000 rmp
Digital thermometer	Sato Keiryoki, Model SK-250WP II-R
Xenon lamp	CERMAX 300-W LX300F, USA, ILC
Olympus microscope with digital camera	CKX41
Multifunction generator	Hyperthermia instrument, 30 MHz, WF1973
High speed Bipolar amplifier	Hyperthermia instrument, HAS 4012, DC 1-MHz/100VA
Oscilloscope	Hyperthermia instrument, Hewleft Packard 54602B
Superconducting quantum interference device (SQUID)	Quantum Design MPMS-5
Field emission scanning electron microscope (FE-SEM)	Hitachi S-4100H
Transmission electron microscope (TEM)	JEOL JEM-3010 VII TEM
UV-Vis absorption spectrophotometer	Shimadzu Corporation, UV-2450, Japan
Energy dispersive X-ray spectrometer (EDX)	Philips, XL 30CP
X-ray diffraction (XRD) mechine	Using a PANalytical Advance X-ray diffractometer with CuKα radiation.

References

[1] G. Bate, In Magnetic Oxides Part 2, Craik, D. J. Ed., John Wiley & Sons, New York, **1975**, pp.705-707.

[2] H. Deng, X. Li, Q. Peng, X. Wang, J. Chen and Y. Li, *Angew. Chem.* **2005**, *117*, 2842.

[3] L. Sophie, F. Delphine, P. Marc, R. Alain, R. Caroline, V. E. Luce and N. M. Robert, *Chem. Rev.* **2008**, *108*, 2064.

[4] Y. Li, X. Xu, D. Qi, C. Deng, P. Yang, X. Zhang, *J. Proteome Res.* **2008**, *7* , 2526.

[5] S. Laurent, D. Forge, M. Port, A. Roch, C. Robic, L.V. Elst and R.N. Muller, *Chem. Rev*., **2008**, *108*, 2064.

[6] S. Sun, H. Zeng, D. B. Robinson, S. Raoux, P. M. Rice, S. X. Wang and G. Li, *J. Am. Chem. Soc*., **2004**, *126*, 273.

[7] R. Rahbari, T. Sheahan, V. Modes, *et al., Biotechniques,* **2009***, 46 (4)*, 277.

[8] W. F. Scherer, T. S. Jerome, O. G. George, *J. Exp. Med.* **1953**, *97*, 695.

[9] A. Capes-Davis, G. Theodosopoulos, I. Atkin, *et al., Int J Cancer* **2010***, 127 (1),* 1.

[10] Watts, Denise Watson, "HeLa Cancer Cells Killed Henrietta Lacks. Then They Made Her Immortal.". *The Virginian-Pilot*, **2010**, pp. 1, 12–14.

CHAPTER 3

NOVEL ROSE-TYPE MAGNETIC NANOPLATES (Fe_3O_4, γ-Fe_2O_3 AND α-Fe_2O_3) SYNTHESIZED BY SIMPLE HYDROTHERMAL DECOMPOSITION

Abstract

Rose-type magnetic nanoplates (RTMNPs) were synthesized by a simple hydrothermal decomposition method where $FeCl_2 \cdot 4H_2O$ was solely used as a precursor. The synthesized nanoplates were characterized using XRD, FE-SEM, UV-Vis absorption (reflectance) spectra and magnetic hysteresis loops. The resulting nanoplates were in the ranges of size 350–500 nm and width 60-70 nm with high crystallinity, purity (shown by XRD) and reproducibility. These iron oxide nanoplates have great potential in magnetic nanodevices and biomagnetic applications. The work has already been published in Materials Letters, 2011, 66(1), 165-167.

3.1 Introduction

Magnetic iron oxide nanoparticles and their dispersions in various media have long been of scientific and technological interest. Iron oxides exist in many forms in nature, with magnetite (Fe_3O_4), maghemite (γ-Fe_2O_3), and hematite (α-Fe_2O_3) being probably most common [1]. These three oxides are also very important technologically and they are therefore the subject of our current study. Magnetite and maghemite have attracted attention in biomedical applications because of their biocompatibility and low toxicity in the human body [2-5]. Magnetite and hematite are semiconductors and can catalyze oxidation/reduction reactions [6-8].

Another application of magnetic nanoparticles is hyperthermia in cancer therapy. Superparamagnetic nanoparticles when exposed to an alternating magnetic field can be used to heat tumor cells to 41- 45 °C, where the damage for normal tissues is reversible while the tumor cells are irreversibly damaged [9]. In this work, we synthesized novel rose-type magnetite (Fe_3O_4) nanoplates by a new and very simple hydrothermal decomposition. We further transferred them into maghemite (γ-Fe_2O_3) and hematite (α-Fe_2O_3) using the method modified by us [10].

3.2 Synthesis and Formation

Typical syntheses of rose-type magnetite (Fe_3O_4) nanoplates were carried out in a hydrothermal system by modified reduction reactions between $FeCl_2$ and ethylene glycol. In this experiment chemicals used were iron chloride tetrahydrate ($FeCl_2$•$4H_2O$, Wako Pure chemical industries Ltd., Japan), ethylene glycol (99.5%, Wako Pure chemical industries Ltd., Japan), polyethylene glycol 4000 (Tokyo Kasei Kogyo Co. Ltd, Japan) and anhydrous sodium acetate (NaAc, 98%, Nacalai Tesque, Japan). All chemicals were of analytical grade and used without any further purification.

$FeCl_2$•$4H_2O$ (1.98 g,10 mmol) was dissolved in ethylene glycol (100 mL) to form a clear solution, followed by the addition of NaAc (7.2 g) and polyethylene glycol (2.0 g). The mixture was stirred vigorously at 90 °C to get a clear solution and then sealed in a teflonlined stainless-steel autoclave (200 ml capacity). The autoclave was heated to and maintained at 200 °C for 5 h and allowed to cool to room temperature. After cooling, decantation was done by a permanent magnet to get the sedimented black products. The black products were washed several times with ethanol and dried at 70 °C for 3 h. Finally, we obtained 1.62g (82% of precursor) of Fe_3O_4 nanoplates. It is known that Fe_3O_4 can be oxidized to γ-Fe_2O_3, which can be further transformed

into α-Fe_2O_3 at higher temperature [11]. However, magnetite (Fe_3O_4) is not very stable and is sensitive to oxidation. Magnetite is transformed into maghemite (γ-Fe_2O_3) in the presence of oxygen [12].

3.3 Analytical Methods

The crystal structure and overall phase purity of the nanoplates with different sizes were examined using XRD. The surface morphology and nanoplates size were determined using a field emission scanning electron microscope (FE-SEM, model Hitachi S-4100H). Absorption (reflectance) spectra were recorded on UV-Vis spectrophotometer (Shimadzu Corporation, UV-2450, Japan). The magnetic hysteresis loops were measured by superconducting quantum interference device (SQUID, Quantum Design Model MPMS-5).

3.4 Results and Discussion

The crystal structure of the prepared rose-type nanoplates was observed by the XRD measurements using a PANalytical Advance X-ray diffractometer with CuKα (α = 1.5405 nm) radiation and a Ni filter. Typical XRD patterns of Fe_3O_4, γ-Fe_2O_3 and α-Fe_2O_3 are shown in Fig. 3-1A. Fig. 3-1A (a) is the XRD pattern from the as-synthesized, black rose type Fe_3O_4 nanoplates assembly. After oxidation under O_2 at 250 °C for 6 h, the black assembly is transformed into a red-brown one. Fig. 3-1A (b) shows all XRD peak positions and relative intensities of this red-brown material. Fig. 3-1A (c) shows the XRD of the dark red-brown materials, α-Fe_2O_3, obtained after 500 °C annealing of γ-Fe_2O_3 in Fig. 3-1A (b) under Ar gas for 1 h. To confirm the three types of iron oxides nanoplates prepared through this study, a comparative XRD analysis was done with commercial ones (see supplemental materials). Fig. 3-1A shows that all XRD peak positions and relative intensities of our as-prepared nanomaterials match well with those of commercial Fe_3O_4, γ-Fe_2O_3 and α-Fe_2O_3 powder materials (Wako

catalog No. 093-01035, 324-94282 and 322-94283, respectively), indicating that the synthesis and oxidation of Fe_3O_4 under O_2 and annealing in the presence of Ar gas lead to formation of γ-Fe_2O_3 and α-Fe_2O_3, respectively. No diffraction peaks from other crystalline forms are detected, which demonstrates that these Fe_3O_4, γ-Fe_2O_3 and α-Fe_2O_3 samples have high purity and crystallinity (JCPDS, PDF, File No. 01-086-1340, 00-025-1402 and 00-024-0072, respectively). Fig. 3-1B gives the UV-Vis absorption (reflectance) spectra of rose-type magnetic nanoplates and their comparison with commercial ones (Wako Pure chemical industries Ltd., Japan). It can be seen clearly that the absorption intensity of our synthesized nanoplates is higher than that of the commercial ones in a certain range of wavelength.

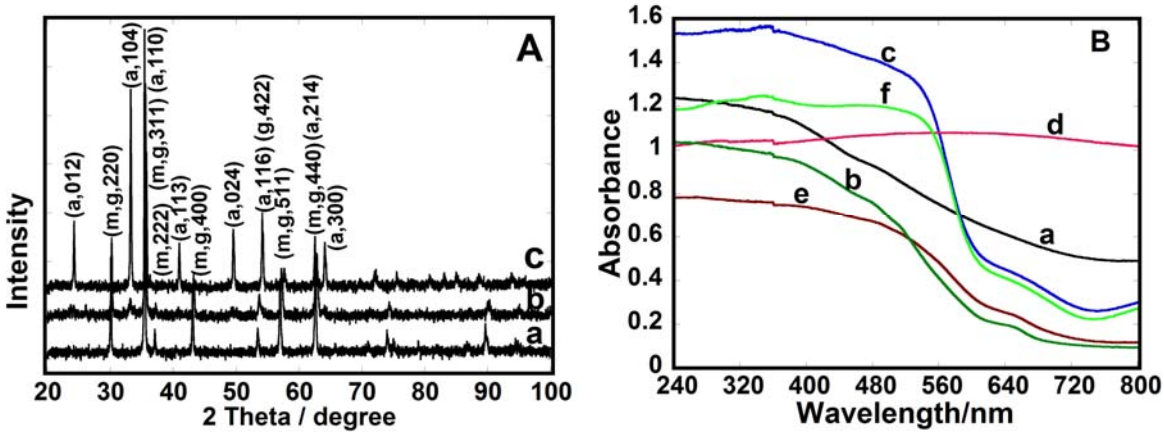

Fig. 3-1: XRD patterns (A) and UV -Vis absorption (reflectance) spectra (B) of rose-type magnetite, maghemite and hematite nanoplates are represented by (a), (b) and (c), respectively, for both plates. Comparative UV -Vis absorption (reflectance) spectra (B) with commercial magnetite, maghemite and hematite nanoparticles (Wako Pure chemical industries Ltd., Japan) are represented by (d), (e) and (f), respectively. Magnetite, maghemite and hematite are represented by (m), (g) and (a), respectively, for peak indexing.

The clear rose-shaped morphology was observed by FE-SEM in all the samples (Fig. 3-2). Such type of beautiful and unique morphology was observed for the first time in iron oxides with excellent magnetic properties. The length and width of the nanoplates were roughly estimated in accordance to SEM to be 350–500 nm and 60-70 nm, respectively, as shown in Fig. 3-2d.

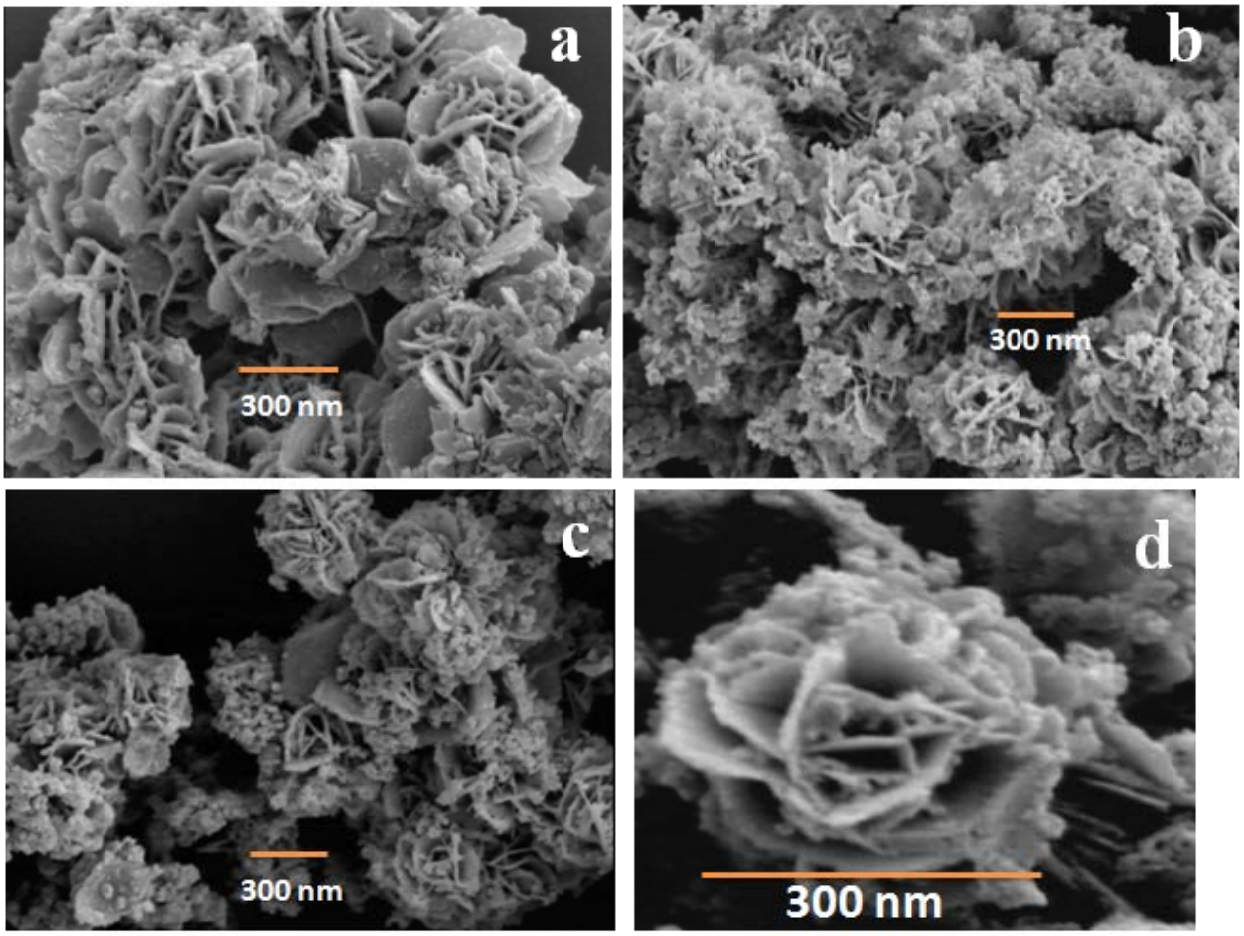

Fig.3-2: SEM images of rose-type magnetic nanoplates. Magnetite, maghemite and hematite nanoplates are represented by (a), (b) and (c), respectively, and (d) shows an example of single rose-type (maghemite) crystallinity.

The hysteresis curves obtained at room temperature (Fig.3-3) show that the saturation of magnetization (M_S) is complete with the values of 78.3, 65.5 and 0.8 emu/g for Fe_3O_4, γ-Fe_2O_3

and α-Fe_2O_3, respectively, which almost matched with the report by Cornell *et al.* [1]. The M_S values for substances (γ-Fe_2O_3 and α-Fe_2O_3) treated with oxygen and annealed are different from the mother sample, indicating that the oxidation of magnetite into maghemite was completed and that maghemite was transformed at high temperature to hematite during annealing which was also supported by the XRD analysis.

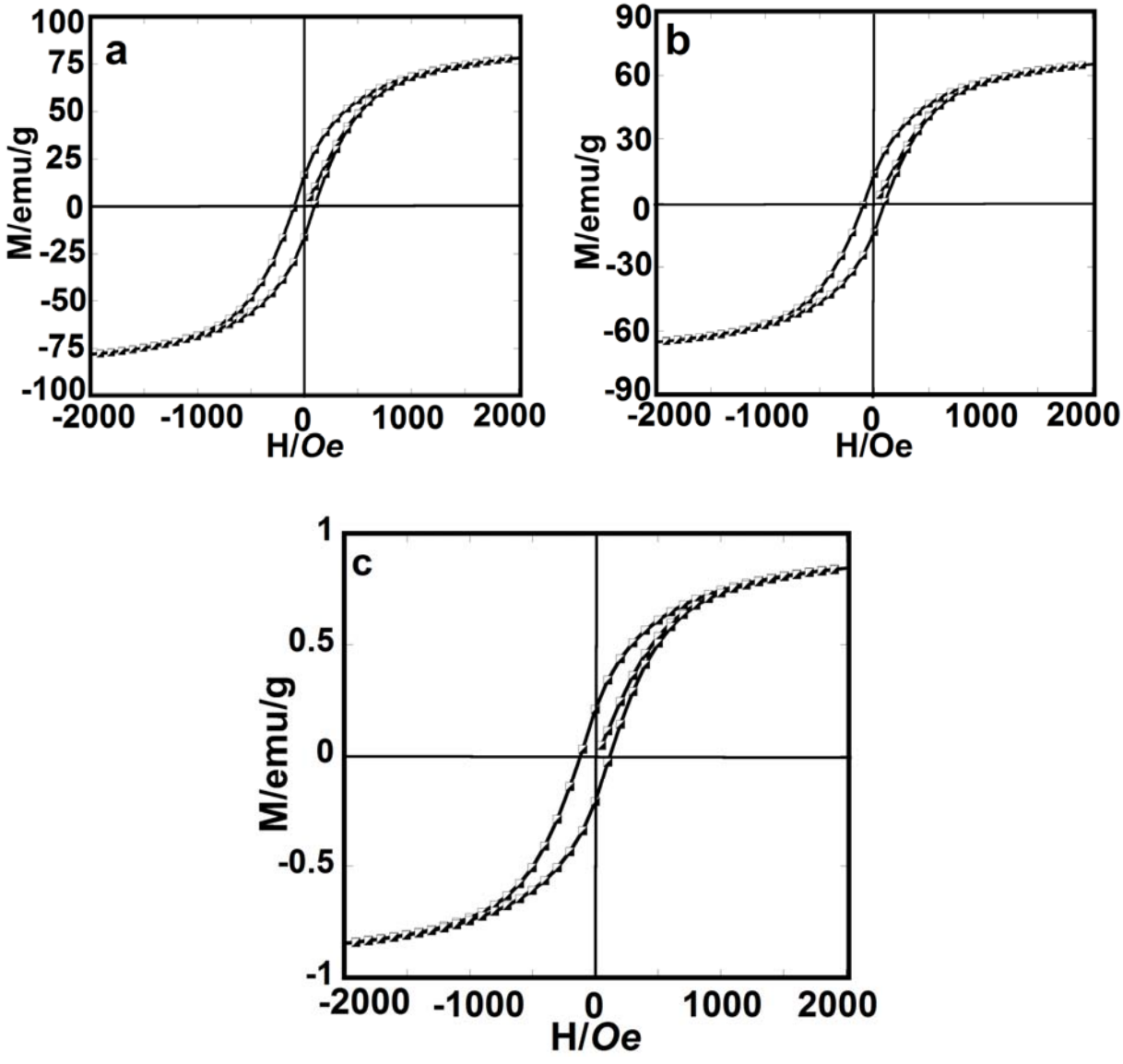

Fig.3-3: Magnetic hysteresis loops of rose-type magnetic nanoplates at room temperature. Magnetite, maghemite and hematite nanoplates are represented by (a), (b) and (c), respectively.

An important aspect of the synthesis of magnetic nanomaterials is the reproducibility when they are synthesized using identical conditions. To test the reproducibility of the rose-type magnetic nanoplates, three samples were synthesized under an optimum condition that was already described in section 2 and these three samples were found to have fairly consistent values for maximum reproducing capability, when characterized. Nowadays magnetic nanoparticles with good stability are the great interest in catalysis and in biotechnology/biomedicine applications. So, this type of beautiful magnetic nanoplates can be very useful to assist an effective separation of catalysts, nuclear waste management, water purification, biochemical products, magnetic nanodevices, biomagnetic application and cell separations. Hopefully, we will investigate the comparative capability of our synthesized nanomaterials in the applied filed in our next full paper.

To the best of our knowledge, this is the first report of synthesis of rose-type magnetic nanoplates by the simple hydrothermal method. Other advantages of this method are in the use of iron chloride tetrahydrate as the sole iron precursor, and to be very simple and cost-effective.

3.5 Conclusions

We for the first time synthesized the rose-type magnetic nanoplates through simple hydrothermal decomposition solely using $FeCl_2 \cdot 4H_2O$ as a precursor with the nanoplates size range from 350-500 nm and width 60-70 nm. Synthesized nanoplates showed excellent reproducing capability and cost effectiveness, which may be important for commercial production of such beautiful nanoplates.

References

[1] Cornell RM, Schwertmann U. The Iron Oxides. 2nd ed. Weinheim: VCH Publishers; 2003.

[2] Majewski P, Thierry B, Crit Rev Solid State Mater Sci 2007; 32: 203-215.

[3] Tartaj P, Morales MD, Veintemillas-Verdaguer S, Gonzalez-Carreno T, Serna CJ, J. Phys D: Appl Phys 2003; 36: R182-R197.

[4] Kim JS, Yoon TJ, Kim BG, Park SJ, Kim HW, Lee KH, Park SB, Lee JK, Cho MH, Toxicol Sci 2006; 89: 338-347.

[5] Tartaj P, Morales MP, Gonzalez-Carreno T, Veintemillas-Verdaguer S, Serna CJ, J Magn Magn Mater 2005; 290: 28-34.

[6] Al-Sayari S, Carley AF, Taylor SH, Hutchings GJ, Top Catal 2007; 44: 123-128.

[7] Zhong Z, Ho J, Teo J, Shen S, Gedanken A, Chem Mater 2007; 19: 4776-4782.

[8] Peterson ML, Brown JGE, Parks GA, Stein CL, Geochim Cosmochim Acta 1997; 61: 3399-3412.

[9] Neuberger T, Schopf B, Hofmann H, Hofmann M, Rechenberg BV, J Magn Magn Mater 2005; 293: 483-496.

[10] Sun S, Zeng H, Robinson DB, Raoux S, Rice PM, Wang SX, Li G, J Am Chem Soc 2004; 126: 273-279.

[11] Bate G, In Magnetic Oxides Part 2, Craik, D. J. Ed., John Wiley & Sons, New York, 1975, pp.705-707.

[12] Laurent S, Forge D, Port M, Roch A, Robic C, Elst LV, Muller RN, Chem Rev 2008; 108: 2067-2110.

CHAPTER 4

SYNERGISTIC CELL-KILLING BY MAGNETIC AND PHOTOIRRADIATION EFFECTS OF NECK-STRUCTURED α-Fe_2O_3 AGAINST CANCER (HeLa) CELLS

Abstract

Nanosized neck-structured α-Fe_2O_3 nanoparticles were prepared successfully from iron chloride tetrahydrate solely by the hydrothermal method. The FE-SEM and TEM studies revealed a unique necked structure with a particle size of ca. 50–60 nm. The synthesized nanomaterials showed the excellent colloid stability and magnetization ability. Finally, the as-prepared α-Fe_2O_3 nanoparticles suspensions showed almost 100% cancer cell killing by the significant temperature increment when an AC (alternating current) magnetic-field and photoirradiation were applied at a concentration of 80μg/mL MEM (minimum essential medium). This report has already been published in Chemistry Letters, 2011, 40(7), 773-775.

4.1 Introduction

Iron oxides exist in nature in many forms in which magnetite (Fe_3O_4), maghemite (γ-Fe_2O_3), and hematite (α-Fe_2O_3) are probably most common [1]. Hematite (α-Fe_2O_3) is the oldest iron oxide and is widespread in rocks and soils. It is the most stable iron oxide under ambient conditions and has significant scientific and technological importance [2]. The stability and semiconductor properties of α-Fe_2O_3 allow it to be used as a photocatalyst [3]. Currently the α-Fe_2O_3 photoelectrode has received considerable attention as a solar energy conversion material

due to its excellent properties, such as a small band gap (2.1 eV), high resistivity to corrosion, and low cost [4].

In an alternating current (AC) magnetic field, induced currents are generated in metallic objects, and as a consequence, heat is generated in the metal. This phenomenon is greatly enhanced in metals showing collective magnetic behavior. Thus, when a magnetic fluid is exposed to an AC magnetic field, the particles become powerful heat sources, destroying tumor cells since these cells are more sensitive to temperatures in excess of 41 °C than their normal counterparts [5]. Hyperthermia is a therapeutic procedure that promotes the increase of temperature in body tissues in order to change the functionality of the cellular structures. Its activity is based on the fact that a temperature increase to 41°C - 42°C can induce tumor cell death, as the tumor cells are less resistant to sudden increases in temperature than the normal surrounding cells [6].

Alpha-Fe_2O_3 is a famous semiconductor but cannot produce sufficient OH radicals under photoirradiation and its low saturation magnetization value cannot produce enough heat to a hyperthermia level to kill the cancer cells. In view of this, in this letter, we deal with the preparation and characterization of neck-structured α-Fe_2O_3 nanoparticles and their successful utilization for thermal cancer cell killing under combined AC magnetic-field induction and visible light irradiation.

4.2 Nanoparticle synthesis and experimental method

Typical syntheses of magnetite (Fe_3O_4) nanoparticles were carried out in a hydrothermal system. $FeCl_2 \cdot 4H_2O$ (0.99 g, 5 mmol) was dissolved in ethylene glycol (40 mL) to form a clear solution, followed by the addition of sodium acetate (anhydrous, 3.6 g) and polyethylene glycol (1.0 g). The mixture was stirred vigorously for 45 min until getting a clear solution and then

sealed in a teflonlined stainless-steel autoclave (50 mL capacity). The autoclave was heated to and maintained at 190 °C for 5 h and allowed to cool to room temperature. After cooling, decantation was done by a permanent magnet to get the sedimented black products. The black products were washed several times with ethanol and dried at 70 °C for 3 h. Finally, we obtained 0.81 g of Fe_3O_4 nanoparticles and then the magnetite nanoparticles were oxidized into maghemite (data not shown) and hematite at 250 °C for 8 h in the presence of oxygen and at 500 °C for 3 h in the presence of Ar gas, respectively [7]. The prepared nanoparticles were characterized by using FE-SEM, TEM, XRD, and UV-Vis absorption (reflectance) spectra. Colloidal stability was observed by dispersing the nanoparticles in distilled water using a permanent magnet and magnetic hysteresis loops were measured by superconducting quantum interference devices (SQUID, Quantum Design MPMS-5).

4.3 Cell culture and cytotoxicity evaluation

HeLa cells were provided by the RIKEN BRC through the National Bio-Resource Project of the MEXT, Japan. The mentioned cancer cell line was cultured in a minimum essential medium (MEM) solution with 10% newborn calf serum (NBS) in a humidified incubator with an atmosphere of 5% CO_2 in air at 37°C and the cells were plated at a concentration of about 3×10^5 in 60 mm Petri dishes and allowed to grow for 3 days. Monolayer cultures of cancer cell line (HeLa Cells) were maintained as described by Abdulla-Al-Mamun *et al*. [8].

The *in vitro* cytotoxicity and anti-cancer effect of the as-prepared nanoparticles against the HeLa cell line were evaluated by trypan blue exclusion method. In the experiment, the AC magnetic-field was created by using a magnetic oscillator with desired frequency and strength of 560 kHz and 5.0 kA/m, respectively, and a Xenon lamp (CERMAX 300-W LX300F, USA) with heat cut-off and band-pass filters (400–800 nm) with an average intensity of 30 mW cm^{-2} was

used for the light irradiation on HeLa cells. To investigate the cytotoxicity efficacy, every Petri dish was subjected to apply under simultaneous AC magnetic-field induced and photoirradiated conditions for 5, 10, 15, 20, and 25 min with a dose 80 μg/mL of α-Fe_2O_3 nanoparticles. Temperature increment for every dish was recorded by using a digital thermometer (Model SK-250WP II-R).

4.4 Results and discussion

Particles morphology of the sample was studied using FE-SEM and TEM. Fig. 4-1 (a) represents the FE-SEM micrographs of neck-structured α-Fe_2O_3 and the nanoparticles size was roughly estimated to be about 50-60 nm based on SEM and TEM data. Fig. 4-1(b), (c), and (d) depict the TEM image, color, and colloidal stability of α-Fe_2O_3, respectively. The nano-structural homogeneities and remarkably unique neck-structured morphology were clearly observed by both FE-SEM and TEM. Such a type of unique morphology was observed for the first time in iron oxide with excellent magnetic properties.

To examine the colloid stability of iron oxide samples, 10 mg nanoparticles were dispersed in 50 mL doubly distilled water by sonication. As shown in Fig. 1(c, lower), the as-prepared nanoparticles were well dispersed into water without any aggregation and precipitation and were firmly dragged by the permanent magnetic force and the magnetic nanoparticles remained in suspension for more than 1 day, which demonstrates that they can be well-dispersed in aqueous solution.

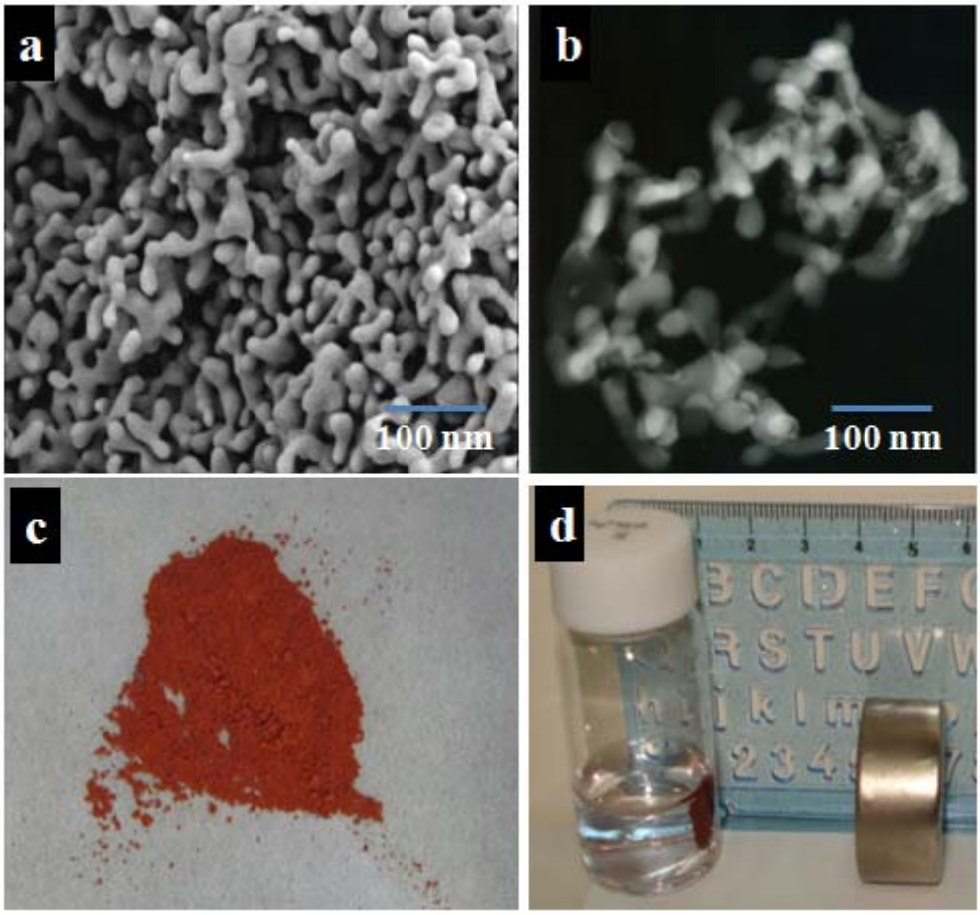

Fig.4-1: SEM (a), TEM (b) images, (c) color, and (d) colloidal stability of neck-structured α-Fe_2O_3 nanoparticles.

The crystal structures and band gap of the prepared neck-structured hematite nanoparticles were observed by XRD and UV-Vis absorption (reflectance) spectra. Typical XRD patterns and UV-Vis absorption (reflectance) spectra of as-prepared and commercial (Wako, catalog No. 322-94283) α-Fe_2O_3 are shown in Fig.4-2. The XRD pattern of Fe_3O_4 is shown in Fig.4-2A (a) which was transferred to α-Fe_2O_3 (Fig. 4-2A (c)), and it was clear that the diffraction peaks of as-prepared α-Fe_2O_3 (Fig. 4-2A (c)) were found to be consistent with the diffraction peak patterns of the commercial one (Fig. 4-2A (b)). No diffraction peaks from other crystalline forms are detected, which demonstrates that our prepared α-Fe_2O_3 sample has high purity and crystallinity

(JCPDS, PDF, File No. 01-089-0596). UV-Vis spectroscopic studies were performed to ascertain the absorption edge of the as-prepared nanomaterials. Fig.4-2B (a) and (b) represent the UV-visible diffused reflectance spectra of commercial and as-prepared α-Fe_2O_3, respectively. The absorption edge for both samples was at around 570–580 nm. The band gap estimated from the onset of the absorption edge was observed at 2.16–2.18 eV, which was in good agreement with a band gap value of 2.2 eV for α-Fe_2O_3 [9].

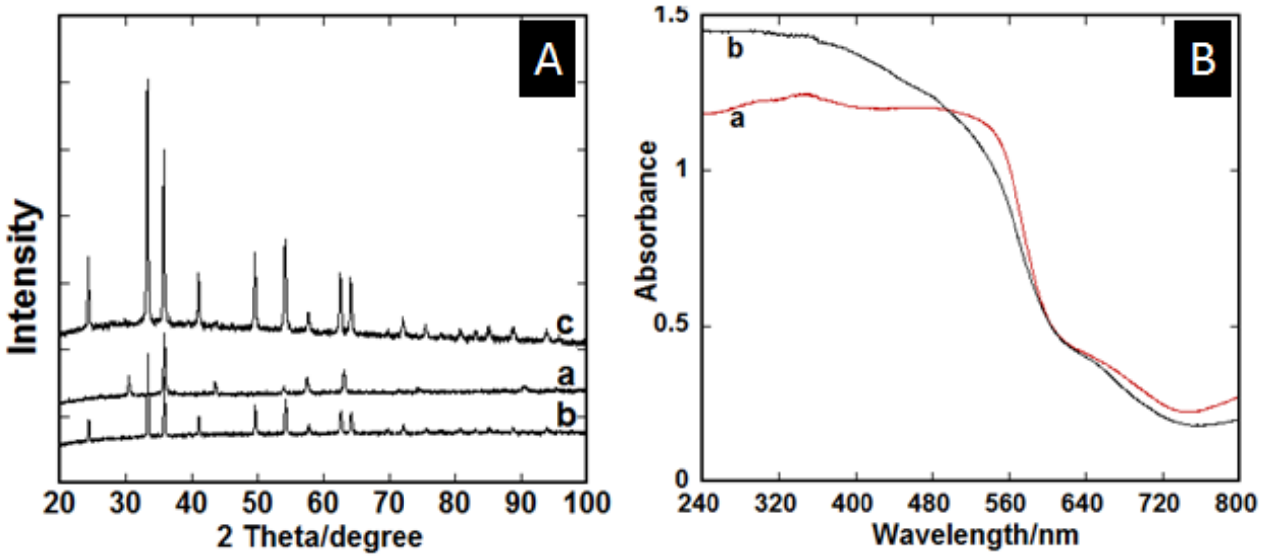

Fig.4-2: XRD patterns (A) and UV-Vis absorption (reflectance) spectra (B) of neck-structured α-Fe_2O_3 nanoparticles in comparison with commercial ones; (a) Fe_3O_4 (mother sample), (b) commercial, and (c) as-prepared α-Fe_2O_3 for plate (A) and (a) commercial and (b) as-prepared α-Fe_2O_3 for plate (B).

Fig.4-3A shows the hysteresis loops of commercial (a) and as-prepared (b) α-Fe_2O_3, and Fe_3O_4 (Fig.4-3A, inset) measured at room temperature. We noticed that the saturation magnetization values were 0.45, 0.67, and 65.8 emu/g, respectively, for commercial, α-Fe_2O_3, and Fe_3O_4 nanoparticles, almost similar to the findings reported by Cornell *et al*. [1].

This is excellent evidence of the completion of the phase transfer of Fe_3O_4 to γ-Fe_2O_3 (data not shown) and α-Fe_2O_3. Heat dissipation capability of Fe_3O_4 (Fig. 3B (a)) and as-prepared α-Fe_2O_3 (Fig. 3B (b)) was evaluated by using an AC magnetic-field generator. The heat generated was evaluated by 80 µg/mL magnetic nanoparticle suspension dispersed in MEM with exposing time 5, 10, 15, 20, and 25 min under both AC magnetic-field and photoirradiation conditions. The highest temperatures achieved were 52.1 and 45.5 °C for Fe_3O_4 and α-Fe_2O_3, respectively, for 25 min exposure time whereas Ito *et al.* achieved 42.0 °C for 30 min exposure time using 100 µg/mL concentration of magnetite nanoparticles under only AC magnetic field [10]. However, in this study we assumed that heat was generated through the combination of Brownian and Néel relaxation and magnetic hysteresis loss; to clarify it further detailed study is needed.

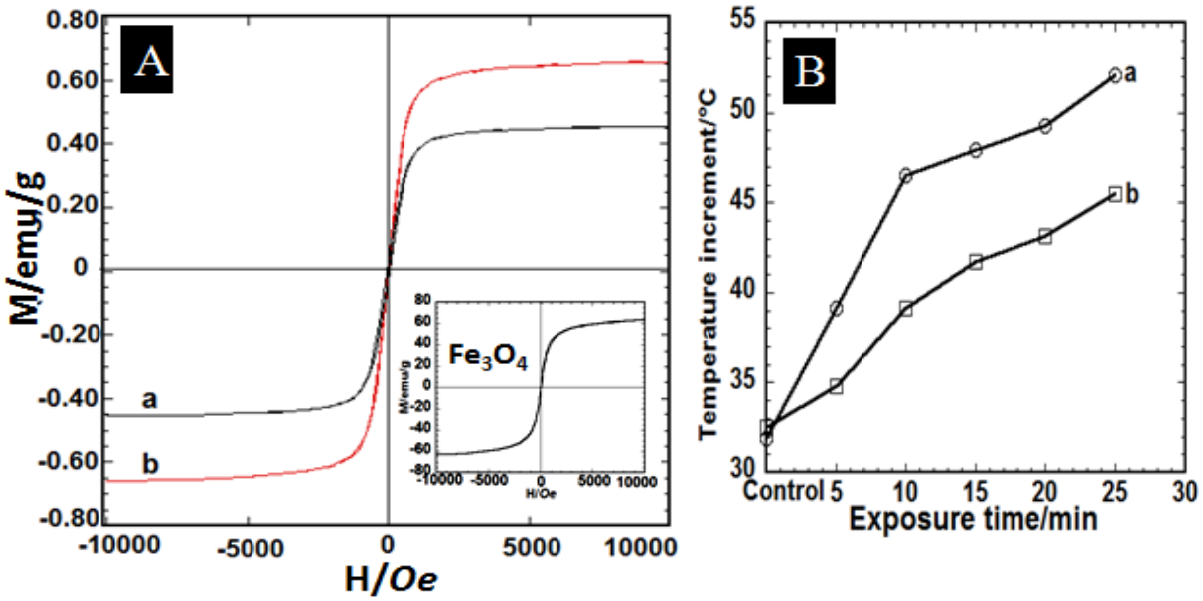

Fig.4-3: (A) Magnetic hysteresis loops of neck-structured α-Fe_2O_3 nanoparticles (b) in comparison with commercial ones (a) and Fe_3O_4 (inset). (B) Time dependent heat increment of Fe_3O_4 (a) and as-prepared α-Fe_2O_3 (b) under combined AC magnetic-field induction and photoirradiation.

To evaluate the cytotoxicity, cell dishes were incubated for 24 h with 80 μg/mL of α-Fe_2O_3 and another dish without any nanoparticle solution (control dish) was also incubated for 24 h (Fig.4-4). The cancer cell viability under AC magnetic-field induced and photoirradiated conditions for exposing time 5, 10, 15, 20, and 25 min are shown in Fig.4-4.

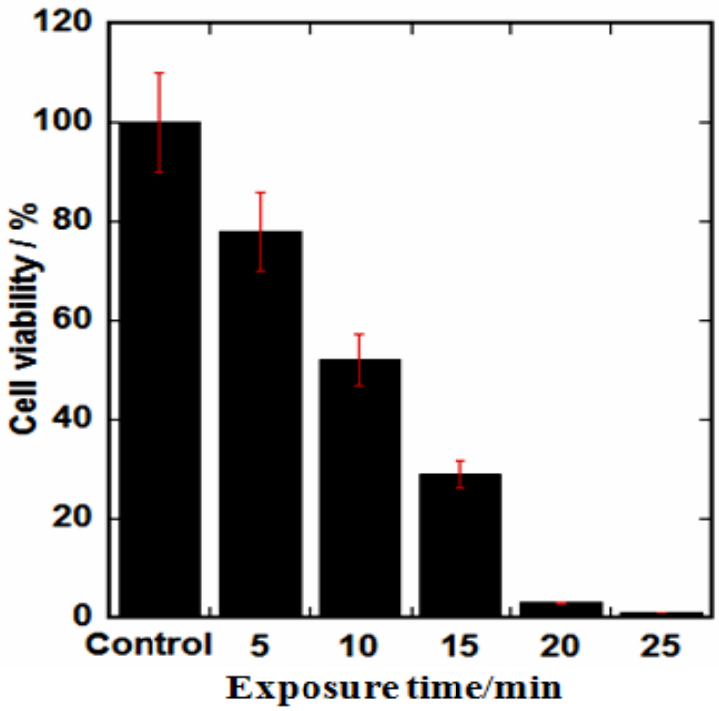

Fig.4-4: Time dependent cell viability using neck-structured α-Fe_2O_3 nanoparticles under AC magnetic-field and photoirradiated conditions.

We compared the heat increment and cytotoxicity of the same sample under three distinct conditions such as AC magnetic-field induction alone, photoirradiation alone, and combined AC magnetic-field induction and photoirradiation with the same dose for 20 and 25 min (Table 4-1). The results revealed that highest temperature achieved was 45.5 °C along with almost 100% cells destruction under the combined AC magnetic-field induction and photoirradiation conditions (T_3) whereas for only AC magnetic-field induction (T_1) and only photoirradiated

condition (T_2), temperature increment and cell destruction were 40.2 °C (T_1) , 38.5 °C (T_2) and 42% (T_1) (viability: 58%), 24% (T_2) (viability: 76%), respectively, for 25 min exposure time.

Table 4-1. Comparative heating and cell killing potentiality of neck-structured α-Fe_2O_3 nanoparticles under different conditions

Parameter	Exposure time /min					
	20			25		
	T_1[a]	T_2[b]	T_3[c]	T_1[a]	T_2[b]	T_3[c]
Heat increment /°C	39.3	37.1	43.1	40.2	38.5	45.5
Cell viability /%	77	86	3.1	58	76	0.5

[a]AC magnetic-field induction alone, [b]photoirradiation alone, and [c]AC magnetic-field induction + photoirradiation.

So, it can be clearly stated that under combined AC magnetic-field induction and photoirradiated conditions for 25 min almost 100% of the cells were killed in the presence of 80 μg/mL of α-Fe_2O_3 (Fig.4-4).

Fig.4-5 shows microscopic images of HeLa cells. Fig.4-5a shows that the cell morphology is unchanged under simultaneous AC magnetic-field induced and photoexcited conditions without any nanoparticles. However, Fig.4-5b shows that the HeLa cells suffer severe thermal shock at 25 min exposure time under the same condition with α-Fe_2O_3 nanoparticles. Finally, it can be concluded that increased exposure time increased heat increment and thus, increased cancer cell killing efficiency.

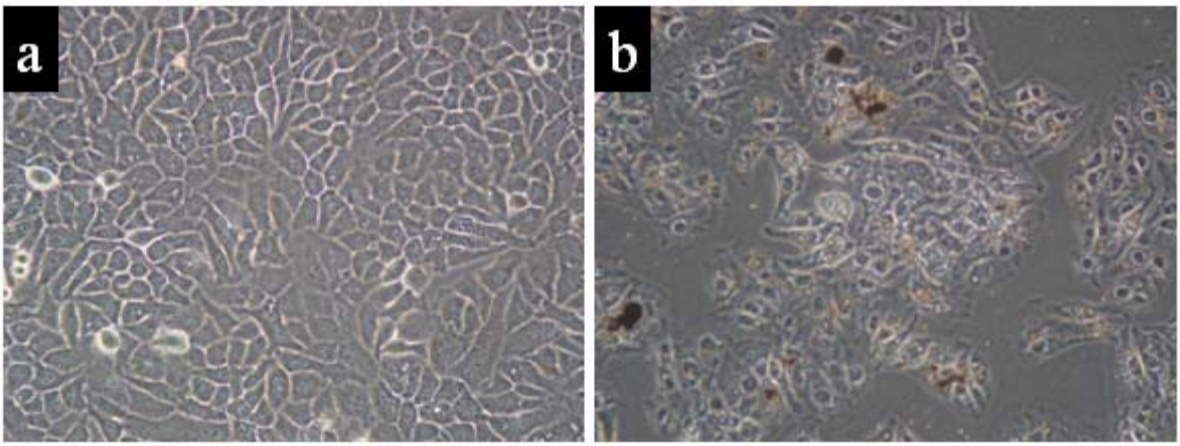

Fig.4-5. Microscopic images of HeLa cells (Magnification 200). (a) Control and (b) 25 min exposure under both AC magnetic-field and photoirradiated conditions.

4.5 Conclusion

To the best of our knowledge, we synthesized for the first time α-Fe_2O_3 nanoparticles of neck-structured shape with excellent colloidal stability and magnetic properties. This is the first report using α-Fe_2O_3 nanoparticles for cancer cell killing under combined AC magnetic-field induced and photoirradiated conditions.

References

[1] R .M. Cornell, U. Schwertmann, *The Iron Oxides: Structure, Properties, Reactions, Occurrences and Uses*, 2nd Edition. Wiley-VCH, Weinheim, **2003**.

[2] R. Dieckmann, *Philos. Mag. A* **1993**, *68*, 725.

[3] H. H. Kung, *Transition Metal Oxides: Surface Chemistry and Catalysis*, Elsevier, New York, **1989**.

[4] T. Ohmori, H. Takahashi, H. Mametsuka, E. Suzuki, *Phys. Chem. Chem. Phys.* **2000**, *2*, 3519.

[5] An-Hui Lu, E. L. Salabas, S. Ferdi, *Angew. Chem. Int. Ed*., **2007**, *46*, 1222.

[6] R. Cavaliere, E.C. Ciocatto, B.C. Giovanella, C. Heidelberger, R.O Johnson, M. Margottini, B. Mondovi, G. Moricca, A. Rossi-Fanelli, *Cancer*. **1967**, *20*, 1351.

[7] S. Sun, H. Zeng, D.B. Robinson, S. Raoux, P. M. Rice, S.X. Wang, Guanxiong, *J. Am. Chem. Soc.* **2004**, *12*6, 273.

[8] M. Abdulla-Al-Mamun, Y. Kusumoto, A. Mihata, M. S. Islam, B. Ahmmad, *Photochem. Photobiol Sci*. **2009**, *8*, 1125.

[9] W. B. Jr. Ingler, S. U. M Khan, *Int. J. Hydrogen Energ*. **2005**, *30,* 821.

[10] A. Ito, M. Shinkai, H. Honda, K, Yoshikawa, S. Saga, T. Wakabayashi, J. Yoshida, T. Kobayashi *Cancer Immunol. Immunother*. **2003**, *52*, 80.

CHAPTER 5

PHOTOCATALYTIC AND AC MAGNETIC-FIELD INDUCED ENHANCED CYTOTOXICITY OF Fe_3O_4@TiO_2 CORE-SHELL NANOCOMPOSITES AGAINST HeLa CELLS

Abstract

Fe_3O_4@TiO_2 core-shell nanocomposites were successfully prepared and characterized by FE-SEM, XRD, UV-Vis absorbance spectra, and EDX. The FE-SEM and EDX studies revealed core-shell structure with a particle size of ca. 40–50 nm. We adopted HeLa cells as a model to investigate the thermal-photocatalytic cell killing efficiency of Fe_3O_4@TiO_2 using 150 μg/mL dose content for 10 min exposure time. We found neither only AC magnetic-field induction nor only photoirradiation condition could kill the cancer cells up to satisfactory level using Fe_3O_4@TiO_2 nanocomposites. Finally, the results revealed that almost 100% cancer cells were destructed by Fe_3O_4@TiO_2 nanocomposites whereas for bare Fe_3O_4 and bare TiO_2, 90% and 56% cancer cells were killed, respectively, under combined AC (alternating current) magnetic-field induction and UV-Vis photoirradiated conditions. This work has already been published in Catalysis Communications, 2011, 16, 39-44.

5.1 Introduction

Magnetic nanoparticles are currently being investigated because of their numerous applications in several fields such as magnetic fluids, medicine, magnetic resonance imaging, data storage, sensing, and water remediation [1, 2]. Magnetite and maghemite have attracted attention in biomedical applications because of their biocompatibility and low toxicity in the

human body [3]. Magnetite and hematite are semiconductors and can catalyze oxidation/reduction reactions [4, 5]. But it is often necessary to coat their surface with an organic or inorganic shell, in order to protect them from chemical degradation or agglomeration according to the environments in which they will be used [2]. The coating can also be performed in order to add new functionalities to the magnetic core. Therefore, the addition of a TiO_2 shell to a magnetic core at the nanometer scale may lead to bifunctional nanoparticles which could be applied for example as a magnetic photocatalyst. Among various oxide semiconductor photocatalysts, TiO_2 [6-9] has proven to be the most suitable material for widespread environmental application for its biological and chemical inertness, strong oxidizing power, cost effectiveness, and long-term stability against photocorrosion and chemical corrosion. Nanostructured TiO_2 exhibits superior photocatalytic activity compared to conventional bulk materials because of its high surface area. To enhance its photocatalytic ability, nanostructured TiO_2 with various morphologies including nanoparticles, nanofibers, nanostructured films or coatings, and nanotubes have been prepared, and much progress on the synthesis of nanostructured TiO_2 with excellent catalytic properties has been made [10-13].

Fortunately, research has been carried out by immobilizing TiO_2 onto various magnetic supports, such as magnetite ferrite, barium ferrite and $Fe_3O_4@SiO_2$ particles [14-17]. TiO_2 nanoparticles are an excellent material. It is widely used in water and air purification, disinfection, waste treatment, and malignant tumor therapy [18–24]. Especially in the field of malignant tumor therapy, TiO_2 has some extra advantages such as extremely strong oxidation reaction which kills tumor cells. Although the photothermal, photocatalytic and hyperthermia cancer cell killing is already reported by our group [25, 26], we are interested in observing the enhanced cytotoxicity of $Fe_3O_4@TiO_2$ core-shell nanocomposites under combined AC magnetic-

field induction and photoirradiation conditions. The hyperthermia takes place at the cellular level and is mainly due to the heat-induced malfunction of repair processes after radiation-induced DNA damage [27]. So, to demonstrate that Fe_3O_4@TiO_2 core-shell nanocomposites have much more advantages than that of traditional one (TiO_2) in malignant tumor therapy, we synthesized superparamagnetic magnetite (Fe_3O_4) nanoparticles and then coated them with TiO_2 to prepare the Fe_3O_4@TiO_2 core-shell nanocomposites (NCs) and was applied in cancer therapy.

Because of our interest in the enhanced toxic effect of AC (alternating current) magnetic-field induction and chemical reactions of Fe_3O_4@TiO_2 particles produced by UV-Vis irradiation, we studied the cancer cell killing effects with bare Fe_3O_4, bare TiO_2, and Fe_3O_4@TiO_2 NCs under combined AC magnetic-field induction and UV-Vis photoirradiation conditions. We adopted HeLa cells as a model to investigate the thermal-photocatalytic cancer cell killing efficiency of Fe_3O_4@TiO_2 core-shell NCs under three distinct conditions (only AC magnetic-field induction, only photoirradiation and combined AC magnetic-field induction and photoirradiation conditions) using a dose of 150 μg/mL for 10-min induction and irradiation.

5.2 Experimental

5.2.1 Synthesis of Fe_3O_4@TiO_2 Core-shell Nanocomposites

Fe_3O_4 nanoparticles with diameter of ca. 20 nm were first synthesized via the co-precipitation method. In the next step, Fe_3O_4@C and finally, Fe_3O_4@TiO_2 core-shell NCs were synthesized by modifying (see supplemental material) the synthesis method of Li *et al*. [28]. In a typical co-precipitation method, for the synthesis of Fe_3O_4, $FeCl_3$ (2.6 g) and $FeCl_2$ (1.3 g) were dissolved in nitrogen gas (N_2) purged 2.0 M hydrochloric acid solution and magnetically stirred under a continuous flow of N_2. The mixture was heated at 70 °C for 30 min and then the mixture was heated for another 5 min under a blanket of N_2. Ammonia was added drop by drop to precipitate

the magnetic nanoparticles and the black product formed was treated hydrothermally at 70 °C for 30 min. All aqueous solutions and suspensions were made using nanopure water (resistivity 18 MΩ cm). The resulting nanoparticles were subsequently separated from the reaction media under magnetic field and washed three times with nanopure water before drying. Finally the MNPs were oven dried at 70 °C for 3 h to get Fe_3O_4. The overall synthesis routes of Fe_3O_4@C and Fe_3O_4@TiO_2 are described by the **Scheme 5-1**.

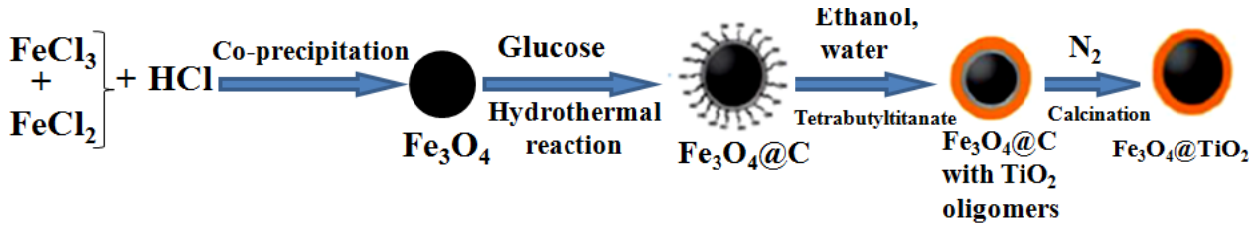

Scheme 5-1. Diagrammatic representation of the overall synthetic routes of Fe_3O_4@TiO_2 core-shell nanocomposites.

5.2.2 Cell Culture

HeLa cells were provide by the RIKEN BRC through the National Bio-Resource Project of the MEXT, Japan and stored in liquid N_2 to ensure the best quality. The mentioned cancer cell line was cultured in a minimum essential medium (MEM) solution with 10% newborn calf serum (NBS) in a humidified incubator with an atmosphere of 5% CO_2 in air at 37 °C and the cells were plated at a concentration of about 3×10^5 in 60 mm Petri dishes and allowed to grow for 3 days. Monolayer cultures of cancer cell line (HeLa Cells) were maintained as described by Abdulla-Al-Mamun *et al*. [29].

5.3 Characterization

The general structure characterization, including size, size distribution and crystal structure of the as-synthesized Fe_3O_4@TiO_2 core-shell NCs was performed for all the samples without any

size sorting. To further confirm the crystal structure and overall phase purity, the NCs with different sizes were examined using XRD with CuKα radiation and a Ni filter (for details, see the supplemental information). The surface morphology and NCs size were determined using a field emission scanning electron microscope (FE-SEM, model Hitachi S-4100H) using accelerating voltage, extraction voltage and absorbed current 10 kV, 5 kV and 10 μA, respectively. The FE-SEM sample was prepared by using an Ag sheet. A carbon tape was attached on the Ag sheet and a small amount of Fe_3O_4@TiO_2 NCs was taken over that carbon tape and then the sample was coated with Pt to escape from the heavy charges of the magnetic Fe_3O_4@TiO_2 NCs during analysis. Further, the core-shell morphology of the NCs was analyzed by a transmission electron microscope (TEM, JEOL JEM-3010 VII TEM) operating at 300 kV. Absorption (reflectance) spectra were recorded on UV-Vis absorption (reflectance) spectra (Shimadzu Corporation, UV-2450, Japan). The samples were standardized with barium sulphate coated glass substrate and its spectrum was used as the baseline. The spectra of all samples were measured in a wavelength range between 240 and 850 nm. The quantitative chemical composition of the Fe_3O_4@TiO_2 core-shell nanocomposites was also measured using an energy dispersive X-ray spectrometer (EDX, Philips, XL 30CP) attached to the cold field SEM.

5.4 In-vitro Cytotoxicity and Anti-cancer Assay

The *in vitro* cytotoxicity and anti-cancer effect of the nanocomposites against the HeLa cell line was evaluated by trypan blue exclusion method. In the experiment, the alternative current (AC) magnetic-field was created by using a magnetic oscillator with desired frequency and strength of 560 kHz and 5.0 kA/m, respectively, and a Xenon lamp (CERMAX 300-W LX300F, USA, ILC) with heat cut-off and band-pass filters (350–600 nm) with an average intensity of 30 mW cm^{-2} was used for the light irradiation on HeLa cells. The light power was measured by a

spectroradiometer (Model LS-100, EKO Instrument Co. Ltd.). A table rotator was used for the Petri dish to ensure the homogeneous light irradiation on the cells. To investigate and compare the cytotoxicity efficacy, every Petri dish was subjected to apply the three above mentioned treatments for 10 minutes and immediately after the treatment, temperature increment for the every dish was measured by a digital thermometer (Sato Keiryoki-250WP II-R).

Cancer cell viability was examined by treating with bare Fe_3O_4, bare TiO_2 and $Fe_3O_4@TiO_2$ colloidal solution for 24 h incubation in an incubator. To investigate the cytotoxicity of synthesized nanomaterials, one dish was used as control without any nanomaterials and the other five dishes were treated with different doses, like 0.2, 0.4, 0.6, 0.8 and 1.0 mL of nanocomposites colloidal solution per mL of MEM solution where the actual colloidal solution concentration was 150 μg/mL. A haemocytometer was used to estimate the total number of viable cells (by counting cells in the four 1 mm^2 corners of the haemocytometer) and average number of the cells per unit volume (mL) of medium was calculated as the sum of the counted cell number/ 3×10^5. Every treatment was conducted by doing three-time independent experiments.

5.5 Results and Discussion

5.5.1 Particles Morphology and Crystalline Phase

Figure 5-1 gives the SEM (A) and TEM (B) photographs of (a) bare Fe_3O_4 and (b) $Fe_3O_4@TiO_2$ core-shell NCs and EDX is shown in Fig.5-1(C). According to Fig.5-1A (b), $Fe_3O_4@TiO_2$ NCs with well-defined core-shell structure are rather monodispersed and the shape of $Fe_3O_4@TiO_2$ core-shell NCs is definitely globular. The SEM image (Fig. 5-1A (b)) also clearly shows round whitish structure of the TiO_2 shell around the Fe_3O_4 core. Further, Fig. 5-1B (b) confirms that Fe_3O_4 nanoparticles were well-surrounded by TiO_2 shell structure whereas Fig.

5-1B (a) approved the bare Fe_3O_4 nanoparticles without any shell structure and the shape of Fe_3O_4@TiO_2 core-shell NCs is definitely globular (see also an inset in Fig. 5-1(C)). The core is uniformly covered by the shell with TiO_2 particles. The EDX spectrum of Fe_3O_4@TiO_2 indicates the clear presence of Fe, O and Ti components. The strong Ti and O signals in the EDX spectrum indicate that Ti consists of mixed oxides surrounding the outer layer of the Fe_3O_4 core.

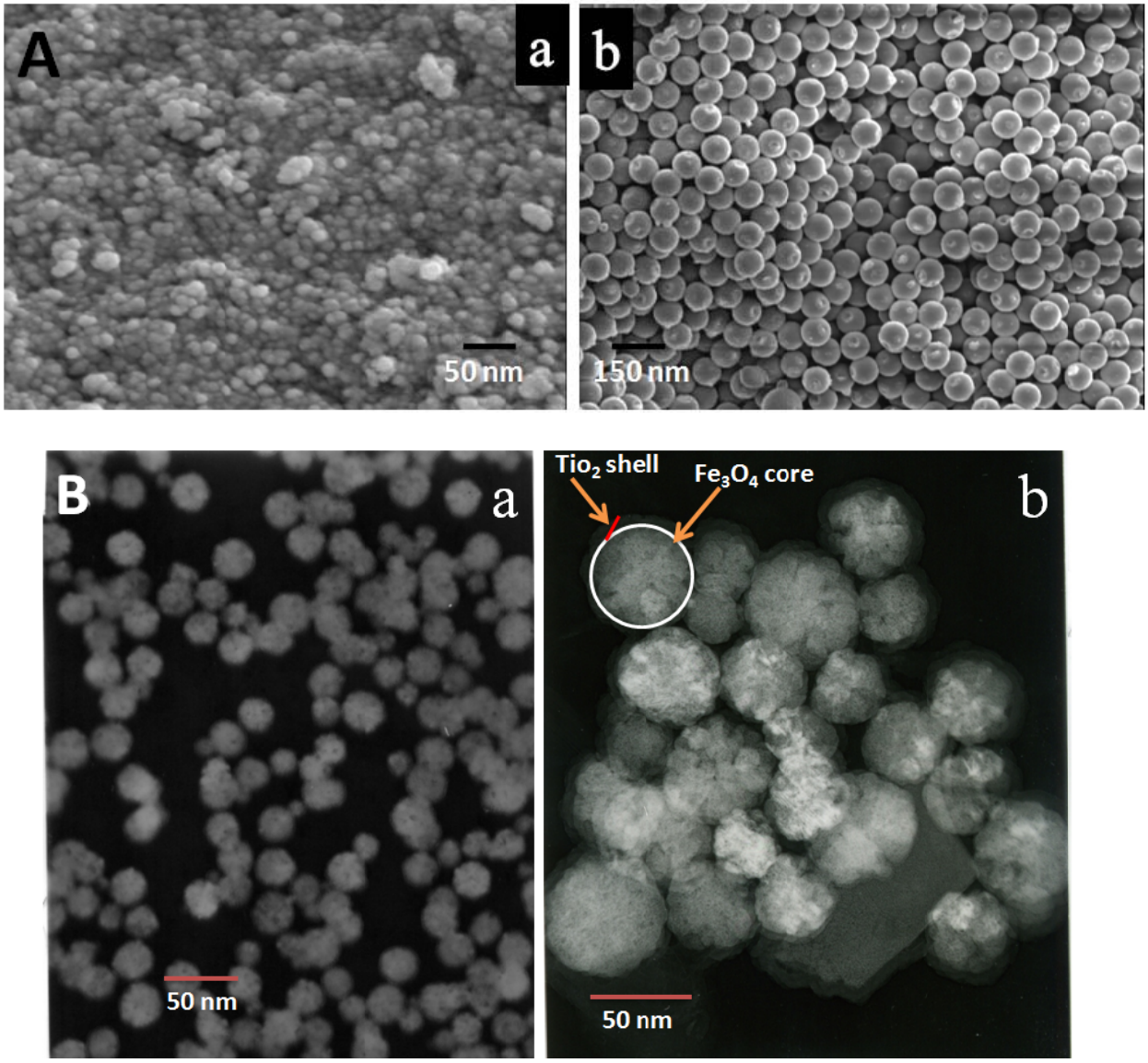

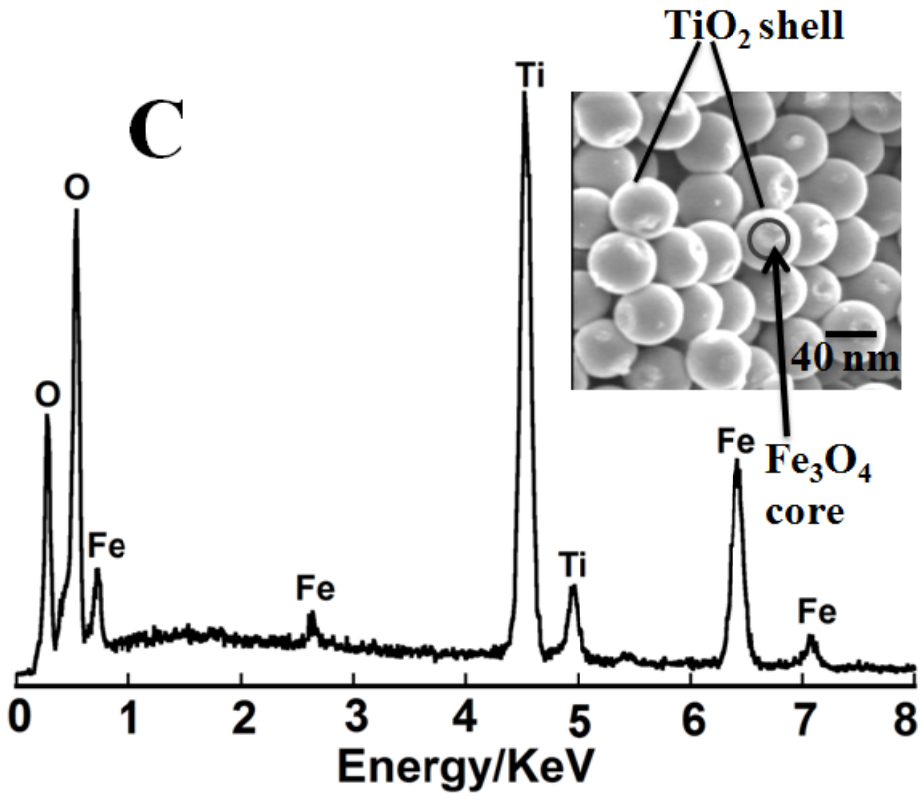

Fig.5-1: SEM (A) and TEM (B) images of Fe_3O_4 (a) and Fe_3O_4@TiO_2 (b) and EDX (C) spectrum of Fe_3O_4@TiO_2.

The wide-angle X-ray diffraction (XRD) patterns of (a) bare Fe_3O_4, (b) bare TiO_2, and (c) Fe_3O_4@TiO_2 NCs are shown in Fig. 5-2A. Compared with bare Fe_3O_4, Fe_3O_4@TiO_2 NCs exhibit similar peaks at 2θ = 30.124, 35.483, 43.124, and 62.629 ° which can be attributed to the diffraction peaks of (220), (311), (400), and (440) planes of Fe_3O_4 and in comparison with bare TiO_2, Fe_3O_4@TiO_2 NCs exhibit similar peaks at 2θ = 25.625 and 55.660° which can be attributed to the diffraction peaks of (101) and (211) planes of TiO_2 (JCPDS, PDF, File No. 01-075-0033 and 00-002-0406), respectively, demonstrating the formation of Fe_3O_4@TiO_2 NCs.

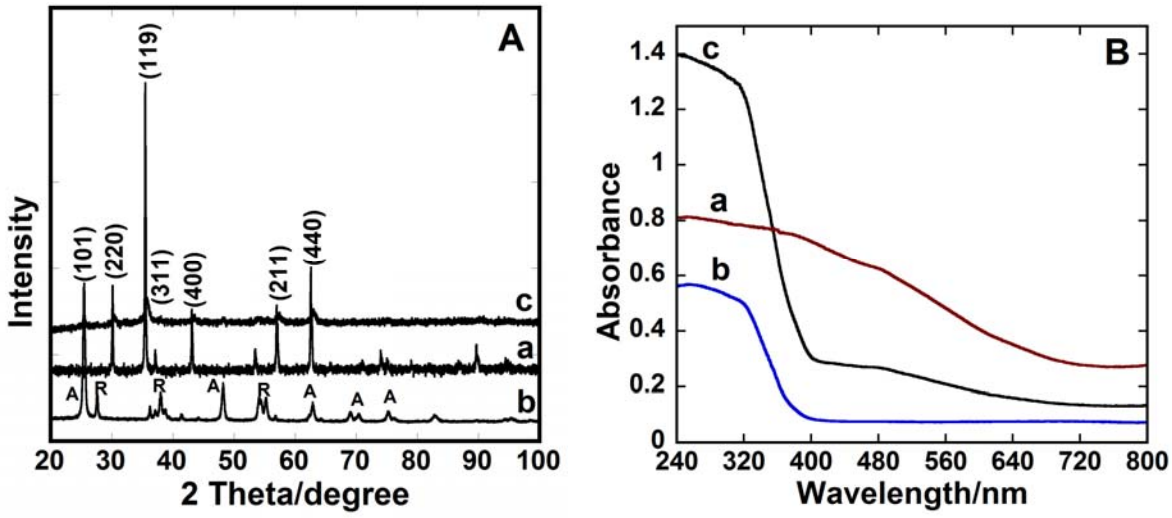

Fig. 5-2: XRD patterns (A) of (a) bare Fe_3O_4, (b) bare TiO_2, and (c) Fe_3O_4@TiO_2 and UV-Vis absorption spectra (B) of (a) bare Fe_3O_4, (b) bare TiO_2, and (c) Fe_3O_4@TiO_2. Here, A: anatase, R: rutile phase for TiO_2

Figure 5-2B shows the UV–Vis absorption spectra of (a) bare Fe_3O_4, (b) bare TiO_2, and (c) Fe_3O_4@TiO_2. The UV–Vis absorption spectra of Fe_3O_4@TiO_2 NCs show the absorption in the visible region raging from 400 to 700 nm which is originated from Fe_3O_4.

5.5.2 Hyperthermia Ability and Cell Viability

We compared the heat increment and cytotoxicity using bare Fe_3O_4, bare TiO_2, and Fe_3O_4@TiO_2 NCs suspension under combined AC magnetic-field induction and photoirradiation conditions with a dose of 150 μg/mL for exposing time 10 min (Fig. 5-3 a). The heat generated was evaluated by using bare Fe_3O_4, bare TiO_2, and Fe_3O_4@TiO_2 NCs suspension dispersed in MEM. The temperature rising of the three nanomaterials suspensions against the dose quantity is shown in Fig. 5-3a.

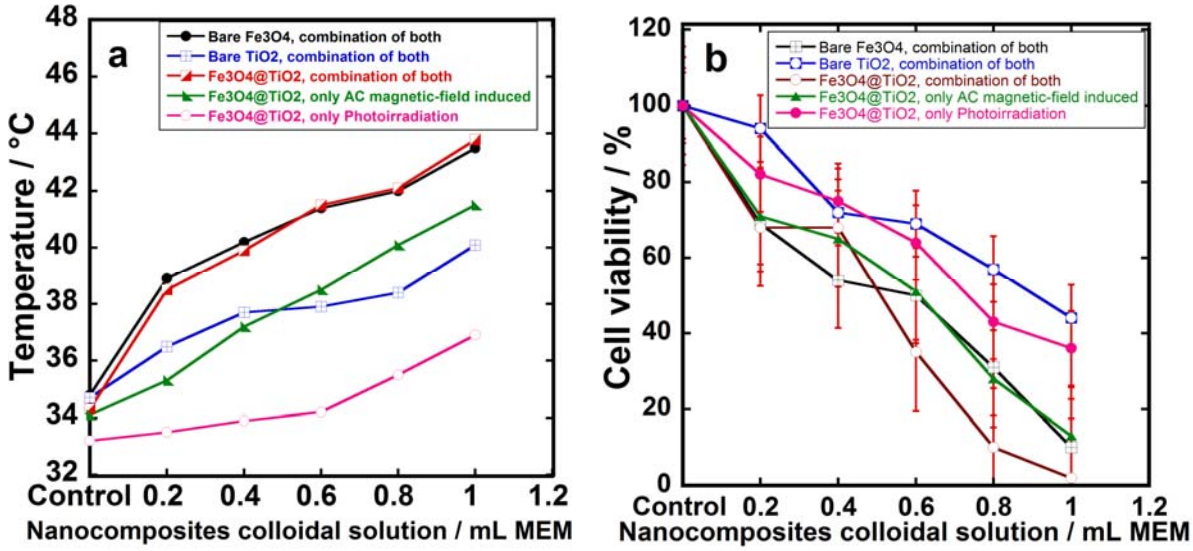

Fig.5-3: Comparative hyperthermia ability (a) and cell viability (b) of bare Fe_3O_4, bare TiO_2, and Fe_3O_4@TiO_2 under combined AC magnetic-field induction and photoirradiation conditions and under only AC magnetic-field induction or only photoirradiation condition using Fe_3O_4@TiO_2 NCs.

The highest temperature achieved was 43.8 °C for Fe_3O_4@TiO_2 in contrast to 43.5 and 40.1 °C for bare Fe_3O_4 and bare TiO_2, respectively, whereas Ito *et al.* [30] achieved 42.0 °C for 30 min exposure time using 100 µg/mL concentration of magnetite nanoparticles.

Furthermore, we investigated the hyperthermia ability of Fe_3O_4@TiO_2 core-shell NCs under only AC magnetic-field induction and only photoirradiation condition using the same dose and exposure time and the heat generated by using Fe_3O_4@TiO_2 NCs suspension dispersed in MEM in both of the conditions are shown in Fig. 5-3a. The temperature achieved was 41.5 and 36.9 °C under only AC magnetic-field induction and only photoirradiation condition, respectively.

To evaluate the cytotoxicity, cell dishes were incubated for 24 h with a concentration of 150 µg/mL of nanomaterials and another dish without any nanoparticles solution (control dish) was also incubated for 24 h. The cancer cell viability under AC magnetic-field induced and

photoirradiated conditions for exposing time 10 min for three samples are shown in Fig. 5-3b. The results revealed that almost 100% (viability 1%) cancer cells were destroyed by Fe_3O_4@TiO_2 NCs whereas 90% (viability 10%) and 56% (viability 44%) cancer cells were killed for bare Fe_3O_4 and bare TiO_2, respectively, using the same dose under the same conditions.

The thermal-photocatalytic cancer cell killing efficiency of Fe_3O_4@TiO_2 core-shell NCs under only AC magnetic-field induction and only photoirradiation condition is shown in Fig. 3b. It is noteworthy that in all doses under combined AC magnetic-field induction and photoirradiation conditions, the cancer cell killing percentage was higher than only AC magnetic-field induction and only photoirradiation condition and finally almost 100% (viability 1%) cancer cells were destroyed by Fe_3O_4@TiO_2 NCs under combined conditions using a dose of 150 μg/mL whereas under only AC magnetic-field induction or only photoirradiation condition, the cancer cell killing percentage was 87% (viability 13%) and 64% (viability 36%), respectively.

Although only 10% cancer cells can survive after treating with bare Fe_3O_4, it is not negligible because according to the nature of the cancer cells even single live cancer cell may be a great threat for the patient when its growth is uncontrolled. Cancers derived from epithelial cells are called carcinoma and it is fundamentally a disease by failure of regulation of tissue growth.Cancer cell growth is different from normal cell growth. Instead of dying, cancer cells continue to grow and form new, abnormal cells. It can also invade (grow into) other tissues, something that normal cells cannot do. Cancer costs billions of dollars and it is the second most common cause of death in the United States, exceeded only by heart disease. Cancer accounts for nearly 1 out of every 4 deaths in the United States and it caused about 13% of all human deaths worldwide (7.9 million), in 2007. With the growth and aging of the population, prevention efforts are important to help reduction of new cancer cases, human suffering, and economic costs

[31]. Considering this facts, it can be logically concluded that Fe_3O_4@TiO_2 NCs preserve the significant role to kill (almost 100%) cancer cells under combined AC magnetic-field induction and photoirradiation conditions.

So, it is interesting to note that either bare Fe_3O_4 or bare TiO_2 and either only AC magnetic-field induction or only photoirradiation condition could not kill the cancer cells up to the mark, but when Fe_3O_4@TiO_2 NCs were used under combined AC magnetic-field induction and photoirradiation conditions, the cell killing potentiality was significantly increased and finally almost 100% HeLa cells were killed.

5.3 Cell Killing Mechanisms

Figure 4 shows microscopic images of HeLa cells under combined AC magnetic-field induced and photoexcited conditions. Figure5-4a (control) shows that the cell morphology is unchanged. Figure 5-4b (with bare TiO_2) shows almost no change, Fig. 5-4c (with bare Fe_3O_4) shows moderate change and Fig. 5-4d (with Fe_3O_4@TiO_2 NCs) shows severe change. Especially, Fig. 5-4d shows that the HeLa cells suffer severe hyperthermal and photocatalytic shock at 10 min exposure time under the same condition.

To the best of our knowledge, the mechanism of cell killing can be ascribed to cumulative effects of hyperthermia and photocatalytic cell-killing. Hyperthermia is a famous tool for cancer therapy nowadays and photocatalytic cell-killing is also well known and recently we reported the mechanism of synergistic photocatalytic and photothermal cancer cell killing of Ag@TiO_2 and AC magnetic-field induced hyperthermia of α-Fe_2O_3 [25, 26]. However, the stability of Fe_3O_4@TiO_2 NCs is an important consideration. In this report, we used Fe_3O_4 as a core and TiO_2 was used as a shell. It was reported that TiO_2 is broadly used as a photocatalyst because it is photochemically stable, nontoxic and economical and its band gap or even doped TiO_2 make it

one of the most promising materials in photochemical generation of hydrogen from water in the presence of solar light [29, 36]. Ji *et al.* reported that the superparamagnetic iron oxide nanocore-Au nanoshells acted as an efficient photothermal mediator [37].

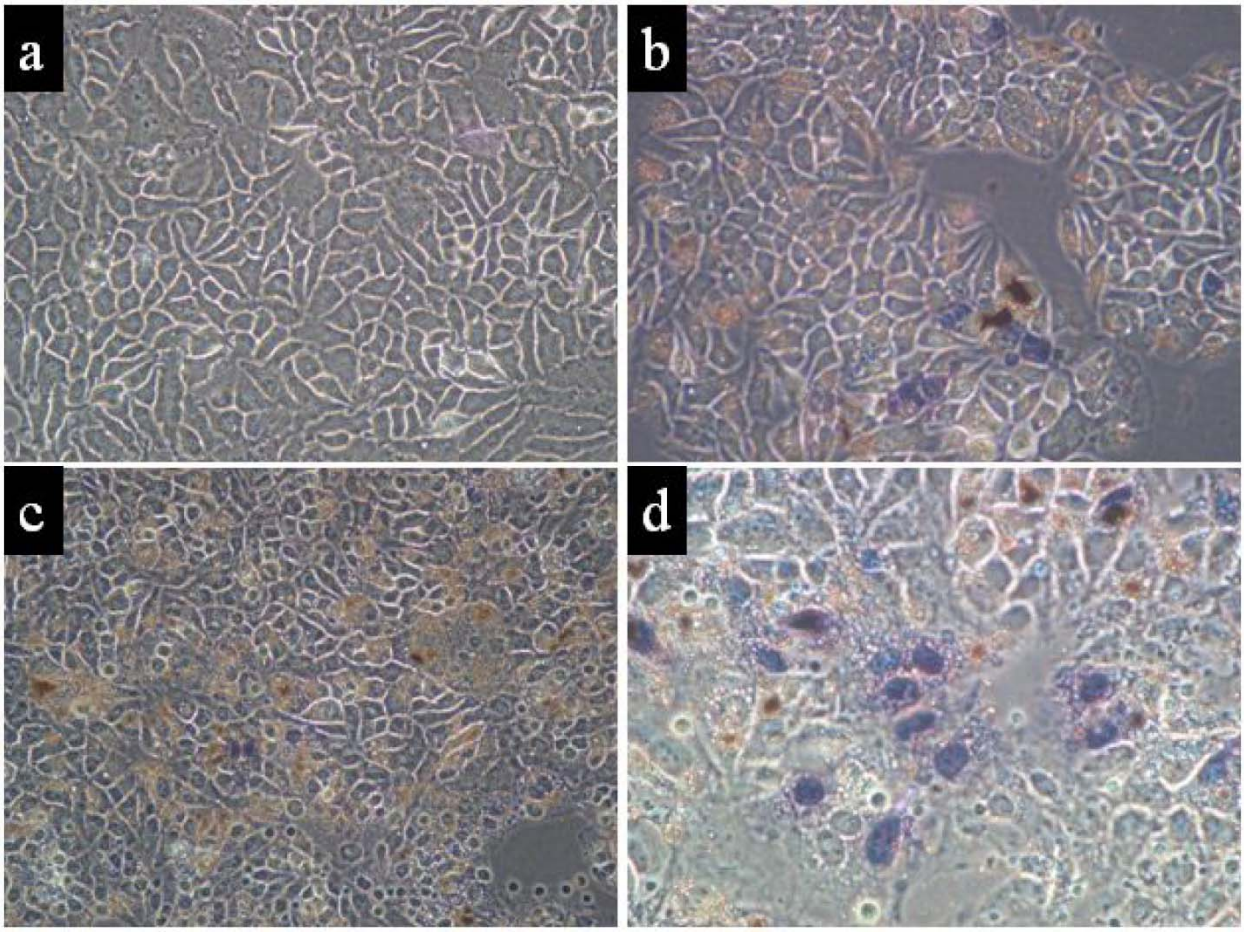

Fig. 5-4: Microscopic images of (a) control, (b) bare TiO_2, (c) bare Fe_3O_4, and (d) Fe_3O_4@TiO_2 with HeLa (cancer) cells using a dose of 150 μg/mL and exposure time of 10 min under combined conditions (Magnification 200).

When TiO_2 is excited by a photon whose energy is greater than the TiO_2 band gap (3.2 eV), an electron from the valence band can be excited to the conduction band, thus creating an electron-hole pair. The electron and hole can then, if they do not recombine, reduce or oxidize

species in the electrolyte solution. For instance, the hole oxidizes a water molecule to yield OH radicals (·OH), and the electron reduces oxygen (O_2) to give superoxide anion (O°) and H_2O_2. These reactive oxygen species can drive various chemical reactions.

It is well known that reactive oxygen species such as OH radicals and H_2O_2 are formed on photoexcited TiO_2 particles in water solution [32, 33]. The formation of OH radicals and H_2O_2 from photoexcited TiO_2 particles is illustrated in Fig. 5-5. OH radicals are formed by the oxidation of water via reaction (1), and H_2O_2 is formed by the reduction of oxygen (O_2) via reaction (2).

$$H_2O + h^+ \rightarrow \cdot OH + H^+ \qquad (1)$$

$$O_2 + 2e^- + 2H^+ \rightarrow H_2O_2 \qquad (2)$$

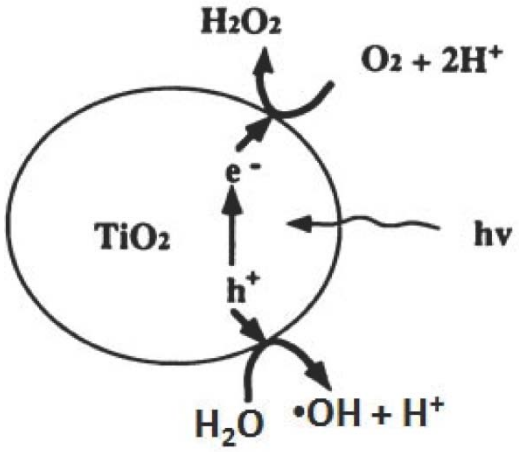

Fig.5-5: Schematic illustration of the photocatalytic formation of H_2O_2 and OH radicals on photoexcited TiO_2 particles. e^- : electron, h^+ : hole.

Furthermore, some of H_2O_2 might be cleaved into OH radicals by UV irradiation or by the Fenton reaction [33]. Some of photoinduced electrons of TiO_2 can be transferred to the TiO_2 surface and reduce the dissolved O_2 easily, because dissolved oxygen is also one of the good accepters of electrons.

$$TiO_2\,(h) + H_2O \rightarrow \bullet OH + H^+ \quad (3)$$

$$O_2\bullet^- + H^+ \rightarrow HO_2\bullet \quad (4)$$

$$2HO_2\bullet \rightarrow O_2 + H_2O_2 \quad (5)$$

$$H_2O_2 + O_2^- \rightarrow \bullet OH + OH^- + O_2 \quad (6)$$

The photo-generated holes on the TiO_2 surface can react with water to produce powerful oxidative radicals •OH and HO_2• as shown in photocatalytic reaction mechanism (Reaction (3) and (4)) [29]. The reactive oxygen species such as hydroxyl radicals and hydrogen peroxide are formed on the photoexcited Fe_3O_4@TiO_2 NCs in MEM solution. These highly oxidizing OH radicals and H_2O_2 can be expected to be toxic to cells [34]. Moreover, it was reported that a photogenerated hole reacts with a water molecule to form •OH and H_2O_2 which can be expected to be toxic to cells as shown in reactions (3)–(6) [32, 35].

5.6 Conclusions

We synthesized ca. 20 nm Fe_3O_4 and coated with TiO_2 to prepare Fe_3O_4@TiO_2 nanocomposites. The characterization revealed the successful preparation of Fe_3O_4@TiO_2 nanocomposites with hyperthermia ability. Finally, it can be concluded that the cancer cell killing efficiency of Fe_3O_4@TiO_2 nanocomposites was always higher than bare Fe_3O_4 and bare

TiO_2 and the cell killing capability was significantly enhanced under combined AC magnetic-field induced and photoexcited conditions.

References

[1] U. Jeong, X. Teng, Y. Wang, H. Yang, Y. Xia, Adv Mater. 19 (2007) 33.

[2] Lu A-H, E.L. Slabas, F. Schüth, Angew Chem Int Ed. 46 (2007) 1222.

[3] J. S Kim, T. J Yoon, B. G Kim, S. J Park, H. W Kim, K.H Lee, S.B Park, J.K Lee, M. H Cho, Toxicol Sci. 89 (2006) 338.

[4] S. Al-Sayari, A.F Carley, S.H Taylor, G.J Hutchings, Top Catal. 44 (2007) 123.

[5] Z. Zhong, J. Ho, J. Teo, S. Shen, A. Gedanken, Chem Mater. 19 (2007) 4776.

[6] M.A Fox, M. T Dulay, Chem. Rev. 93 **(**1993) 341.

[7] A. Heller, Acc. Chem. Res. 28 (1995) 503.

[8] A. Nakajima, H. Obata, Y. Kameshima, K. Okada, Catal. Commun. 6 (2005) 716.

[9] L. Zhang, Y. Zhu, Y. He, W. Li, H. Sun, Appl. Catal., B 40 (2003) 287.

[10] H. Shibata, T. Ogura, T. Mukai, T. Ohkubo, H. Sakai, M. Abe, J. Am. Chem. Soc. 127 (2005) 16396.

[11] H. Luo, C. Wang, Y. Yan, Chem. Mater., 15 (2003) 3841.

[12] Z.Y Yuan, T. Z Ren, B. L Su, Adv. Mater., 15 (2003)1462.

[13] S. H Zhan, D. R Chen, X. L Jiao, C.H. Tao, J. Phys. Chem. B, 110 (2006) 11199.

[14] D. Beydoun, R. Amal, G. K. C Low, S. Mcevoy, J. Phys. Chem. B 104 (2000) 4387.

[15] B. P Zhang, J. L Zhang, F. Chen, Res. Chem. Int. 34 (2008) 375.

[16] S. W Lee, J. Drwiega, C.Y Wu, D. Mazyck, W.M Sigmund, Chem. Mater. 16 (2004)1160.

[17] T. A Gad-Allah, S. Kato, S. Satokawa, T. Kojima, Solid State Sci. 9 (2007) 737.

[18] A. Kleiman, A. Marquez, D.G. Lamas, Surf. Coat. Technol. 201 (2007) 6358.

[19] M.F. Dadjour, C. Ogino, S. Matsumura, S. Nakamura, N. Shimizu, Water Res. 40 (2006) 1137.

[20] M.A. Behnajady, N. Modirshahla, N. Daneshvar, M. Rabbani, Chem. Eng. J. 127 (2007) 167.

[21] H. Choi, M.G. Antoniou, A.A. de la Cruz, E. Strathatos, D.D. Dionysiou, Desalination 202 (2007) 200.

[22] J.Y. Li, W.H. Ma, C.C. Chen, J.C. Zhao, H.Y. Zhu, X.P. Gao, J. Mol. Catal. A-Chem. 261 (2007) 131.

[23] Y. Tachibana, H.Y. Akiyama, S. Kuwabata, Sol. Energ. Mat. Sol. C. 91 (2007) 201.

[24] C. Sichel, M. de Cara, J. Tello, J. Blanco, P. Fernandez-Ibanez, Appl. Catal. B Environ. 74 (2007) 152.

[25] M. Abdulla-Al-Mamun, Y. Kusumoto, T. Zannat, M. S. Islam, Appl. Catal. A. 398 (2011) 134.

[26] M. S. Islam, Y. Kusumoto, M. Abdulla-Al-Mamun, and Y. Horie, Chem. Lett. 40 (2011) 773.

[27] A.W.T. Konings, in: M.H. Seegenschmiedt, P. Fessenden, C.C. Vernon (Eds.), Thermoradiotherapy and Thermochemotherapy, vol. 1: Biology, Physiology, Physics, Springer, Berlin, 1995.

[28] Y. Li, X. Xu, D. Qi, C. Deng, P. Yang, X. Zhang, J. Proteome Res. *7* (2008) 2526.

[29] M. Abdulla-Al-Mamun, Y. Kusumoto, B. Ahmmad, M. S. Islam, Top. Catal. 53 (2010) 571.

[30] A. Ito, M. Shinkai, H. Honda, K, Yoshikawa, S. Saga, T. Wakabayashi, J. Yoshida, T. Kobayashi, Cancer Immunol. Immunother. 52 (2003) 80.

[31] American Cancer Society, Cancer Facts & Figures, Atlanta, GA. 2009.

[32] C.D. Jaeger, A.J. Bard, J. Phys. Chem. 93 (1979) 3146–3152.

[33] M. Inulina, Y. Satoh, and T. Osa, Nature (Lond.) 293 (1981) 206.

[34] R. Cai, Y. Kubota, T. Shuin, H. Sakai, K. Hashimoto, A. Fujishima, Cancer Res. 52 (1992) 2346.

[35] R. Cai, Y. Kubota, T. Shuin, H. Sakai, K. Hashimoto, A. Fujishima, Chem. Lett. 3 (1992) 427.

[36] J. Nowotny, T. Bak, M. K Nowotny, L. R Sheppard, Int. J. Hydrogen Energy 32 (2007) 2609.

[37] X. Ji, R. Shao, A. M Elliott *et al*. J. Phys. Chem. C 111(2007) 6245.

Supplemental information

Synthesis of Fe_3O_4@C magnetic nanocomposite

Fe_3O_4 nanoparticles with diameter of ca. 20 nm were first synthesized *via* the co-precipitation method. In the next step, 0.05 g nanoparticles were ultrasonicated for 10 min in 0.1 M HNO_3, followed by washing with deionized water. Then, the treated Fe_3O_4 nanoparticles were redispersed in 0.5 M aqueous glucose solution. After vigorous stirring for 10 min, the suspension was transferred to an autoclave and kept at 190 °C for 4 h. After the reaction, the autoclave was cooled naturally in air and the suspension was isolated with the help of a magnet and washed with deionized water and alcohol three times, respectively. The final sample was obtained after oven-drying at 90 °C for more than 5 h.

Synthesis of Fe_3O_4@TiO_2 core-shell nanocomposite

Tetrabutyltitanate (5 mL) was dissolved in ethanol (35 mL) to form a clear solution. Fe_3O_4@C magnetic nanocomposites (~100 mg) were then dispersed in the freshly prepared solution with the aid of ultrasonication for 5 min. A 1:5 (v/v) mixture of water and ethanol was added drop wise to the suspension of Fe_3O_4@C magnetic nanocomposites with vigorous magnetic stirring over a period of approximately 15 min. Thereafter, the suspension was stirred for further 1 h before separation and washed with ethanol. After five cycles of separation/washing/redispersion with ethanol, the powder obtained was oven-dried and calcined at 500 °C under nitrogen gas.

CHAPTER 6

ENHANCED CANCER CELL (HELA) KILLING EFFICACY OF MIXED ALPHA AND GAMMA IRON OXIDE SUPERPARAMAGNETIC NANOPARTICLES UNDER COMBINED AC (ALTERNATING CURRENT) MAGNETIC-FIELDS AND PHOTOEXCITATION

Abstract

We synthesized mixed α and γ-Fe_2O_3 nanoparticles and investigated their toxic effects against HeLa cells under induced AC (alternating current) magnetic-fields and photoexcited conditions at room temperature. The findings revealed that the cell-killing percentage was increased with increasing dose for all types of treatments. Finally, 99% cancer cells were destructed at 1.2 mL dose when exposed to combined AC magnetic-field and photoexcited conditions (T_3) whereas 89 and 83 % of HeLa cells were killed under only AC magnetic-field induced (T_1) or only photoexcited (T_2) condition at the same dose. This research work has already been published in IIUM Engineering Journal, Vol. 12, No.4, 67-72, **2011**,(Special issue on Biotechnology).

6.1 Introduction

Preferential heating of certain organs or tissues to temperatures between 41 °C and 46 °C for cancer therapy is called "Hyperthermia". Higher temperatures up to 56 °C, which yield widespread necrosis, coagulation or carbonization (depending on temperature) is called "thermo-ablation" [1]. Magnetic iron oxide nanoparticles and their dispersions in various media have long

been of scientific and technological interest. Maghemite (γ-Fe_2O_3) is biocompatible and therefore is one of the most extensively used biomaterials for different applications like cell separation, drug delivery in cancer therapy, magnetic induced hyperthermia, MRI contrast agent, immunomagnetic separation and others [2]. Hematite has been used as photocatalyst for the degradation of chlorophenol and azo dyes [3] whereas maghemite and magnetite/carbon composites have been found to be useful for reducing the amount of undesirable N_2 in fuel oil [4]. Superparamagnetic nanoparticles when exposed to an alternating magnetic field can be used to heat tumor cells to 41- 45 °C, where damage for normal tissues is reversible while the tumor cells are irreversibly damaged [5]. In an alternating magnetic field, induced currents are generated in metallic objects, and as a consequence, heat is generated in the metal. Thus, when a magnetic fluid is exposed to an alternating magnetic field, the particles become powerful heat sources, destroying tumor cells since these cells are more sensitive to temperatures in excess of 41 °C than their normal counterparts [6]. In view of these, in this report we describe a method for the synthesis of superparamagnetic magnetite (Fe_3O_4) nanoparticles with modification of the method as described by Omoike [7]. Then, Fe_3O_4 was transferred into mixed α and γ-Fe_2O_3 superparamagnetic nanoparticles with modification of the method as described by Sun *et al.* [8]. In our study, as-synthesized mixed α and γ-Fe_2O_3 nanoparticles were applied to HeLa cancer cell killing in different ways such as AC (alternating current) magnetic-field induction (T_1), photoexcitation (T_2) and combination of both (T_3) to evaluate their cancer cell-killing potentiality.

6.2 Experimental

6.2.1 Materials and Methods

Typical syntheses of magnetic nanoparticles (MNPs) were carried out by using the reaction between Fe^{2+} and Fe^{3+} in co-precipitation method [8]. In this experiment, chemicals used for

synthesis of MNPs were $FeCl_3$, HCl, 25% NH_3 solution (Wako Pure chemical industries Ltd., Japan) and $FeCl_2$ (Strem Chemicals, Newburyport). For HeLa cell culture, phosphate buffer saline (PBS), new born calf serum (NBS) (Invitrogen Corporation, Gibco), enzyme trypsine-EDTA (Gibco) solution, 0.5% trypan blue stain solution (Nacalai Tesque, Inc., Kyoto, Japan) and minimum essential medium (MEM) solution (Sigma) were purchased and used as received.

6.2.2 Synthesis and formation of MNPs by Co-precipitation Method

In a typical co-precipitation method, $FeCl_3$ (2.6 g) and $FeCl_2$ (1.3 g) were dissolved in nitrogen gas (N_2) purged 2.0 M hydrochloric acid solution and magnetically stirred under a continuous flow of N_2. The mixture was heated at 70 °C for 30 min and again heated for another 5 min under a blanket of N_2. Ammonia was added drop by drop to precipitate the MNPs and the black product formed was treated hydrothermally at 70 °C for 30 min. The resulting nanoparticles were subsequently separated from the reaction media under a magnetic field and washed three times with Millipore water before drying. Finally the MNPs were oven dried at 70 °C for 3 h to get Fe_3O_4. It is well known that Fe_3O_4 can be oxidized to γ-Fe_2O_3, which can be further transformed into α-Fe_2O_3 at higher temperature [7]. In this report, we simply transferred the Fe_3O_4 (Fig. 6-1a) to mixed α- and γ-Fe_2O_3 superparamagnetic nanoparticles by annealing it at 400 °C for 6 h in the presence of oxygen.

6.3 Structure and Magnetic Characterization

The as-synthesized MNPs were characterized using XRD, FE-SEM and TEM. AC magnetic field induced heating capability of MNPs were performed to observe the hyperthermia potentiality of the mixed α and γ-Fe_2O_3 by dispersing the nanoparticles in distilled water as well

as in a MEM and magnetic hysteresis loops were measured by superconducting quantum interference device (SQUID, Quantum Design MPMS-5).

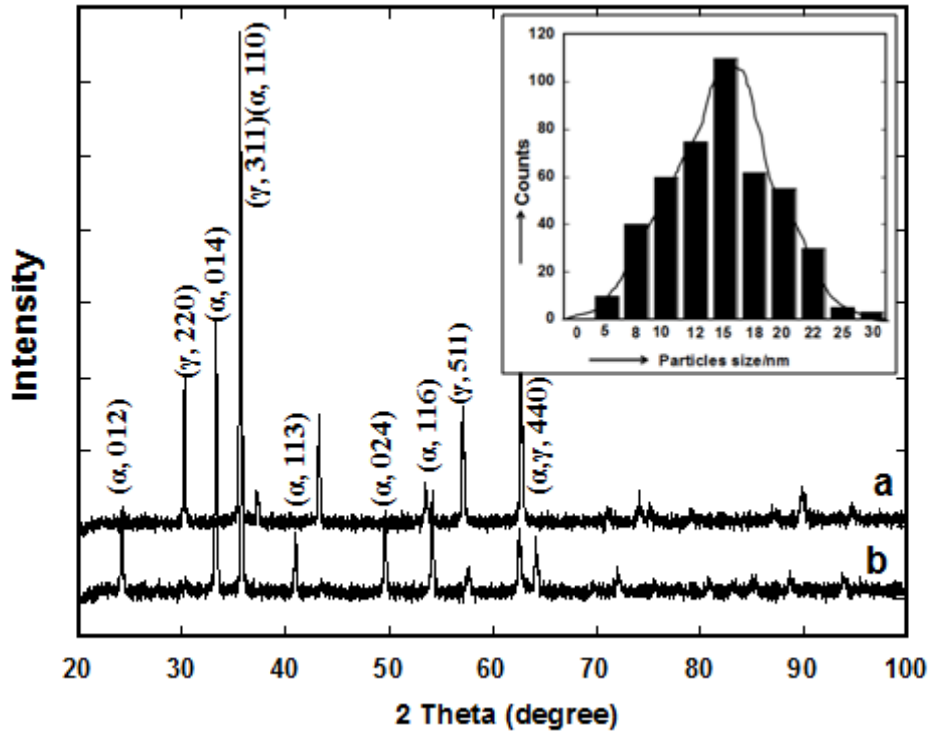

Fig. 6-1: XRD patterns of Fe_3O_4 (a) and mixed α and γ-Fe_2O_3 (b) and particle size distribution of mixed α and γ-Fe_2O_3 obtained from TEM data with approximation by a normal distribution (inset).

6.4 In-vitro Cytoxicity and Anti-cancer Assay

HeLa cells provided by the RIKEN BRC through the National Bio-Resource Project of the MEXT, Japan were cultured in MEM solution with 10% NBS in a humidified incubator with an atmosphere of 5% CO_2 in air at 37 °C for 3 days. The *in vitro* cytotoxicity and anti-cancer effect of the mixed iron oxide nanoparticles against the HeLa cell line was evaluated by a trypan blue exclusion method [9]. In the experiment, the alternative current (AC) magnetic-field was created by using a magnetic oscillator with desired frequency and strength of 560 kHz and 5.0 kA/m,

respectively, and a Xenon lamp (CERMAX 300-W LX300F, USA, ILC) with heat cut-off and band-pass filters (350–600 nm) with an average intensity of 30 mW cm^{-2} was used for the light irradiation on HeLa cells. The light power was measured by a spectroradiometer (Model LS-100, EKO Instrument Co. Ltd.). A table rotator was used for the Petri dish to ensure the homogeneous light irradiation on the cells and temperature increment for the every dish was measured by a digital thermometer (Sato Keiryoki, Model SK-250WP II-R). To investigate the cytotoxicity of synthesized nanomaterials, one dish was used as control without any nanomaterials and the other five dishes were treated with different doses, like 0.2, 0.4, 0.8, 1.0 and 1.2 mL of nanoparticles colloidal solution per 5 mL of MEM solution where the actual colloidal solution concentration was 10 mg/mL. A haemocytometer was used to estimate the total number of viable cells.

6.5 Results and Discussion

Superparamagnetic Fe_3O_4 nanoparticles prepared by the co-precipitation method had high crystallization and good magnetic properties. SEM and TEM images (Fig.6-2a, 6-2b) showed that the mean particle size was ca. 15 nm. The as-synthesized Fe_3O_4 nanoparticles were transferred to mixed α- and γ-Fe_2O_3 superparamagnetic nanoparticles by annealing it at 400 °C for 6h in the presence of oxygen (Fig. 6-1) with the high crystallinity and mean particle size of ca. 15 nm (in set in Fig. 6-1, Fig. 6-2c, 6-2d).

Fig. 6-1 shows X-ray diffraction (XRD) plots of the Fe_3O_4 (a), mixed iron (III) oxide (α- and γ-Fe_2O_3) (b) nanoparticles of optimum properties. Heat dissipation of magnetic particles was evaluated by using an AC magnetic field generator. The heats generated from three distinct treatments (T_1, T_2 and T_3) were evaluated by exposing various doses of mixed iron oxide MNPs suspension dispersed in a MEM to an AC magnetic field.

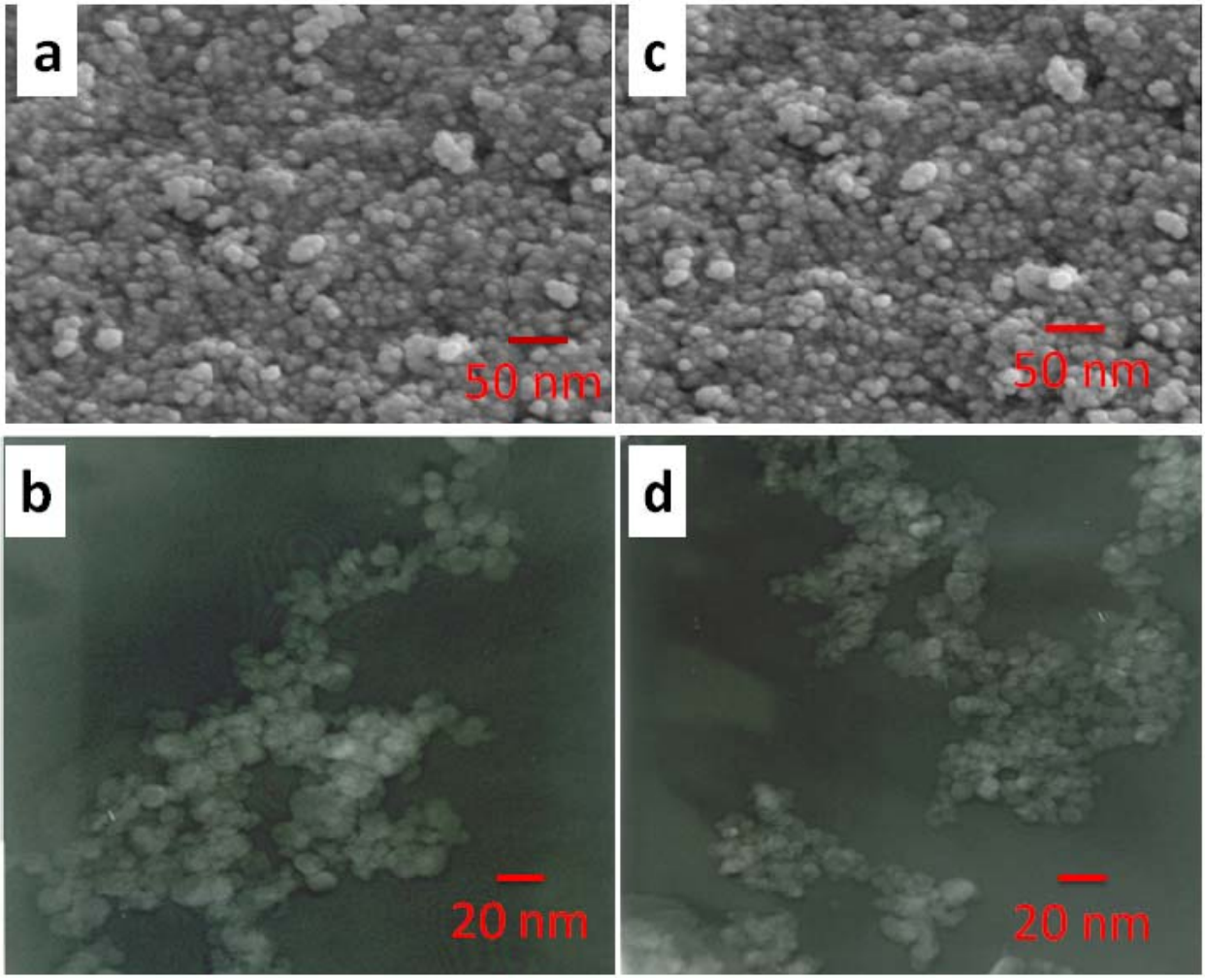

Fig.6-2: SEM images of Fe_3O_4 (a) and mixed α and γ-Fe_2O_3 (c) and TEM images of Fe_3O_4 (b) and mixed α and γ-Fe_2O_3 (d), respectively.

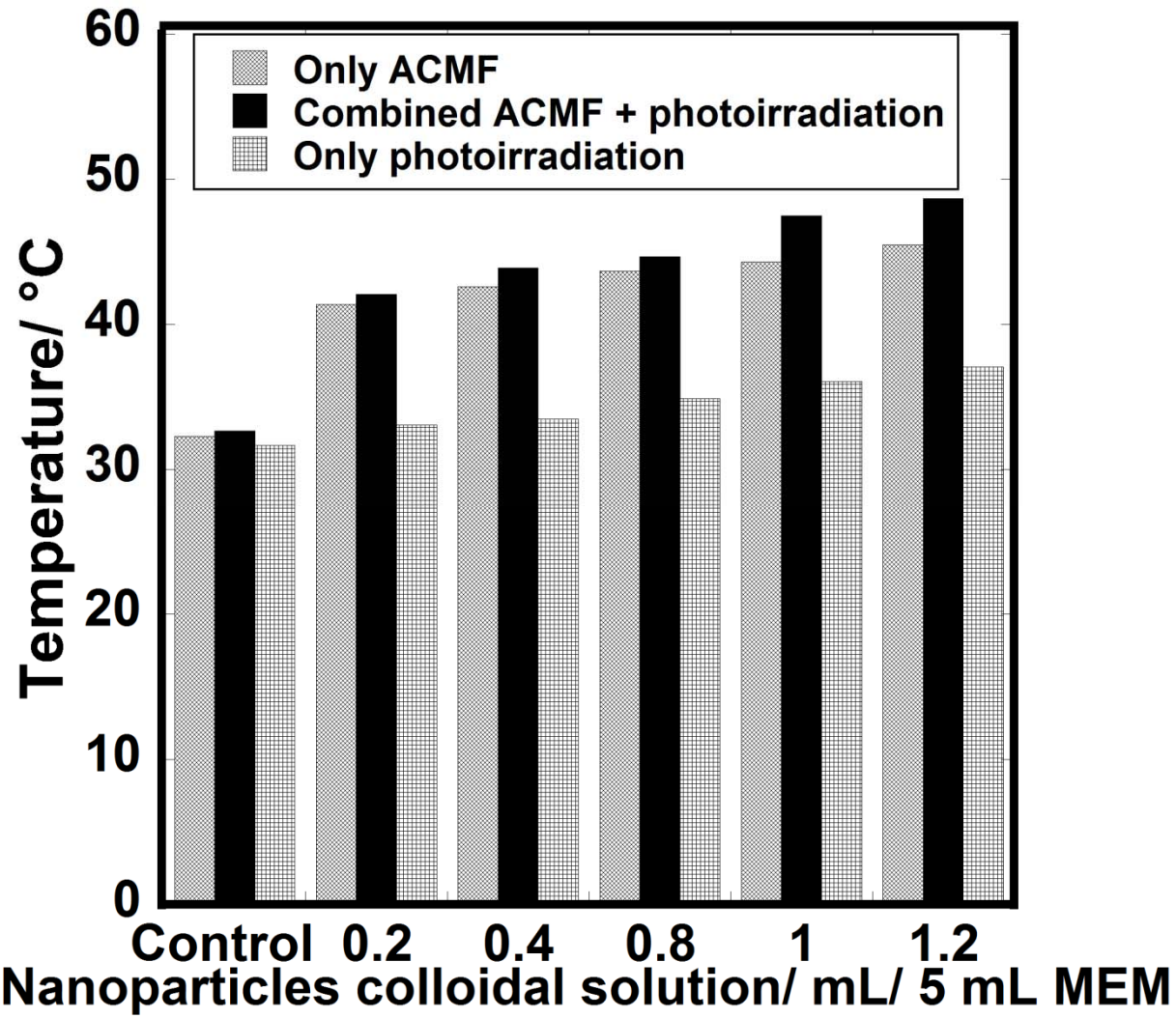

Fig. 6-3: Heat dissipation capability of mixed iron oxide nanoparticles under different conditions.

The temperature increment of magnetite nanoparticles suspensions against different doses is shown in Fig. 6-3. The results revealed that highest temperature increment was obtained 48.7 °C under combined AC magnetic-field induced and photoexcited (T_3) conditions at dose of 1.2 mL whereas for only AC magnetic field induced (T_1) or only photoexcited (T_2) condition the temperature increment was 45.5 °C and 37.1 °C, respectively. Similar results were reported by Atsumi *et al*. [10] that maximum heat dissipation was observed for the MNPs suspension with an average particle diameter of 14 nm, synthesized by the co-precipitation method. The toxic effect

of mixed iron oxide nanoparticles was obtained by counting the percentage of viable cells after all the treatments (Fig.6-4). The cancer cell viability was 59, 62 and 41 % for T_1, T_2 and T_3, respectively, at a dose of 0.2 mL. Similarly the findings (Fig.6-4) revealed the cell killing percentage was increased with increasing dose for all types of treatments.

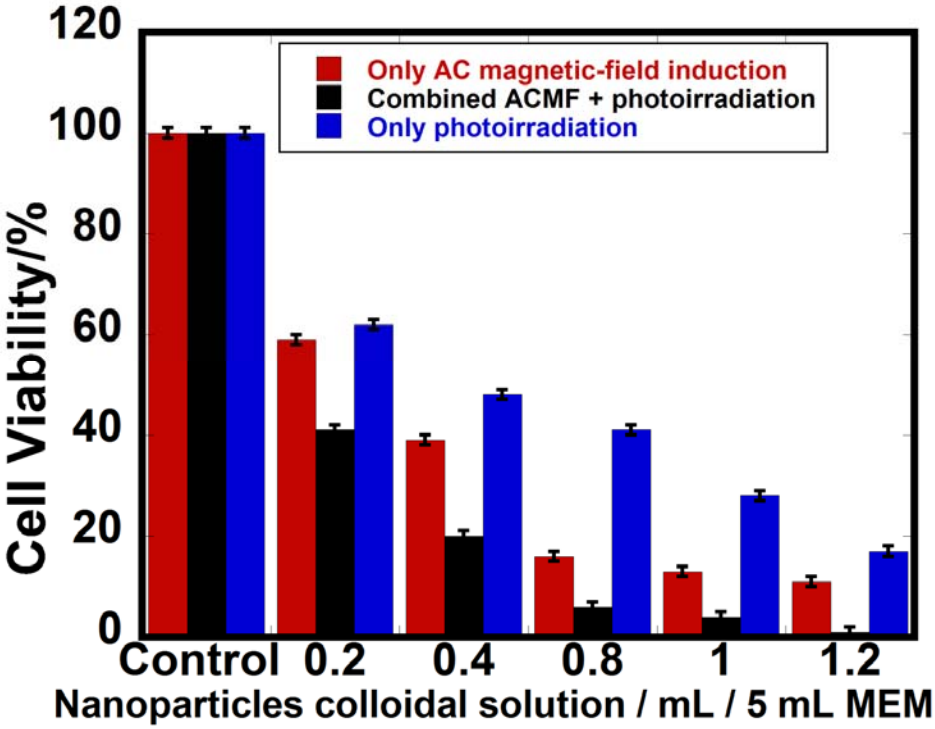

Fig.6-4: Cancer cell killing efficacy of mixed iron oxide nanoparticles under three distinct conditions. Error bars are the standard errors.

Finally, 99% cancer cells were destructed at a dose of 1.2 mL when exposed to combined AC magnetic-field induced and photoexcited conditions (T_3) whereas 89 and 83 % of HeLa cells were killed in only AC magnetic-field induced (T_1) or only photoexcited (T_2) condition at the same dose (Fig.4). However, instrumentation modeling of AC-magnetic field and photoexcitation, for the first time used by us indicates that ca.15 nm (Fig.1, inset) mixed iron oxide MNPs has maximum heating rates as well as cancer (HeLa) cell killing efficacy within the biologically safe frequency range. To the best of our understanding, the mechanism or reason for

99% HeLa cell killing under T_3 condition can be ascribed to the combined or synergistic effect of AC magnetic-field induced hyperthermia and photocatalytic cytotoxicity.

6.6 Conclusions

We described the synthesis of superparamagnetic magnetite nanoparticles and the phase transfer to the mixed α and γ-Fe_2O_3 phase which due to their uniformity and monodispersity appear ideal for AC-magnetic field induced hyperthermia applications. To the best of our knowledge, for the first time we studied the cytotoxicity of mixed α and γ-Fe_2O_3 nanoparticles under the AC magnetic-field induced and photoirradiated conditions with almost 100% cancer cell killing efficacy.

References

[1] A. Jordan, R. Scholz, P. Wust, H. Fähling, R. Felix, *J. Magn. Magn. Mater.* **1999**, *201*, 413.

[2] M. Chirita, I. Grozescu, *Chem. Bull. "POLITEHNICA" Univ. (Timisoara)*, **2009,** *54(68)*, 1.

[3] J. Bandara, U. Klehm, J. Kiwi, *Appl. Catal. B*, **2007**, *76*, 73.

[4] M. Brebu, M.A. Uddin, A. Muto, Y. Sakata, C. Vasile, *Energy & Fuels*, **2001,** *15*, 559.

[5] T. Neuberger, B. Schopf, H. Hofmann, M. Hofmann, B. von Rechenberg, *J. Magn. Magn. Mater.* **2005**, *293*(1), 483.

[6] An-Hui Lu, E. L. Salabas, S. Ferdi, *Angew. Chem. Int. Ed.* **2007***, 46*, 1222.

[7] A. Omoike, *ACS Symposium Series 996*, **2008**, Chapter 8, pp 90-107.

[8] S. Sun, H. Zeng, D. B. Robinson, S. Raoux, P.M. Rice, S. X. Wang, G. Li, *J. Am. Chem. Soc.* **2004***, 126(1)*, 273.

[9] M. Abdulla-Al-Mamun, Y. Kusumoto, A. Mihata, M. S. Islam, B. Ahmmad, *Photochem. Photobiol. Sci.* **2009***, 8*, 1125.

[10] T. Atsumi, B. Jeyadevan, Y. Sato, K. Tohji, *J. Magn. Magn. Mater.* **2007**, *310*, 2841

CHAPTER 7

ENHANCEMENT OF CUMULATIVE PHOTOIRRADIATED AND AC MAGNETIC-FIELD INDUCED CANCER (HeLa) CELL KILLING EFFICACY OF MIXED α AND γ-Fe_2O_3 MAGNETIC NANOPARTICLES

Abstract

In this current study we synthesized mixed α and γ-Fe_2O_3 nanoparticles and their synergistic toxic effect against HeLa cells was investigated under AC (alternating current) magnetic-fields induction and photoirradiation conditions at room temperature. The experiment was designed to find out the cancer cell killing efficacy of as-synthesized bare γ-Fe_2O_3, bare α-Fe_2O_3 and mixed α and γ-Fe_2O_3 nanoparticles under combined AC magnetic-fields induction and photoirradiation conditions. The toxic effect of nanoparticles was obtained by counting the percentage of viable cells after all the treatments using various concentrations. The results revealed that the highest toxic effect was obtained using mixed α and γ-Fe_2O_3 nanoparticles under combined AC magnetic-field induction and photoirradiation conditions at a dose of 60 μg/mL MEM (minimum essential medium), i.e., approximately 98% cancer cells were killed, whereas under only AC magnetic-field induction or only photoirradiation condition, only 89% and 66% cancer cells were destroyed using the same dose of same nanomaterials, respectively. We also noticed that 55% and 79% cancer cells were destroyed using bare α-Fe_2O_3 and bare γ-Fe_2O_3 nanoparticles, respectively, under combined AC magnetic-field induction and photoirradiation conditions using the same dose. To the best of our understanding, the mechanism or reason for almost 100% HeLa cell killing under the combined condition can be ascribed to the combined or additive effect of

AC magnetic-field induced hyperthermia and photocatalytic cytotoxicity. This report has already been accepted in New Journal of Chemistry, 2012(in press).

7.1 Introduction

Magnetic iron oxide nanoparticles and their dispersion in various media have long been of scientific and technological interest. Iron oxides exist in nature in many forms such as magnetite (Fe_3O_4), maghemite (γ-Fe_2O_3), and hematite (α-Fe_2O_3) being probably most common [1]. Magnetic nanoparticles are interesting candidates for a variety of biomedical applications and hyperthermia or the controlled heating of tissue to promote cell necrosis. The magnetic nanoparticles are a prominent example which has been shown to be powerful for the cancer treatment [2, 3]. Heating of certain organs or tissues to temperatures between 41 °C and 46 °C preferentially for cancer therapy is called 'Hyperthermia'. Higher temperatures up to 56 °C, which yield widespread necrosis, coagulation or carbonization (depending on temperature), are called 'thermo–ablation' [4]. Superparamagnetic nanoparticles when exposed to an alternating magnetic field can be used to heat tumor cells to 41- 45 °C, where damage for normal cells is reversible while the tumor cells are irreversibly damaged [5]. Maghemite (γ-Fe_2O_3) is biocompatible and therefore is one of the most extensively used biomaterials for different applications like cell separation, drug delivery in cancer therapy, magnetic induced hyperthermia and others [6].

Hematite (α-Fe_2O_3) is one of the known oldest iron oxides and is widespread in rocks and soils. It is also known as ferric oxide and has been used as photocatalyst for the degradation of chlorophenol and azo dyes [7]. Hematite is also a well-known semiconductor but cannot produce sufficient OH radicals under photoirradiation, and its low saturation magnetization value cannot produce enough heat for a hyperthermia level to kill cancer cells [8]. Superparamagnetic

colloids can be seen as a very promising agent for hyperthermia therapy, but this new field of application requires an improvement of the reproducibility and the size control during the synthesis of particles [6].

In an alternating magnetic field, induced currents generate heat in the metallic objects. This phenomenon is greatly enhanced in metals showing collective magnetic behavior. Thus, when a magnetic fluid is exposed to an alternating magnetic field the particles become powerful heat sources, destroying tumor cells since these cells are more sensitive to temperatures in excess of 41 °C than their normal counterparts [9]. The temperature increase required by hyperthermia can be achieved via different heat sources, such as electromagnetic radiation waves (hyperthermia by radiofrequency or microwave), ultrasound waves, or electrically induced hyperthermia [10-15]. These techniques have shown good results, however, the major problem with present conventional methods is to reach homogenous heat distribution and therapeutic temperatures in the deep region of the tumor to be treated.

The efficiency of the magnetic-fluid hyperthermia technique is extremely dependent on the different properties of the particles, such as size, magnetization, and the value of the Curie temperature [16]. It is well known that α-Fe_2O_3 is a famous semiconductor, easily excited by light irradiation and γ-Fe_2O_3 has most magnetic potentiality to produce heat under magnetic fields. In these sense, in this report we describe a method for the synthesis of superparamagnetic magnetite (Fe_3O_4) nanoparticles by a co-precipitation method and then transferred Fe_3O_4 to mixed α and γ-Fe_2O_3 superparamagnetic nanoparticles. Furthermore, for the first time we assembled and used combined instrumentation modeling of AC (alternating current) magnetic-field and photoexcitation (Fig.7-1).

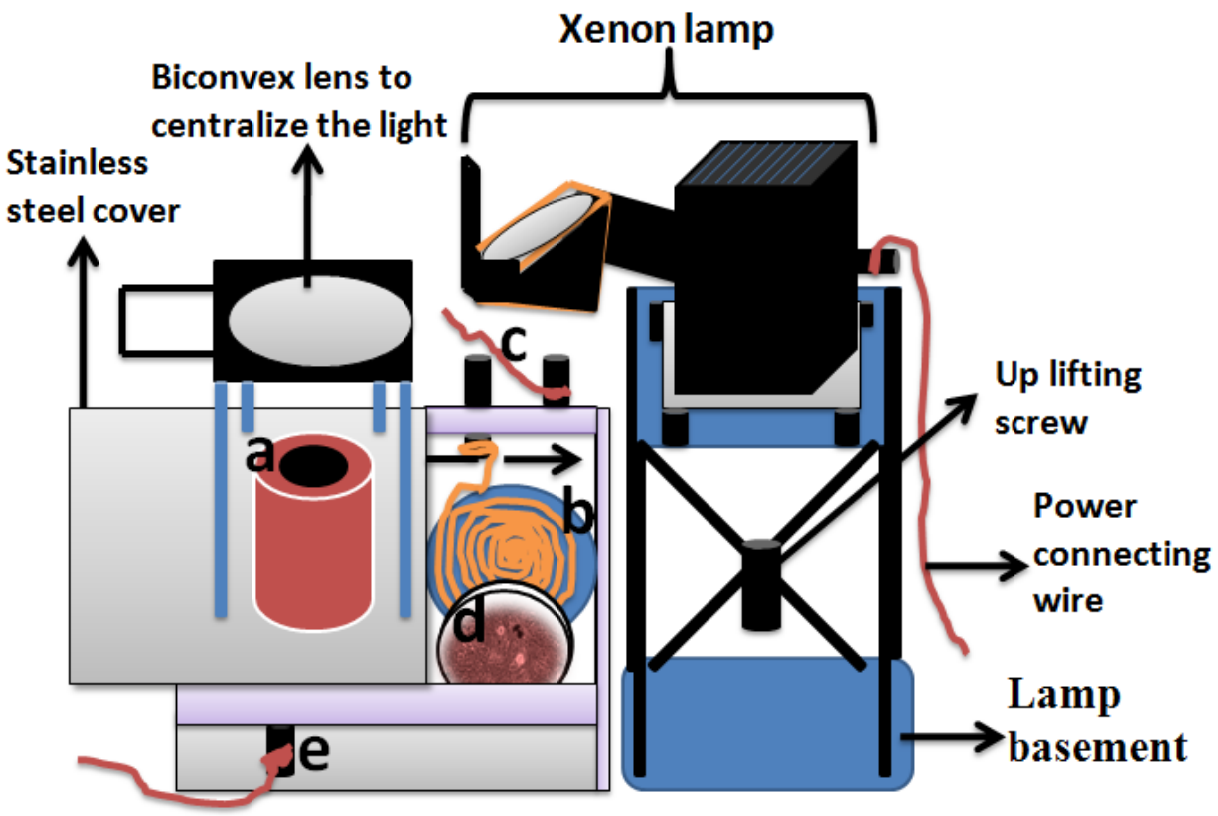

Fig.7-1: Combined assembles of AC magnetic-fields induction and photoirradiation instruments. Here, (a) stands for hole, to pass the light, (b) magnetic-filed creating coil, (c) connecting wire to magnetic oscillator, (d) cultured cells and (e) connection to monitor.

Because of our interest in the enhanced toxic effect of AC magnetic-field induction and photocatalytic reactions of mixed α and γ-Fe_2O_3 nanoparticles produced by visible light irradiation, we studied the cancer cell killing effects with bare α -Fe_2O_3, bare γ-Fe_2O_3 and mixed α and γ-Fe_2O_3 nanoparticles under combined AC magnetic-field induction and visible photoirradiation conditions. We adopted HeLa cells as a model to investigate the thermal-photocatalytic cancer cell killing efficiency of mixed α and γ-Fe_2O_3 nanoparticles under three distinct conditions (only AC magnetic-field induction, only photoirradiation and combined AC magnetic-field induction and photoirradiation conditions) using various dose of 20, 30, 40, 50

and 60 μg/mL for 10-min induction and irradiation. To the best of our knowledge, for the first time we studied the cytotoxicity of mixed α and γ-Fe_2O_3 nanoparticles under the AC magnetic-field induced and photoirradiated conditions.

7.2 Experimental

7.2.1 Materials and Methods

Typical syntheses of magnetic nanoparticles (MNPs) were carried out using the reaction between Fe^{2+} and Fe^{3+} in a co-precipitation method. In this experiment chemicals used for the synthesis of MNPs were $FeCl_3$, HCl, 25% NH_3 solution (Wako Pure chemical industries Ltd., Japan) and $FeCl_2$ (Strem Chemicals, Newburyport). For HeLa cell culture, phosphate buffer saline (PBS), New Born Calf Serum (NBS) (Invitrogen Corporation, Gibco), enzyme Trypsine-EDTA (Gibco) solution, 0.5% trypan blue stain solution (Nacalai Tesque, Inc., Kyoto, Japan), minimum essential medium (MEM) (Sigma) were used as purchased. All chemicals were of analytical grade and used without any further purification.

7.2.2 Synthesis and Formation

In a typical co-precipitation method, $FeCl_3$ (2.6 g) and $FeCl_2$ (1.3 g) were dissolved in nitrogen gas (N_2) purged 2.0 M hydrochloric acid solution and magnetically stirred under a continuous flow of N_2. The mixture was heated at 70 °C for 30 min and then the mixture was heated for another 5 min under a blanket of N_2. Ammonia was added drop by drop to precipitate the magnetic nanoparticles and the black product formed was treated hydrothermally at 70 °C for 30 min. All aqueous solutions and suspensions were made using nanopure water (18 MΩ cm resistivity). The resulting nanoparticles were subsequently separated from the reaction media under a magnetic field and washed three times with nanopure water before drying. Finally the MNPs were oven dried at 70 °C for 3 h to get Fe_3O_4. Chemical reaction of Fe_3O_4 precipitation is

given by the following equations [17].

$$Fe^{2+} + 2OH^- \rightarrow Fe(OH)_2 \quad (1)$$

$$Fe^{3+} + 3OH^- \rightarrow Fe(OH)_3 \quad (2)$$

$$Fe(OH)_2 + 2Fe(OH)_3 \rightarrow Fe_3O_4 + 4H_2O \quad (3)$$

It is well known that Fe_3O_4 can be oxidized to γ-Fe_2O_3, which can be further transformed into α-Fe_2O_3 at higher temperature [18]. Magnetite (Fe_3O_4) is not very stable and is sensitive to oxidation. Magnetite is transformed into maghemite (γ-Fe_2O_3) in the presence of oxygen [19]. However, as-synthesized Fe_3O_4 was oxidized into γ-Fe_2O_3 at 250 °C for 8 h in the presence of oxygen and then γ-Fe_2O_3 was calcinated at 500 °C for 3 h in the presence of Ar gas to get α-Fe_2O_3 [20]. In this report, we simply transferred Fe_3O_4 to mixed α- and γ-Fe_2O_3 superparamagnetic nanoparticles by annealing it at 400 °C for 6 h in the presence of oxygen.

7.2.3 Characterization

The general structure characterization, including size, size distribution and crystal structure of the as-synthesized magnetic nanoparticles was performed for all the samples without any size sorting. To further confirm the crystal structure and overall phase purity, the nanoparticles with different sizes were examined using X-ray powdered diffractometer (XRD). The surface morphology and nanoparticles size were determined using a field emission scanning electron microscope (FE-SEM, model Hitachi S-4100H). Further, the shapes of the nanoparticles were analyzed by a transmission electron microscope (TEM, JEOL JEM-3010 VII TEM) operating at 300 kV. Absorption spectra were recorded on UV-Vis absorption spectrophotometer (Shimadzu Corporation, UV-2450, Japan). The samples were standardized with barium sulphate coated

glass substrate and its spectrum was used as the baseline. The spectra of all samples were measured in a wavelength range between 240 and 800 nm. AC magnetic-field induced heating capability of magnetic nanoparticles was performed to observe the hyperthermia potentiality of the mixed α and γ-Fe_2O_3 by dispersing the nanoparticles in MEM and magnetic hysteresis loops were measured by superconducting quantum interference device (SQUID, Quantum Design MPMS-5).

7.2.4 Colloidal Stability

The photographs of red-brown mixed α and γ-Fe2O3 is represented by Fig. 7-2. The colloidal stability of the as-prepared mixed iron oxides magnetic nanoparticles is very essential to apply for hyperthermia. So, to examine the colloid stability of iron oxide samples, magnetic nanoparticles (10 mg) were dispersed in doubly distilled water (50 mL) by sonication. As shown in Fig. 7-2, the as-prepared nanoparticles were well dispersed into water without any aggregation and precipitation and firmly dragged by the permanent magnetic force (Fig. 7-2(b)).

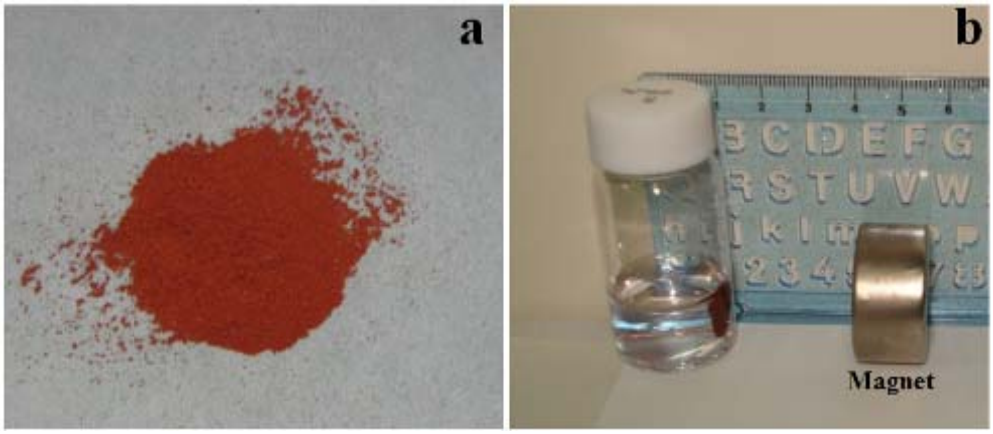

Fig. 7-2. Photographs of (a) red-brown mixed α and γ-Fe2O3 nanoparticles. Water-dispersed mixed α and γ-Fe2O3 dragged by permanent magnetic force is represented by (b).

The magnetic nanoparticles remained in suspension for 1 day, which demonstrates that they can be well-dispersed in aqueous solution. Therefore, with the appropriate surface modifications,

these magnetic nanoparticles may be suitable for clinical diagnosis and in the transport of drugs, proteins, viruses, or bacteria. The nanomaterials synthesized in this study offer several important advantageous features for the technical application of nanoparticles. First, the nanoparticles are magnetic, which means that they can be manipulated by an external magnetic field. Second, our strategy allows the direct production of highly crystalline, monodispersed, and hydrophilic nanoparticles. Finally, the raw materials are inexpensive and the yields are relatively high (85%), which makes this process amenable to large-scale reactions for industrial needs.

7.2.5 HeLa Cell Culture

HeLa cells were provide by the RIKEN BRC through the National Bio-Resource Project of the MEXT, Japan and stored in liquid N_2 to ensure the best quality. The mentioned cancer cell line was cultured in a MEM solution with 10% newborn calf serum (NBS) in a humidified incubator with an atmosphere of 5% CO_2 in air at 37 °C and the cells were plated at a concentration of about 3×10^5 in 60 mm Petri dishes and allowed to grow for 3 days. The culture medium was changed every two days after for approximately 5-6 days until cells reached approximately 80%-90% confluency. Before changing the medium every culturing Petri dish was subjected to wash with PBS buffer at least 2 times. Cells were detached from the culturing Petri dish by trypsinization and resuspended in culture media and the viability was counted.

7.2.6 In vitro Cytotoxicity and Anti-cancer Assay

The *in vitro* cytotoxicity and anti-cancer effect of the mixed iron oxide nanoparticles against the HeLa cell line were evaluated by a trypan blue exclusion method [21]. In the experiment, the AC magnetic field was created by using a magnetic oscillator with desired frequency and strength of 560 kHz and 5.0 kA/m, respectively, and a Xenon lamp (CERMAX 300-W LX300F, USA, ILC) with heat cut-off and band-pass filters (350–600 nm) with an average intensity of 30

mW cm^{-2} was used for the light irradiation on HeLa cells. The light power was measured by a spectroradiometer (Model LS-100, EKO Instrument Co. Ltd.). A table rotator was used for the Petri dish to ensure the homogeneous light irradiation on the cells. To investigate and compare the cytotoxicity efficacy, every Petri dish was subjected to apply under only AC magnetic-field induction, only photoirradiation and combined AC magnetic-field induction and photoirradiation conditions with bare α -Fe_2O_3, bare γ-Fe_2O_3 and mixed α and γ-Fe_2O_3 nanoparticles using a dose of 150 μg/mL for 10 minutes and immediately after the treatment, temperature increment for the every dish was measured by a digital thermometer (Sato Keiryoki, Model SK-250WP II-R).

Cancer cell viability was examined by treating with nanoparticles colloidal solution for 24 h incubation in an incubator. To investigate the cytotoxicity of synthesized nanomaterials, one dish was used as control without any nanomaterials and the other five dishes were treated with different doses, like like 20, 30, 40, 50 and 60 μg of nanoparticles per 1 mL of MEM solution. A haemocytometer was used to estimate the total number of viable cells (by counting cells in the four 1 mm^2 corners of the haemocytometer) and average number of the cells per unit volume (mL) of medium was calculated as the sum of the counted cell number/ 3×10^5.

7.3 Results and Discussion

7.3.1 Shape Analysis by FE-SEM and TEM

Superparamagnetic iron oxide nanoparticles were prepared by the co-precipitation method from ferrous and ferric ion solutions with a molar ratio of 1:2. To obtain the stoichiometric ratio, both ferrous chloride and ferric chloride chemicals were used. Nitrogen gas was used to prevent oxidation of ferrous ions in aqueous solution. The Fe_3O_4 nanoparticles prepared had high crystallization and good magnetic properties. SEM images (Fe_3O_4, γ-Fe_2O_3, α-Fe_2O_3 and mixed α and γ-Fe_2O_3) showed that the mean particle size was 15-20 nm and mostly spherical in shape

(Fig.7 3a ~ d).

Fig. 7-4 (a), (b), (c) and (d) depict the TEM images of Fe_3O_4, γ-Fe_2O_3, α-Fe_2O_3 and mixed α and γ-Fe_2O_3, respectively. Although it is very difficult to differentiate between α-Fe_2O_3 and γ-Fe_2O_3 nanoparticles through TEM analysis but α-Fe_2O_3 is weakly ferromagnetic or antiferromagnetic whereas γ-Fe_2O_3 is ferrimagnetic. In hematite, oxygen ions are in a hexagonal close-packed arrangement with Fe (III) ions occupying octahedral sites. In magnetite and maghemite, the oxygen ions are in a cubic close-packed arrangement [22, 23]. TEM images also clearly showed the nano-structural homogeneities and remarkably spherical-shapes with sizes of around 20 nm. For particle size distribution see the supplemental information.

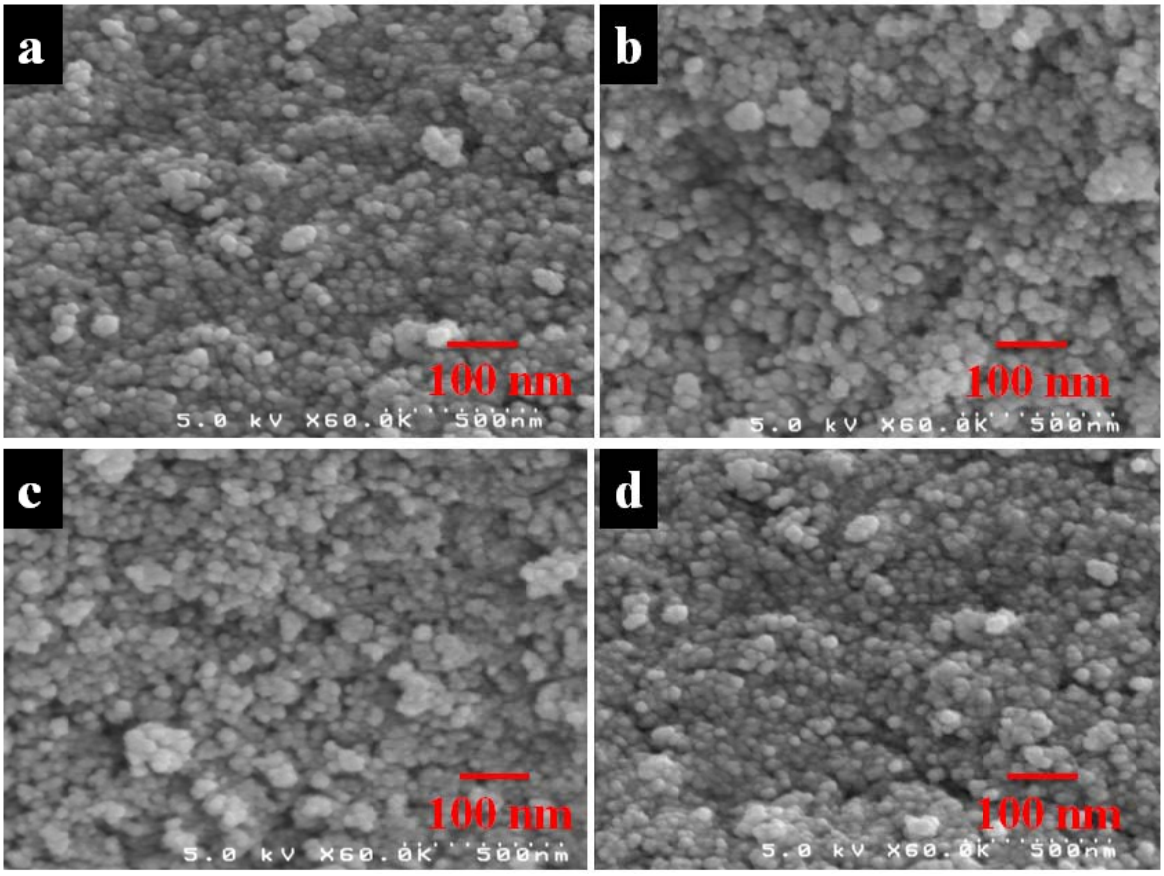

Fig. 7-3. SEM images of (a) Fe_3O_4, (b) γ-Fe_2O_3, (c) α-Fe_2O_3 and (d) mixed α and γ-Fe_2O_3 nanoparticles synthesized by co-precipitation method.

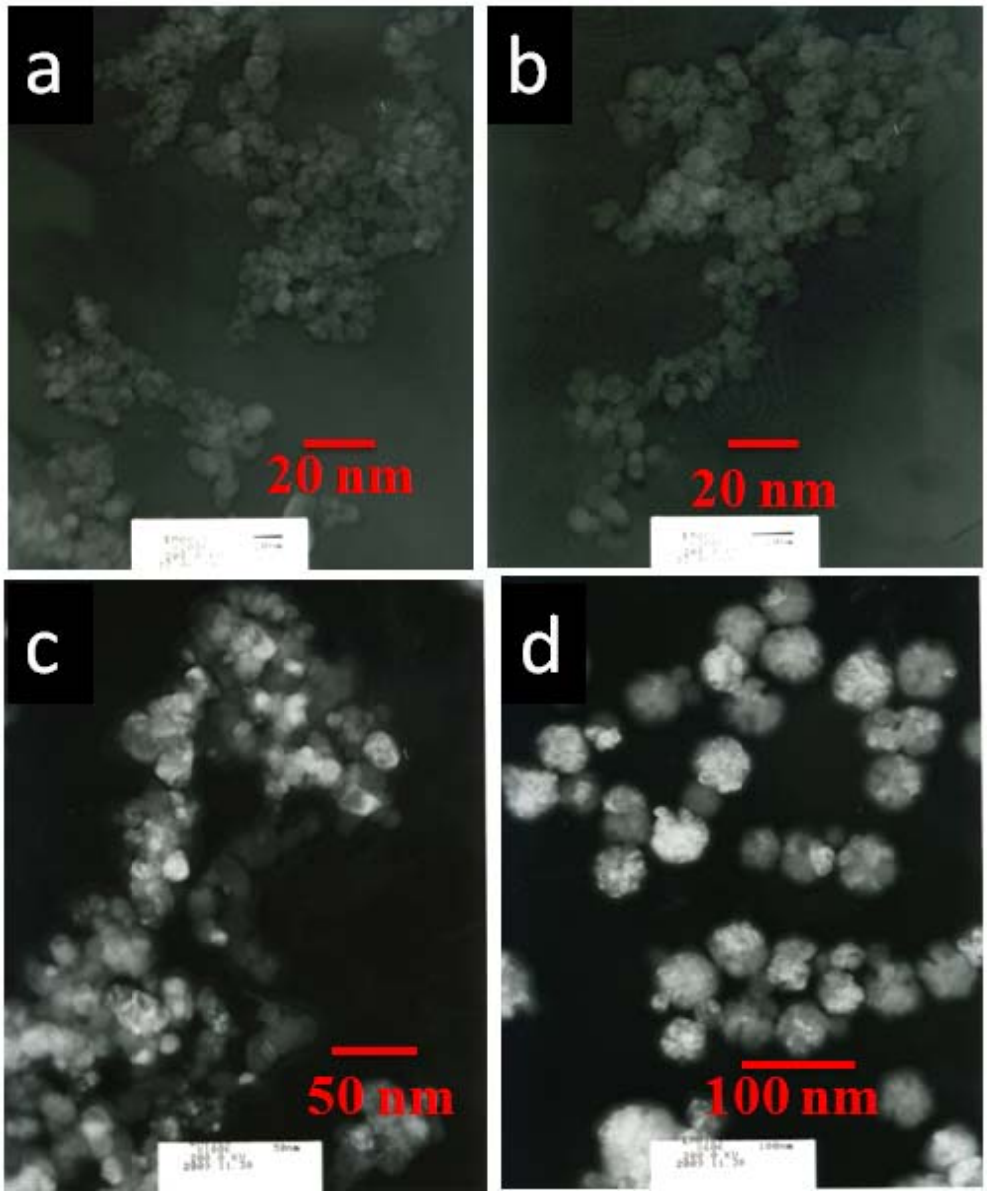

Fig.7-4. TEM images of (a) Fe_3O_4, (b) γ-Fe_2O_3, (c) α-Fe_2O_3 and (d) mixed α and γ-Fe_2O_3 nanoparticles synthesized by co-precipitation method.

7.3.2 XRD Analysis

Fig. 7-5 showed XRD plots of (a) Fe_3O_4, (b) γ-Fe_2O_3, (c) α-Fe_2O_3 and (d) mixed iron (III)

oxide (α- and γ-Fe_2O_3) nanoparticles of optimum properties. The as-synthesized Fe_3O_4 nanoparticles were transferred to mixed α and γ-Fe_2O_3 superparamagnetic nanoparticles by annealing it at 400 °C for 6h in the presence of oxygen (Fig. 7-5d) with the high crystallization.

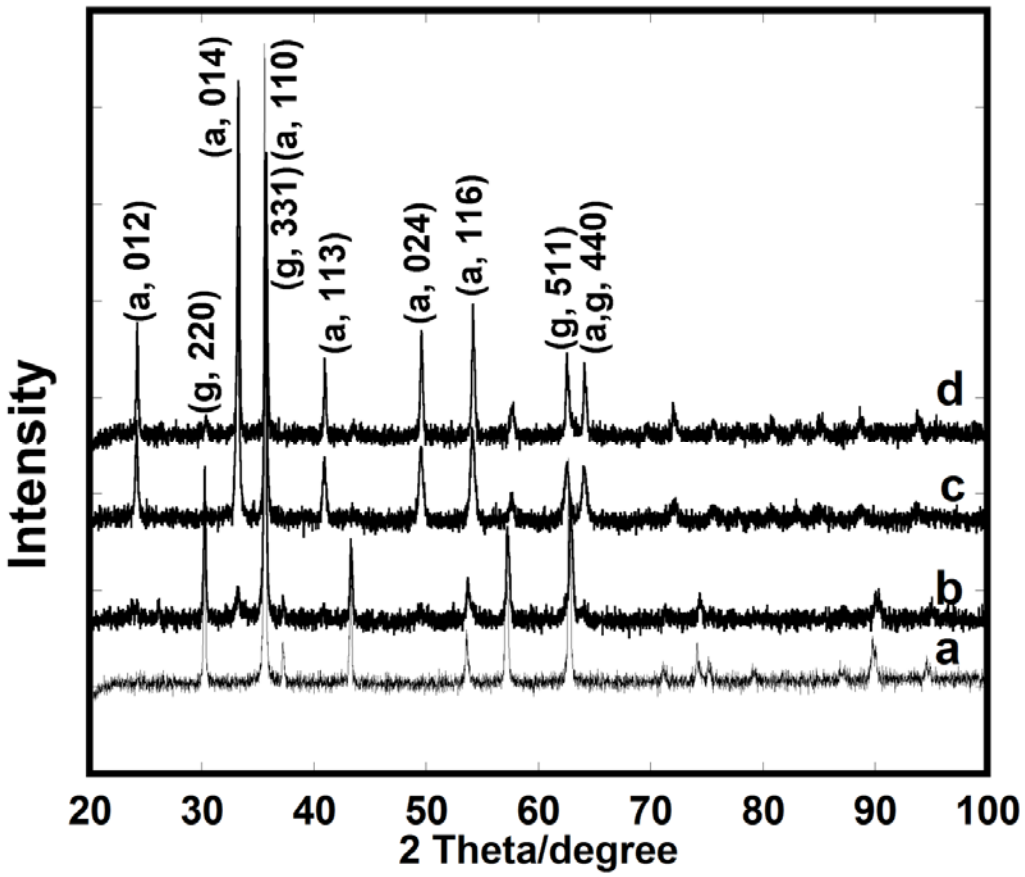

Fig. 7-5. XRD patterns of (a) Fe_3O_4, (b) γ-Fe_2O_3, (c) α-Fe_2O_3 and (d) mixed α and γ-Fe_2O_3 nanoparticles synthesized by co-precipitation method (a = alpha, g = gamma).

The peaks on the plots were identified as α -Fe_2O_3 and γ -Fe_2O_3 (Fig. 4d). Two peaks at 2θ = 35.6 and 62.9 were labeled as α and γ, because these peaks are common in both forms of Fe_2O_3. Other five peaks at 2θ = 24.1, 33.1, 40.9, 49.5, and 54.1with hkl of 012, 014,113,024, and 116,

respectively, were identified as being in common with α- Fe_2O_3 and two peaks at 2θ = 30.2 and 57.3 were for γ-Fe_2O_3 only. These peaks indicate that our as-synthesized mixed iron oxides have mixed structures of α- and γ- iron (III) oxide (JCPDS, PDF, File No. 00-024-0072 and 00-039-1346, respectively). The almost similar study was reported by William *et al.* using the annealing temperature of about 390 °C [24].

Though magnetite and maghemite crystallizes under spinel structure, hematite does not. Thus, it is easy to differentiate between hematite and other magnetic iron oxides. However, it is very hard to identify magnetite and maghemite. But, in order to authenticate the three types of iron oxides nanoparticles prepared through this study, a comparative XRD analysis was done with commercial ones (see the supplemental information).

7.3.3 Magnetic Properties and Hyperthermia Ability of As-prepared Nanomaterials

We observed the magnetic potentiality or the magnetic behavior of synthesized magnetic nanomaterials as magnetic saturation values (*M* vs *H*) at room temperatures. The hysteresis curves obtained at room temperature (Fig.7-6) showed that the saturation of magnetization (M_S) is completed with the values of 79.8 emu/g and 59.9 emu/g for Fe_3O_4 and mixed α- and γ-Fe_2O_3 at room temperature, respectively, whereas for comparison the M_S values observed for γ-Fe_2O_3 and α-Fe_2O_3 were 69.0 and 0.41 emu/g, respectively. The reduction of *M*s from its bulk value can be attributed partly to the presence of non-magnetic (dead) surface layer due to the compositional variations from magnetite to maghemite and hematite, superparamagnetic relaxation and spin canting because of the ultrafine nature of the material [25]. The M_S values for substances treated with oxygen and annealed are different from the mother sample. The difference in magnetization of both oxidized and non-oxidized samples indicates that the oxidation of magnetite into mixed iron oxides

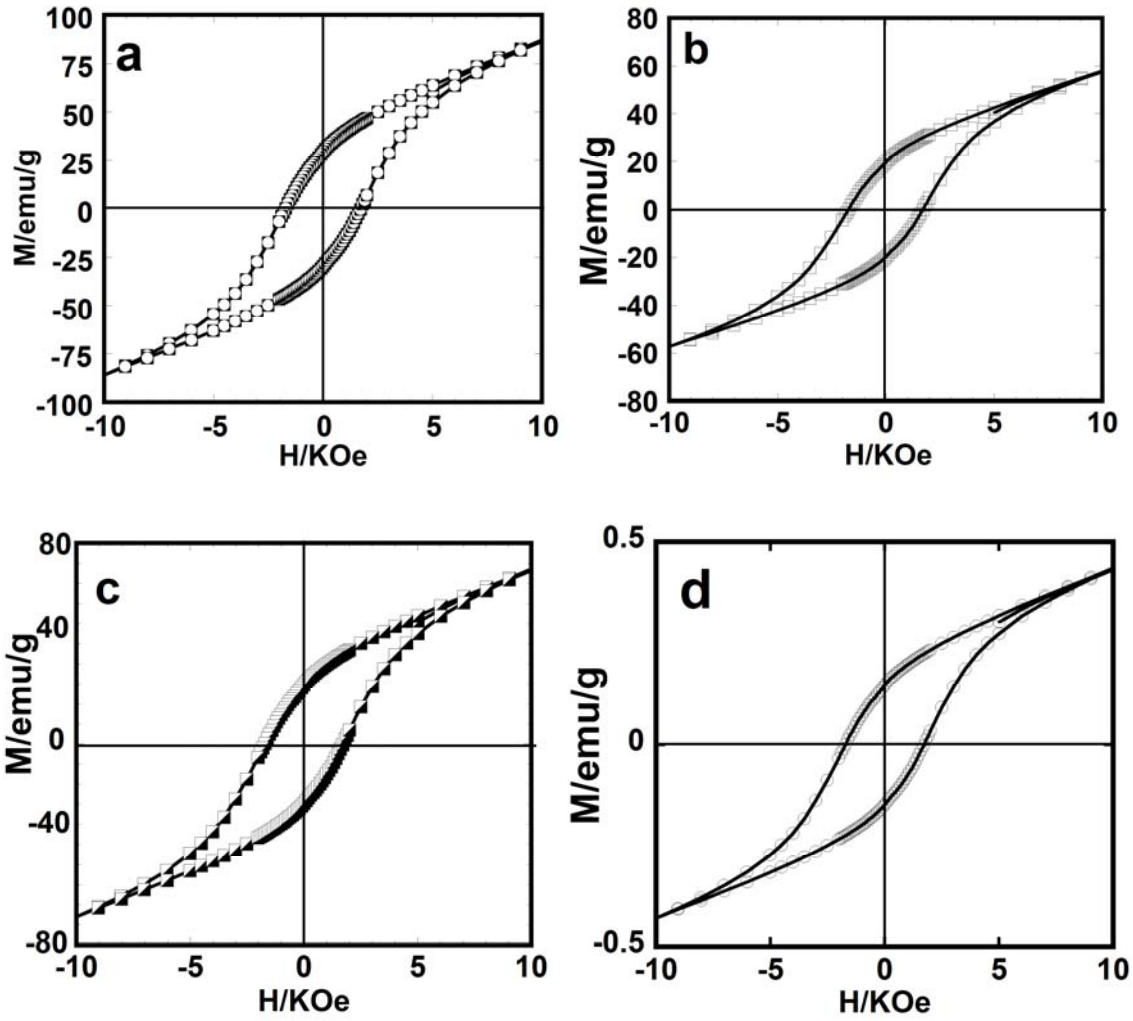

Fig. 7-6. Magnetic hysteresis loops of (a) Fe_3O_4, (b) mixed α and γ-Fe_2O_3, (c) only γ-Fe_2O_3 and (d) only α-Fe_2O_3 nanoparticles at room temperature.

To further explore the low temperature magnetic properties of Fe_3O_4 and mixed α and γ-Fe_2O_3 nanoparticles, M–T curves in zero field cooling (ZFC) and field cooling (FC) processes with a 1kOe applied field were measured, as shown in Fig. 7-7. For both samples, the ZFC magnetization curves showed no peak at any temperatures. Furthermore, the ZFC and FC magnetization curves of two samples exhibit distinct values of 8.9 emu/g and 13.5 emu/g for Fe_3O_4 and mixed α and γ-Fe_2O_3 nanoparticles, respectively, (Fig. 7-7 a and b) at 350 K, indicating the presence of a ferrimagnetisms/ferromagnetism in both samples. Besides, we

measured the ZFC and FC magnetization curves for only γ-Fe_2O_3 and only α-Fe_2O_3 nanoparticles to differentiate the mixed α and γ-Fe_2O_3 nanoparticles among them with the distinct values of 11.1 emu/g and 0.04 emu/g for γ-Fe_2O_3 and α-Fe_2O_3 nanoparticles, respectively (Fig. 7-7 c and d).

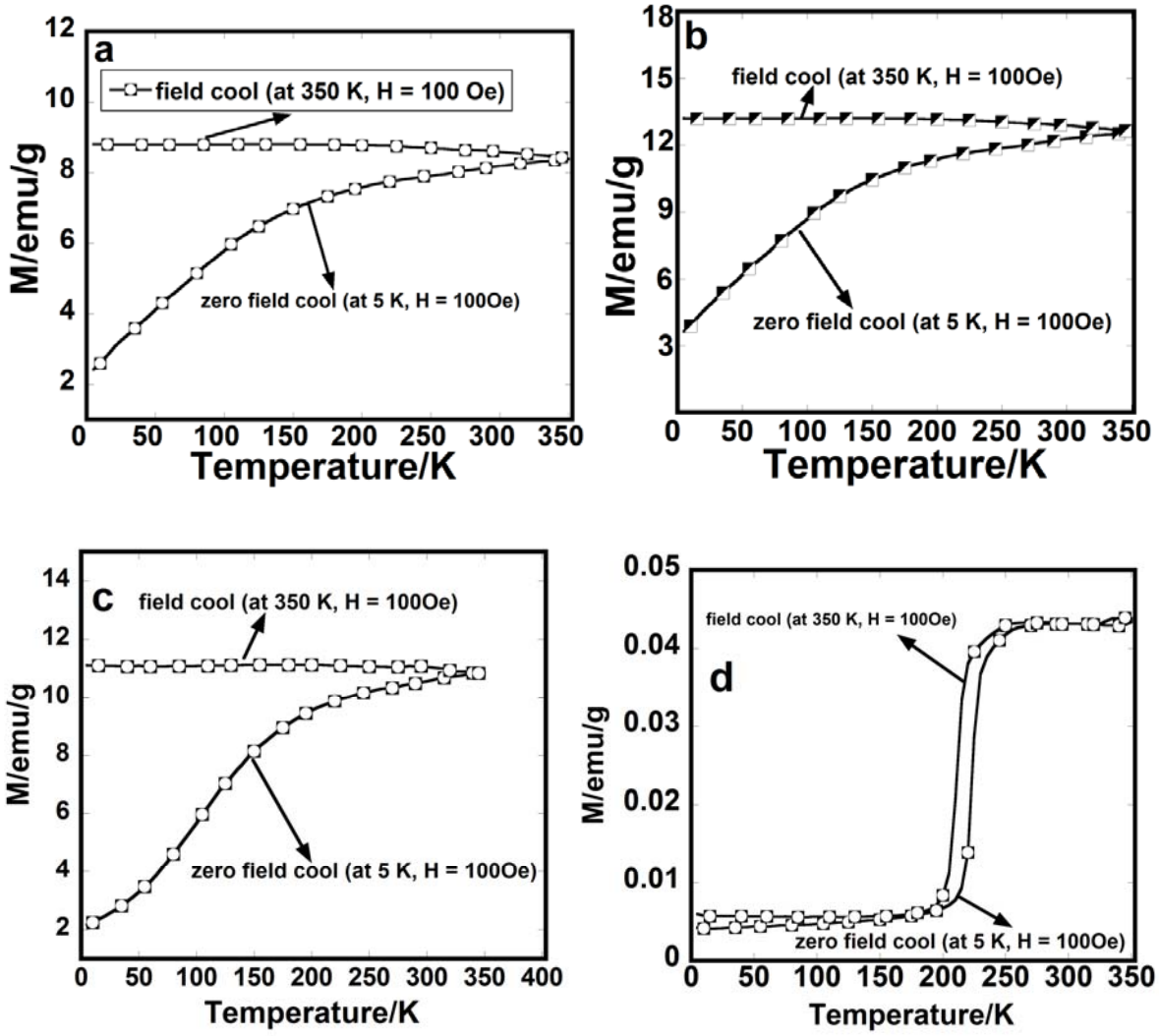

Fig.7-7. Temperature dependent magnetization in ZFC and FC processes for (a) Fe_3O_4, (b) mixed α and γ-Fe_2O_3, (c) only γ-Fe_2O_3 and (d) only α-Fe_2O_3 nanoparticles.

Heat dissipation of magnetic particles was evaluated by using an AC magnetic field generator

whose magnetic field intensity and frequency was 5.0 kA/m and 560 kHz, respectively. The heats generated from three distinct nanoparticles (γ-Fe_2O_3, α-Fe_2O_3 and mixed α and γ-Fe_2O_3) were evaluated by exposing of various doses of nanoparticles suspension dispersed in MEM under only AC magnetic-field induction, only photoirradiation or combined AC magnetic-field induction and photoirradiation conditions for about 10 minutes. The temperature increment of nanoparticles suspensions against different doses is shown in Fig. 7-8.

The results revealed that highest temperature increment was 45.7 °C in combined AC magnetic-field induced and photoexcited condition at 60 µg/mL dose whereas for only AC magnetic field induced or only photoexcited condition the temperature increment was 43.9 °C and 37.5 °C, respectively, using same dose of mixed α and γ-Fe_2O_3 nanoparticles. In contrast, highest temperature increment was 42.9 °C and 39.6 °C in combined AC magnetic-field induced and photoexcited conditions at 60 µg/mL dose using bare γ-Fe_2O_3 and bare α-Fe_2O_3 nanoparticles, respectively.

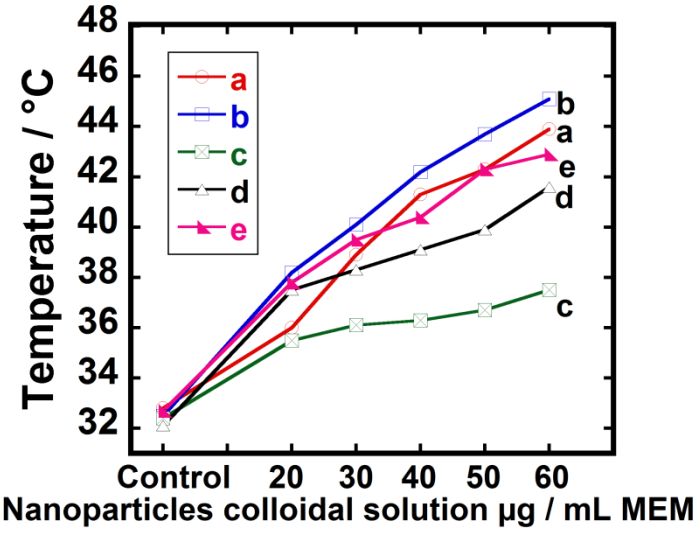

Fig. 7-8. Comparative hyperthermia ability of mixed α and γ-Fe_2O_3 under (a) only AC magnetic-field induction, (b) combined AC magnetic-field induction and photoirradiation and (c) only photoirradiation condition whereas (d) and (e) indicate the hyperthermia ability under combined AC magnetic-field induction and photoirradiation conditions using bare α-Fe_2O_3 and bare γ-Fe_2O_3 nanoparticles, respectively.

It is worth noting from Fig. 8, although there was only about 2 degree temperature difference between combined AC magnetic-fields induction and photoirradiation and only AC magnetic-fields induction (Fig. 7-8 (a) and (b)), as α-Fe_2O_3 is a famous semiconductor, easily excited by light irradiation and γ-Fe_2O_3 has most magnetic potentiality, we understood the mixed state of α and γ-Fe_2O_3 nanoparticles might be more effective to kill cancer cells. We noticed that although bare γ-Fe_2O_3 nanoparticles produced hyperthermia suitable temperature in combined conditions but mixed α and γ-Fe_2O_3 nanoparticles produced optimal temperature for hyperthermia therapy whereas bare α-Fe_2O_3 nanoparticles could not attain hyperthermia suitable temperature at all.

The results clearly indicated that both the combined AC magnetic-field induced and photoexcited conditions and the mixed iron oxides phase had dominant effect over only AC magnetic-field induced or only photoirradiation and any single iron oxide phase.

7.3.4 Cytotoxicity Evaluation

Controlled experiments in the absence of any kind of nanoparticles were done for the cancer cell killing under combined AC magnetic-field induction and photoirradiation conditions. In the ordinates of Fig. 7-9, 100% mean the number of living cells in a control dish. To compare the cell killing ability of mixed α and γ-Fe_2O_3 nanoparticles under only AC magnetic-field induction with that of combined AC magnetic-field induction and photoirradiation conditions and only photoirradiation condition for 10 min exposure time, the cell dishes were incubated with different doses of nanoparticles colloidal solution (20, 30, 40, 50 and 60 μg /mL) (Fig. 7-9 a~c).

Furthermore, we studied the toxic effects of bare α-Fe_2O_3 and bare γ-Fe_2O_3 nanoparticles under combined AC magnetic-field induction and photoirradiation conditions using the same dose and the same exposure time (Fig. 7-9d and 7-9e). The cells were stained by the trypan blue indicator; the dead cell accumulates the dye, resulting in blue color, whereas the live cells have

no color. The cell viability was determined as the percentage of the number of the unstained cells against that of the control dish cells.

The results revealed that the highest toxic effect was obtained using mixed α and γ-Fe_2O_3 nanoparticles under combined AC magnetic-field induction and photoirradiation conditions at a dose of 60 μg /mL MEM; approximately 98% cancel cells were killed. On the other hand, under only AC magnetic-field induction or only photoirradiation condition, only 89% and 66% cancel cells were destroyed, respectively, using the same dose of same nanomaterials. We also noticed that 55% and 79% cancer cells were destroyed using bare α-Fe_2O_3 and bare γ-Fe_2O_3 nanoparticles, respectively, under combined AC magnetic-field induction and photoirradiation conditions using the same dose.

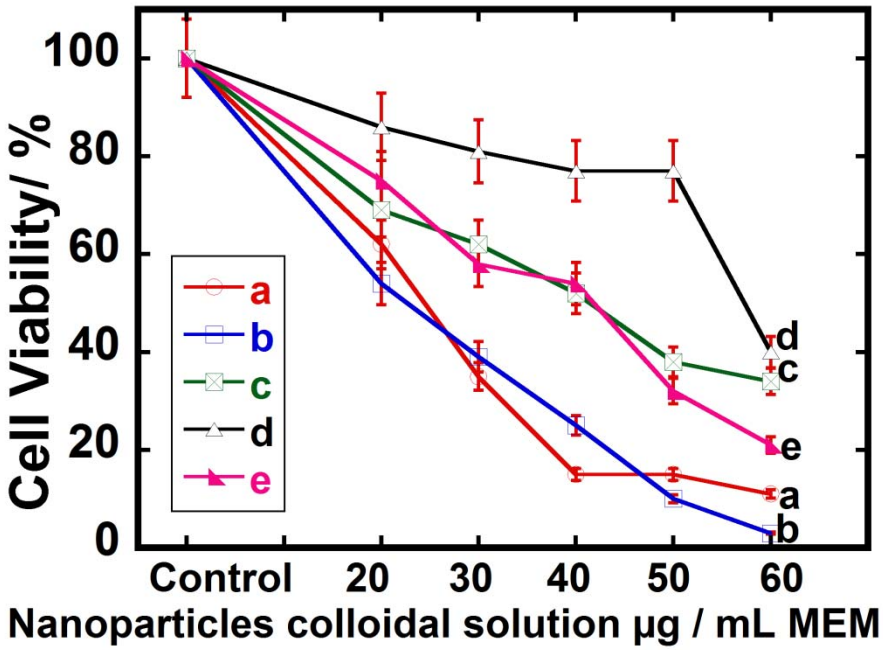

Fig.7-9. Comparative surviving fractions of HeLa cells incubated in MEM medium using mixed α and γ-Fe_2O_3 under (a) only AC magnetic-field induction, (b) combined AC magnetic-field induction and photoirradiation conditions and (c) only photoirradiation condition, whereas (d) and (e) indicate the cell viability under combined AC magnetic-field induction and photoirradiation conditions using bare α-Fe_2O_3 and bare γ-Fe_2O_3 nanoparticles, respectively.

Although it was noticed from Fig. 7-9 that only 9% cancer cells were killed more efficiently under combined AC magnetic-field induction and photoirradiation conditions in comparison with only AC magnetic-field induction using as-prepared mixed phase nanomaterials, in terms of oncological aspects it is not negligible because according to the nature of the cancer cells even single live cancer cell may be a great threat for the patient when its growth is uncontrolled. Cancers derived from epithelial cells are called carcinoma and it is fundamentally a disease by failure of regulation of tissue growth. Cancer cell growth is different from normal cell growth. Instead of dying, cancer cells continue to grow and form new, abnormal cells. It can also invade (grow into) other tissues, something that normal cells cannot do. Cancer costs billions of dollars and it is the second most common cause of death in the United States, exceeded only by heart disease. Cancer accounts for nearly 1 out of every 4 deaths in the United States and it caused about 13% of all human deaths worldwide (7.9 million), in 2007. With the growth and aging of the population, prevention efforts are important to help reduction of new cancer cases, human suffering, and economic costs [26, 27].

So, it is interesting to note that neither single phase of iron oxide (α-Fe_2O_3 or γ-Fe_2O_3) nor single state of energy induction (AC magnetic-field induction or photoirradiation) can destroy the cancer cells up to the satisfactory level until we use the mixed iron oxides under combined states of heat induction. To the best of our understanding the reason of killing almost 100% cancer cells under combined AC magnetic-field induction and photoirradiation conditions using mixed α and γ-Fe_2O_3 nanoparticles, can be ascribed as the additive or cumulative effects of hyperthermia and photocatalytic reactions.

Fig. 7-10 shows microscopic images of HeLa cells after 24 h incubation only in a MEM solution (control dish), 20, 30, 40, 50 and 60 μg of nanoparticles per 1 mL of MEM solution,

represented by (a) ~ (f), respectively, under combined AC magnetic-field induction and photoirradiation conditions using mixed α and γ-Fe_2O_3 nanoparticles. From these images it is seen that the cell morphological structure has almost no change after treatment of the control dish whereas in nanoparticle-treated dishes cell morphology is changed, especially in Fig. 7-10 (f). It is clearly noticed that increase in the nanoparticles dose rate decreases the survival rate of cancer cells (Fig. 7-9).

However, in relation to the biological safety issue of using superparamagnetic iron oxide nanoparticles (SPIONs) in human it is urgent need to know their toxic effects in body fluids. A precise analysis of the literature shows results on the toxicity of nanomaterials and specifically of SPIONs. For instance, Karlsson et al. [28] evaluated the toxicity of bare SPIONs on human lung epithelial cell line (i.e., A549) and found that there was no or low toxicity of SPIONs at the applied concentrations (20~80 μg/mL), In addition, there was no trace of bare SPION toxicity on mouse fibroblast cells even at higher concentrations (500 μg/mL) [29-31].

Although, there are plenty of additional examples on the toxicity of SPIONs on various cancer cell line, we evaluated the toxic effect of bare α-Fe_2O_3, bare γ-Fe_2O_3 and mixed α- and γ-Fe_2O_3 nanoparticles without exposing any external energy neither using AC magnetic-field induction nor photoirradiation condition. Recently, we introduced an automated cell counter (TC10^{TM} Automated Cell Counter, BIO-RAD, Japan) in our laboratory and we noticed no or very negligible toxic effect of bare α-Fe_2O_3, bare γ-Fe_2O_3 and mixed α- and γ-Fe_2O_3 nanoparticles in HeLa cancer cells (see the supplemental information).

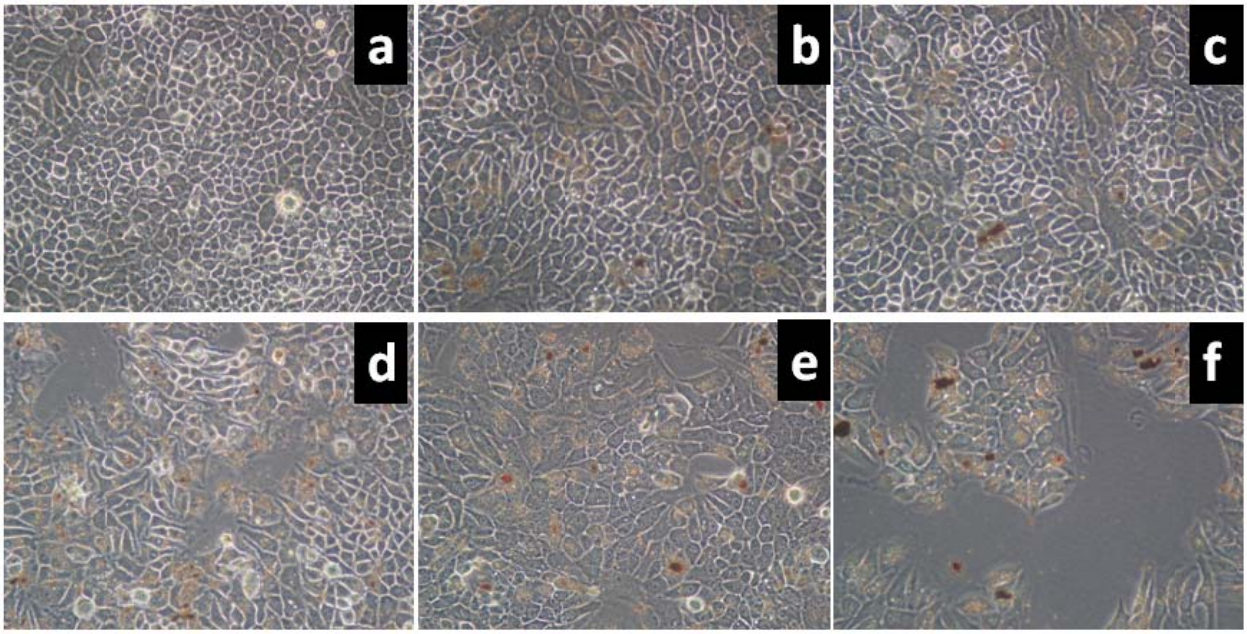

Fig. 7-10. Microscopic images of (a) control (without nanoparticles), (b) 20, (c) 30, (d) 40, (e) 50 and (f) 60 μg /mL of mixed α and γ-Fe_2O_3 suspension with HeLa (cancer) cells and exposure time of 10 min under combined conditions (Magnification 200×).

Fig. 7-11 showed trypan-blue stained microscopic images of HeLa cells in (a) control (without nanoparticles) and also suspension containing mixed α and γ-Fe_2O_3 nanoparticles under (b) only photoirradiation, (c) only AC magnetic-field induction and (d) combined AC magnetic-field induction and photoirradiation conditions. It was obviously noticed from Fig. 7-11 (a) that no cells was stained (100% live cells) but very few dead cells (stained) were found in Fig. 7-11 (b). Further, when the cancer cells were subjected to treat under AC magnetic-field induction using mixed α and γ-Fe_2O_3 nanoparticles, cancer cell killing rate was increased, as shown in Fig. 7-11 (c). Finally, when the cancer cells were subjected to treat under combined AC magnetic-field induction and photoirradiation conditions, almost 100% cancer cells were efficiently destroyed by using the mixed iron oxide nanoparticles (Fig.7-11(d), almost 100% stained cells).

Intracellular magnetite nanoparticle uptake alone has been reported several times. Besides, nanoparticles smaller than 20 nm can move out of a blood vessel as they circulate through the body [32]. Smaller particles which are more soluble in hydrophobic or nonpolar oil diffuse more rapidly across the lipid bilayer by passive diffusion [33, 34]. The pore size of the blood vessel endothelium wall of a normal cell is *ca.* 10 nm while that of a cancer cell is 10–100 nm [35, 36]. The anatomical difference in the structure of blood vessel endothelia near the cancer and the normal cells makes size-tunable nanoparticles feasible to reach selectively on the surface of cancer cells [37, 38]. Most recently, Liang *et al*. [39] reported that the uptake amount of gold nanoparticles increased quickly in first 12 h, then rose slowly from 12 to 24 h, and reached a plateau after 24 h. So, we treated the cancer cells with nanoparticles and incubated for 24 h before exposed to the instruments.

In photodynamic therapy (PDT), light energy delivered to the tumor site promotes the photosensitiser to an electronically excited state from which a number of reactive oxygen species, including singlet oxygen, are generated *via* electron or energy transfer processes. As a result, irreversible chemical modifications of a variety of cell constituents are induced. However, such photosensitisers often have the limited selectivity of tumor targeting; moreover, PDT treatment may generate generalized skin photosensitivity which can last for some weeks depending on the PDT agent used [40]. However, the combined AC-magnetic field induced and photoexcited instrumental method used by our group indicates that mixed iron oxide magnetic nanoparticles have maximum heating rates as well as cancer (HeLa) cell killing efficacy within the biologically safe frequency range. To the best of our understanding, the mechanism or reason for almost 100% HeLa cell killing under combined AC magnetic-field induction and photoirradiation conditions can be ascribed to the combined or additive effect of AC magnetic-

field induced hyperthermia and photocatalytic cytotoxicity.

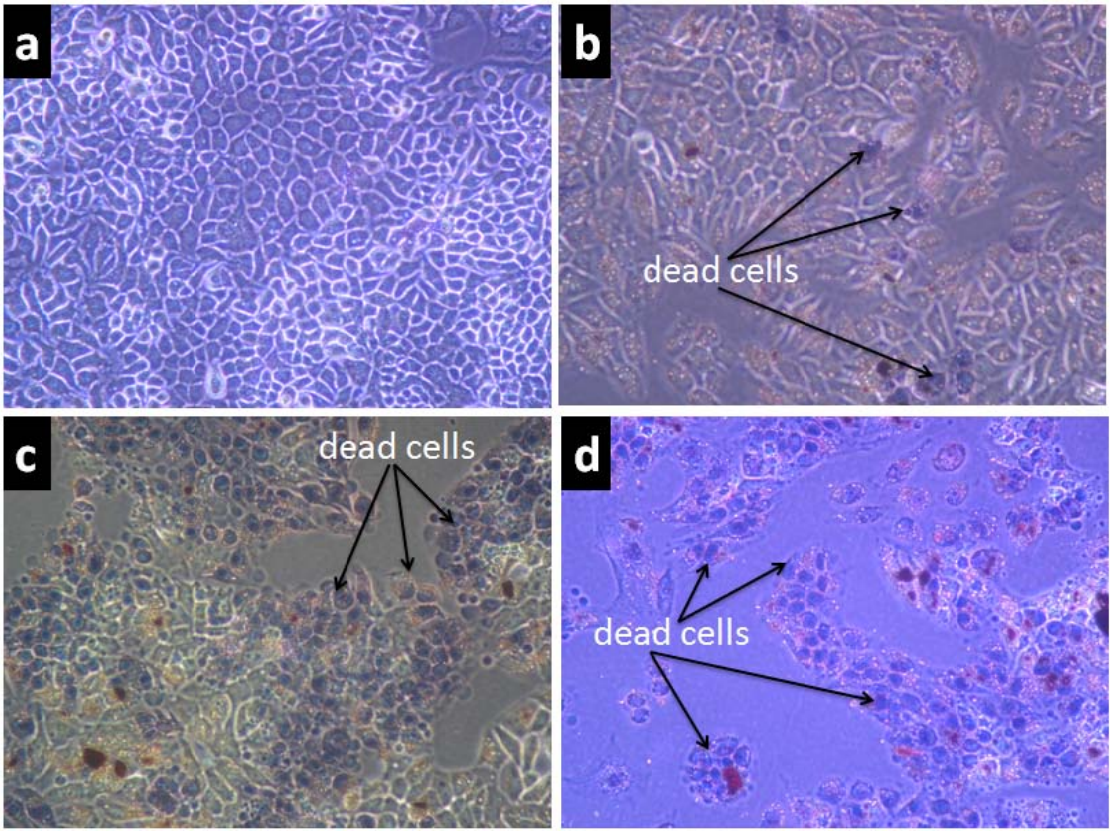

Fig. 7-11. Microscopic images of (a) control (without nanoparticles), suspension containing mixed α and γ-Fe2O3 nanoparticles under (b) only photoirradiation, (c) only AC magnetic-field induction and (d) combined AC magnetic-field induction and photoirradiation conditions (Magnification 200×). Dead cells stained with trypan blue show blue color.

7.4 Conclusions

We described the synthesis of superparamagnetic magnetite nanoparticles and the phase transfer to the mixed α and γ-Fe_2O_3 phase which due to their uniformity and monodispersity appear ideal for AC-magnetic field induced hyperthermia applications. The as-synthesized nanomaterials significantly enhanced the cancer cell destruction rate due to the mixed iron phase (α and γ) and the combined state of heat induction and photoirradiation. To the best of our

knowledge, for the first time we studied the cytotoxicity of mixed α and γ-Fe_2O_3 nanoparticles under the AC magnetic-field induced and photoirradiated conditions with almost 100% cancer cell killing efficacy.

References

[1] R.M. Cornell and U. Schwertman. The Iron Oxides: Structure, Properties, Reactions, Occurrences and Uses, Second Ed. Wiley-VCH, Weinheim, 2003.

[2] A. Jordan, P. Wust, R. Scholz, et al., in: U. Häfeli, W. Schütt, J. Teller, M. Zborowski (Eds.), Scientific and Clinical Applications of Magnetic Carriers, Plenum Press, NewYork, 1997.

[3] R. Hergt, W. Andra¨, C.G. d'Ambly, I. Hilger, W. A. Kaiser, U. Richter and H. G. Schmidt, *IEEE Trans. Magn*., 1998, **34**, 3745.

[4] A. Jordan, R. Scholz, P. Wust, H. Fähling and R. Felix, *J. Magn. Magn. Mater.*, 1999, **201**, 413.

[5] T. Neuberger, B. Schopf, H. Hofmann, M. Hofmann and B. von Rechenberg, *J. Magn. Magn. Mater.*, 2005, 293, 483-496.

[6] M. Chirita and I. Grozescu, *Chem. Bull. "POLITEHNICA" Univ. (Timisoara)*, 2009, **54**, 1.

[7] J. Bandara, U. Klehm and J. Kiwi, *Appl. Catal. B*, 2007, **76**, 73.

[8] M. S. Islam, Y. Kusumoto, M. Abdulla-Al-Mamun and Y. Horie, *Chem. Lett*., 2011, **40**, 773.

[9] An-Hui Lu, E. L. Salabas and S. Ferdi, *Angew. Chem. Int. Ed.*, 2007, **46**, 1222.

[10] P. K Sneed, P. R Stauffer, M. W McDermott, et al. Int. J. Radiat. *Oncol. Biol. Phys*., 1998, **40**, 287.

[11] H. Stahl, P. Wust, K. Maier-Hauff, M. Seebass, M. Mischel, M. Gremmler, G. Golde, J. Löffel and R. Felix, *Strahlenther Onkol.*, 1995, **171**, 510.

[12] M. Mitsumori, M. Hiraoka, Y. Okuno, Y. Nishimura, Y. P Li, S. Fujishiro, Y. Nagata, M. Abe, M. Koishi, T. Sano, T. Marume and N. Takayama, *Int. J. Radiat. Oncol. Biol. Phys*., 1996, **36**, 1169.

[13] A. N Guthkelch , L. P Carter, J.R Cassady, K. H Hynynen, R.P Iacono, P.C Johnson, E. A Obbens, R. B Roemer, J. F Seeger, D.S Shimm et al, *J. Neurooncol*., 1991, **10**, 271.

[14] E. Guilhon, P. Voisin, J. A. de Zwart, B. Quesson, R. Salomir, C. Maurange, V. Bouchaud, P. Smirnov, H. de Verneuil, A. Vekris, P. Canioni and C. T. W. Moonen, *J. Gene Med.,* 2003, **5**, 333.

[15] C. Wismeth, C. Dudel, C. Pascher, P. Ramm, T. Pietsch, B. Hirschmann, C. Reinert, M. Proescholdt, P. Rümmele, G. Schuierer, U. Bogdahn, and P. Hau, *J. Neurooncol*., 2010, **98**, 395.

[16] A. C Silva, T. R Oliveira, J. B. Mamani, S. MF Malheiros, L. Malavolta, L. F Pavon, T. T. Sibov, E. Amaro Jr, A. Tannús, E. LG Vidoto, M. J. Martins, R. S Santos and L. F. Gamarra, *Int. J. Nanomedicine,* 2011, **6**, 591.

[17] Q. He, Z. Zhang, J. Xiong, Y. Xiong and H. Xiao, *Opt. Mater*., 2008, **31**, 380.

[18] G .Bate, In Magnetic Oxides Part 2; Craik, D. J., Ed.; John Wiley & Sons, New York, 1975, pp 705-707.

[19] S. Laurent, D. Forge, M. Port, A. Roch, C. Robic, L.V. Elst and R.N. Muller, *Chem. Rev*., 2008, **108**, 2064

[20] S. Sun, H. Zeng, D. B. Robinson, S. Raoux, P. M. Rice, S. X. Wang and G. Li, *J. Am. Chem. Soc*., 2004, **126**, 273.

[21] M. Abdulla-Al-Mamun, Y. Kusumoto, A. Mihata, M. S. Islam and B. Ahmmad, *Photochem. Photobiol Sci.*, 2009, **8**, 1125.

[22] A. S. Teja and P. Y. Koh, *Prog. Cryst. Growth Charact. Mater*., 2009, **55**, 22.

[23] S. Klotz, G. Steinle-Neumann, T. Strassle, J. Philippe, T. Hansen and M.J. Wenzel, *Physical Review B*, 2008, **77** (1).

[24] B. William, I. Jr and S. U.M. Khan, *Thin Solid Films*, 2004, **461**,301.

[25] C. Karunakaran and S. Senthilvelan, *Electrochem. Commun*., 2006, **8**, 95.

[26] M. S. Islam, Y Kusumoto, M. Abdulla-Al-Mamun, and Y. Horie, *Catal. Comm.*, 2011, **16**, 39.

[27] American Cancer Society, Cancer Facts & Figures, Atlanta, GA. 2009.

[28] H. L. Karlsson, P. Cronholm, J. Gustafsson and L. Moller, *Chem. Res. Toxicol*. 2008, **21**, 1726.

[29] M. Mahmoudi, M. A. Shokrgozar, A. Simchi, M. Imani, A. S. Milani, P. Stroeve, H. Vali, U.O. Hafeli and S. Bonakdar, *J. Phys. Chem. C*, 2009, **113**, 2322.

[30] M. Mahmoudi, A. Simchi and M. Imani, *J. Phys. Chem. C,* 2009, **113**, 9573.

[31] M. Mahmoudi, A. Simchi, H. Vali, M. Imani, M. A. Shokrgozar, K. Azadmanesh and F. Azari, *Adv. Eng. Mater.* 2009, **11**, B243.

[32] T. Ozkayaa, M. S. Toprakb, A. Baykala, H. Kavas, Y. Köseoğluc and B. Aktas, *J. Alloys Compd*., 2009, **472**, 18.

[33] S. E McNeil, *J. Leukocyte Biol*. 2005, **78**, 585.

[34] B. Alberts , A. Johnson, J. Lewis, M. Raff, K. Roberts and P. Walter, in: Molecular biology of the cell. Gibbs S (Ed.), Garland Science, Taylor & Francis Group, New York, 2002, pp. 616.

[35] I. Brigger, C. Dubernet and P. Couvreur, *Adv. Drug Delivery Rev.* 2002, **54**, 631.

[36] Y. Matsumura and H. Maeda, *Cancer Res.*, 1986, **46**, 6387.

[37] D.R. Siwak,A. M. Tari and G. Lopez-Berestein, *Clin. Cancer Res*., 2002, **8**, 955.

[38] N. Kohler, C. Sun, J. Wang and M. Zhan, *Langmuir* , 2005, **21**, 8858.

[39] Z. Liang, Y. Liu, X. Li, Q. Wu, J. Yu, S. Luo, L. Lai and S. Liu, *J. Biomed. Mater. Res. Part A,* 2011, **98A**, 479.

[40] I. H. El-Sayed, X. Huang and M. A. El-Sayed, *Cancer Lett*., 2006, **239**, 129.

CHAPTER 8

AC MAGNETIC-FIELD INDUCED ENHANCED CYTOTOXICITY OF NOVEL NECK-STRUCTURED MAGNETIC (Fe_3O_4 AND γ-Fe_2O_3) NANOPARTICLES AGAINST HUMAN EPITHELIAL CARCINOMA (HeLa) CELLS

Abstract

The current study was designed to find out the cancer cell killing efficacy of as-synthesized neck-structured Fe_3O_4 and γ-Fe_2O_3 magnetic nanoparticles under AC magnetic-fields induction condition. Novel neck-structured Fe_3O_4 and γ-Fe_2O_3 magnetic nanoparticles were successfully prepared by a modified hydrothermal method. Ferrous chloride tetrahydrate was solely used as a precursor for the novel nanomaterials. The as-synthesized nanomaterials were characterized by using XRD, FE-SEM and TEM. Neck-structured particle morphology was observed for the first time in all of iron oxides with magnetic properties. The particle size observed was 50–60 nm. The synthesized nanomaterials showed excellent magnetization values when magnetic hysteresis loops were measured using a superconducting quantum interference device (SQUID) as well as excellent colloidal stability. Moreover, the as-prepared magnetic nanoparticles suspensions showed significant temperature increments and cancer (HeLa) cell destroying potentiality (91% and 95% for Fe_3O_4 and γ-Fe_2O_3, respectively) under an AC (alternating current) magnetic-field induction condition at room temperature using the concentration of 150 μg/mL. This work is now under review in Current Nanoscience.

8.1 Introduction

Materials with reduced dimensions, for instance, nanotubes, nanowires, nanorods, and nanoparticles, etc., are of substantially different properties from their bulk state counterparts [1, 2] and have attracted great interest in the past decade. The synthesis of nanostructured magnetic materials has become a particularly important area of research and is attracting a growing interest because of the potential applications such as materials in ferrofluids, advanced magnetic materials, catalysts, colored pigments, high-density magnetic recording media and medical diagnostics [3-8]. The iron oxide (Fe_2O_3), the most common oxide of iron, has the important magnetic properties. From the viewpoint of the basic research, iron (III) oxide is a convenient compound for the general study of polymorphism and the magnetic and structural phase transitions of nanoparticles. Iron oxides exist in nature in many forms in which magnetite (Fe_3O_4), maghemite (γ-Fe_2O_3) and hematite (α-Fe_2O_3) are probably the most common [9].

Magnetite and maghemite have attracted attention in biomedical applications because of their biocompatibility and low toxicity in the human body [10-13]. Maghemite (γ-Fe_2O_3) is biocompatible and therefore is one of the most extensively used biomaterials for different applications like cell separation, drug delivery in cancer therapy, magnetic induced hyperthermia and others [14]. A major area of application has been the field of bio-assays where the magnetic properties have been exploited *in vitro* to manipulate magnetite nanoparticles with an external magnetic field [10, 15]. In an alternating magnetic field, induced currents are generated in metallic objects, and as a consequence, heat is generated in the metal. This phenomenon is greatly enhanced in metals showing collective magnetic behavior. Thus, when a magnetic fluid is exposed to an alternating magnetic field, the particles become powerful heat sources, destroying

tumor cells since these cells are more sensitive to temperatures in excess of 41 °C than their normal counterparts [16].

The catalytic and other properties depend on the morphology, particle size and surface area. Besides, this preparation method plays a key role in determining the particle size and shape, size distribution, surface chemistry and therefore the applications of the material. Increased heating rates of magnetic fluids are an important challenge in order to minimize dosages of magnetic fluids needed to reach therapeutic temperatures in magnetic fluid hyperthermia (MFH). Possible approaches to increase heating rates of superparamagnetic particles for MFH would be to increase the anisotropy of the nanoparticles (shape or magneto-crystallinity) or to increase the field strength used for treatment [17]. Many of the nanoparticles currently studied are made using the co-precipitation method [18] which results in particles that can be polydispersed in size and shape and tend to agglomerate.

In this sense, in the present study we describe the synthesis of neck-structured magnetite (Fe_3O_4) nanoparticles by a hydrothermal method and then transferred Fe_3O_4 to γ-Fe_2O_3 and α-Fe_2O_3 nanoparticles. It is noteworthy that we already reported the synergistic cancer cell killing effect of neck-structured α-Fe_2O_3 under combined AC magnetic-filed induction and photoirradiation conditions [19]. Because of our interest in the enhanced toxic effect of neck-structured magnetic (Fe_3O_4 and γ-Fe_2O_3) nanoparticles under AC magnetic-field induction (**Fig.8-1**), we adopted HeLa cells as a model to investigate the thermal cancer cell killing efficiency and also observed the comparative cytotoxicity of spherical Fe_3O_4 and γ-Fe_2O_3 nanoparticles using the same dose under the same condition at room temperature.

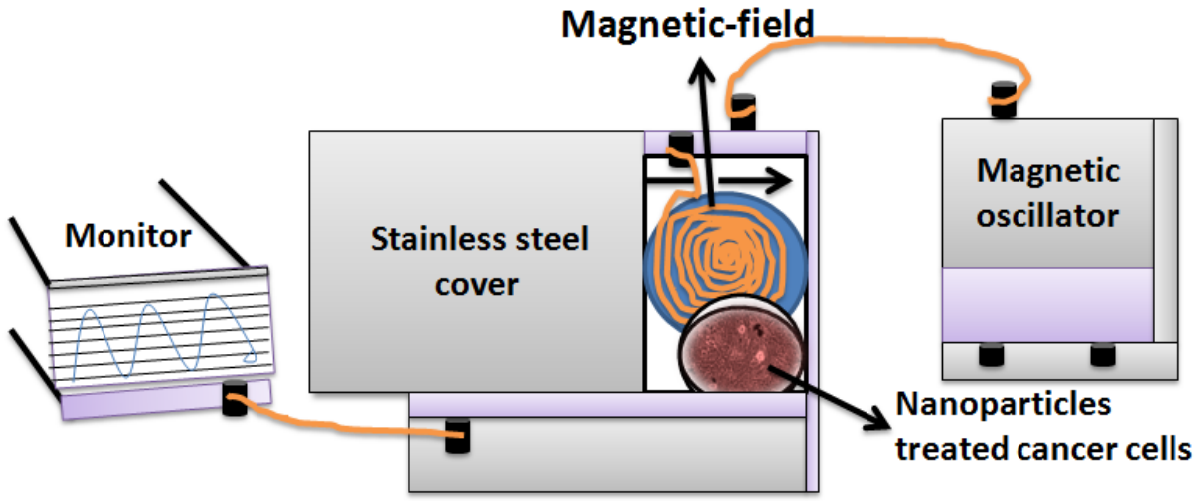

Fig.8-1: Assembles of AC magnetic-fields induction instruments.

8.2 Experimental

8.2.1 Materials and methods

Typical syntheses of magnetite (Fe_3O_4) nanoparticles were carried out in a hydrothermal system by modified reduction reactions between $FeCl_2$ and ethylene glycol and then the magnetite nanoparticles were oxidized into maghemite and hematite at 250 °C for 8 h in the presence of oxygen and at 500 °C for 3 h in the presence of Ar gas, respectively. In this experiment chemicals used were iron (II) chloride tetrahydrate ($FeCl_2.4H_2O$, Wako Pure Chemical Industries Ltd., Japan), ethylene glycol (99.5%, Wako Pure Chemical Industries Ltd., Japan), polyethylene glycol (4000, Tokyo Kasei Kogyo Co. Ltd, Japan) and sodium acetate, anhydrous (NaAc, 98%, Nacalai Tesque, Japan). All chemicals were of analytical grade and were used without any further purification.

8.2.2 Synthesis and formation of magnetic nanoparticles

In this report, we synthesized neck-structured Fe_3O_4 nanoparticles by a modified hydrothermal method. Deng *et al.* prepared magnetic microspheres using $FeCl_3$•$6H_2O$ as a

precursor and autoclaved the mixture at 200 °C for 8-72 h [15]. However, we used $FeCl_2 \cdot 4H_2O$ as a precursor and the mixture was autoclaved at 190 °C for 5 h with air pressure 0.2 MPa to synthesize Fe_3O_4 magnetic nanoparticles. $FeCl_2 \cdot 4H_2O$ (0.99 g, 5 mmol) was dissolved in ethylene glycol (40 mL) to form a clear solution, followed by the addition of NaAc (3.6 g) and polyethylene glycol (1.0 g). The mixture was stirred vigorously for 45 min until getting a clear solution and then sealed in a teflonlined stainless-steel autoclave (50 mL capacity). The autoclave was heated to and maintained at 190 °C for 5 h and allowed to cool to room temperature. After cooling, decantation was done by a permanent magnet to get the sedimented black products. The black products were washed several times with ethanol and dried at 70 °C for 3 h. Finally, we obtained 0.81 g of Fe_3O_4 nanoparticles.

In hydrothermal synthesis, metal oxides particles are generally synthesized in aqueous solution of starting metal salts. In this case, oxygen of resulting oxide is derived from water as a reservoir but in our study $FeCl_2 \cdot 4H_2O$ was the source of water during reaction. Moreover, polyethylene glycol (PEG) added in this reaction system acts as an oxidant, surfactant, and dispersing agent. This ultimately prevents the particle agglomeration and results in the formation of high surface area free-flowing Fe_2O_3. It is well known that Fe_3O_4 can be oxidized to γ-Fe_2O_3, which can be further transformed into α-Fe_2O_3 at higher temperatures [13]. However, magnetite (Fe_3O_4) is not very stable and is sensitive to oxidation. Magnetite is transformed into maghemite (γ-Fe_2O_3) in the presence of oxygen [20]. First, as-synthesized Fe_3O_4 was oxidized into γ-Fe_2O_3 at 250 °C for 8 h in the presence of oxygen and then γ-Fe_2O_3 was calcinated at 500 °C for 3 h in the presence of Ar gas to get α-Fe_2O_3.

8.3. Characterization

The general structure characterization, including size, size distribution and crystal structure of

the as-synthesized neck-structured Fe_3O_4 and γ-Fe_2O_3 was performed for the samples without any size sorting. To further confirm the crystal structure and overall phase purity, the nanoparticles with different sizes were examined using X-ray powder diffractometer (XRD, PANalytical Advance) with CuKα radiation. The surface morphology and nanoparticles size were determined using a field-emission scanning electron microscope (FE-SEM, model Hitachi S-4100H). Further, the shape of the nanoplates was analyzed by transmission electron microscopy (TEM, JEOL JEM-3010 VII TEM) operating at 300 kV. Confirmation of Fe_3O_4 formation was evaluated by FT-IR analysis using Perkin Elmer (FT-IR) spectrum One-B. A simple magnetization test was performed to observe the magnetic potentiality as well as colloidal stability of the all samples by using a permanent magnet by dispersing the nanoparticles in distilled water and magnetic hysteresis loops were measured by a superconducting quantum interference device (SQUID, Quantum Design MPMS-5). Finally, AC magnetic-field induced heating capability of prepared nanoparticles was studied to examine the hyperthermia potentiality of the as-synthesized neck-structured Fe_3O_4 and γ-Fe_2O_3 nanoparticles by dispersing in distilled water as well as in a minimum essential medium (MEM) and temperature increment for the every dish was measured by a digital thermometer (Sato Keiryoki-250WP II-R).

8.4 Results and discussion

8.4.1 XRD analysis

The crystal structures of the prepared neck-structured magnetic (magnetite, maghemite and hematite) nanoparticles were observed by the XRD measurement. Typical XRD patterns of Fe_3O_4, γ-Fe_2O_3 and α-Fe_2O_3 are shown in Fig.8-2. As shown in Fig. 8-2, all samples were found to be consistent with the expected diffraction pattern of the *fcc* FeO structures. No diffraction peaks from other crystalline forms were detected, which demonstrates that these Fe_3O_4, γ-Fe_2O_3

and α-Fe_2O_3 samples had high purity and crystallinity (JCPDS, PDF, File No. 01-071-6336, 00-039-1346 and 01-085-0599, respectively).

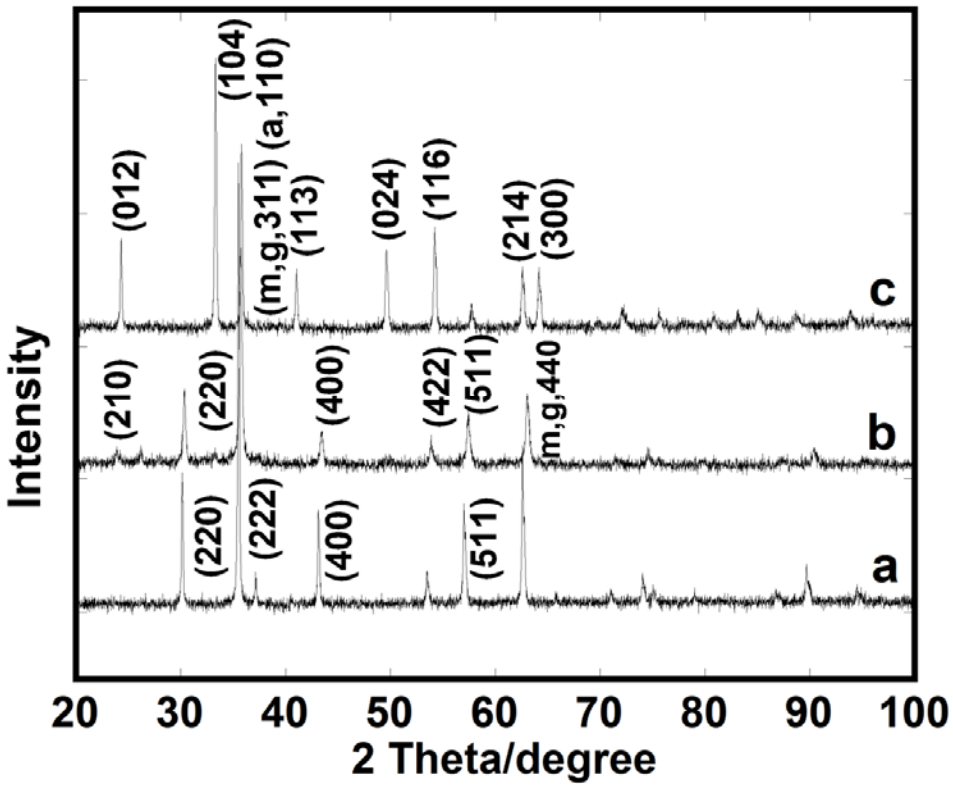

Fig.8-2: XRD patterns of (a) Fe_3O_4, (b) γ-Fe_2O_3 and (c) α-Fe_2O_3 neck-structured nanoparticles synthesized by the hydrothermal method (a = alpha, g = gamma)

Fig.8-2(a) is the XRD pattern of Fe_3O_4 nanoparticles assembly obtained after oven drying at 70 °C for 3 h. Fig. 8-2 (b) shows the XRD pattern of the red-brown materials, γ-Fe_2O_3 obtained after oxidation of Fe_3O_4 at 250 °C for 8 h in the presence of oxygen and Fig. 7-2 (c) shows the XRD pattern of the dark red-brown materials, α-Fe_2O_3 obtained after 500 °C annealing of γ-Fe_2O_3 in Fig. 8-2 (b) under Ar gas for 3 h.

In this paper, the structures of magnetic iron oxides were characterized by using X-ray diffraction analysis. Though magnetite and maghemite crystallizes under spinel structure, hematite does not. Thus, it is easy to differentiate between hematite and other magnetic iron

oxides. However, it is very hard to identify magnetite and maghemite. But, in order to confirm the three types of iron oxides nanoparticles prepared through this study, a comparative XRD analysis was done with commercial ones. Fig.8-2 shows that all XRD peak positions and relative intensities of our as-prepared nanomaterials match well with those of commercial Fe_3O_4, γ-Fe_2O_3 and α-Fe_2O_3 powder materials (Wako catalog No. 093-01035, 324-94282 and 322-94283, respectively), indicating that the synthesis and oxidation of Fe_3O_4 under O_2 and annealing in the presence of Ar gas lead to formation of γ-Fe_2O_3 and α-Fe_2O_3, respectively.

8.4.2 Shape analysis by FE-SEM and TEM

Particles morphology of the samples was studied using FE-SEM. Fig.8-3 (a) and (b) represent the FE-SEM micrographs of Fe_3O_4 and γ-Fe_2O_3, respectively. The nanoparticles size was roughly estimated to be about 60-70 nm from the SEM data, as shown in Fig.8-3.

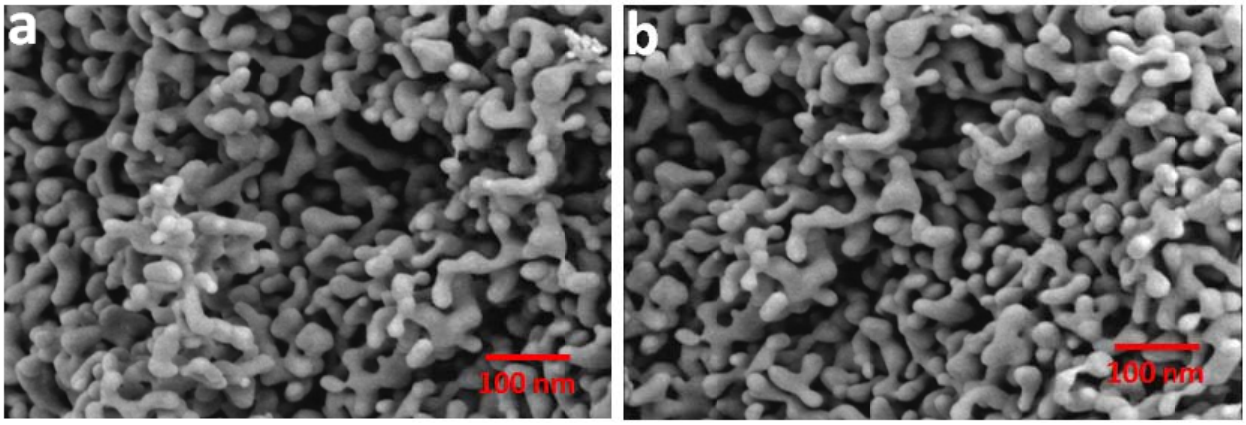

Fig. 8-3: SEM images of neck-structured (a) magnetite and (b) maghemite nanoparticles.

The samples were also characterized using TEM. Fig.8- 4 (a) and (b) depict the TEM images of Fe_3O_4 and γ-Fe_2O_3, respectively. The neck-structured morphology was observed by FE-SEM

in all the samples. Such a type of unique morphology was observed for the first time for iron oxide with excellent magnetic properties. TEM images also clearly showed the nano-structural homogeneities and remarkably unique neck-structured morphology with average size of 50-60 nm. Although the neck-structure shaping mechanism is unclear, low temperature during autoclave, long time oxidation and annealing may be responsible to the neck-structure formation. Further study is needed to clarify the mechanism.

8.4.3 Colloid stability

The photographs of the neck-structured black Fe_3O_4 and red-brown γ-Fe_2O_3 are represented by Fig. 8-5 (a) and (c), respectively. To examine the colloid stability of iron oxide samples, magnetic nanoparticles (10 mg) were dispersed in doubly distilled water (50 mL) by sonication. As shown in Fig. 8-5, the as-prepared nanoparticles were well dispersed into water without any aggregation and precipitation and firmly dragged by the permanent magnetic force (Fig.8-5 (b) and (d), respectively).

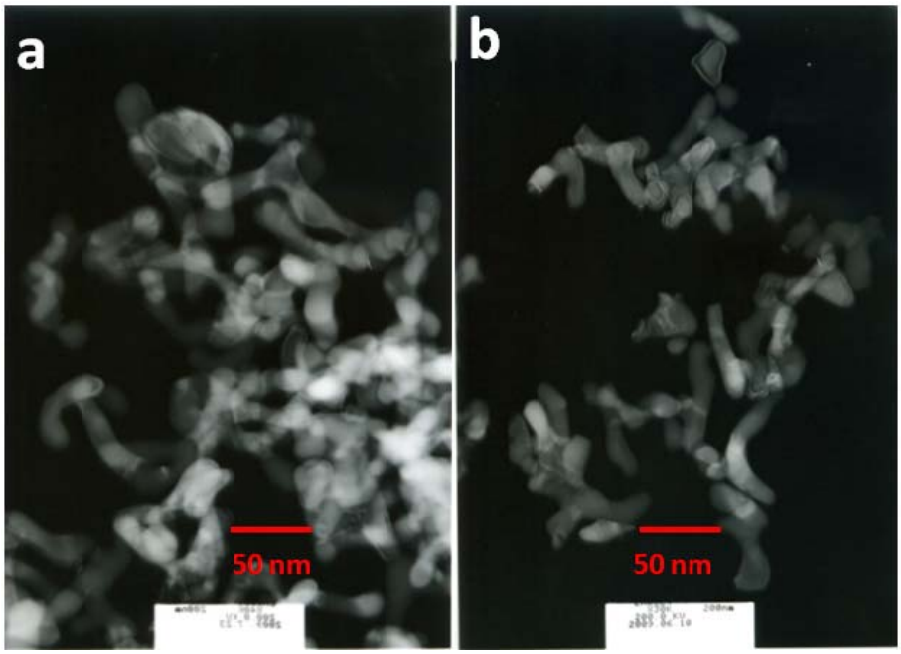

Fig. 8-4: TEM images of neck-structured (a) magnetite and (b) maghemite nanoparticles.

The magnetic nanoparticles remained in suspension for more than 1 day, which demonstrates that they can be well-dispersed in aqueous solution. Therefore, with the appropriate surface modifications, these magnetic nanoparticles may be suitable for clinical diagnosis and in the transport of drugs, proteins, viruses, or bacteria. The nanomaterials synthesized in this study offer several important advantageous features for the technical application of nanoparticles. First, the nanoparticles are magnetic, which means that they can be manipulated by an external magnetic field. Second, our strategy allows the direct production of highly crystalline, monodispersed, and hydrophilic nanoparticles. Finally, the raw materials are inexpensive and the yields are relatively high (82%), which makes this process amenable to large-scale reactions for industrial needs.

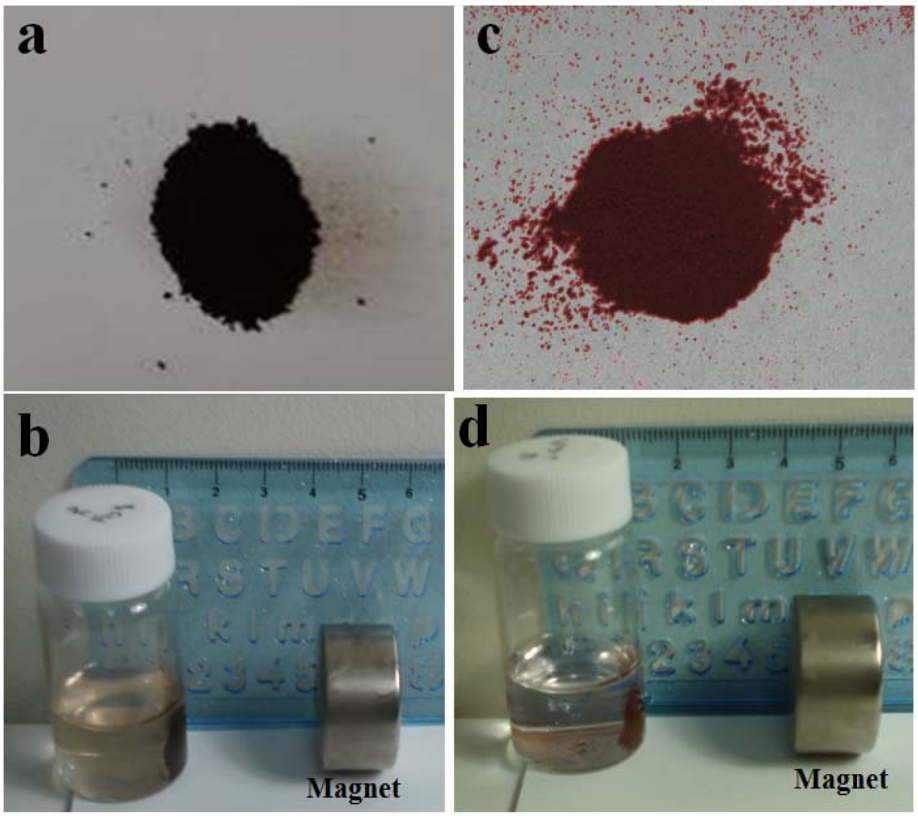

Fig.8-5: Photographs of the neck-structured black (a) Fe_3O_4 and red-brown (c) γ-Fe_2O_3 nanoparticles. Water-dispersed Fe_3O_4 and γ-Fe_2O_3 dragged by permanent magnetic force are represented by (b) and (d), respectively.

8.4.4 FT-IR analysis

The FTIR spectra of commercial Fe_3O_4 powder and our as-synthesized Fe_3O_4 nanoparticles are shown in Fig. 8-6. The FT-IR analysis was done to confirm the formation of Fe_3O_4. Moreover, it was performed to understand the surfactant effect of PEG whether it was present or absent around the Fe_3O_4 nanoparticles. As-prepared magnetite nanoparticles present characteristic peaks that are exhibited by the commercial magnetite powder: a metal-oxygen band, υ_1, observed at 590cm^{-1} corresponds to intrinsic stretching vibrations of the metal at the tetrahedral site ($Fe_{tetra}\leftrightarrow O$), whereas a metal-oxygen band observed at 445 cm^{-1}, υ_2, is assigned to the octahedral-metal stretching ($Fe_{octa}\leftrightarrow O$). Characteristic peaks for magnetite well matched with commercial ones prove that there was no surfactant effect during preparation and formation of Fe_3O_4 nanoparticles.

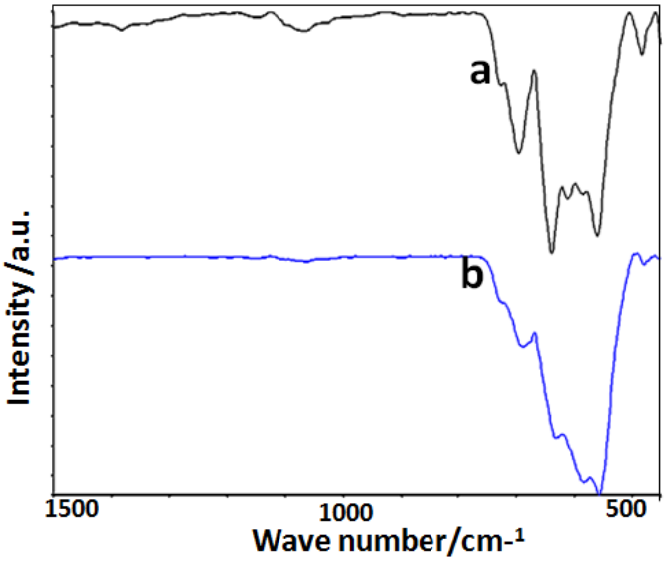

Fig. 8-6: FTIR spectra of as-synthesized (a) magnetite nanoparticles and (b) commercial magnetite powder.

8.4.5 Magnetic properties of as-prepared nanomaterials

Magnetic measurements on all kind nanoparticles indicate that the particles were superparamagnetic at room temperature, meaning that the thermal energy can overcome the

anisotropy energy barrier of a single particle, and the net magnetization of the particle assemblies in the absence of an external field is zero. Fig. 8-7 (a) and (b) show the hysteresis loops of the as-prepared Fe_3O_4 and γ-Fe_2O_3 nanoparticles, respectively, measured at room temperature. At room temperature there was no hysteresis (Fig. 8-7).

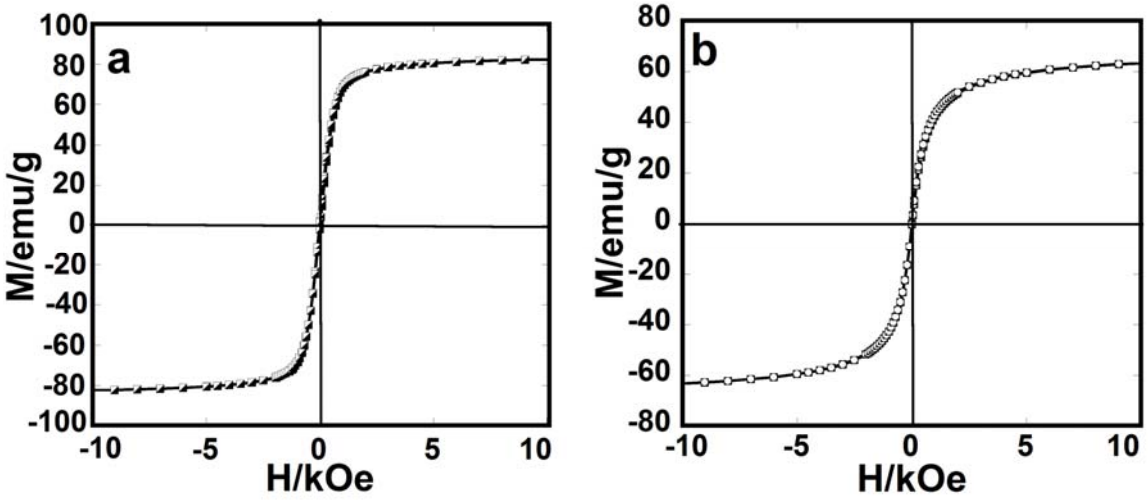

Fig.8-7: Magnetic hysteresis loops of neck-structured (a) magnetite and (b) maghemite nanoparticles at room temperature.

Under a large external field, the magnetization of the particles aligns with the field direction and reaches its saturation value for Fe_3O_4 and γ-Fe_2O_3 nanoparticles; we noticed that the saturation magnetization (*Ms*) values were 87 and 69 emu/g, respectively, almost similar to the findings reported by Cornell *et al.* [9]. This is excellent evidence of the completion of the phase transfer of Fe_3O_4 to γ-Fe_2O_3.

8.4.6 Heating capability

A comparative heat dissipation capability of as-prepared neck-structured and spherical-shaped magnetic nanoparticles (Fe_3O_4 and γ-Fe_2O_3) were evaluated by using an AC magnetic-

field generator using magnetic field intensity and a frequency of 5.0 kA/m and 560 KHz, respectively. The heat generated from all samples was evaluated by exposing 150 μg/mL magnetic particle suspension dispersed in distilled water and then their different doses like 0.2, 0.4, 0.6, 0.8 and 1.0 mL/ mL MEM under AC magnetic-field induction for 10 min. The temperature rising of the as-prepared magnetic nanoparticles suspensions against the exposure time is shown in Fig. 7-8. The highest temperature was achieved as 44.5 and 45.3 °C for neck-structured Fe_3O_4 and γ-Fe_2O_3, respectively, whereas for spherical Fe_3O_4 and γ-Fe_2O_3 (supplemental materials) the highest temperature achieved was 42.2 and 42.9 °C, respectively, for 10 min exposure time at a dose of 1.0 mL/ mL MEM.

The results revealed the supremacy of the neck-structured nanoparticles over the spherical-shaped ones in respect of hyperthermia ability. The generation of heat by magnetic particles exposed to the alternating magnetic field depends very much on the magnetic particle characteristics such as saturation magnetization, particle size and shape, magnetic field strength and frequency. When magnetic particles with diameters very much larger than the superparamagnetic limit (20 nm) are exposed to an AC magnetic-field, the heat is generated due to the hysteresis loss. On the other hand, in the case of particles closer to superparamagnetic limit, they dissipate heat through Brownian or Néel relaxation depending on the alternating magnetic field frequency. Here again, the relaxation time depends on the particle diameter and when the particles are small and the relaxation time is comparable to the frequency, large amount of heat is generated [21].

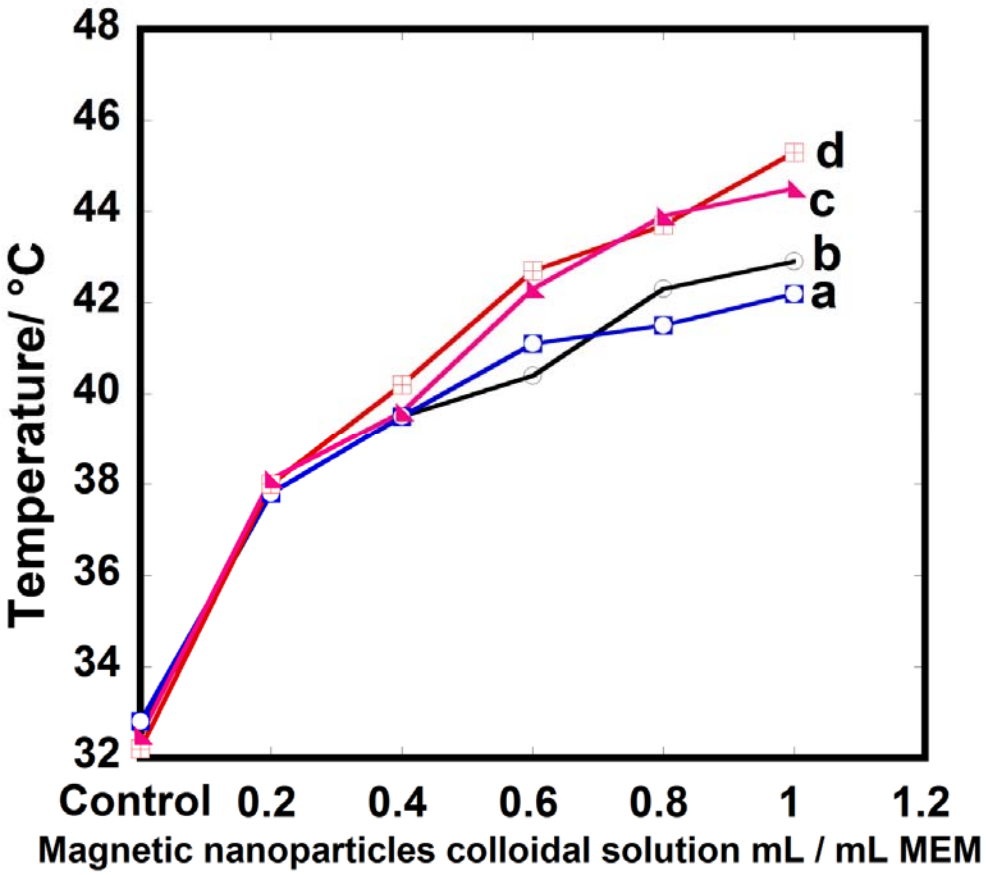

Fig.8-8: Comparative heat dissipation capability of spherical-shaped and neck-structured magnetic nanoparticles synthesized by hydrothermal methods. Here (a), (b) and (c), (d) stand for Fe_3O_4 and γ-Fe_2O_3 nanoparticles for spherical-shaped and neck-structured, respectively.

8.4.7 In-vitro cytotoxicity and anti-cancer assay

The *in vitro* cytotoxicity and anti-cancer effect of the nanomaterials against the HeLa cell line was evaluated by trypan blue exclusion method. To investigate and compare the cytotoxicity efficacy, every Petri dish was subjected to apply under the AC magnetic-field induction for 10 min and immediately after the treatment; temperature increment for the every dish was measured by a digital thermometer (Sato Keiryoki-250WP II-R).

Cancer cell viability was examined by treating with nanoparticles colloidal solution for 24 h incubation in an incubator. To investigate the cytotoxicity of synthesized nanomaterials, one dish was used as control without any nanomaterials and the other five dishes were treated with different doses, like 0.2, 0.4, 0.6, 0.8 and 1.0 mL of nanoparticles colloidal solution per mL of MEM solution where the actual colloidal solution concentration was 150 μg/mL. A haemocytometer was used to estimate the total number of viable cells (by counting cells in the four 1 mm^2 corners of the haemocytometer) and average number of the cells per unit volume (mL) of medium was calculated as the sum of the counted cell number/ 3×10^5. Every treatment was conducted by doing three-time independent experiments.

8.4.8 Cytotoxicity evaluation

Comparative surviving fractions of HeLa cells incubated in the MEM medium using as-prepared neck-structured and spherical-shaped magnetic nanoparticles (Fe_3O_4 and γ-Fe_2O_3) were evaluated by using different doses like 0.2, 0.4, 0.6, 0.8 and 1.0 mL/ mL MEM under AC magnetic-field induction for 10 min (Fig.8-9). In the ordinate of Fig.8-9, 100% means the number of living cells in a control dish.

The cells were stained by the trypan blue indicator; the dead cell accumulates the dye, resulting in blue color, whereas the live cells have no color. The cell viability was determined as the percentage of the number of the unstained cells against that of the control dish cells. The results revealed that the highest toxic effect was obtained using neck-structured γ-Fe_2O_3 nanoparticles under AC magnetic-field induction condition at a dose of 1.0 mL/ mL MEM; approximately 95% cancel cells were killed and ca. 91% cancer cells destruction was followed by using neck-structured Fe_3O_4 nanoparticles. On the other hand, approximately 79% and 75%

cancer cells were killed by using spherical-shaped γ-Fe_2O_3 and Fe_3O_4 nanoparticles, respectively, under the same condition at the same dose.

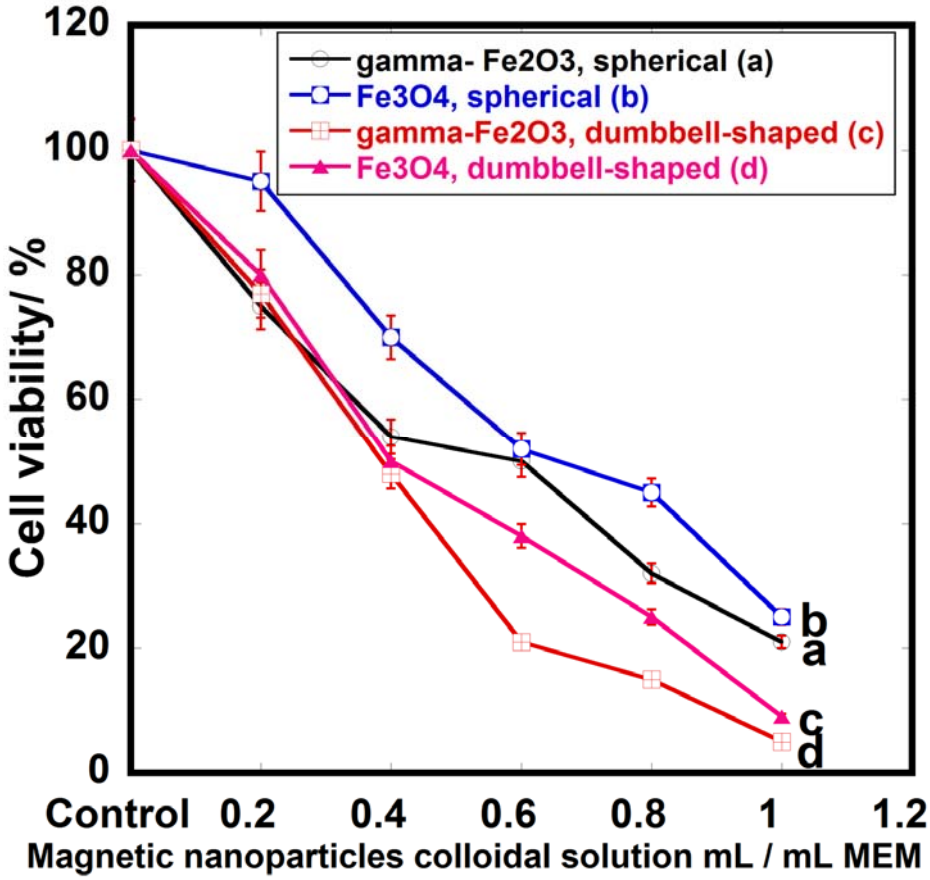

Fig. 8-9: Comparative surviving fractions of HeLa cells incubated in the MEM medium using spherical-shaped and neck-structured Fe_3O_4 and γ-Fe_2O_3 nanoparticles under AC magnetic-field induction. Here (a), (b) and (c), (d) stand for Fe_3O_4 and γ-Fe_2O_3 nanoparticles for spherical-shaped and neck-structured, respectively. 100% correspond to the control dish and the cell viability percentage was calculated using the number of live cells against the control dish cells.

Fig. 8-10 shows microscopic images of HeLa cells after 24 h incubation in a MEM medium control dish (without nanoparticles) (a) and 1.0 mL of neck-structured Fe_3O_4 (b) and γ-Fe_2O_3 (c) nanoparticles colloidal solution per mL of MEM solution under AC magnetic-field induction condition. From these images it is seen that the cell morphological structure has almost no

change after treatment of the control dish. Fig. 8-10 (b) and (c) show the micrographic cell images of nanoparticles-treated HeLa cells after 24 h incubation where some aggregated particles are seen. It is clearly noticed in Fig. 8-9 that increase in the nanoparticles dose rate decreased the survival rate of cancer cells.

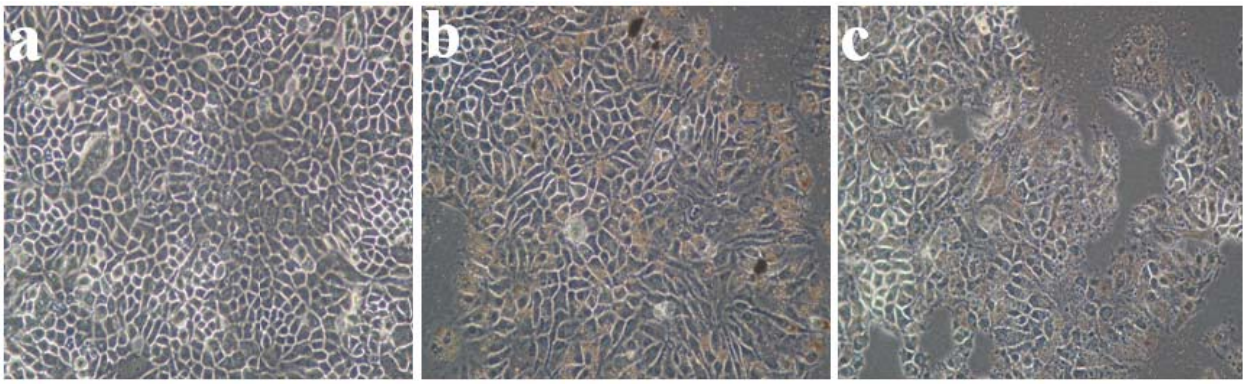

Fig. 8-10: Microscopic images of (a) control (without nanoparticles), 1.0 mL of (b) Fe_3O_4 and (c) γ-Fe_2O_3 suspension with HeLa (cancer) cells using a dose of 150 μg/mL and exposure time of 10 min under AC magnetic-field induction (Magnification: 200).

The dye exclusion test was used to determine the number of viable cells present in a cell suspension. It is based on the principle that live cells possess intact cell membranes that exclude certain dyes, such as trypan blue, eosin or propidium, whereas dead cells do not. In this test, a cell suspension was simply mixed with trypan blue and then visually examined to determine whether cells take up (dead cells) or exclude dye (live cells). Based on the protocol presented here, a viable cell showed a clear cytoplasm whereas a nonviable (dead) cell showed a blue cytoplasm (Fig. 8-11).

Fig. 8-11 showed trypan-blue stained microscopic images of HeLa cells in (a) control (without nanoparticles) and also suspension containing neck-structured (b) Fe_3O_4 and (c) γ-Fe_2O_3 nanoparticles under AC magnetic-field induction condition. It was obviously noticed from Fig.

7-11 (a) that no cells was stained (100% live cells) but a large number of dead cells (stained) were found in Fig. 7-11 (b) using neck-structured Fe_3O_4. Finally, when the cancer cells were subjected to treat under AC magnetic-field induction condition, approximately 95% cancer cells were efficiently destroyed by using neck-structured γ-Fe_2O_3 nanoparticles, indicating almost 100% stained cells (Fig.8-11 (c)).

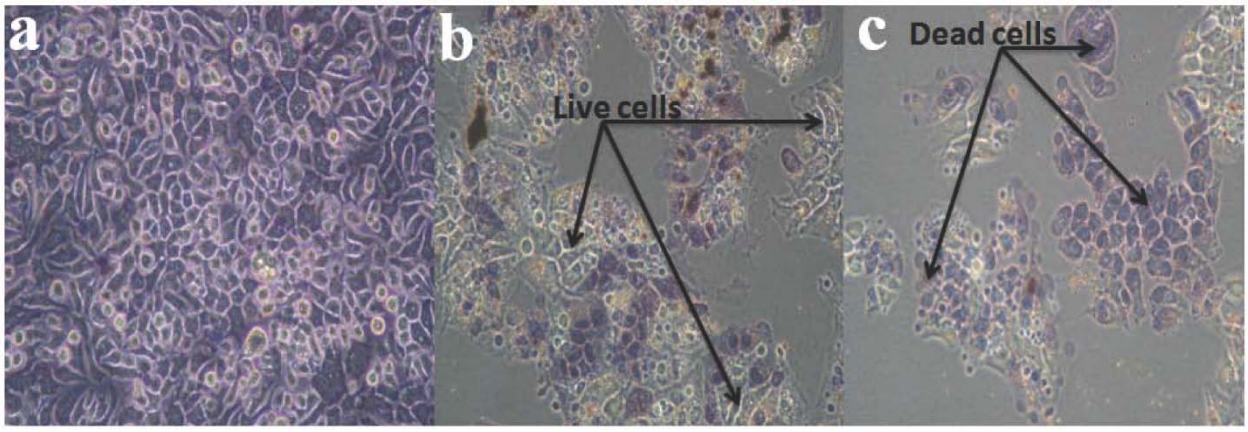

Fig. 8-11: Microscopic images of (a) control (without nanoparticles), suspension containing neck-structured Fe_3O_4 and γ-Fe_2O_3 nanoparticles under AC magnetic-field induction (Magnification: 200). Dead cells stained with trypan blue show blue color.

It is noteworthy that due to some excellent advantages, ethylene glycol was used as a solvent instead of water in this experiment. The major use of ethylene glycol is as a medium for convective heat transfer, for example, in automobiles and liquid cooled computers. Ethylene glycol disrupts hydrogen bonding when dissolved in water. However, the boiling point for aqueous ethylene glycol increases monotonically with increasing ethylene glycol percentage. Both the literature [22, 23] and experimental evidence have led us to believe that ethylene glycol plays an important role in ferrite formation. Ethylene glycol is a strong reducing agent with a relatively high boiling point [23] and has been widely used in the polyol process to provide monodispersed fine metal or metal oxide nanoparticles. However, magnetic spinel ferrite

particles have a strong tendency to agglomerate during their formation in the liquid-phase process. To obtain monodispersed Fe_3O_4 nanoparticles, we designed a modified synthetic route in which three added features were found to be critical. First, NaAc was added for electrostatic stabilization to prevent particle agglomeration. Such benefits of NaAc were found in similar syntheses with Ru, Pt and Rh particles [24, 25]. In our system, NaAc was even more important, as its addition seems to assist in the ethylene glycol-mediated reduction of $FeCl_2$ to Fe_3O_4 [15]. Control experiments showed that Fe^{2+} could not be reduced by ethylene glycol alone under the same reaction conditions. Second, polyethylene glycol was added as a surfactant and as an additional preventative measure against particle agglomeration. The third feature is the increased reaction temperature of 190 °C, which is necessary for the production of Fe_3O_4.

8.5 Conclusions

Nanosized neck-structured Fe_3O_4 and γ-Fe_2O_3 magnetic materials have been prepared successfully from iron chloride tetrahydrate solely by the hydrothermal method. The FE-SEM and TEM studies revealed a unique necked structure with a particle size in the range of 50–60 nm. The synthesized nanomaterials also showed the colloidal stability when dispersed in doubly distilled water and excellent magnetization values. Furthermore, the as-prepared magnetic nanoparticles suspensions showed significant temperature increments under an AC magnetic-field induction condition at room temperature. Finally, the neck-structured Fe_3O_4 and γ-Fe_2O_3 nanoparticles showed supremacy in cancer (HeLa) cell killing over spherical-shaped ones under the same condition including the same dose.

References

[1] P. Alivisatos, et al., *Adv. Mater*. **10** (1998), p. 1297.

[2] S. H. Tolbert and A. P. Alivisatos, *Annu. Rev. Phys. Chem*. **46** (1995), p. 595.

[3] F. Caruso, M. Spasova, A. Susha, M. Giersig, R. A. Caruso, Chem. Mater. 13 (2001) 109.

[4] T. Hyeon, S. S. Lee, J. Park, Y. Chung, and H. B. Na, *J. Am. Chem. Soc.* **123** (2001), p. 12798.

[5] Y. Xiong, X. Xie, S. Chen and Z. Li, *Chem. Eur. J*. **9** (2003), p. 4991.

[6] K. Woo, H. J. Lee, J. Ahn and Y. S. Park, *Adv. Mater.* **15** (2003), p. 1761.

[7] Y. Wang, X. Teng, J. Wang and H. Yang, *Nano. Lett*. **3** (2003), p. 789.

[8] A.C.C Yu, M. Mizuno, Y. Sasaki, H. Kondo, K. Hiraga, *Appl. Phys. Lett.* **81** (2002), p. 3768.

[9] R .M. Cornell and U. Schwertmann, The Iron Oxides: Structure, Properties, Reactions, Occurrences and Uses, 2nd Edition. (Wiley-VCH, Weinheim, 2003).

[10] P. Tartaj, M. D. Morales, S. Veintemillas-Verdaguer, T. Gonzalez-Carreno and C.J. Serna, *J. Phys. D: Appl. Phys.* **36** (2003), p. R182.

[11] J. S. Kim, T. J. Yoon, B. G. Kim, S. J. Park, H. W. Kim, K. H. Lee, S. B. Park, J. K. Lee and M. H. Cho, *Toxicol. Sci*. **89** (2006), p. 338.

[12] P. Tartaj, M. P. Morales, T. Gonzalez-Carreno, S. Veintemillas-Verdaguer and C. J. Serna, *J. Mag. Mag. Mater*. **290** (2005), p. 28.

[13] G. Bate, In Magnetic Oxides Part 2; D. J. Craik, Ed.; John Wiley & Sons (New York, 1975), p 705.

[14] M. Chirita and I. Grozescu, *Chem. Bull. "POLITEHNICA" Univ. (Timisoara)*, **54** (2009), p. 1.

[15] H. Deng, X. Li, Q. Peng, X. Wang, J. Chen and Y. Li, *Angew. Chem.* **117** (2005), p. 2842.

[16] An-Hui Lu, E. L. Salabas and S. Ferdi, *Angew. Chem. Int. Ed*. **46** (2007), p. 1222.

[17] M. Gonzales-Weimuller, M. Zeisberger and K. M. Krishnan, *J. Magn. Magn. Mater*. **321** (2009), p. 1947.

[18] I. Nedkov, T. Merodiiska, L. Slavov, R.E. Vandenberghe, Y. Kusano and J. Takada, *J. Magn. Magn. Mater*. **300** (2006), p. 358.

[19] M. S. Islam, Y. Kusumoto, M. Abdulla-Al-Mamun and Y. Horie, *Chem. Lett.* **40** (2011), p. 773.

[20] L. Sophie, F. Delphine, P. Marc, R. Alain, R. Caroline, V. E. Luce and N. M. Robert, *Chem. Rev.* **108 (**2008), p. 2064.

[21] J.P. Fortin, F. Gazeau and C. Wilhelm, *Eur. Biophys J*. **37** (2008), p. 223.

[22] a) Y. Sun and Y. Xia, *Science* **298** (2002), p. 2176; b) Y. Lu, Y. Yin, B. T. Mayers and Y. Xia, *Nano Lett.* **2** (2002), p. 183; c) Y. L.Wang and Y. N. Xia, *Nano Lett*. **4** (2004), p. 2047.

[23] Q. Peng, Y. J. Dong and Y. D. Li, *Angew. Chem.* **115** (2003), p. 3135.

[24] a) G. Viau, P. Toneguzzo, A. Pierrard, O. Acher, F. Fiévet- Vincent and F. Fiévet, *Scr. Mater*. **44** (2001), p. 2263; b) G. Viau, R. Brayner, L. Poul, N. Chakroune, E. Lacaze, F. Fiévet-Vincent and F. Fiévet, *Chem. Mater*. **15** (2003), p. 486.

[25] K. R. Brown, D. G. Walter and M. J. Natan, *Chem. Mater.* **12** (2000), p. 306.

CHAPTER 9

INFLUENCES OF PRECURSOR TYPE, CONCENTRATION AND INCUBATION TIME ON THE MORPHOLOGY OF MAGNETIC NANOPARTICLES SYNTHESIZED BY HYDROTHERMAL DECOMPOSITION

Abstract

We synthesized magnetite (Fe_3O_4) nanoparticles using precursor $FeCl_3 \cdot 6H_2O$ or $FeCl_2 \cdot 4H_2O$ with 5 or 8 mmol concentration and 3 or 5 h incubation time with the constant pH (7.5) by simple hydrothermal decomposition and then transferred them into maghemite (γ-Fe_2O_3) and hematite (α-Fe_2O_3). Precisely, the objectives of the study were to evaluate the influences of the precursor type, its concentration and incubation time on the morphology of the as-synthesized magnetic nanoparticles. Synthesized nanoparticles were characterized by means of XRD, FE-SEM, TEM, UV-Vis absorption (reflectance) spectra and magnetic hysteresis loops by superconducting quantum interference device (SQUID), without any size sorting. In case of iron hexahydrate ($FeCl_3 \cdot 6H_2O$), 5 mmol precursor concentration along with 5 h incubation period results in homogeneous spherical-shaped particles. On the other hand, the same precursor but 8 mmol concentration and 3 h incubation period produced heterogeneous spherical-shaped particles with bigger particle sizes. In case of iron tetrahydrate ($FeCl_2 \cdot 4H_2O$) almost neck-structured heterogeneous particles were obtained by using both types of precursor concentrations and incubation period (5 or 8 mmol and 5 or 3 h). Finally, our study revealed that in both type of precursors, increased precursor concentration and decreased incubation period result in increased particles size. This work is under review in Applied Sciences.

9.1 Introduction

Materials with reduced dimensions, for instance, nanotubes, nanowires, nanorods, and nanoparticles, etc., are of substantially different properties from their bulk state counterparts [1, 2] and have attracted great interest in the past decade. The synthesis of nanostructured magnetic materials has become a particularly important area of research and is attracting a growing interest because of the potential applications such materials have in ferrofluids, advanced magnetic materials, catalysts, colored pigments, high-density magnetic recording media, and medical diagnostics [3-8]. Magnetic iron oxide nanoparticles and their dispersions in various media have long been of scientific and technological interest. Iron oxides exist in many forms in nature, with magnetite (Fe_3O_4), maghemite (γ-Fe_2O_3), and hematite (α-Fe_2O_3) being probably most common [9]. Magnetite (Fe_3O_4) has recently been considered an ideal candidate for biological applications, both as a tag for sensing and imaging and as an active agent for antitumor therapy [10–12] and it (Fe_3O_4) is a common magnetic iron oxide that has a cubic inverse spinel structure with oxygen forming a fcc closed packing and Fe cations occupying interstitial tetrahedral sites and octahedral sites [13]. The electrons can hop between Fe^{2+} and Fe^{3+} ions in the octahedral sites at room temperature, rendering magnetite an important class of half-metallic materials [14]. Maghemite nanoparticle, bearing a high positive charge density can easily be dispersed in acidic water, forming cationic sols practically free from aggregation [15–17]. Magnetite and hematite have been used as catalysts for a number of industrially important reactions [1, 6, 8, 18, 19] including the synthesis of NH_3 (the Haber process), the high temperature water gas shift reaction, and the desulfurization of natural gas. They (magnetite and hematite) are semiconductors and can catalyze oxidation/reduction reactions [20, 21, 22]. Hematite has also been used as a support material for gold in catalysts for the oxidation of carbon monoxide at low temperature [23, 24].

Numerous chemical methods can be used to synthesize magnetic nanoparticles for medical imaging applications: microemulsions, sol-gel syntheses, sonochemical reactions, hydrothermal reactions, hydrolysis and thermolysis of precursors, flow injection syntheses, and electrospray syntheses. Under hydrothermal conditions a broad range of nanostructured materials can be formed. Li *et al*. reported a generalized hydrothermal method for synthesizing a variety of different nanocrystals by a liquid–solid–solution reaction. The system consists of metal linoleate (solid), an ethanol– linoleic acid liquid phase, and a water–ethanol solution at different reaction temperatures under hydrothermal conditions [25]. To control particle size, parameters such as temperature, solvent concentration and terminal ligand are important. There have been a number of chemical methods reported in the literature concerning synthesis of monodisperse iron oxide nanocrystallites with progressive increase in size. Since these last decades, there has been a sustained interest for the synthesis of magnetic nanoparticles of controlled size. It has been shown that the magnetic properties of nanoparticles are strongly related to their size [26, 27]. In addition, the therapeutic potential of nanoparticles with a controlled and adapted size has been demonstrated in cases, where hyperthermia has been recognized as a promising therapy to treat tumorous areas [28, 29].

However, in this report, we synthesized magnetite (Fe_3O_4) nanoparticles using $FeCl_3 \bullet 6H_2O$ or $FeCl_2 \bullet 4H_2O$ as precursor with 5 or 8 mmol concentration and 3 or 5 h incubation time with the constant pH (7.5) by the simple hydrothermal decomposition and then transferred them into maghemite (γ-Fe_2O_3) and hematite (α-Fe_2O_3) described by Sun *et al.* [30]. Precisely, the objective of the study was to evaluate the influences of the precursor type, its concentration rate and incubation time on the morphology of the synthesized magnetic nanoparticles.

9.2 Synthesis and Formation

9.2.1 Materials and methods

Typical synthesis of magnetite (Fe_3O_4) nanoparticles was carried out in a hydrothermal system by modified reduction reactions between $FeCl_3$ or $FeCl_2$ and ethylene glycol and then the magnetite nanoparticles were oxidized into maghemite and hematite at 250 °C for 6 h in the presence of oxygen and at 500 °C for I h in the presence of Ar gas, respectively. In this experiment chemicals used were iron chloride hexahydrate, iron chloride tetrahydrate ($FeCl_3$•$6H_2O$, $FeCl_2$•$4H_2O$, Wako Pure chemical industries Ltd., Japan), ethylene glycol (99.5%, Wako Pure chemical industries Ltd., Japan), polyethylene glycol 4000 (Tokyo Kasei Kogyo Co. Ltd, Japan) and sodium acetate, anhydrous (NaAc, 98%, Nacalai Tesque Ltd., Japan). All chemicals were of analytical grade and used without any further purification.

9.2.2 Synthesis of magnetite (Fe_3O_4) nanoparticles

$FeCl_3$•$6H_2O$ or $FeCl_2$•$4H_2O$ (5 mmol or 8 mmol) was dissolved in ethylene glycol (40 mL) to form a clear solution, followed by the addition of NaAc (3.6 g) and polyethylene glycol (1.0 g). The mixture was stirred vigorously for 45 min until getting a clear solution and then sealed in a teflonlined stainless-steel autoclave (50 mL capacity). The autoclave was heated to and maintained at 200 °C for 5 h or 3 h and allowed to cool to room temperature. After cooling, decantation was done by a permanent magnet to get the sedimented black products. The black products were washed several times with ethanol and dried at 70 °C for 3 h. Finally, we obtained Fe_3O_4 nanoparticles.

9.2.3 Phase transfer of Fe_3O_4 to γ-Fe_2O_3 and α-Fe_2O_3

It is well known that Fe_3O_4 can be oxidized to γ-Fe_2O_3, which can be further transformed into

α-Fe_2O_3 at higher temperature [32]. However, magnetite (Fe_3O_4) is not very stable and is sensitive to oxidation. Magnetite is transformed into maghemite (γ-Fe_2O_3) in the presence of oxygen [33].

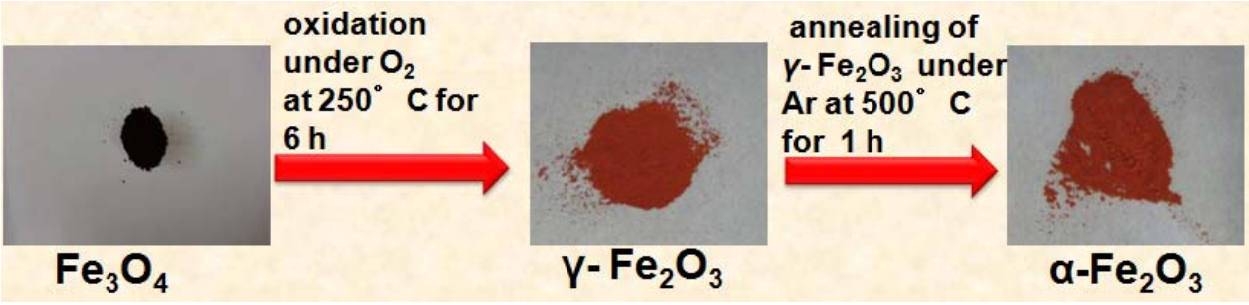

Fig. 9-1: Photograph of Phase transfer of Fe_3O_4 to γ-Fe_2O_3 and α-Fe_2O_3

Fig. 9-1 shows the phase transfer of as-synthesized black Fe_3O_4 nanoparticles assembly to red-brown γ-Fe_2O_3 and dark red-brown α-Fe_2O_3. After oxidation of Fe_3O_4 at 250 °C for 6 h, the black assembly is transformed into a red-brown one (γ-Fe_2O_3) and the dark red-brown materials, α-Fe_2O_3 was obtained after 500 °C annealing of γ-Fe_2O_3 under Ar gas for 1 h.

9.3 Structure Characterization

The general structure characterization, including size, size distribution and crystal structure of the as-synthesized magnetic nanoparticles (MNPs) was performed for the all samples without any size sorting. To further confirm the crystal structure and overall phase purity, the nanoparticles with different sizes were examined using a PANalytical Advance X-ray diffractometer (XRD) with CuKα radiation and a Ni filter. The surface morphology and nanoparticles size were determined using a field emission scanning electron microscope (FE-SEM, model Hitachi S-4100H). Absorption spectra were recorded on UV-Vis absorption (reflectance) spectra (Shimadzu Corporation, UV-2450, Japan). The samples were standardized with barium sulphate coated glass substrate and its spectrum was used as the baseline. The

spectra of all samples were measured in a wavelength range between 240 and 800 nm. Further, the shape of the nanoparticles were analyzed by transmission electron microscopy (TEM) using a JEOL JEM-3010 VII TEM operating at 300 kV. Magnetic hysteresis loops were measured by a superconducting quantum interference device (SQUID, Quantum Design MPMS-5).

9.4 Results and Discussion

There are two main routes for the formation of ferrites via hydrothermal conditions: hydrolysis and oxidation or neutralization of mixed metal hydroxides. These two reactions are very similar, except that ferrous salts are used in the first method [34].

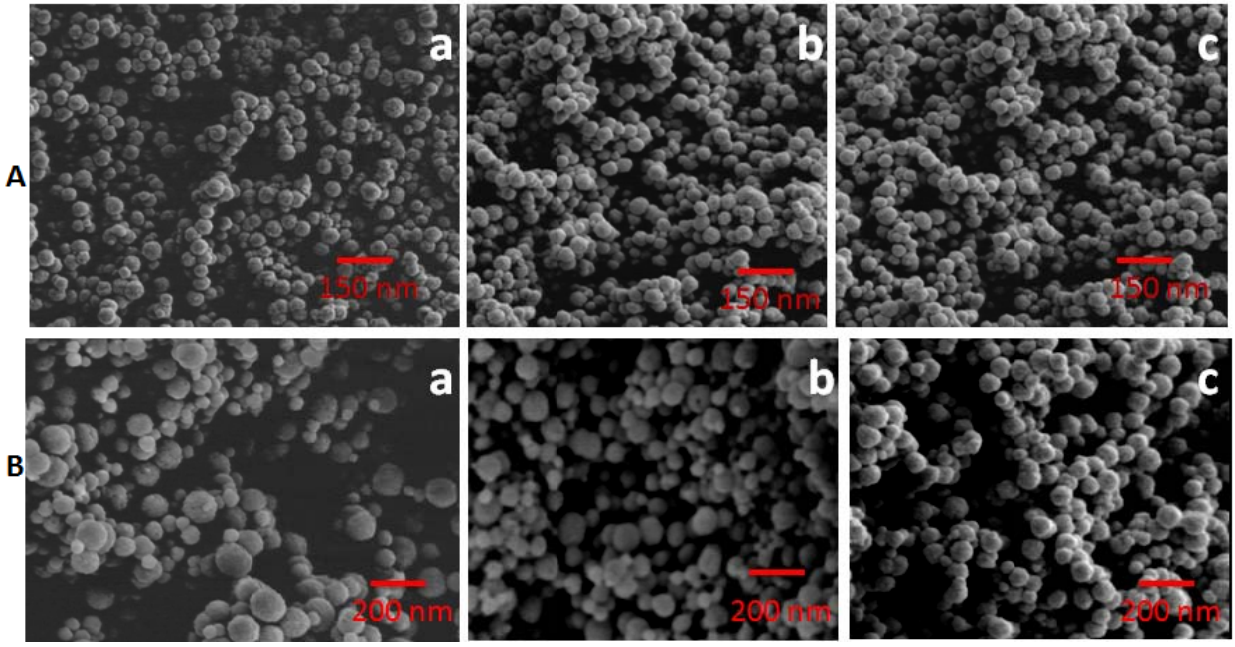

Fig.9-2: SEM images of MNPs. Magnetite, maghemite and hematite are represented by (a), (b) and (c) for plate **A** and **B** where $FeCl_3 \cdot 6H_2O$ was the precursor with concentration and incubation time, 5 mmol and 5 h and 8 mmol and 3 h, respectively.

In this process, the reaction conditions, such as solvent, temperature and time, usually has important effects on the products [35]. Indeed, it was observed that the particle size of Fe_3O_4

powders increased with a prolonged reaction time and that higher water content resulted in the precipitation of larger Fe_3O_4 particles. In the hydrothermal process, the particle size in crystallization is controlled mainly through the rate processes of nucleation and grain growth, which compete for the species. Their rates depend upon the reaction temperature, with other conditions held constant [35].

9.4.1 Shape analysis by FE-SEM and TEM

The morphological structure and nanoparticles size of as-prepared nanomaterials were estimated in accordance to the SEM (Fig. 2 and 3). Fig.2 and 3 (a), (b) and (c) represent the FE-SEM micrographs of Fe_3O_4, γ-Fe_2O_3 and α-Fe_2O_3, respectively for both plate (A) and (B). Fig.2 plate **A** stands for MNPs synthesized using $FeCl_3 \bullet 6H_2O$ as a precursor with concentration 5 mmol and incubation time 5 h. From the FE-SEM observation of plate (A) it was clear that ca. 40-50 nm homogeneous spherical-shaped magnetic nanoparticles were obtained for all three kinds of iron oxides. On the other hand, ca. 80 nm heterogeneous spherical-shaped magnetic nanoparticles were obtained for all three kinds of iron oxides using $FeCl_3 \bullet 6H_2O$ as a precursor with concentration 8 mmol and incubation time 3 h (plate B, Fig.2). Furthermore, ca. 50 nm spherical-shaped heterogeneous, neck-structured homogeneous and neck-structured heterogeneous nanoparticles were obtained for Fe_3O_4, γ-Fe_2O_3 and α-Fe_2O_3, respectively, using $FeCl_2 \bullet 4H_2O$ as a precursor with concentration 5 mmol and incubation time 5 h (Fig. 3, plate A), whereas ca. 65 nm magnetic nanoparticles with similar shape were obtained by using $FeCl_2 \bullet 4H_2O$ as a precursor with concentration and incubation time, 8 mmol and 3 h, respectively (Fig. 3, plate B) (**Table 1**).

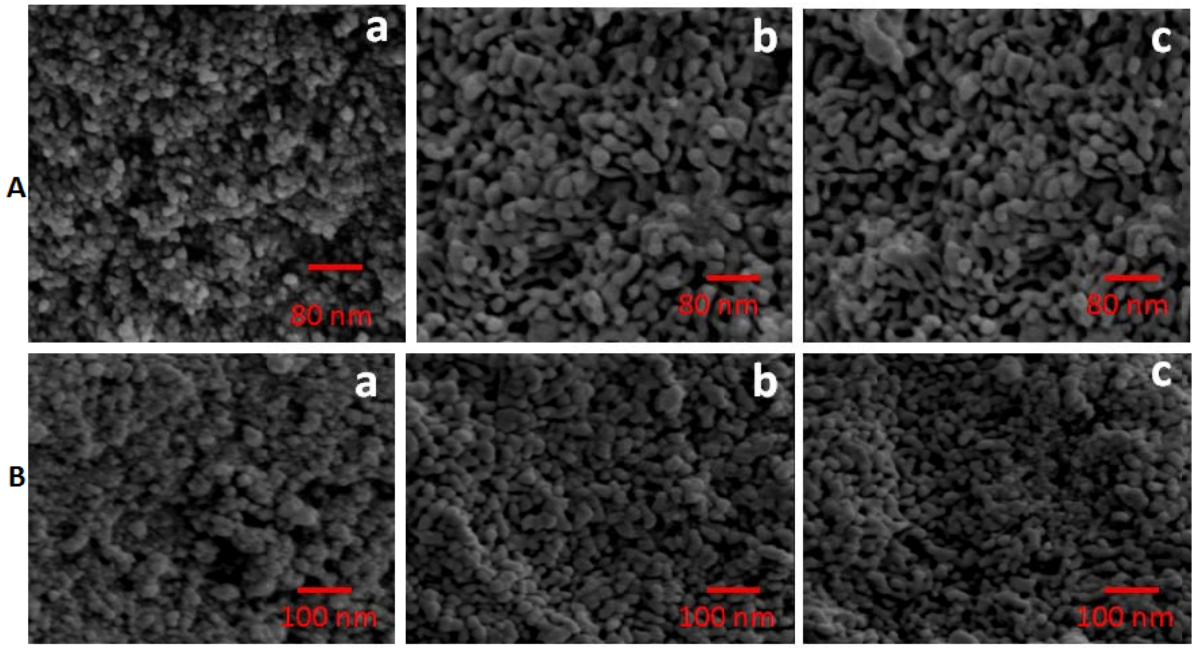

Fig.9-3: SEM images of MNPs. Magnetite, maghemite and hematite are represented by (a), (b) and (c) for plate **A** and **B** where $FeCl_2 \cdot 4H_2O$ was the precursor with concentration and incubation time 5 mmol and 5 h and 8 mmol and 3 h, respectively.

The samples were also characterized using TEM. In Fig. 4 and 5 (a), (b) and (c) were depicted the TEM images of Fe_3O_4, γ-Fe_2O_3 and α-Fe_2O_3, respectively, for both plate (A) and (B) using $FeCl_3 \cdot 6H_2O$ and $FeCl_2 \cdot 4H_2O$ as a precursor (Fig. 4 and 5, respectively). Almost in all cases FE-SEM observation was firmly supported by the TEM analysis with little variation in particle sizes. The TEM (Fig. 4 and 5) analysis revealed that $FeCl_3 \cdot 6H_2O$ facilitates spherical, homogenous and smaller size nanoparticles with 5 mmol precursor concentration along with 5 h incubation period. But increased concentration (8 mmol) of the same precursor along with 3 h incubation period was the cause of the spherical, heterogeneous and comparatively larger size of MNPs (**Table 1**). The utilization of the precursor $FeCl_2 \cdot 4H_2O$ with 5 mmol concentration and 5 h incubation period produced the heterogeneous spherical (Fe_3O_4), homogeneous neck-structured (γ-Fe_2O_3) and heterogeneous neck-structured (α-Fe_2O_3) MNPs. When the precursor

concentration was increased to 8 mmol and incubation period was decreased to 3 h, the shape became unchanged but particles size became larger (**Table 1).**

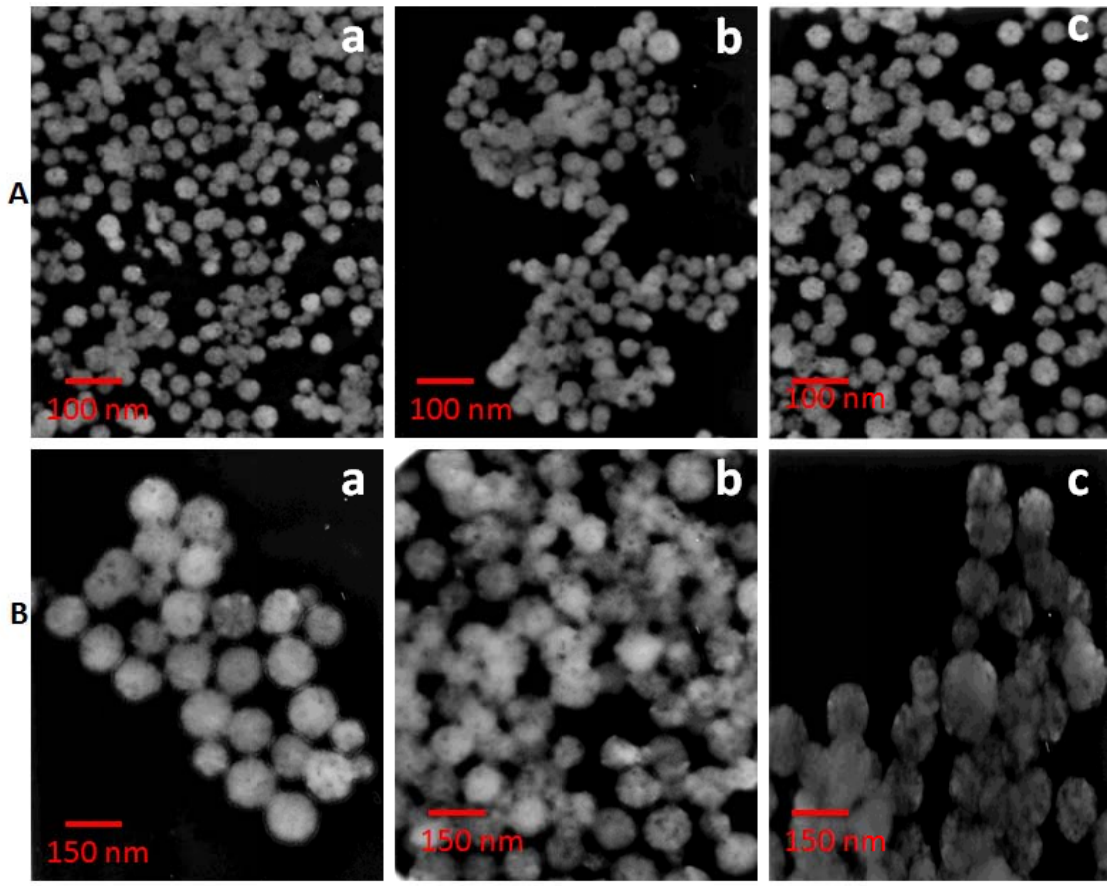

Fig.9-4: TEM images of MNPs. Magnetite, maghemite and hematite are represented by (a), (b) and (c) for plate **A** and **B** where $FeCl_3 \cdot 6H_2O$ was the precursor with concentration and incubation time, 5 mmol and 5 h and 8 mmol and 3 h, respectively.

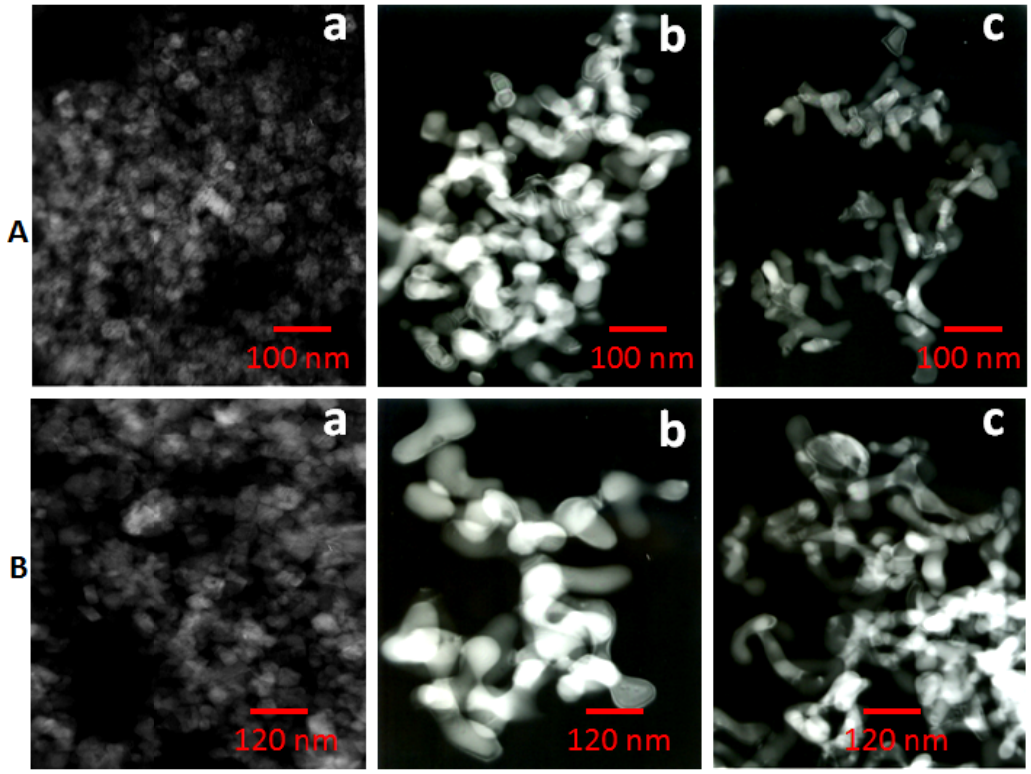

Fig.9-5: TEM images of MNPs. Magnetite, maghemite and hematite are represented by (a), (b) and (c) for plate **A** and **B** where $FeCl_2 \cdot 4H_2O$ was the precursor with concentration and incubation time, 5 mmol and 5 h and 8 mmol and 3 h, respectively.

9.4.2 XRD analysis

The crystal structures of the prepared MNPs were observed by the XRD measurement. Observed XRD patterns of Fe_3O_4, γ-Fe_2O_3 and α-Fe_2O_3 are shown in Fig. 9-6 and 9-7. As shown in Fig. 9-6 and 9-7, all samples were found to be consistent with the expected diffraction patterns of the *fcc* FeO structures by using both of the precursors. In Fig. 9-6 for both plates, no diffraction peaks from other crystalline forms are detected, which demonstrates that these Fe_3O_4, γ-Fe_2O_3 and α-Fe_2O_3 samples have high purity and crystallinity using the precursor $FeCl_3 \cdot 6H_2O$ with 5 mmol concentration and 5 h incubation period (plate A) and 8 mmol concentration and 3 hours incubation period (plate B). Furthermore, in Fig. 9-7 (A) using the precursor $FeCl_2 \cdot 4H_2O$ with 5 mmol concentration and 5 h incubation period produced the Fe_3O_4, γ-Fe_2O_3 and α-Fe_2O_3

MNPs having high purity and crystallinity but when the concentration increased (8 mmol) and incubation period decreased (3 h), both purity and crystallinity decreased (Fig. 9-7 (B)).

Table9-1. Morphological characteristics of magnetic nanoparticles synthesized by hydrothermal decomposition.

Precursor	Concentration	Incubation Time	Particle Type	Particle Size (nm) (SEM)	Particle Size (nm) (TEM)	Shape	Homogeneity
$FeCl_3•6H_2O$	5 mmol	5 h	Fe_3O_4	40-50	30-40	Spherical	Homogeneous
			γ-Fe_2O_3	40-50	30-40	Spherical	Homogeneous
			α–Fe_2O_3	40-50	30-40	Spherical	Homogeneous
$FeCl_3•6H_2O$	8 mmol	3 h	Fe_3O_4	80-90	90-100	Spherical	Heterogeneous
			γ-Fe_2O_3	70-80	75-85	Spherical	Heterogeneous
			α–Fe_2O_3	70-80	80-100	Spherical	Heterogeneous
$FeCl_2•4H_2O$	5 mmol	5 h	Fe_3O_4	35-45	30-40	Spherical	Heterogeneous
			γ-Fe_2O_3	40-50	60-70	Neck-structured	Homogeneous
			α–Fe_2O_3	50-60	70-80	Neck-structured	Heterogeneous
$FeCl_2•4H_2O$	8 mmol	3 h	Fe_3O_4	35-45	40-50	Spherical	Heterogeneous
			γ-Fe_2O_3	60-70	90-100	Neck-structured	Homogeneous
			α–Fe_2O_3	55-65	100-120	Neck-structured	Heterogeneous

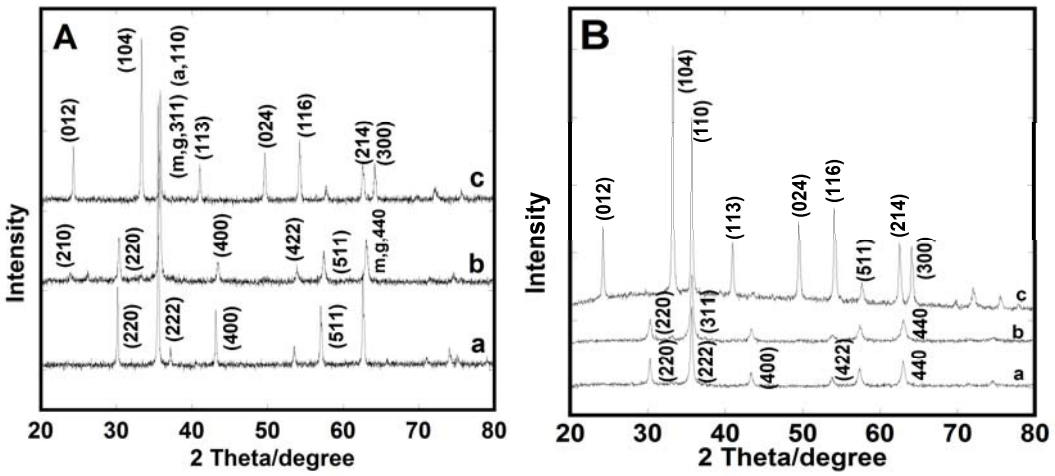

Fig.9-6: XRD patterns of MNPs. Magnetite, maghemite and hematite are represented by (a), (b) and (c) for plate **A** and **B** where $FeCl_3 \cdot 6H_2O$ was the precursor with concentration and incubation time, 5 mmol and 5 h and 8 mmol and 3 h, respectively.

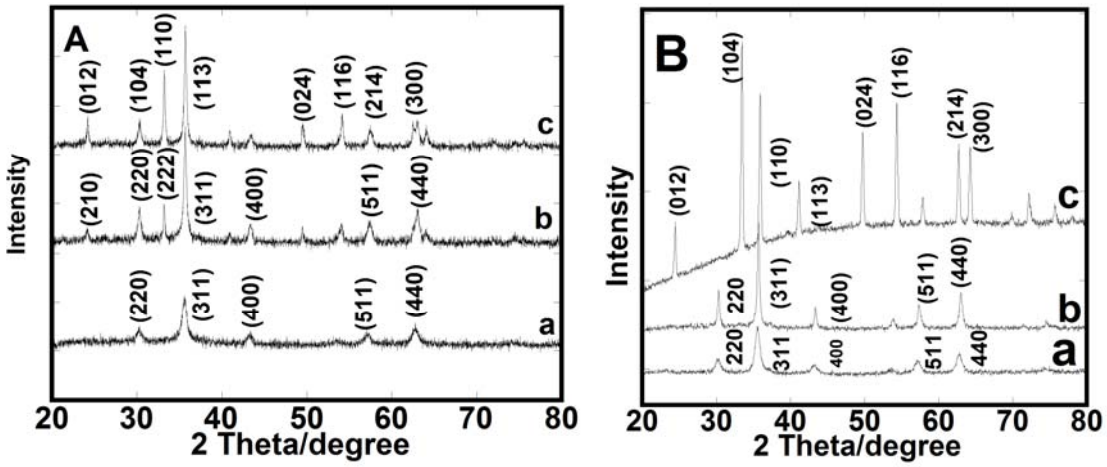

Fig.9-7: XRD patterns of MNPs. Magnetite, maghemite and hematite are represented by (a), (b) and (c) for plate **A** and **B** where $FeCl_2 \cdot 4H_2O$ was the precursor with concentration and incubation time, 5 mmol and 5 h and 8 mmol and 3 h, respectively.

9.4.3 UV–visible absorption spectra

UV–visible absorption spectra of as-prepared magnetic nanoparticles colloidal suspensions using $FeCl_3 \cdot 6H_2O$ or $FeCl_2 \cdot 4H_2O$ (5 mmol or 8 mmol) with 5 h or 3 h incubation period are shown in Fig. 8 and 9. In Fig. 8 it can be seen that the absorption edges of synthesized MNPs

were better in certain wavelength when the precursor concentration was increased with decreased incubation period. Further, all of the synthesized magnetic nanoparticles exhibited strong absorption bands in the visible region. For MNPs prepared using 5 mmol precursor concentration and 5 h incubation period, the absorption edges of the sample have some blue shifts when the calcination temperature was increased to 250 and 500 °C. The band gap energy of Fe_2O_3 is 2.2 eV and can be activated by the light below 563 nm [24]. In Fig. 9 no differential absorption edge was observed whether in different precursor concentrations or different incubation periods.

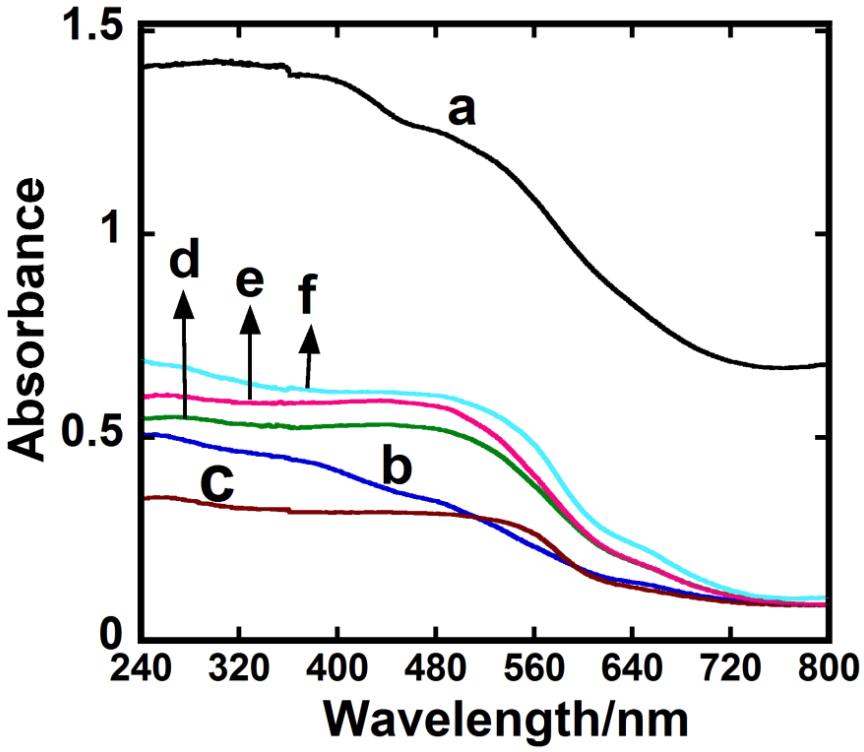

Fig.9-8: UV-Vis absorption (reflectance) spectra of MNPs. Magnetite, maghemite and hematite are represented by (a), (b), (c) and (d), (e), (f) where $FeCl_3 \cdot 6H_2O$ was the precursor with concentration and incubation time, 5 mmol and 5 h and 8 mmol and 3 h, respectively.

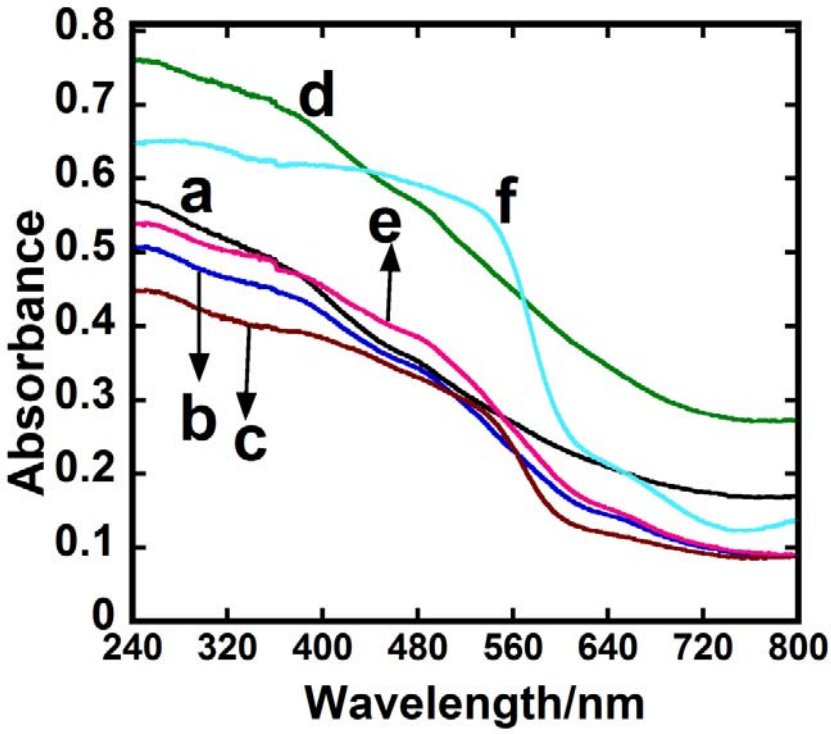

Fig.9-9: UV-Vis absorption (reflectance) spectra of MNPs. Magnetite, maghemite and hematite are represented by (a), (b), (c) and (d), (e), (f) where $FeCl_2 \cdot 4H_2O$ was the precursor with concentration and incubation time, 5 mmol and 5 h and 8 mmol and 3 h, respectively.

9.4.4 Magnetic hysteresis loops of as-prepared nanomaterials

A great deal of information can be learned about the magnetic properties of a material by studying its hysteresis loop. A hysteresis loop shows the relationship between the induced magnetic flux density and the magnetizing force**.** Fig. 10 shows the magnetic hysteresis loops of as-synthesized MNPs using $FeCl_3 \cdot 6H_2O$ or $FeCl_2 \cdot 4H_2O$ as a precursor with 5 mmol concentration and 5 h incubation period as the mentioned concentration and incubation period showed better performance according to FE-SEM and TEM analyses. The comparative hysteresis curves obtained at room temperature (Fig. 10) show that the saturation of magnetization (M_S) value of Fe_3O_4 and γ-Fe_2O_3 was 69.1 and 46.5 emu/g, respectively (plate A), using $FeCl_3 \cdot 6H_2O$ whereas these values were 60.6 and 59.2 emu/g for Fe_3O_4 and γ-Fe_2O_3,

respectively (plate B), using $FeCl_2 \cdot 4H_2O$ with the same concentration and incubation time with very negligible coercive values. Furthermore, the saturation of magnetization (M_S) value of α-Fe_2O_3 samples using $FeCl_3 \cdot 6H_2O$ and $FeCl_2 \cdot 4H_2O$ as a precursor with 5 mmol concentration and 5 h incubation period was 0.80 and 0.50 emu/g, respectively (plate C). This result revealed that the saturation values of magnetization (M_S) of Fe_3O_4 and α-Fe_2O_3 MNPs prepared by using $FeCl_3 \cdot 6H_2O$ were always higher than that prepared by using $FeCl_2 \cdot 4H_2O$ through the hydrothermal method.

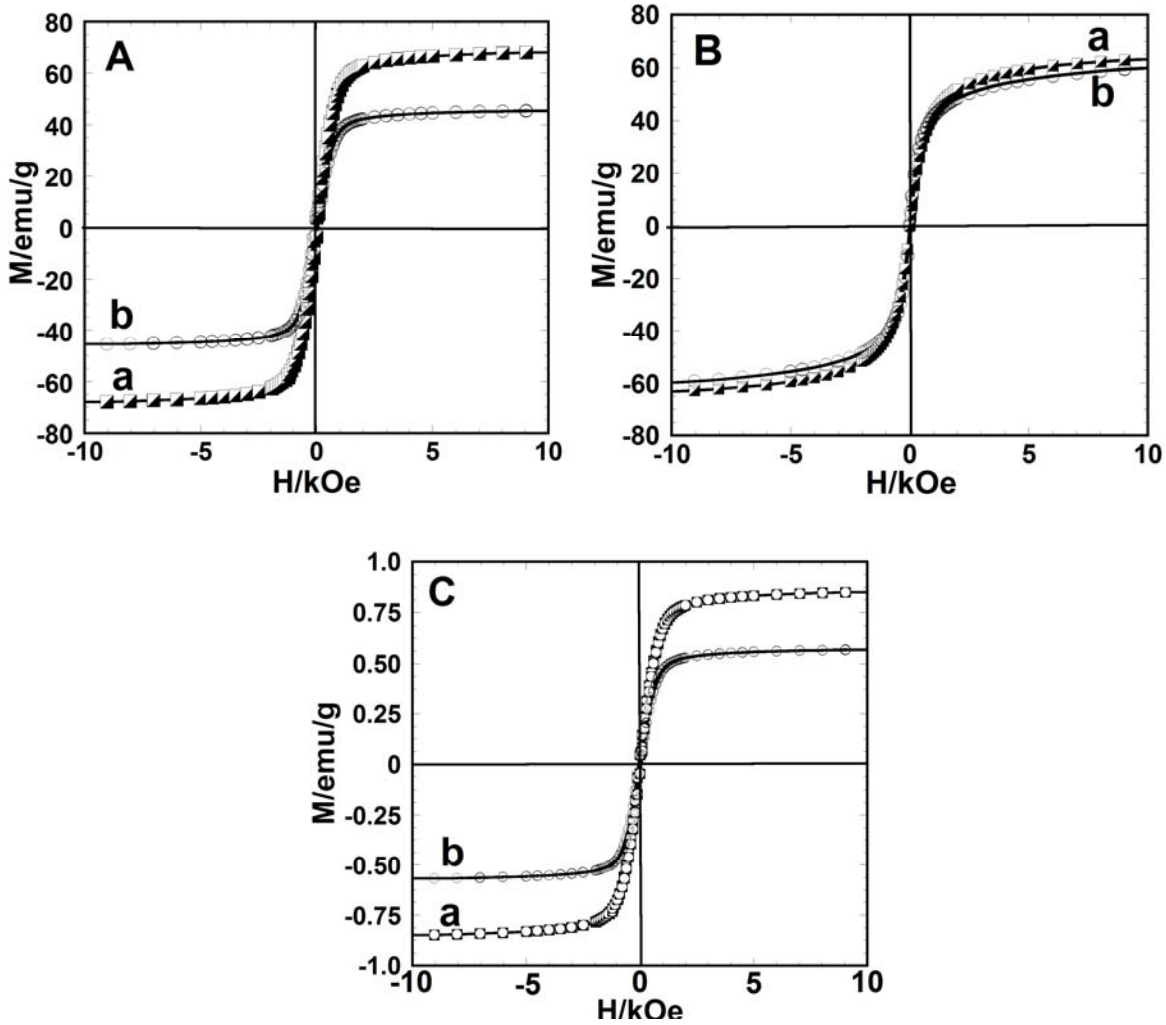

Fig.9-10: Magnetic hysteresis loops of MNPs. Plate **A** and **B** indicate the M_S value for Fe_3O_4 (a) and γ-Fe_2O_3 (b) using $FeCl_3 \cdot 6H_2O$ and $FeCl_2 \cdot 4H_2O$, respectively, as the precursor with 5 mmol concentration and 5 h incubation time. Plate **C** indicates the M_S value for α-Fe_2O_3 using $FeCl_3 \cdot 6H_2O$ (a) and $FeCl_2 \cdot 4H_2O$ (b)**,** respectively, with same concentration and incubation period.

As according to the FE-SEM, TEM and XRD analyses, using 5 mmol concentration and 5 h incubation time for both precursor $FeCl_3 \cdot 6H_2O$ and $FeCl_2 \cdot 4H_2O$, produced better particle shape and sizes, we were only interested to analyze the hysteresis loops of the nanomaterials prepared by only above mentioned conditions.

Usually, the average size of the nanoparticles increased when incubation time increased. This behavior is likely to favor the Oswald ripening process [35]. In case of iron hexahydrate ($FeCl_3 \cdot 6H_2O$) 5 mmol precursor concentration along with 5 h incubation period results in homogeneous spherical-shaped particles. On the other hand, the same precursor but 8 mmol concentration and 3 h incubation period produced bigger particle size with heterogeneous spherical-shaped particles. Further, in case of iron tetrahydrate ($FeCl_2 \cdot 4H_2O$) almost neck-structured heterogeneous particles were obtained in both type of precursor concentrations and incubation periods. Finally, our study revealed that in both type of precursors, increased precursor concentration and decreased incubation period results in increased particles size. It was reported from the previous study [36, 37] that higher incubation period results in increased particle size but in our study shorter incubation period result in increased particle size. This is maybe due to precursor's higher concentration dominant over incubation period and further study is needed to clarify it.

9.5 Conclusion

In summary, we synthesized three popular (magnetite, maghemite and hematite) type of magnetic nanoparticles by the simple hydrothermal method with different precursor concentration and incubation time. From the overall observations, we may conclude that all types of parameter have significant influence on the shape, size and morphology of the synthesized

magnetic nanoparticles. Finally, our study revealed that in both type of precursors, increased concentration and decreased incubation period results in increased particles size.

References

[1] A.P. Alivisatos, et al., *Adv. Mater.* 1998, **10**, 1297.

[2] S.H. Tolbert, A.P. Alivisatos, Annu. *Rev. Phys. Chem*. 1995, **46**, 595.

[3] F. Caruso, M. Spasova, A. Susha, M. Giersig, R. A. Caruso, *Chem. Mater.* 2001, **13**, 109.

[4] a) T. Hyeon, *Chem. Commun*. 2003, **8**, 927; b) T. Hyeon, Y. Chung, J. Park, S. S. Lee, Y. W. Kim, B. H. Park, *J. Phys. Chem. B* 2002, **106**, 6831; c) T. Hyeon, S. S. Lee, J. Park, Y. Chung, H. B. Na, *J. Am. Chem. Soc*. 2001, **123**, 12 798.

[5] Y. Xiong, X. Xie, S. Chen, Z. Li, *Chem. Eur. J.* 2003, **9**, 4991.

[6] K.Woo, H. J. Lee, J. Ahn, Y. S. Park, *Adv. Mater.* 2003, **15**, 1761.

[7] a) X. Teng, H. Yang, *J. Mater. Chem.* 2004, **14**, 774; b) Y. Wang, J. Wong, X. Teng, X. Lin, H. Yang, *Nano. Lett.* 2003, **3**, 1554; c) Y. Wang, X. Teng, J. Wang, H. Yang, *Nano. Lett.* 2003, **3**, 789.

[8] A. Yu, M. Mizuno, Y. Sasaki, H. Kondo, *Appl. Phys. Lett.* 2002, **81**, 3768.

[9] R.M. Cornell, U. Schwertmann, The Iron Oxides: Structure, Properties, Reactions, Occurrences and Uses, second ed. Wiley-VCH, Weinheim, 2003.

[10] a) J. M. Perez, T.O`Loughlin, F. J. Simeone, R. Weissleder, L. Josephson, *J. Am. Chem. Soc.* 2002, **124**, 2856; b) J. M. Perez, F. J. Simeone, A. Tsourkas, L. Josephson, R. Weissleder, *Nano Letter.* 2004, **4**, 119; c) J. M. Perez, L. Josephson, T.O_Loughlin, D. Hogemann, R. Weissleder, *Nat. Biotechnol.* 2002, **20**, 816.

[11] A. Y. Louie, M. M. Huber, E. T. Ahrens, U. Rothbacher, R. Moats, R. E. Jacobs, S. E. Fraser, T. J. Meade, *Nat. Biotechnol.* 2000, **18**, 321.

[12] A. Jordan, P. Wust, R. Scholz, et al., in: U. Häfeli, W. Schütt, J. Teller, M. Zborowski (Eds.), Scientific and Clinical Applications of Magnetic Carriers, Plenum Press, NewYork, 1997.

[13] Cornell, R. M.; Schwertmann, U. *The Iron Oxides: Structure, Properties,Reactions, Occurrence and Uses*; VCH: New York, 1996, pp28-29.

[14] (a) E.J.W. Verwey, *Nature* 1939, **144**, 327. (b) J.M.D. Coey, A.E. Berkowitz, L.I. Balcells, F.F. Putris, F.T. Parker, *Appl. Phys. Lett.* 1998, **72**, 734. (c) S. Soeya, J. Hayakawa, H. Takahashi, K. Ito, C. Yamamoto, A. Kida, H. Asano, M. Matsui, *Appl. Phys. Lett*. 2002, **80**, 823.

[15] J.P. Jolivet, R. Massart, J.M. Fruchart, *Nouv. J. Chim.* 1983, **7**, 325.

[16] P. Prené, et al., *IEEE Trans. Magn.* 1993, **29**, 2658.

[17] J.P. Jolivet, C. Chanéac, P. Prené, L. Vayssières, E. Tronc, J. *Phys. IV France* 1997, **7 C**, 1–573.

[18] F. Shi, M.K. Tse, M.M. Pohl, A. Bruckner, S.M. Zhang, M. Beller, *Angew. Chem., Int. Ed.* 2007, **46 (46)**, 8866.

[19] S. Al-Sayari, A.F. Carley, S.H. Taylor, G.J. Hutchings, *Top. Catal.* 2007, **44 (1-2)**, 123.

[20] F.M. Bautista, J.M. Campelo, D. Luna, J.M. Marinas, R.A. Quiros, A.A. Romero, *Appl. Catal., B* 2007, **70 (1-4)**, 611.

[21] Z. Zhong, J. Ho, J. Teo, S. Shen, A. Gedanken, *Chem. Mater.* 2007, **19 (19)**, 4776.

[22] M.L. Peterson, J.G.E. Brown, G.A. Parks, C.L. Stein, *Geochim. Cosmochim. Acta* 1997, **61 (16)**, 3399.

[23] Z. Zhong, J. Lin, S.P. Teh, J. Teo, F.M. Dautzenberg, *Adv. Funct. Mater.* 2007, **17 (8)**, 1402.

[24] G.J. Hutchings, M.S. Hall, A.F. Carley, P. Landon, B.E. Solsona, C.J. Kiely, A. Herzing, M. Makkee, J.A. Moulijn, A. Overweg, J.C. Fierro-Gonzalez, J. Guzman, B.C. Gates, *J. Catal.* 2006, **242 (1)**, 71.

[25] X. Wang, J. Zhuang, Q. Peng, Y Li, *Nature* 2005, **437**, 121.

[26] S. Mornet, S. Vasseur, F. Grasset, E. Duguet, *J. Mater. Chem.* 2004, **14**, 2161.

[27] A.K. Gupta, M. Gupta, *Biomaterials* 2005, **26**, 3995.

[28] F. Bertorelle, C. Wilhelm, J. Roger, F. Gazeau, C. Me´nager, V. Cabuil, *Langmuir* 2006, **22**, 5385.

[29] L.A. Perrin-Cocon, P.N. Marche, C.L. Villiers, *Biochem J.*, 1999, **338**, 123.

[30] S. Sun, H. Zeng, D.B. Robinson, S. Raoux, P.M. Rice, S.X. Wang, G. Li, *J. Am. Chem. Soc*., 2004, **126**, 273.

[31] G. Bate, In *Magnetic Oxides Part 2*; Craik, D. J., Ed.; John Wiley & Sons: New York, 1975, 705-707.

[32] S. Laurent, D. Forge, M. Port, A. Roch, C. Robic, L.V. Elst, R.N. Muller, *Chem. Revi.*, 2008, **108(6)**, 2067.

[33] M.A. Willard, L.K. Kurihara, E.E. Carpenter, S. Calvin, V.G. Harris, *Encyclopedia of Nanoscience and Nanotechnology*; Nalwa, H. S., Ed.; American Scientific Publishers: Valencia, CA, 2004, **1**, 815.

[34] D. Chen, R. Xu, *Mater. Res. Bull.* 1998, **33,** 1015.

[35] A. Baldan, *J. Mater. Sci*., 2002, **37**, 2171.

[36] H. Deng, X. Li, Q. Peng, X. Wang, J. Chen, Y. Li, *Angew. Chem.,* 2005, **117**, 2842.

[37] J. Xu, H. Yang, W. Fu, K. Du, Y. Sui, J. Chen, Y. Zeng, M. Li, G. Zou, *J. Magn. Magn. Mater*. 2007,**309**, 307.

CHAPTER 10

A COMPARATIVE STUDY ON HEAT DISSIPATION, MORPHOLOGICAL AND MAGNETIC PROPERTIES OF HYPERTHERMIA SUITABLE NANOPARTICLES PREPARED BY CO-PRECIPITATION AND HYDROTHERMAL METHOD

Abstract

Magnetite (Fe_3O_4) nanoparticles were prepared by co-precipitation and hydrothermal methods and their phase transfer was done successfully to compare their performances in different aspects. Synthesized nanoparticles were characterized for XRD, FE-SEM, TEM, UV-Vis absorption (reflectance) spectra, magnetic hysteresis loops and AC magnetic field induced hyperthermia. The magnetic nanoparticles prepared by the co-precipitation method show superior performances in respect of heat dissipation capability, saturation of magnetization values and particle size when compared to those prepared by the hydrothermal method. This work is under review in Bulletin of Materials Science.

10.1 Introduction

The synthesis of nanostructured magnetic materials has become a particularly important area of research and is attracting a growing interest because of the potential applications such materials have in ferrofluids, advanced magnetic materials, catalysts, colored pigments, high-density magnetic recording media, and medical diagnostics [1–6]. Magnetic iron oxide nanoparticles and their dispersions in various media have long been of scientific and technological interest. Iron oxides exist in many forms in nature, with magnetite (Fe_3O_4), maghemite (γ-Fe_2O_3), and hematite (α-Fe_2O_3) which are probably most common [7]. Magnetite

(Fe_3O_4) has recently been considered an ideal candidate for biological applications, both as a tag for sensing and imaging, and as an activity agent for antitumor therapy [8–10]. Magnetite and maghemite have attracted attention in biomedical applications because of their biocompatibility and low toxicity in the human body [11, 12]. Magnetite and hematite have been used as catalysts for a number of industrially important reactions [13, 14, 15], including the synthesis of NH_3 (the Haber process), the high temperature water gas shift reaction, and the desulfurization of natural gas. The therapeutic potential of nanoparticles with a controlled and adapted size has been demonstrated in cases, where hyperthermia has been recognized as a promising therapy to treat tumorous areas [16, 17].

Superparamagnetic nanoparticles when exposed to an alternating magnetic field can be used to heat tumor cells to 41- 45 °C, where tissue damage for normal tissue is reversible while the tumor cells are irreversibly damaged [18]. Under hydrothermal conditions a broad range of nanostructured materials can be formed; this strategy is based on a general phase transfer and separation mechanism occurring at the interfaces of the liquid, solid, and solution phases present during the synthesis. In the co-precipitation method, size, shape, and composition of the magnetic nanoparticles strongly depend on the type of salts used (e.g. chlorides, sulfates, nitrates), the Fe^{2+}/Fe^{3+} ratio, the reaction temperature, the pH value and ionic strength of the media [19]. While a number of suitable methods have been developed for the synthesis of magnetic nanoparticles (MNPs) of various different compositions, successful application of such magnetic nanoparticles in the areas listed above is highly dependent on the stability of the particles under a range of different conditions. Although hydrothermal and co-precipitation methods are based on the wet chemical synthesis, there are some significant differences in

synthesized MNPs followed by both methods and they are also discussed for comparison in our study to find out their hyperthermia potentiality.

10.2 Experimental

10.2.1 Materials and methods

Typical syntheses of magnetic nanoparticles (MNPs) were carried out in a hydrothermal system by modified reduction reactions between $FeCl_2$ and ethylene glycol and the reaction between Fe^{2+} and Fe^{3+} in a co-precipitation method [20, 21]. In this experiment chemicals used for synthesis of MNPs by both methods were iron chloride tetrahydrate ($FeCl_2 \cdot 4H_2O$), ethylene glycol (99.5%), $FeCl_3$, HCl, 25% NH_3 solution (Wako Pure chemical industries Ltd., Japan), $FeCl_2$ (Strem Chemicals, Newburyport), polyethylene glycol 4000 (Tokyo Kasei Kogyo Co. Ltd, Japan), and sodium acetate, anhydrous (NaAc, 98%, Nacalai Tesque Ltd., Japan). All chemicals were of analytical grade and used without any further purification.

10.2.2 Hydrothermal synthesis of magnetic nanoparticles (MNPs)

$FeCl_3 \cdot 6H_2O$ (1.352 g, 5 mmol) was dissolved in ethylene glycol (40 mL) to form a clear solution, followed by the addition of NaAc (3.6 g) and polyethylene glycol (1.0 g). The mixture was stirred vigorously for 45 min until getting a clear solution and then sealed in a teflonlined stainless-steel autoclave (50 mL capacity). The autoclave was heated to and maintained at 200 °C for 5 h and allowed to cool to room temperature. After cooling, decantation was done by a permanent magnet to get the sedimented black products. The black products were washed several times with ethanol and dried at 70 °C for 3 h. Finally, we obtained Fe_3O_4 nanoparticles.

10.2.3 Synthesis of MNPs by co-precipitation method

In a typical co-precipitation method, $FeCl_3$ (2.6 g) and $FeCl_2$ (1.3 g) were dissolved in nitrogen gas (N_2) purged 2.0 M hydrochloric acid solution and magnetically stirred under a continuous

flow of N_2. The mixture was heated at 70 °C for 30 min. and then the mixture was again heated for another 5 min under a blanket of N_2. Ammonia was added drop by drop to precipitate the magnetic nanoparticles and the black product formed was treated hydrothermally at 70 °C for 30 min. All aqueous solutions and suspensions were made using nanopure water (18 MΩ cm resistivity). The resulting nanoparticles were subsequently separated from the reaction media under magnetic field and washed three times with nanopure water before drying. Finally the MNPs were oven dried at 70 °C for 3 h to get Fe_3O_4.

10.2.4 Phase transfer of Fe_3O_4 to γ-Fe_2O_3 and α-Fe_2O_3

It is well known that Fe_3O_4 can be oxidized to γ-Fe_2O_3, which can be further transformed into α-Fe_2O_3 at higher temperature [22]. However, magnetite (Fe_3O_4) is not very stable and is sensitive to oxidation. Magnetite is transformed into maghemite (*γ*-Fe_2O_3) in the presence of oxygen [23]. In Fig. 10-1 A and B, (a) is the XRD patterns of the as-synthesized black Fe_3O_4 nanoparticles assembly by both methods. After oxidation at 250 °C for 6 h, the black assembly is transformed into a red-brown one. Image (b) for both plates of Fig. 10-1 shows all XRD peak positions and relative intensities of this red-brown material, whereas image (c) shows the XRD of the dark red-brown materials, α-Fe_2O_3 obtained after 500 °C annealing of *γ*-Fe_2O_3 in Fig.10-1A(b) and 1B (b) under Ar gas for 1 h. However, the as-synthesized Fe_3O_4 nanoparticles do not go through such a change if annealed under inert atmosphere. Even at 650 °C, the Fe_3O_4 structure is still retained, as evidenced by both XRD and TEM (data not shown). This confirms that the valence state of the iron cations in the as-synthesized sample closely matches that of Fe_3O_4 rather than similarly structured γ-Fe_2O_3 [24].

10.3 Structure and magnetic characterization

The general structure characterization, including size, size distribution and crystal structure of the as-synthesized magnetic nanoparticles by both methods was performed for all the samples without any size sorting. To further confirm the crystal structure and overall phase purity, the nanoparticles with different sizes were examined using a PANalytical Advance X-ray diffractometer (XRD) with CuKα radiation and a Ni filter. The surface morphology and nanoparticles size were determined using a field emission scanning electron microscope (FE-SEM, model Hitachi S-4100H). Absorption spectra were recorded on UV-Vis absorption (reflectance) spectrophotometer (Shimadzu Corporation, UV-2450, Japan). The samples were standardized with barium sulphate coated glass substrate and its spectrum was used as the baseline. The spectra of all samples were measured in a wavelength range between 240 and 800 nm. AC magnetic field induced heating capability of magnetic nanoparticles was examined to observe the hyperthermia potentiality of Fe_3O_4 and γ-Fe_2O_3 (for both methods) by dispersing the nanoparticles in distilled water as well as a minimum essential medium (MEM) and magnetic hysteresis loops were measured by a superconducting quantum interference device (SQUID, Quantum Design MPMS-5). Further, the shapes of the nanoparticles were analyzed by transmission electron microscopy (TEM) using a JEOL JEM-3010 VII TEM operating at 300 kV.

10.4 Reproducibility of magnetic (Fe_3O_4, γ-Fe_2O_3 and α-Fe_2O_3) nanoparticles

An important aspect of the synthesis of magnetic nanomaterials is the reproducibility when they are synthesized using identical conditions. To test the reproducibility of magnetic nanoparticles, three samples were synthesized under optimum conditions already described in section *10.2.2, 10.2.3* and *10.2.4*. All the characterizations of these samples were performed in accordance to section **3** and these three samples were found to have fairly consistent values for

maximum reproducing capability. These results show excellent reproducibility for the synthesized magnetic nanoparticles by simple hydrothermal and co-precipitation methods which may be the key point for commercial production.

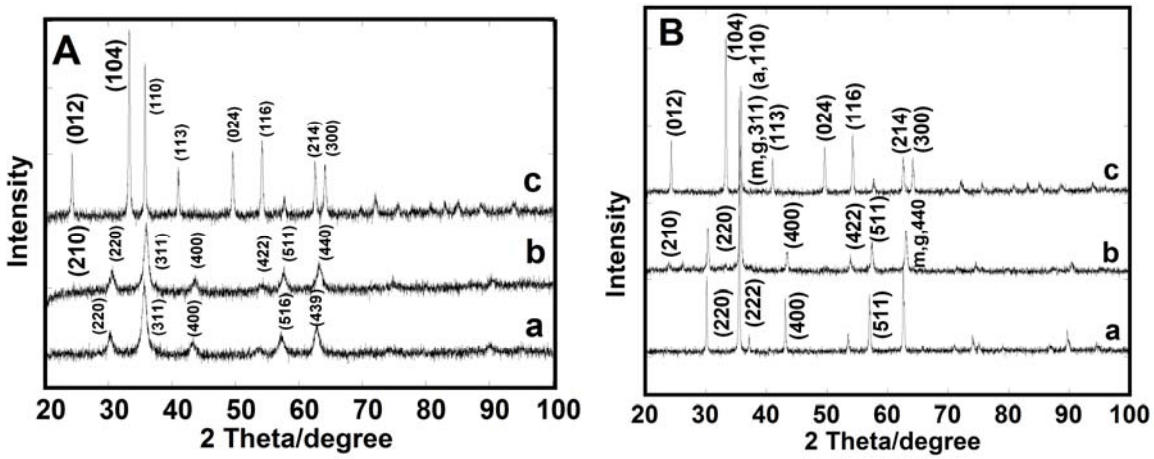

Fig.10-1: XRD patterns of MNPs synthesized by (A) co-precipitatiop and (B) hydrothermal methods. Magnetite, maghemite and hematite are represented by (a), (b) and (c), respectively, in (A) and (B).

10.5 Results and discussion

The crystal structures of the prepared MNPs were observed by the XRD measurement. Typical XRD patterns of Fe_3O_4, γ-Fe_2O_3 and α-Fe_2O_3 are shown in Fig. 10-1. As shown in Fig. 10-1, all samples were found to be consistent with the expected diffraction pattern of the *fcc* FeO structures for both methods. No diffraction peaks from other crystalline forms are detected, demonstrating that these Fe_3O_4, γ-Fe_2O_3 and α-Fe_2O_3 samples have high purity and crystallinity. Fig. 10-1A demonstrated the peak indexes of (a) Fe_3O_4, (b) γ-Fe_2O_3 and (c) α-Fe_2O_3 synthesized by co-precipitation method whereas the peak indexes of (a) Fe_3O_4, (b) γ-Fe_2O_3 and (c) α-Fe_2O_3 synthesized by hydrothermal method is shown in Fig. 10-1B. More sharp narrower peaks were noticed among the all iron oxides prepared by hydrothermal method due to the larger particle

size ca. 45-50 nm. In contrast, wide and broader peaks were noticed among the all iron oxides prepared by co-precipitation method due to the smaller particle size ca. 15-20 nm.

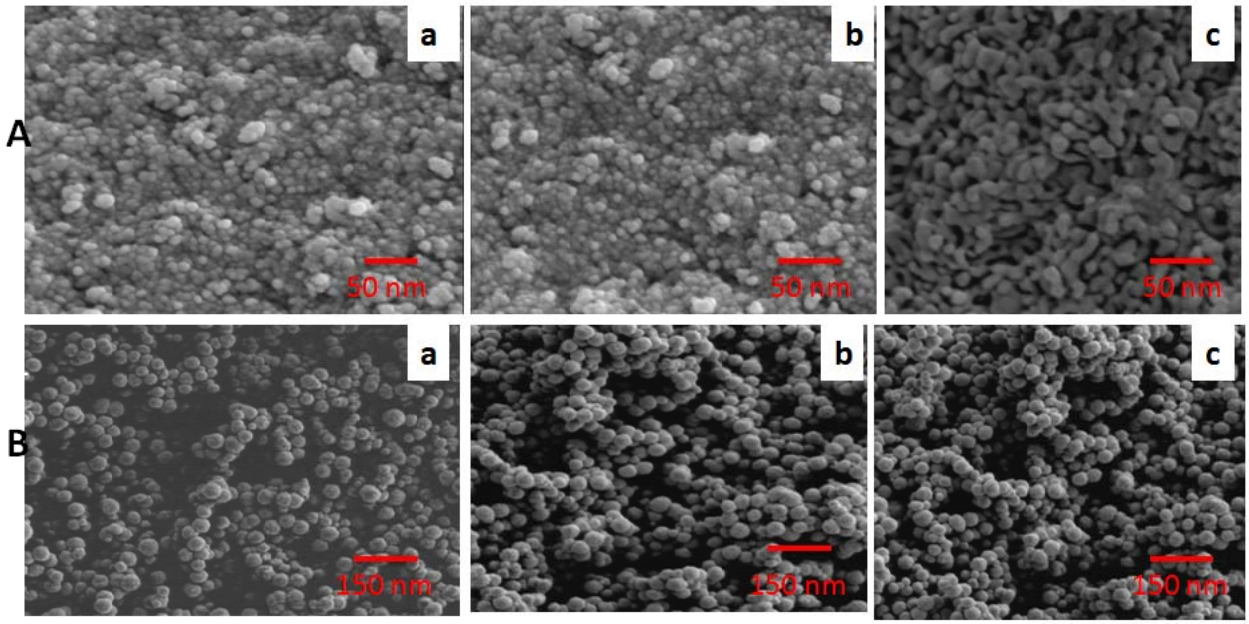

Fig.10-2: Comparative SEM images of magnetite, maghemite and hematite nanoparticles represented by (a), (b) and (c), respectively. Plate A for co-precipitation and B for hydrothermal method.

Particles morphology of the all samples was studied using FE-SEM (Fig.10-2). Fig.10-2A and 2B represent the FE-SEM micrographs of (a) Fe_3O_4, (b) γ-Fe_2O_3 and (c) α-Fe_2O_3 synthesized by co-precipitation and hydrothermal method, respectively. The nanoparticles size was roughly estimated to be about 15-20 nm and 45-55 nm prepared by co-precipitation and hydrothermal method, respectively. This result revealed that the co-precipitation method facilitates smaller size nanoparticles than the hydrothermal method (**Table 1**).

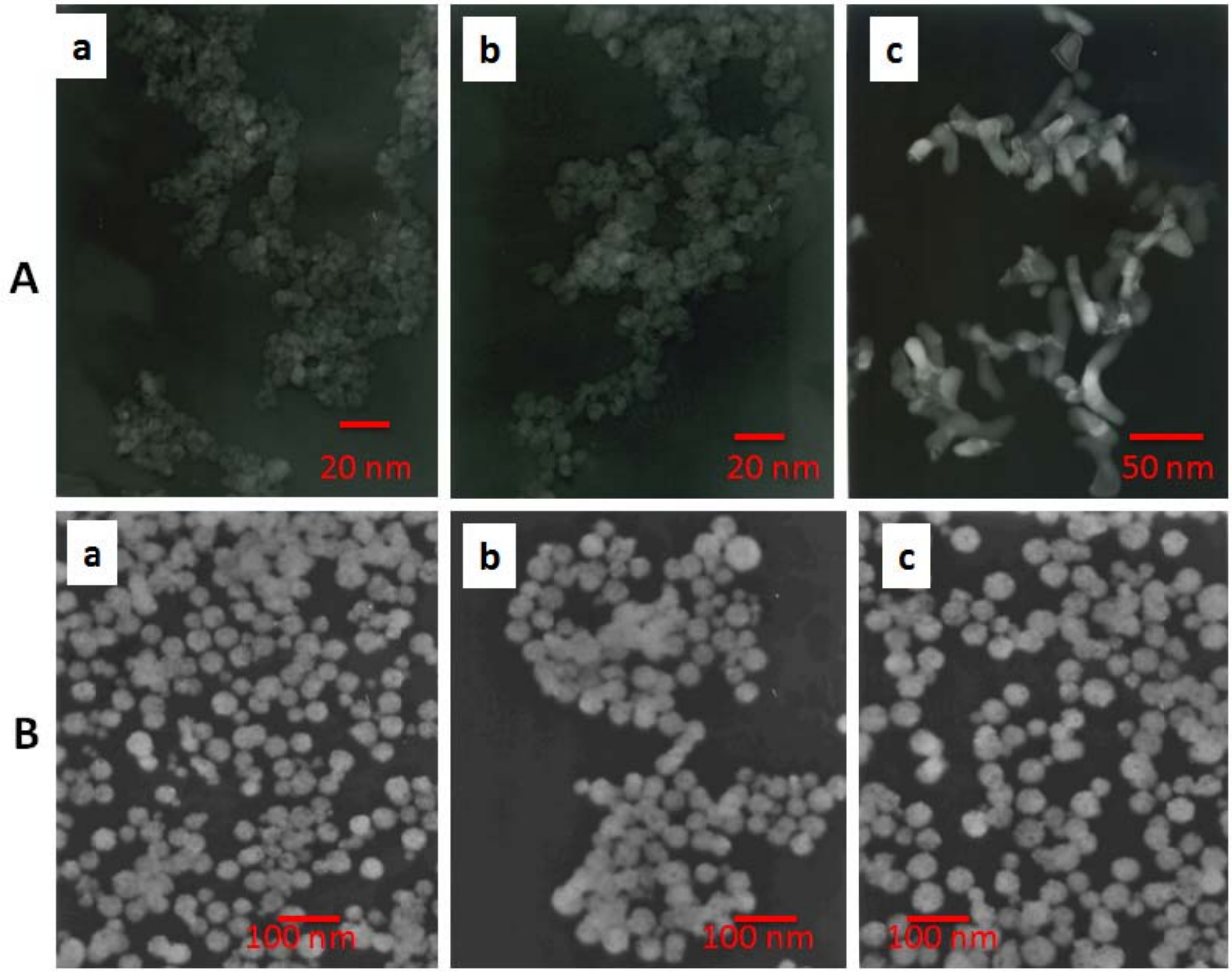

Fig.10-3: Comparative TEM images of magnetite, maghemite and hematite nanoparticles represented by (a), (b) and (c), respectively. Plate A for co-precipitation and B for hydrothermal method.

The samples were also characterized using TEM (Fig.10-3) to analyze shape and size of the particles. Here Fig.10-3A and 3B depict the TEM micrographs of (a) Fe_3O_4, (b) γ-Fe_2O_3 and (c) α-Fe_2O_3 synthesized by co-precipitation and hydrothermal method, respectively. Spherical-shaped morphology was observed by FE-SEM in (a) Fe_3O_4 and (b) γ-Fe_2O_3 but neck-structured in (c) α-Fe_2O_3 (Fig.10-2A) for co-precipitation method whereas all spherical-shaped morphology was found in (a) Fe_3O_4, (b) γ-Fe_2O_3 and (c) α-Fe_2O_3 synthesized by hydrothermal method (Fig.10-2B). TEM images also clearly support the FE-SEM data in terms of morphological and

nano-structural analysis with particle size ca. 12-25 nm and 35-55 nm synthesized by co-precipitation and hydrothermal method, respectively (**Table 1**).

Table 10-1. Comparative performance of MNPs prepared by co-precipitation and hydrothermal methods.

Property	**Co-precipitation**			**Hydrothermal**		
	Magnetite Fe_3O_4	Maghemite γ-Fe_2O_3	Hematite α-Fe_2O_3	Magnetite Fe_3O_4	Maghemite γ-Fe_2O_3	Hematite α-Fe_2O_3
Particle size (SEM)	15-20 nm	15-20 nm	20-25 nm	45-50 nm	45-55 nm	50-60 nm
Particle size (TEM)	12-18 nm	14-20 nm	25-35 nm	35-50 nm	40-55 nm	50-70 nm
Particle shape	Spherical	Spherical	Neck structured	Spherical	Spherical	Spherical
Absorption edge	620 nm	600 nm	565 nm	650 nm	630 nm	570 nm
Saturation value of magnetization (*Ms*)	78 emu/g	59 emu/g	1.8 emu/g	65 emu/g	57 emu/g	1.2 emu/g

Fig. 10-4 gives the UV-Vis absorption (reflectance) spectra of the synthesized magnetic nanoparticles. As shown in Fig.10-4, absorption spectra of (a) Fe_3O_4, (b) γ-Fe_2O_3 and (c) α-Fe_2O_3 represents by co-precipitation method whereas (d) Fe_3O_4, (e) γ-Fe_2O_3 and (f) α-Fe_2O_3 represent the absorption spectra of MNPs synthesized by hydrothermal method. It can be seen that the absorption edges of hydrothermally synthesized MNPs are more red-shifted than those of MNPs synthesized by the co-precipitation method (Table 10-1). With the increase of calcination temperature (500 °C), the absorption edge of the sample has some blue shift. The blue shift is presumably ascribed to the formation of the homogenous Fe_2O_3 nanoparticles for both methods. The band gap energy of Fe_2O_3 is 2.2 eV and can be activated by the light below 563 nm [25].

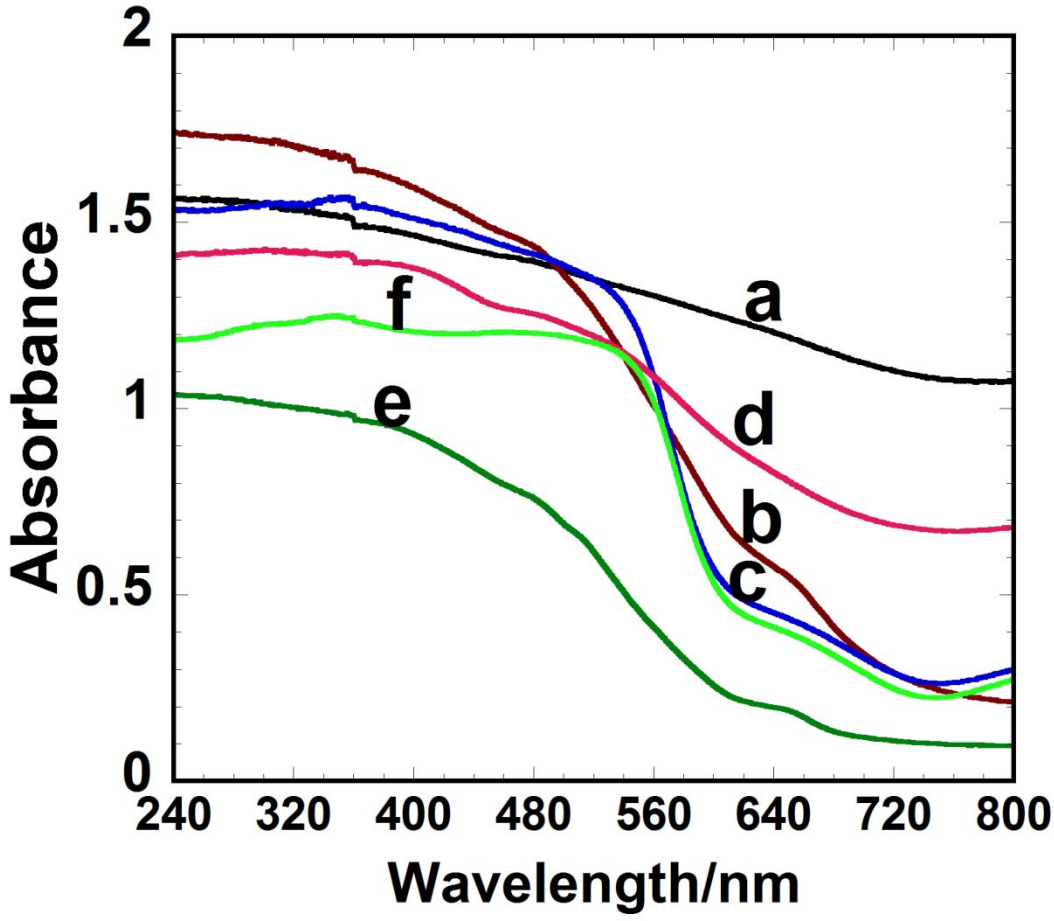

Fig.10-4: UV-Vis absorption (reflectance) spectra of MNPs. Magnetite, maghemite and hematite are represented by (a), (b), (c) and (d), (e), (f) for the co-precipitation and hydrothermal methods, respectively.

To further explore the low temperature magnetic properties of Fe_3O_4 samples from both methods, *M–T* curves in zero field cooling (ZFC) and field cooling (FC) processes with a 1kOe applied field were measured, as shown in Fig.10-5. For the co-precipitation sample, the ZFC magnetization (*Ms*) value was 9.8 emu/g (a) whereas for the hydrothermal Fe_3O_4 sample, the ZFC magnetization (*Ms*) value was 7.8 emu/g (b) but there no peak was observed for both samples by both methods.

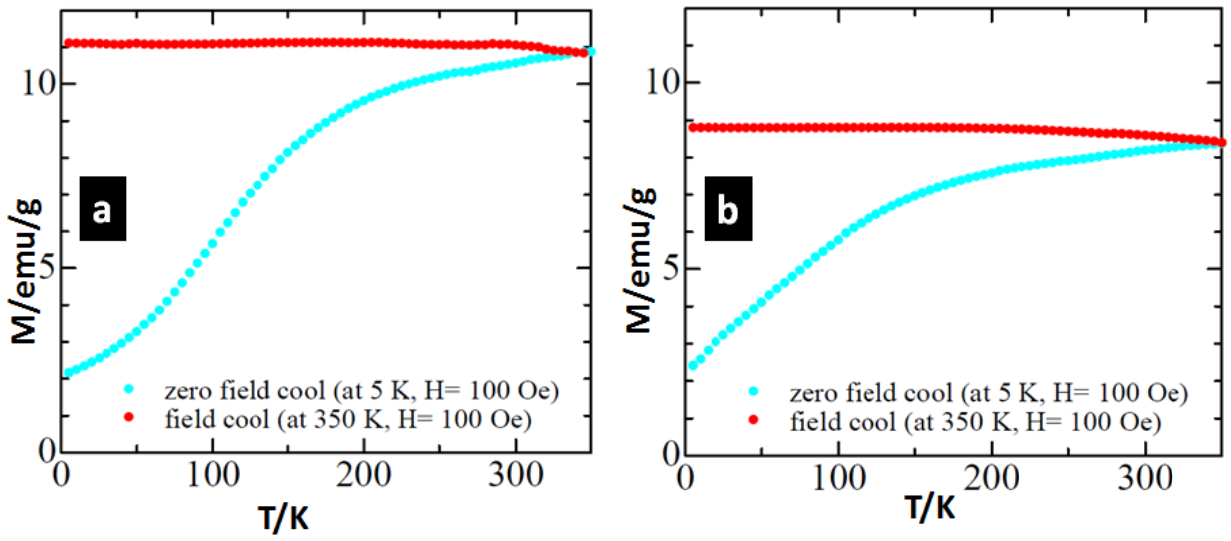

Fig. 10-5: Temperature dependent magnetization in ZFC and FC processes for Fe_3O_4 synthesized by co-precipitation (a) and hydrothermal (b) methods.

The comparative hysteresis curves obtained at room temperature (Fig. 10-6) show that the saturation value of magnetization (M_S) of MNPs prepared by both methods. Fig. 10-6 (A) and (B) represent M_S value of (a) Fe_3O_4 and (b) γ-Fe_2O_3 78, 59 emu/g and 65, 57 emu/g prepared by co-precipitation and hydrothermal method. Moreover Fig. 10-6 (C) shows the M_S value of α-Fe_2O_3 nanoparticles prepared by (a) co-precipitation and (b) hydrothermal method 1.8 and 1.2 emu/g, respectively. Thus the results revealed that M_S values of all samples prepared by co-precipitation method were always higher than that of MNPs prepared by the hydrothermal method (**Table 1**). The M_S values for substances treated with oxygen and annealed are different from the mother sample for both cases. The difference in magnetization of both oxidized and non-oxidized samples indicates that the oxidation of magnetite into maghemite was completed and that maghemite was reduced at high temperature to hematite during annealing which was also supported by an XDR analysis.

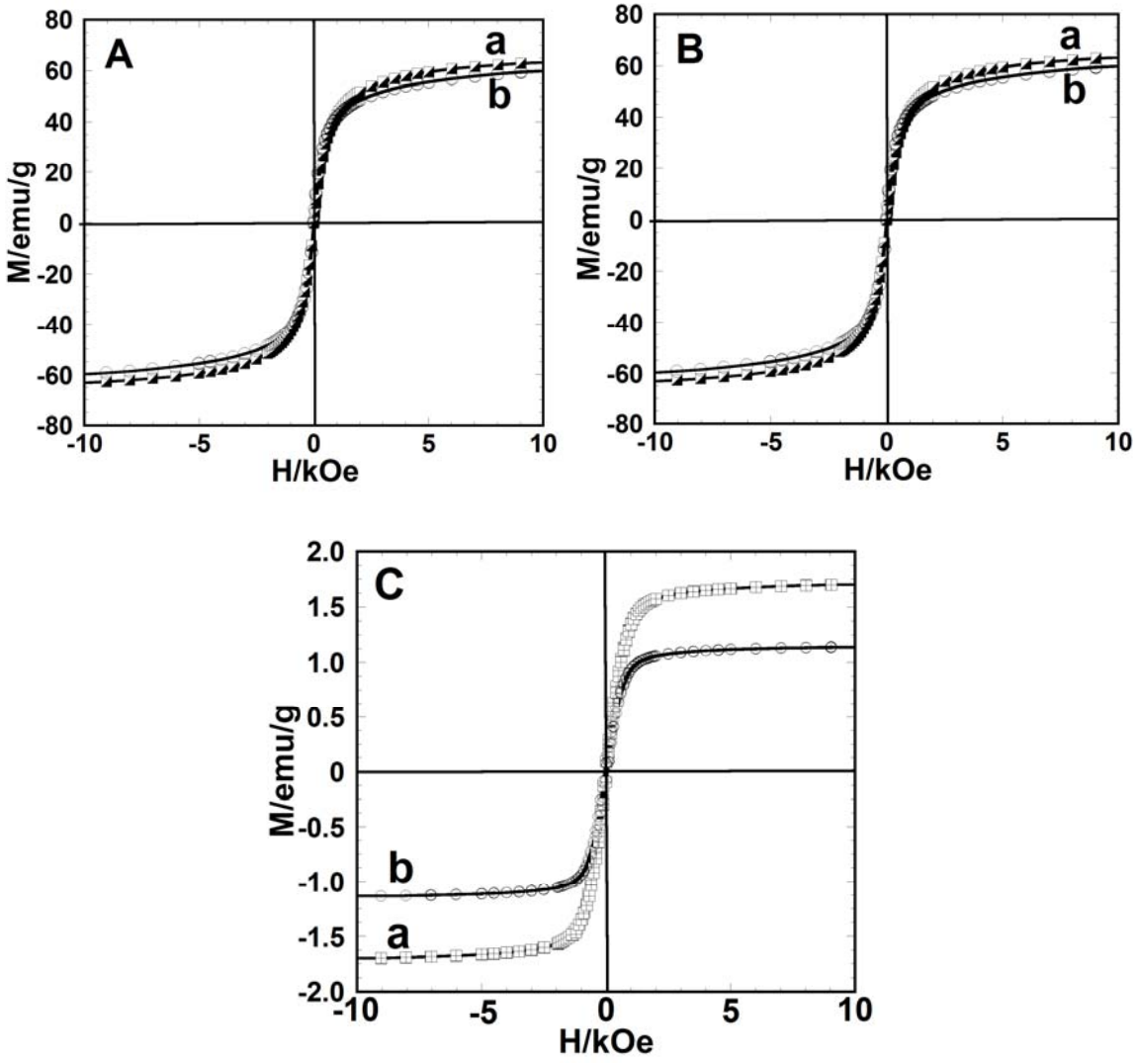

Fig.10-6: Comparative magnetic hysteresis loops of magnetic nanoparticles by co-precipitation (A) and hydrothermal method (B).

Heat dissipation of magnetite and maghemite nanoparticles prepared by both methods was evaluated by using an AC magnetic field generator using maximum magnetic field intensity and a frequency of 5.0 kA/m and 560 Hz, respectively. The heat generated from samples was evaluated by exposing 5 mg/mL magnetic particle suspension dispersed in distilled water and then their different doses like 0.2, 0.4, 0.6, 0.8 and 1.0 mL/5 mL MEM under an AC magnetic-

field for about 10 min exposure time. The comparative temperature rising of the as-prepared magnetic nanoparticles suspensions against the exposure time is shown in Fig.10-7. The highest temperature was achieved by Fe_3O_4 and γ-Fe_2O_3 nanoparticles were 49.9, 50.2 ˚C and 49.2 and 49.7 ˚C prepared by co-precipitation and hydrothermal method, respectively.

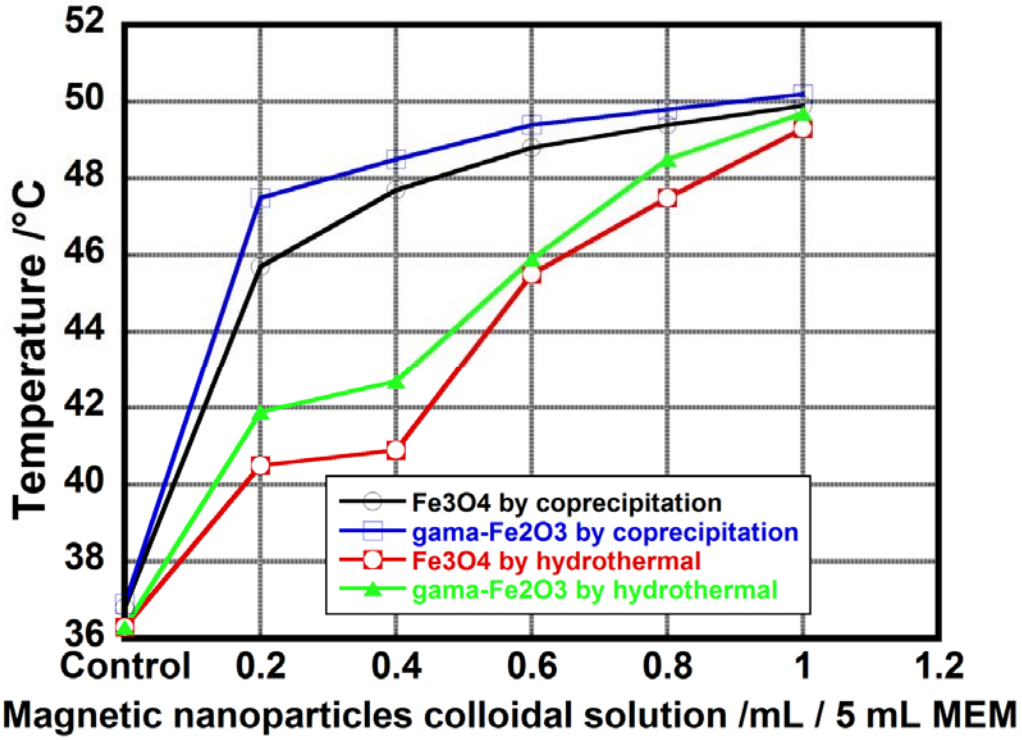

Fig.10-7: Comparative heat dissipation capability of MNPs by co-precipitation and hydrothermal methods.

Thus the findings revealed that the highest temperature was achieved by all the samples prepared by co-precipitation method, whereas the temperature of the hydrothermally prepared sample increased gradually against time and the heat dissipated was well below that of co-precipitation samples (Fig.10-7). Atsumia *et al* and Jeyadevanb *et al* also reported that superparamagnetic nanoparticles prepared by the co-precipitation method dissipated highest heat to an AC magnetic field for hyperthermia [26, 27]. Finally, it is clear to conclude that the

prepared nanomaterials have hyperthermia potentiality synthesized by both methods and hopefully, we are very much interested to use those materials in cancer therapy in future.

10.6 Conclusion

Comparative performances of MNPs prepared by both methods indicate that in respect of heat dissipation capability, saturation values of magnetization and particle size, the co-precipitation method is better, whereas in respect of particle shape and absorbance (reflectance) the hydrothermal method is better. Precisely, we can draw a conclusion that MNPs synthesized by the co-precipitation method is better suited for hyperthermia than that by the hydrothermal method. But studies on AC magnetic field induced hyperthermia for carcinoma cells are our next step.

References

[1] F. Caruso, M. Spasova, A. Susha, M. Giersig, R.A. Caruso, Chem. Mater. 13 (2001) 109-116.

[2] a) T. Hyeon, Chem. Commun. 8 (2003) 927-934, b) T. Hyeon, Y. Chung, J. Park, S.S. Lee, Y.W. Kim, B.H. Park, J. Phys. Chem. B 106 (2002) 6831-6833, c) T. Hyeon, S.S. Lee, J. Park, Y.Chung, H.B. Na, J. Am. Chem. Soc. 123 (2001) 12798-12801.

[3] Y. Xiong, Y. Xie, S. Chen, Z. Li, Chem. Eur. J. 9 (2003) 4991-4996.

[4] K.Woo, H.J. Lee, J.P.Ahn, Y.S. Park, Adv. Mater. 15 (2003) 1761-1764.

[5] a) X. Teng, H. Yang, J. Mater. Chem. 14 (2004) 774-779, b) Y. Wang, J.F. Wong, X. Teng, X.Z. Lin, H. Yang, Nano. Lett. 3 (2003) 1555-1559, c) Y. Wang, X. Teng, J. Wang, H. Yang, Nano. Lett. 3 (2003) 789-793.

[6] A.C.C. Yu, M. Mizuno, Y. Sasaki, H. Kondo, K. Hiraga, Appl. Phys. Lett. 81 (2002) 3768-3770.

[7] R.M. Cornell, U. Schwertmann, The Iron Oxides: Structure, Properties, Reactions, Occurrences and Uses, second ed., Wiley-VCH, Weinheim, 2003.

[8] a) J.M. Perez, T.O`Loughlin, F.J. Simeone, R. Weissleder, L. Josephson, J. Am. Chem. Soc. 124 (2002) 2856-2857, b) J. M. Perez, F. J. Simeone, A. Tsourkas, L. Josephson, Weissleder, Nano Letter. 4 (2004) 119-122, c) J. M. Perez, L. Josephson, T. O`Loughlin, D. Hogemann, R. Weissleder, Nat. Biotechnol. 20 (2002) 816-820.

[9] A.Y. Louie, M.M. Huber, E.T. Ahrens, U. Rothbacher, R. Moats, R.E. Jacobs, S.E. Fraser, T.J. Meade, Nat. Biotechnol. 18 (2000) 321-325.

[10] U. Häfeli, W. Schütt, J. Teller, M. Zborowski, Scientific and Clinical Application of Magnetic Carriers, Plenum, New York, 1997.

[11] J.S. Kim, T.J. Yoon, B.G. Kim, S.J. Park, H.W. Kim, K.H. Lee, S.B. Park, J.K. Lee, M.H. Cho, Toxicological Sciences 89 (2006) 338-347.

[12] P. Tartaj, M.P. Morales, T. Gonzalez-Carreno, S. Veintemillas-Verdaguer, C.J. Serna, J. Magn. Magn. Mater. 290 (2005) 28-34.

[13] C. Li, Y. Shen, M. Jia, S. Sheng, M.O. Adebajo, H. Zhu, Catal. Commun. 9 (2008) 355- 361.

[14] F. Shi, M.K. Tse, M.M. Pohl, A. Bruckner, S.M. Zhang, M. Beller, Angew. Chem., Int. Ed. 46 (2007) 8866-8868.

[15] F.M. Bautista, J.M. Campelo, D. Luna, J.M. Marinas, R.A. Quiros, A.A. Romero, Appl. Catal. B. 70 (2007) 611-620.

[16] F. Bertorelle, C. Wilhelm, J. Roger, F. Gazeau, C. Me´nager, V. Cabuil, Langmuir 22 (2006) 5385-5391.

[17] L.A. Perrin-Cocon, P.N. Marche, C.L. Villiers, Biochem J. 338 (1999) 123-130.

[18] T. Neuberger, B. Schopf, H. Hofmann, M. Hofmann, B. V. Rechenberg, J. Magn. Magn. Mater. 293 (2005) 483-496.

[19] An-Hui Lu, E.L. Salabas, F. Schüth, Angew. Chem., Int. Ed., 46 (2007) 1222-1244.

[20] D. Hong, L. Xiaolin, P. Qing, W. Xun, C. Jinping, L. Yadong, Angew. Chem. 117 (2005) 2842-2845.

[21] O. Anselm, Synthesis and Characterization of Tannic Acid Functionalized Magnetic Nanoparticles, in : *ACS Symposium Series 996*, R. Nagarajan, T. A. Hatton (Eds.), pp. 90-107, American Chemical Society , Washington DC, (2008)

[22] G .Bate, In Magnetic Oxides Part 2; Craik, D. J., Ed.; John Wiley & Sons, New York, 1975, pp 705-707.

[23] S. Laurent, D. Forge, M. Port, A. Roch, C. Robic, L.V. Elst, R.N. Muller, Chemical Reviews, 108 (2008) 2064-2110.

[24] S. Sun, H. Zeng, D.B. Robinson, S. Raoux, P.M. Rice, S.X. Wang, G.Li, J. Am. Chem. Soc. 126 (2004) 273-279.

[25] C. Karunakaran, S. Senthilvelan, Electrochem. Commun. 8 (2006) 95-101.

[26] T. Atsumia, B. Jeyadevanb, Y. Satob, K. Tohji, J. Magn. Magn. Mater. 310 (2007) 2841-2843.

[27] B. Jeyadevanb, T. Atsumia, M. Suto, R. Kasuya, Y. Satob, K. Tohji, Thermal Med, 25 (2009) 43-52.

CHAPTER 11

CYTOXICITY AND CANCER (HeLa) CELL KILLING EFFICACY OF AQUEOUS GARLIC (*Allium sativum*) EXTRACT

Abs tract

Garlic (*Allium sativum*) is an herb that is used mainly as a food in many countries for its medicinal properties since ancient times. It enhances immune functions and has antibacterial, antifungal, antivirus and anticancer activities. Organosulfur compounds originating from garlic inhibit carcinogen activation. In this study we prepared aqueous garlic extract (AGE) and its *in vitro* application to cancer (HeLa) cell line was performed to observe the cancer cell killing efficacy. Different concentrations of AGE like 100, 200, 300, 400, and 500 µL per a 5-mL minimum essential medium solution were used for treatment. The results revealed that 95% cancer cells were destructed in a dose of 500 µL, whereas about 92, 87, 60, and 24% cancer cells were destructed in a dose of 400, 300, 200 or 100 µL of AGE, respectively. This work has already been published in Journal of Scientific Research, 2011, **3** (2), 375-382.

11.1 Introduction

Medicinal properties of garlic (*Allium sativum*) have been widely known and used since ancient times and is probably the oldest and most consumed plant medicine known and it possesses multiple beneficial effects such as antimicrobial, hypolipidemic, antithrombotic, and antitumor activities [1] and used by different cultures. Anticancer properties of garlic were first described by Weisberger and Pensky in 1958. They reported an inhibitory effect of a garlic extract on cancer cell growth both in vitro and in vivo [2]. Medicinal properties of garlic and other representatives of the family *Allium* (onion, shallot), including their anticancer efficacy,

have been attributed to organosulfur compounds. The different health benefits of garlic are attributed to its sulfur-containing constituents. These are classified as oil-soluble and water-soluble compounds. Oil-soluble compounds include diallyl sulfide, diallyl disulfide, and diallyl trisulfide, allyl methyl trisulfide, dithiins, and ajoene. The most important initial sulfur compound occurring in the intact garlic bulbs is alliin (S-allylcysteine sulfoxide). The whole bulbs contain also γ-glutamyl-S-allylcysteine, S-methylcysteine sulfoxide (methiin), Strans-1-propenylcysteine sulfoxide, S-2-carboxypropylglutathione and S-allylcysteine, though they are at much smaller amounts [3]. The reactions of allicin with -SH groups can yield S-allylcysteine or S-allylmercaptocysteine that are water soluble compounds [4]. Unlike oily sulfur compounds, water-soluble compounds are odorless and have more delicate and less characteristic flavor [5]. These compounds are also formed during aqueous garlic extraction, when the initial compound γ-glutamyl-S-allylcysteine is transformed into S-allylcysteine and this reaction is catalyzed by γ-glutamyltranspeptidase (γGT) (Scheme 11-1).

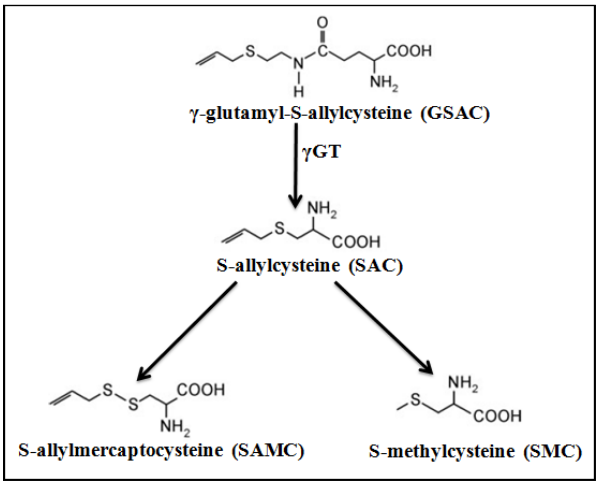

Scheme11-1. Formation of water-soluble garlic-derived organosulfur compounds from γ-glutamyl-S-allylcysteine. γGT: γ-Glutamyltranspeptidase.

S-allylcysteine along with its derivatives, S-methylcysteine and S-allylcysteine, are components of aqueous extracts of garlic and possess biological activity both in vitro and in vivo [6].

Intact garlic cloves contain also steroidal saponins [7] and organic selenium compounds that possess a potential anticancer efficacy [8]. The main selenium compound is γ-glutamyl-S-methylselenocysteine. Like its sulfur analog γ-glutamyl-S-allylcysteine, γ-glutamyl-S-methylselenocysteine can be transformed by γGT to other selenium derivatives, e.g., S-methylselenocysteine. Comparative studies of chemopreventive efficiency of organoselenium compounds and their sulfur analogs demonstrated that diallyl selenide was 300-fold more effective than diallyl sulfide in protecting against 7, 12-dimethylbenz[α]anthracene-induced mammary adenocarcinomas in rats [9]. It is well known that both oil-soluble and water-soluble organosulfur compounds are contained in garlic and onions. Some of these have been shown to be chemopreventive in animal models of carcinogenesis. For example, diallyl sulfide inhibits development of colon carcinomas, esophageal carcinomas, pulmonary adenomas, and forestomach tumors in rodents when administered prior to carcinogen exposure [10, 11, 12, 13]. Since then intensive laboratory and epidemiological studies have been carried out to verify chemopreventive and anticarcinogenic effects of *Allium sativum*, and to explain mechanisms of its action [6]. We prepared the garlic extract for the first time solely using distilled water as solvent and our study is focused on anticancer efficacy of the aqueous extract of garlic on the properly cultured cervical carcinoma (HeLa) cell line using different concentrations.

11.2 Materials and Methods

11.2.1 Preparation of aqueous garlic extracts (AGE)

Fresh raw garlic (*Allium sativum*) was purchased from local market of Kagoshima city, Japan and was identified by Professor Tsuyoshi Yoneda (Faculty of Agriculture, Kagoshima University,

Japan) where its voucher specimen (No. AS0049) was deposited. Cloves from fresh raw garlic were chopped and ground and were made fine paste. Then the garlic paste was weighted and it was 200 g. That paste was soaked in 250 ml distilled water and then magnetically stirred for 3hours. Finally AGE was collected by filtration over whole day and we got AGE with a final concentration of 150mg/200mL. Thereafter AGE was kept undisturbed for further use in cancer cells.

11.2.2 Cell culture

HeLa cells were provide by the RIKEN BRC through the National Bio-Resource Project of the MEXT, Japan and stored in liquid N_2 to ensure the best quality. The mentioned cancer cell line was cultured in a minimum essential medium (MEM) solution with 10% newborn calf serum (NBS) in a humidified incubator with an atmosphere of 5% CO_2 in air at 37 °C and the cells were plated at a concentration of about 3×10^5 in 60 mm Petri dishes and allowed to grow for 3 days. For HeLa cell culture, phosphate buffer saline (PBS, Invitrogen Corporation, Gibco), enzyme Trypsine-EDTA (Gibco) solution, dye trypan blue (Nacalai Tesque, Inc., Kyoto, Japan) were purchased and used. Monolayer cultures of cancer cell line (HeLa Cells) were maintained as described by Abdulla-Al-Mamun *et al*. [14].

11.2.3 In vitro cytotoxicity and anticancer assay

The *in vitro* cytotoxicity and anti-cancer effect of AGE against the HeLa cell line was evaluated by trypan blue exclusion method [14]. Cancer cell viability was examined by treating with AGE solution for 24 h incubation in an incubator. To investigate the cytotoxicity and anticancer efficacy of AGE, one dish was used as control without garlic extract solution and the other five dishes were treated with different concentrations, like 100, 200, 300, 400 and 500 μL of AGE solution per 5 mL of MEM solution. The light power was measured by a spectro-radiometer

(Model: LS-100, EKO Instrument Co. Ltd.) and the images were taken using an Olympus inverted CKX41 microscope with a numerical light field condenser (N.A.0.3),which delivers a very narrow beam of white light from tungsten lamp (6V, 30W halogen illumination) on top of the sample.

Table 11-1. Viable cancer cell counting after treated by AGE at different concentrations.

Treatment	Viable cell counting				Average	In percent
	1st	2nd	3rd	4th		
Control	39	40	42	39	40	100[a]
100 μL	35	34	28	24	30	76
200 μL	14	17	20	13	16	40
300 μL	15	6	4	5	5	13
400 μL	3	3	5	2	3	8
500 μL	2	1	2	3	2	5

[a]Average number of cells counted in control (40) is considered as 100%.

A haemocytometer was used to estimate the total number of viable cells (by counting cells in the four 1 mm^2 corners of the haemocytometer) and average number of the cells per unit volume (mL) of medium was calculated as the sum of the counted cell number/ 3×10^5 (**Table 11-1**) .

11.3. Results

Numerous studies have suggested that garlic possesses anticancer activity. Garlic extracts were prepared by soaking of sliced garlic cloves in extracting solution for a specific time. Then, after separation of the solution the extract was concentrated and was used to find the cytotoxicity and cancer cell killing efficacy. We evaluated AGE cytotoxicity and anticancer efficacy against HeLa cell viability and proliferation using direct cell counts by trypan blue staining. One hundred to 500 μL of AGE significantly reduced the viability of HeLa cells (**Fig.11-1**).

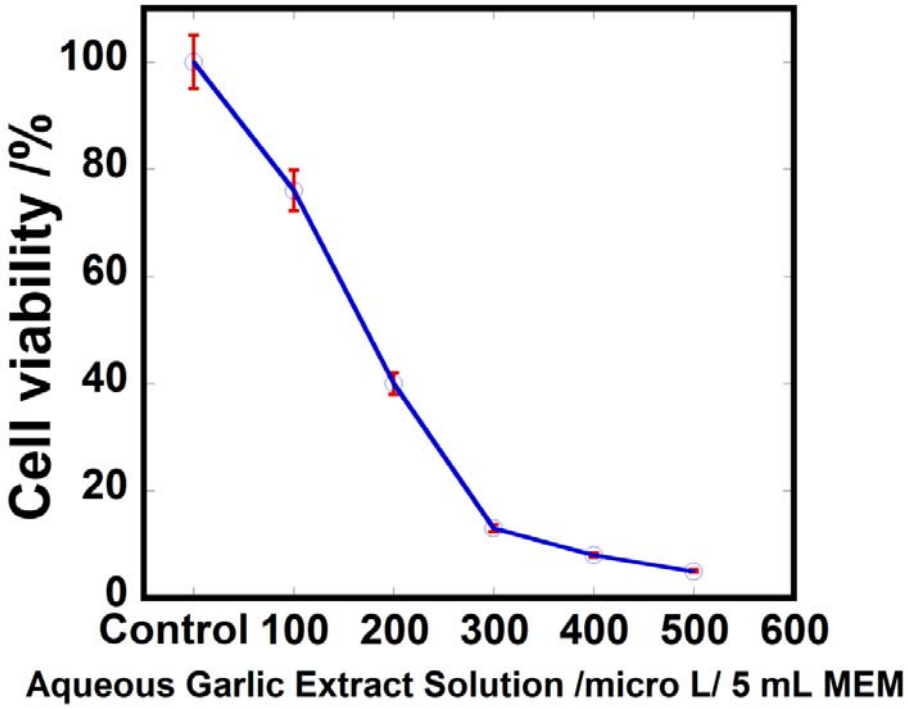

Fig.11-1: Effects of AGE on viability and proliferation of HeLa cells. Cell viability was assessed by trypan blue dyeing assays for 24 h after treatment with the indicated concentrations of AGE.

As shown in Figure 11-1, the percentage of viable cells remained more than 75% even when cells were treated with 100 µL of AGE for 24 h. But when the doses were increased, the percentages of viable cells were decreased and finally at a dose of 500 µL of AGE only 5% cells were viable. These results indicate that AGE shows significant potentiality against the viability and proliferation of cervical carcinoma cell (HeLa cell) line.

11.4 Discussion

Studies of recent years have focused on elucidation of the mechanism of biological activity of garlic. Hundreds studies were conducted both in vivo and in vitro using individual organic sulfur compounds, mostly allyl sulfides and their metabolites or water-soluble compounds, S-allylcysteine and S-allylmercaptocysteine [15, 16, 17]. Accumulating evidence indicates that

various food ingredients may play an essential role in colon cancer prevention. The AGE used in this study is an extract of fresh garlic that is aged over a prolonged period and contains water-soluble allyl amino acid derivatives, which account for most of its organosulfur content, stable lipid-soluble allyl sulfides, flavonoids, saponins, and essential macro- and micronutrients [18].

Fig.11-2(a) ~ (f) show microscopic images of HeLa cells after 24 h incubation only in MEM medium (control dish), 100, 200,300, 400 and 500 µL of AGE / 5 mL of MEM, respectively. It is obvious that AGE has a significant affect against the HeLa cell line because 95% of cancer cells were found to be dead after 24 h incubation with a dose of 500 µL of AGE / 5 mL of MEM (**Fig. 11-1**). According to the available literature, the following mechanisms may be involved in the chemopreventive effects of organosulfur compounds: (i) Enhancement of the activity of specific mixed-function oxidases that depress the activation of carcinogens [19, 20, 21], (ii) induction of phase II enzymes that enhance detoxification and excretion of potential carcinogens and reduction of the formation of DNA adducts [22], (iii) increased synthesis of glutathione, an endogenous tripeptide thiol that directly protects cells from damage by free radicals and (iv) apoptosis induction in cancer cells [23].

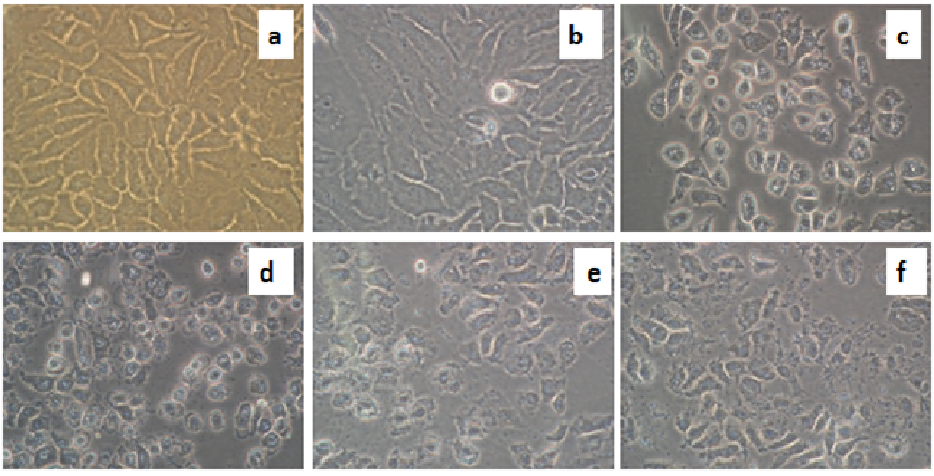

Fig. 11-2: Microscopic images of HeLa cells after 24 h incubation; cells without (a) any treatment (control), with (b) 100 µL, (c) 200 µL, (d) 300 µL, (e) 400 µL, and (f) 500 µL of AGE/ 5mL MEM.

Allicin (diallyl thiosulfinate) which is the main biologically active compound derived from garlic and easily diffuses through cell membranes, exerts its biological effects by reacting with free thiols within the cell. In living cells, reduced glutathione (GSH) is the major free thiol participating in cellular redox reactions and mixed disulfide formation. GSH is therefore the main cellular target of allicin reaction (**Scheme11- 2**) [24].

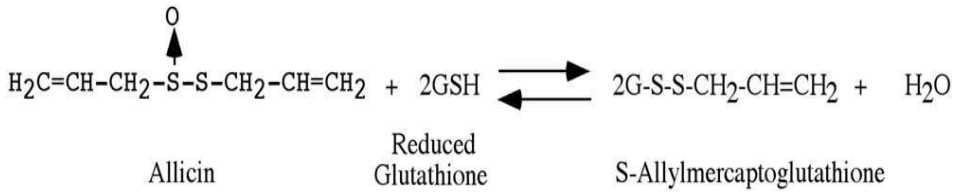

Scheme 11-2: Formation of S-allylmercapto-glutathione

However, its main oxidation products, S-allylmercapto-glutathione and S-allylmercapto-cysteine, could exert their action in more remote sites within the body because they are more stable. Thiol-disulfide exchange reaction can occur between protein sulfhydryl groups and S-cysteinyl compounds from garlic, such as S-allylmercapto-cysteine (reaction 1).

$$\text{Allyl-SS-Cys} + \text{protein-SH} \longrightarrow \text{Protein-S-S-Cys} + \text{allyl-SH} \qquad (1)$$

It is well known that reactive oxygen species fulfill a regulatory role in the cell, while reversible S-thiolation can be considered to be a regulatory redox mechanism for cellular processes. Pinto et al. have suggested that such S-cysteinylation of signaling proteins and transcription factors may be a primary target for development of chemopreventive or therapeutic agents that stimulate pro-apoptotic proteins or inactivate oncogenic factors [25]. Through these

citations, our experimental evidence proof the efficacy of garlic extract against the carcinoma cells line. Although great majority of studies devoted to anticancer action of garlic-derived organosulfur compounds were conducted in vitro but all the reports say that they used ethanol extract and the important fact that ethanol itself cytotoxic, whereas we first prepared and used the aqueous garlic extract to the best of our knowledge. Finally, our experimental results are the clear evidence of cytotoxicity that was firmly effective against the HeLa cell line.

11.6 Conclusion

We prepared aqueous garlic extract (AGE) for the first time to the best of our knowledge and the synthesized AGE showed a significant efficacy against cervical carcinoma cell (HeLa cell) line with different concentrations along with 95% cell killing potentiality in a maximum dose of 500 µL of AGE / 5ml of MEM. So, it may be concluded that AGE preserves the high potentiality against the HeLa cell line but further study is suggested to observe any adverse effect in normal cells.

References

[1] KT. Augusti, Ind. J. Exp. Biol., **34**, 634 (1996).

[2] AS. Weisberger, J. Pensky, Cancer Res., **18**, 1301 (1958).

[3] H. Amagase, J. Nutr., **136**, 716 (2006).

[4] A. Rabinkov, T. Miron, D. Mirelman, M. Wilchek, S. Glozman, E. Yavin, L. Weiner, Biochim. Biophys. Acta **1499**, 144 (2000).

[5] Y. Kodera, A. Suzuki, O. Imada, S. Kasuga, I. Sumioka, A. Kanezewa, N. Taru, M. Fujikawa, S. Nagae, K. Masamoto, K. Maeshige, K. Ono, J. Agric. Food Chem., **50**, 622 (2002). **doi:** 10.1021/jf0106648

[6] I. Małgorzata , K. Inga, W. Lidia, Environmental and Molecular Mutagenesis **50,** 247 (2009) doi :10.1002/em.20474

[7] V. Lanzotti, J. Chromatogr. A., **1112**, 3 (2006). doi:10.1016/j.chroma.2005.12.016

[8] I. Arnault, J. Auger, J. Chromatogr. A., **1112**, 23 (2006). doi:10.1016/j.chroma.2006.01.036

[9] K. El-Bayoumy, R Sinha, JT. Pinto, RS. Rivlin, J. Nutr., **136**, 864 (2006).

[10] MJ. Wargovich, Carcinogenesis **8,** 87 (1987).

[11] MJ. Wargovich, C. Woods, VWS. Eng, LC. Stephens, K. Gray, Cancer Res., **48**, 6872 (1988).

[12] LW. Wattenberg, VL. Sparnins, G. Barany, Cancer Res., **49**, 2689 (1989).

[13] VL. Sparnins, G. Barany, LW. Wattenberg, Carcinogenesis, **9**, 131 (1988). doi:10.1093/carcin/9.1.131

[14] M. Abdulla-Al-Mamun, Y. Kusumoto, A. Mihata, M. S. Islam, B. Ahmmad, Photochem. Photobiol Sci., **8,** 1125 (2009). doi: 10.1039/b907524k

[15] M. Thomson, M. Ali, Curr. Cancer Drug Targets, **3**, 67 (2003).

[16] A. Herman-Antosiewicz, SV. Singh, Mutat. Res., **555**, 121 (2004).

[17] A. Herman-Antosiewicz, AA. Powolny, SV. Singh, Acta Pharmacol. Sin., **28**, 1355 (2007).

[18] H. Amagase, Intake of garlic and its components. Nutritional and Health Benefits of Garlic as a Supplement Conference, Newport Beach, CA, p. 4 (abs), (1998).

[19] JF. Brady, H Ishizaki, JM. Fukuto, MC. Lin, A. Fadel, JM. Gapac, CS. Yang, Chem. Res. Toxicol., **4**, 642 (1991).

[20] HW. Chen, CW. Tsai, JJ. Yang, CT. Liu, WW. Kuo, CK. Lii, J. Nutr., **89**, 189 (2003).

[21] MM. Reicks, DL. Crankshaw. Nutr Cancer **25**, 241 (1996).

[22] D. Guyonnet, C. Belloir, M. Suschetet, MH. Siess, AM. Le Bon, Mutat Res., **495**, 135 (2001).

[23] Kweon S, Park KA, Choi H. Life Sci **73,** 2515 (2003). doi: 10.1016/S0024-3205(03)00660-X

[24] T. Miron, M. Wilchek, A. Sharp, Y. Nakagawa, M. Naoi, Y. Nozawa, Y. Akao, J. Nutri. Biochem. **19**, 524 (2008). doi:10.1016/j.jnutbio.2007.06.009

[25] J.T. Pinto, B. F. Krasnikov, A. J. L. Cooper, J .Nutr., **136**, 835 (2006).

CHAPTER 12

PHOTOCATALYTIC CNACER (HeLa) CELL-KILLING ENHANCED WITH Cu-TiO_2 NANOCOMPOSITE

Abstract

The metallic Cu nanoparticles have been successfully deposited on the heterogeneous TiO_2 surface by the borohydride reduction of copper nitrate in water / CH_3CN mixture under Ar atmosphere. The synthesized Cu-TiO_2 nanocomposite show light absorption in the wide visible region and XPS studies show that Cu exists in metallic form. The catalytic activity of the Cu-TiO_2 nanocomposite was evaluated by the application to the photocatalytic cancer (HeLa) cell-killing under UV-visible light irradiation. The Cu-TiO_2 nanocomposite showed higher photocatalytic activity than commercial TiO_2 (P25) under the similar experimental conditions. Based on the observed results, a plausible mechanism was proposed. This report has already been published in Topics in Catalysis, 2010, 53, 571-577.

12.1 Introduction

Titanium dioxide is broadly used as a photocatalyst because it is photochemically stable, non-toxic and economical. But, unfortunately the band gap (*E*g) of TiO_2 anatase is ~3.2 eV, which corresponds to only a limited portion (3-4%) of the solar spectrum. This relatively large band gap has significantly limited its more widespread application, particularly to indoor situations [1, 2]. Moreover, the efficiency of photocatalytic reaction is limited by the high recombination rate of electrons and holes in the single component of TiO_2 semiconductor leading to relatively poor photocatalytic efficiency (<5%). Many studies have been devoted to the improvement of

photocatalytic efficiency of TiO_2, such as deposition of noble metals [3–8], doping of metal or nonmetal ions [9–13], etc.

The deposition of a noble metal on semiconductor nanoparticles is an essential factor for maximizing the efficiency of photocatalytic reactions. The noble metal (e.g., Pt), which acts as a sink for photoinduced charge carriers, promotes interfacial charge-transfer processes [14, 15]. The TiO_2 lattice with metal ions introduces new energy levels in the band gap which can be tailored to extend the photosensitivity in the visible light region. Recent many studies have shown that metal or metal ion doped semiconductor composites exhibit a shift in the Fermi level to more negative potentials [16-19]. Such a shift in the Fermi level improves the activity of the composite system and enhances the efficiency of interfacial charge-transfer process.

Metal oxide supported copper nanoparticles are employed as highly active heterogeneous catalysts for the photodegradation of organic pollutants [20, 21]. But a direct relationship between absorption and photodegradation of organic compound could not be found. In some cases, copper oxide or copper ions play a photocatalytic role on photodegradation of organic compounds and the absorption of compounds or intermediate compounds on the catalyst surface may act as poison [22]. Some studies have suggested that observed enhancement of the photocatalytic degradation rates was due to electron trapping by the copper ions leading to the prevention of electron-hole recombination [20, 21]. Despite a large number of studies on these Cu / TiO_2 systems, many aspects with regard to the roles of copper species with multivalent states in the photocatalytic reaction remain unclear.

In this paper we report the preparation of highly active TiO_2-Cu supported by copper nanocomposites using a simple chemical method in a mixture of water / CH_3CN. Moreover, to

our best knowledge, we report here for the first time the photocatalytic cancer cell killing using TiO_2-Cu nanocomposites except our preliminary communication [24].

12.2 Experimental

The Cu-TiO_2 nanocomposites were prepared by a very simple chemical method. Commercially available TiO_2 (P25) surface (Degussa Corp., diameter ca. 20 nm, surface area 49.9 m^2/g) were modified by using hydrochloric acid. The modified TiO_2 colloidal suspension (0.01 M) was prepared by dropwise addition of 0.001 M hydrochloric acid until the pH value raised to ca. 3 in 70 vol% acetonitrile-water mixtures under vigorous stirring. Then the copper (II) nitrate (Cu $(NO_3)_2 \cdot 3H_2O$) salt (0.002-0.05M) was mixed at various molar ratios under Ar atmosphere in a rubber septum-capped Pyrex conical flask of ca. 154 cm^3, maintaining the reaction mixture in suspension by magnetic stirring. Under vigorous stirring, freshly prepared sodium borohydride (0.15 M) was injected drop by drop in the reaction medium via a syringe. The injection of the borohydride solution was continued (2 to 8 ml) until the color of reaction medium turned wine-reddish. After completion of reduction, the suspension was centrifuged and the particles were separated, followed by washing by methanol and drying in a vacuum.

The UV-visible absorption spectra of the colloid were recorded with a UV-vis spectrophotometer (Shimadzu Corporation, MPS-2000). The average diameters and size distributions of the Cu-TiO_2 nanocomposite particles were obtained from the enlarged photographs of transmission electron micrograph (TEM, JEOL, JEM-3010 VII, operating at 300 kV). The nanocomposite surface condition was also analyzed by field-emission scanning electron microscope (FE-SEM, Hitachi, S-4100H) and the crystal structure identification was made by X-ray diffraction (XRD) using a PAN alytical Advance X-ray diffractometer with CuKα (λ=1.5405 nm) radiation. The quantitative chemical composition of the Cu-TiO_2

composite nanocluster surface was also measured using an energy dispersive X-ray spectrometer (EDX, Philips, XL 30CP) attached to the cold field SEM. Further evidence for the purity of samples was obtained by X-ray photoelectron spectroscopy (XPS) analysis. The XPS patterns were recorded on an X-ray photoelectron spectrometer (Shimadzu, ESCA-1000) using MgKα X-ray as the excitation source and choose C1s (284.6 eV) as the reference line.

HeLa cells were cultured in minimum essential medium (MEM) solution with 10% newborn calf serum (NBS) in a humidified incubator with an atmosphere of 5% CO_2 in air at 37 °C. The HeLa cells were plated at a concentration of about $3x10^5$ in 60-mm petri dishes and allowed to grow for 3 days. The HeLa cell viability was examined by treating with nanocomposites under 24 h incubation in an incubator. A Xenon lamp with heat cut-off and band-pass filters (350-600 nm) with an average intensity of 30 mW cm^{-2} was used for the light irradiation on HeLa cells. The light power was measured by a spectroradiometer (Model LS-100, EKO Instrument Co., Ltd.). A table rotator was used for the Petri dish to confirm the homogeneous light irradiation on the cells. The images were taken using an Olympus inverted CKX41 microscope with a numerical light field condenser, which delivers a very narrow beam of white light from tungsten lamp on top of the sample. A 40x objective was used to collect the sample images.

12.3 Results and discussion

The Cu-TiO_2 composite nanoclusters were prepared in acetonitrile-water mixed solvent by electrostatic adsorption of $[CuNO_3]^-$ ion on the TiO_2 surface followed by reduction with $NaBH_4$. We reported that unlike water, acetonitrile prevents oxidation during the preparation of Cu nanoparticles to produce the stable copper nanoparticles at room temperature under argon gas atmosphere [23]. Therefore the presence of aprotic solvent (acetonitrile) is useful to protect the oxidation by OH^- ions as protecting solvent for the Cu nanoparticles [23, 24].

The absorption spectra of Cu-TiO_2 nanocomposite suspensions (Fig. 12-1A) show a strong absorption in the wide visible region with clear plasmonic peaks. The plasmonic peaks indicate that Cu is not oxidized, because the absence of plasmonic peak in the absorption spectra is associated with oxidation of Cu nanoparticles. These results imply that the Cu-TiO_2 nanocomposite may possess excellent photocatalytic performance in the visible-light region. The lower ratios of Cu:TiO_2 resulted in the obscurity of the surface plasmon band due to increase in excessive oxygen on the Cu nanoparticles surface (Fig. 12-1A, spectrum a). At higher ratios of Cu:TiO_2 the plasmon bands of Cu nanoparticles result in increase in the absorbance and broadening due to increase in the particle size (Fig. 12-1A (d and e). The results (Fig. 12-1A) indicate that by increasing the Cu content, the plasmon absorption of the Cu–TiO_2 nanocomposite increases with increasing Cu molar ratios.

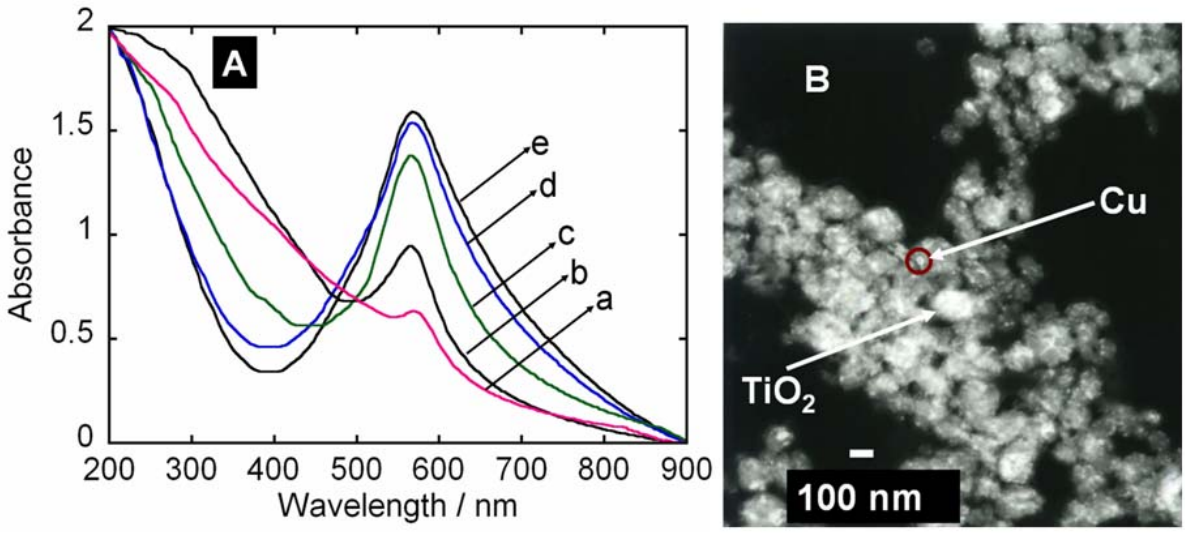

Fig. 12-1: (A) Absorption spectra of Cu-TiO_2 various colloid suspension nanocomposite in water-acetonitrile solution. The Cu:TiO_2 molar ratios were maintained at (a) 0.2:1, (b) 0.5:1, (c) 1:1, (d) 2:1 and (e) 5:1. (B) The Transmission electron microscope picture of Cu-TiO_2 nanocomposites. Cu nanoparticles (white spot) composited with TiO_2 particles are shown in the TEM image (Cu:TiO_2 = 1:1)

The TEM image shows the Cu nanoparticles (white spot) are fairly well dispersed on the TiO_2 surface with particles of overall diameter of 10-100 nm (see also the inset in Fig. 12-3A).

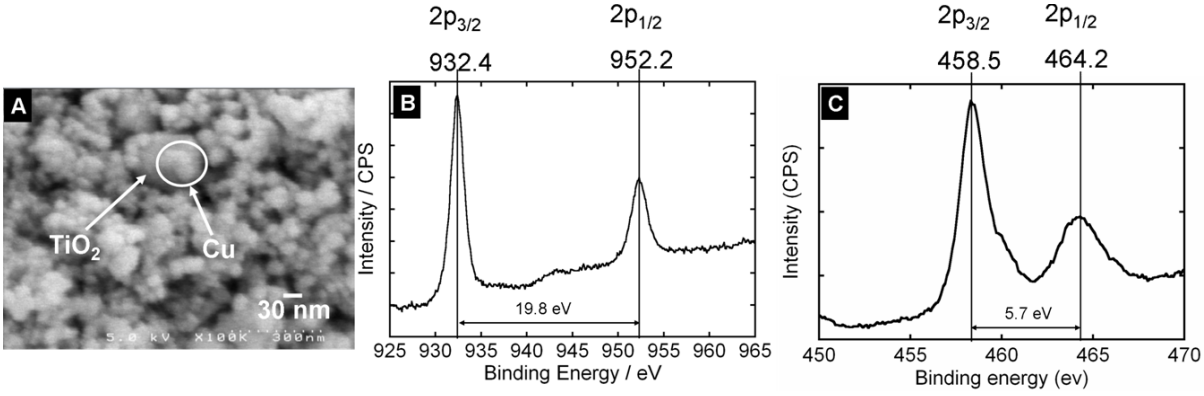

Fig. 12-2: (A) FE-SEM image of the Cu-TiO_2 nanocomposite morphology. The X-ray photoelectron spectroscopic scan survey in the region of (B) Cu 2p (C) Ti 2p of the as-prepared Cu-TiO_2 nanocluster (Cu:TiO_2 = 1:1).

As seen in Fig. 12-2 (A) the FE-SEM image of Cu-TiO_2 composite nanocluster shows that TiO_2 was uniformly covered by Cu nanoparticles. The presence of metallic copper was confirmed by the XPS analysis. The peaks observed $2p_{3/2}$ and $2p_{1/2}$ at 932.4 and 952.2 eV were ascribed to metallic copper (Fig. 2. B). The presence of TiO_2 was also determined by XPS as shown in Fig. 12-2 (C). The peak located at 464.2 eV corresponding to the Ti $2p_{1/2}$ and another one located at 458.5 eV is assigned to Ti $2p_{3/2}$. The splitting between Ti $2p_{1/2}$ and Ti $2p_{3/2}$ is 5.7 eV, indicating a normal state of Ti^{4+} in the as-prepared mesoporous TiO_2 [25].

EDX was employed to obtain the quantitative information on the amount and the distribution of copper and TiO_2 species in the sample. Fig. 12-3 (A) shows the EDX spectra of Cu-capped TiO_2 nanoclusters and it was found that the ratio of Cu:Ti:O is 16:18:66 (in %) and 35:30:35 (wt%) by using average values calculated in three different selected areas. The data indicate that the molar ratio of Cu and TiO_2 is about 1:1.

The wide-angle x-ray diffraction (XRD) patterns of Cu-TiO_2 and bare TiO_2 (P25) nanoclusters are shown in Fig. 12-3. (B). Compared with the bare TiO_2, the Cu-TiO_2 nanocomposite exhibits new peaks emerged at $2\theta = 43.473°$, 50.375°, 73.997°, 89.934° and

95.578° which can be attributed to the diffraction peaks of (1 1 1), (2 0 0), (2 2 0), (3 1 1) and (222) planes of polycrystalline Cu, (JCPDS, PDF, File No. 00-001-1241), respectively, demonstrating the formation of metallic Cu. Another peaks belonged to Cu_2O (JCPDS, PDF, File No. 01-071-3645) indicate that a small amount of Cu_2O coexists with copper particles in some samples. The coexisting Cu_2O may be formed due to the oxidation of some Cu in air.

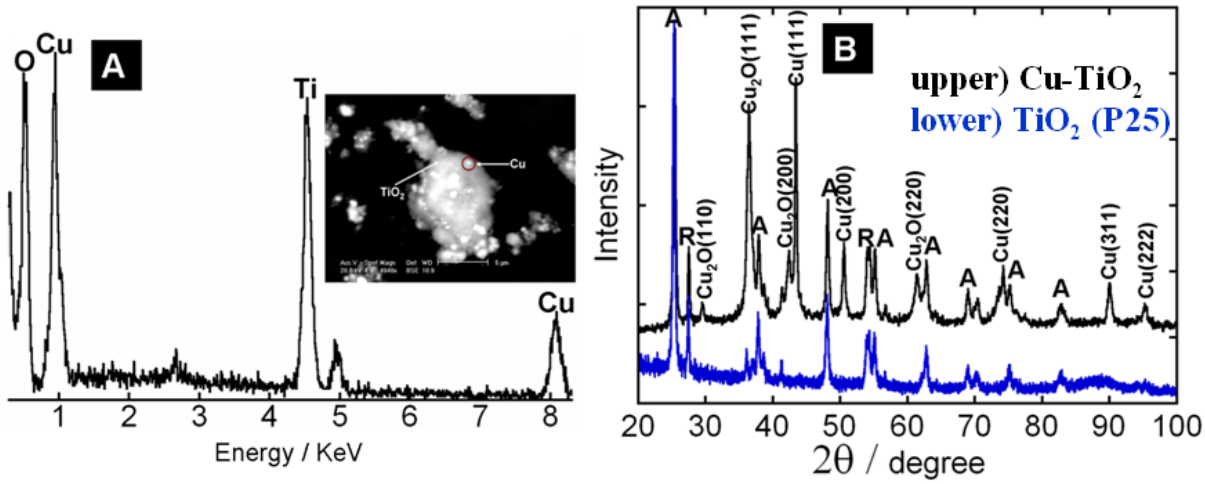

Fig. 12-3. (A) The EDX spectrum of Cu-TiO_2; the strong Cu and Ti signals in the EDX spectrum indicate that Cu is metallic and Ti consists of mixed oxides. Insets; cold–field SEM image showing Cu on the TiO_2 surface. (B) XRD pattern of Cu-TiO_2 composite nanocluster confirming the formation of pure metallic copper-TiO_2 semiconductor composite nanocluster with some partial Cu_2O. A: anatase, R: rutile. The Cu: TiO_2 molar ratio is 1:1 in (A) and (B).

Controlled experiments in the absence of Cu-TiO_2 and TiO_2 were done for the cancer cell killing under UV-visible light irradiation. In the ordinate of Fig. 12-4A and 4B, 100% mean the number of living cells in a control dish. To compare the cell killing ability of TiO_2 (P25) with Cu-TiO_2 nanoparticles, the cell dishes were incubated with different amounts of MEM containing colloidal nanoparticles solution (4, 8, 12, 16 and 20 μL). The cells were stained by the trypan blue indicator; the dead cell accumulates the dye, resulting in blue color, whereas the live

cells have no color. The cell viability was determined as the percentage of the number of the unstained cells against that of the control dish cells.

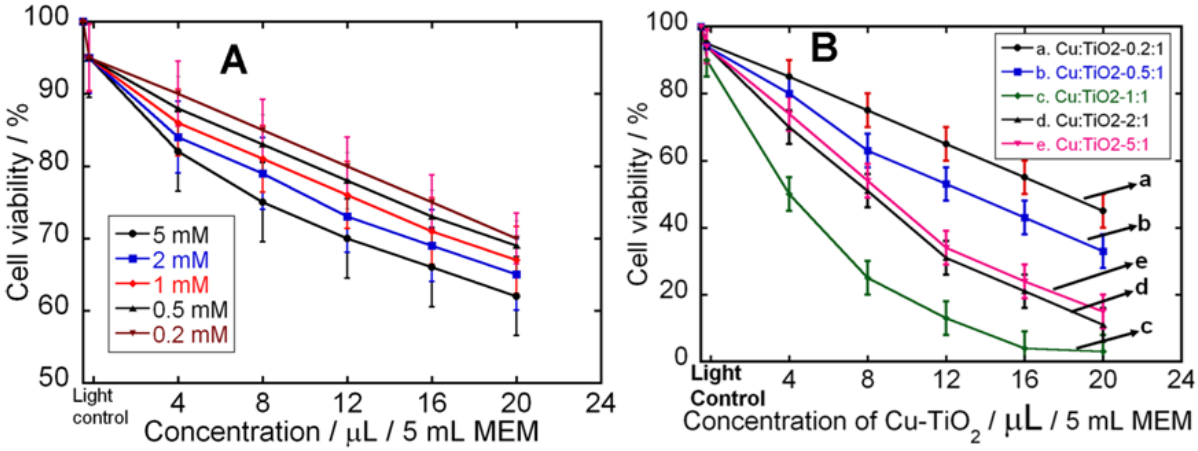

Fig. 12-4: Surviving fractions of HeLa cells incubated in MEM medium containing (A) TiO_2 and (B) Cu-TiO_2 nanocomposite. 100% show the control dish and the cell viability percentage was calculated using the number of live cells against the control dish cells. Bars represent margins of errors of 3 times measured data and each point represents the mean value of three data.

In the absence of light, the cells were found to be mostly viable (ca. 90-100%) under the incubated condition with the nanocluster colloidal solutions (Fig. 12-4A and 12-4B). However, after 5 min light irradiation, the amount of cell killed was maximally ca. 40% in 20 µL MEM containing only TiO_2 (Fig. 12-4A). The destructive cell killing effect was found in the presence of Cu- TiO_2 nanocomposites under light irradiation; maximum cells were killed rapidly. In the presence of 20 µL Cu-TiO_2 (1:1 molar ratio) under 5 min light irradiation almost 100% of the cells were killed (Fig. 12-4B), whereas in the same concentration of TiO_2 alone, ca. 40 % cells were killed (Fig. 12-4A). The error bars in Fig. 12-4 represent the maximum and minimum values of three independent experiments.

In the lower molar ratio region (ratio < 1:1), some Cu_2O particles may be formed and may cover the surface of TiO_2, which may lead to decrease in the photocatalytic cytotoxicity (Fig. 12-

4B). At the optimum ratio (1:1), the photothermal killing due to the plasmonic absorption (Fig.12- 1A) of Cu nanoparticles may also contribute to the cytotoxicity. However, in the higher molar ratio region (ratio > 1:1), excessive Cu nanoparticles obstruct the light absorption by TiO_2, which may also lead to decrease in the photocatalytic cell killing (Fig. 12-4B).

In the case of noble metal such as Cu, an electron from photoexcited TiO_2 is transferred to Cu and then initiates the redox reactions at the interface. The transfer of electrons from the excited TiO_2 into Cu continues until the systems attain equilibration. The electron accumulation increases the Fermi level of the composite so as to shift closer to the conduction band of the semiconductor [17-19, 26]. After the Fermi level equilibration, the photoinduced electrons can transfer to the surface of Cu nanoparticles and can easily reduce the dissolved O_2 as shown in Fig. 5. It is well known that molecular oxygen accepts the photogenerated electrons to form the superoxide anion (O_2^{-}) as shown in reaction (2). Generally, $O_2\cdot^{-}$ is less reactive and has a short lifetime and therefore the role of $O_2\cdot^{-}$ in succeeding reactions is not understood well [27].

$$(TiO_2)Cu + hv \rightarrow (TiO_2\ (e+h))\ Cu \quad (1)$$

$$(TiO_2\ (e))Cu + O_2 \rightarrow (TiO_2)\ Cu + O_2\cdot^{-} \quad (2)$$

The photogenerated holes on the TiO_2 surface can react with water to produce powerful oxidative radicals such as ·OH and $HO_2\cdot$ via reactions (3) and (4). While $O_2\cdot^{-}$ is not considered so reactive and further reduced slowly to H_2O_2 as shown in reaction (5) [28]. H_2O_2 is more reactive than $O_2\cdot^{-}$ and is easily decomposed to ·OH as shown in reaction (6) [29].

$$TiO_2\ (h) + H_2O \rightarrow \cdot OH + H^{+} \quad (3)$$

$$O_2\cdot^{-} + H^{+} \rightarrow HO_2\cdot \quad (4)$$

$$2HO_2\cdot \rightarrow O_2 + H_2O_2 \quad (5)$$

$$H_2O_2 + O_2\cdot^{-} \rightarrow \cdot OH + OH^{-} + O_2 \quad (6)$$

The highly oxidizable hydroxyl radicals (·OH), hydrogen peroxide (H_2O_2) and superoxide radicals ($O_2^{\cdot -}$) which are reported to be formed on the surface of photoexcited TiO_2 particles can be expected to be toxic to cells [27].

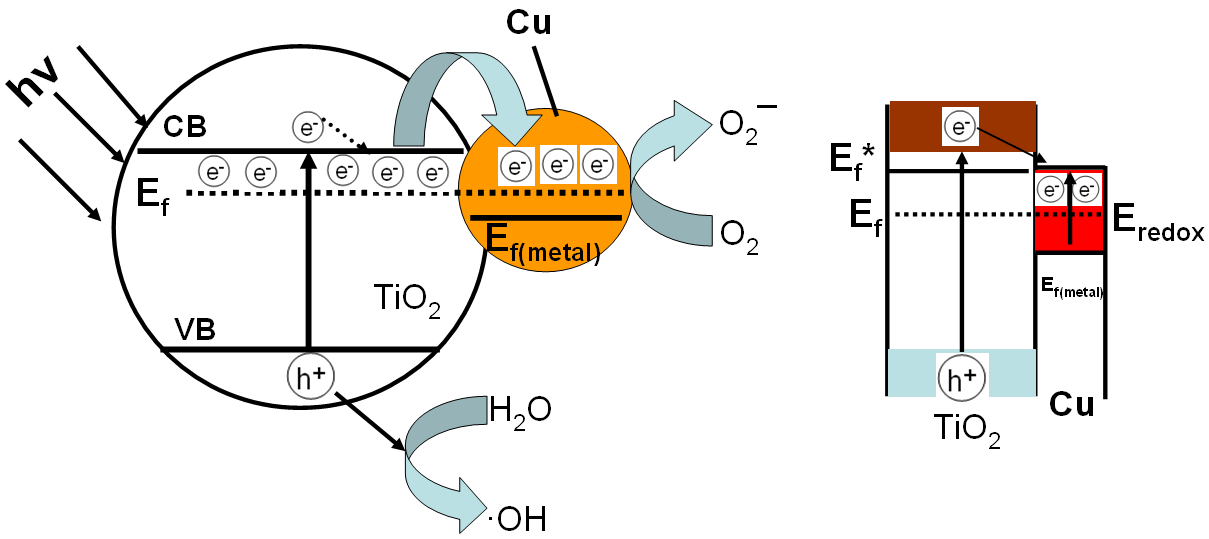

Fig. 12-5. Interfacial charge separation process of Cu-TiO_2 nanocomposites under irradiation of UV-visible (350-600 nm) light. Fermi level (E_f) equilibration of Cu-TiO_2 nanocomposites with the redox reaction after light irradiation. VB: valence band, CB: conduction band, e^-: electron, h^+: hole, E_f*: apparent Fermi level, E_f (metal): E_f of Cu.

The oxidation by the photogenerated holes and the radicals at the TiO_2 / Cu interface is an important process. It can be a major factor in determining the overall photocatalytic efficiency of Cu-TiO_2 nanocomposites. After the excitation the electrons migrate to Cu where they are trapped and the electron-hole recombination is suppressed. The hole is then free to diffuse to the TiO_2 surface where oxidation reactions can occur [30].

In the present Cu-TiO_2 nanocomposites, it is also reasonable to strongly suggest that the photothermal toxicity due to the plasmonic absorption of Cu nanoparticles also strongly

contributes to cytotoxicity against HeLa cells because Au nanoparticles, a noble metal, are known to show strong photothermal cytotoxicity [31].

Experiments to confirm the reaction mechanism, which were performed under dark conditions without light illumination, the cell killing effect was not observed for every measurement using TiO_2 particles or Cu-TiO_2 nanocomposite (data not shown). Light illumination in the absence of TiO_2 particles and Cu-TiO_2 nanocomposites did not result in the photocatalytic cell killing of HeLa cells. Therefore, the presence of both UV-visible light irradiation and TiO_2 particles or Cu-TiO_2 nanocomposites is essential for the efficient cell killing.

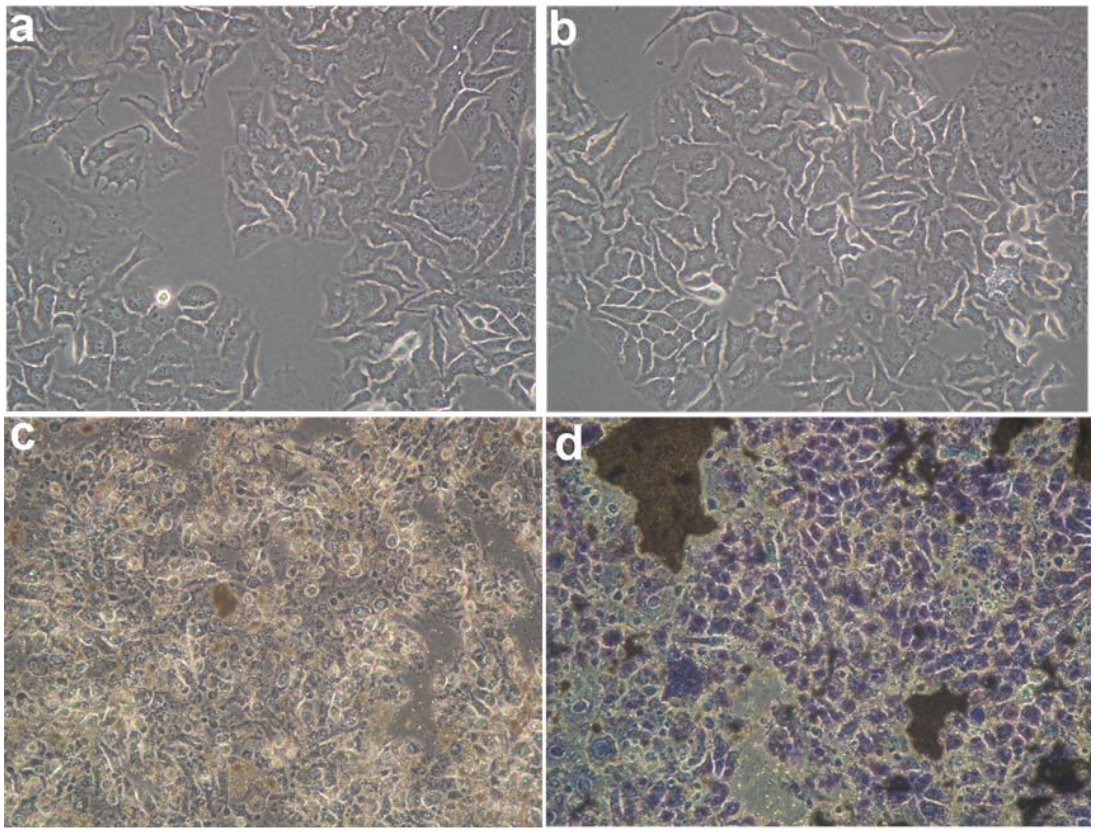

Fig. 12-6: Microscopic images of HeLa cells (Magnification 200). (a) With neither Cu–TiO_2 nanocomposites nor light. (b) After 5-min light irradiation without the nanocomposites. (c) After 5-min light irradiation with the nanocomposite. (d) Dead cells stained with trypan blue.

Fig. 12-6 shows microscopic images of HeLa cells before (a) and after (b)–(d) light irradiation. Fig. 12-6a and 6b show that the cell morphology is largely unchanged after 5-min irradiation. Fig. 12-6c shows that the HeLa cells suffer severe photochemical injury under 5-min irradiation with the Cu–TiO_2 nanocomposites where some red spots and aggregated particles are seen. It can be suggested from this image that the nanocomposites are taken up into or in contact with the cells, because these red spots are not observed when the nanocluster composites are not present in the medium (Fig. 12-6a and 12-6b). Thus, it is considered that the nanocomposites form aggregates in or on the cells. After light irradiation, cells were stained with trypan blue; cells stained blue (Fig. 12-6d) indicated the cell death.

12.4 Concluding Remarks

We have shown that under UV-visible light irradiation, the much deposition of Cu nanoparticles on TiO_2 induces the significant photocatalytic effect. The Cu-TiO_2 nanocomposites gave better results for the photocatalytic cell killing. Comprehensive studies are underway in our laboratory to further reveal the mechanism for the synergy effect of Cu nanoparticles enhancing the photocatalytic activity of TiO_2 against cancer cells.

References

[1] M. Anpo, M. Takeuchi, J. Catal. 216 (2003) 505.

[2] A. Dawson, P. V. Kamat, J. Phys. Chem. B 105 (2001) 960.

[3] M. Bowker, D. James, P. Stone, R. Bennett, N. Perkins, L. Millard, J. Greaves, A. Dickinson, J. Catal. 217 (2003) 427.

[4] J.M. Herrmann, J. Disdier, P. Pichat, J. Catal. 113 (1988) 72.

[5] E. Stathatos, P. Lianos, P. Falaras, A. Siokou, Langmuir 16 (2000) 2398.

[6] T.G. Schaaff, D.A. Blom, Nano. Lett. 2 (2002) 507.

[7] B. Sun, A.V. Vorontsov, P.G. Smirniotis, Langmuir 19 (2003) 3151.

[8] S. Kim, W. Choi, J. Phys. Chem. B 106 (2002) 13311.

[9] S. Jeon, P.V. Braun, Chem. Mater. 15 (2003) 1256.

[10] S. Klosek, D. Raftery, J. Phys. Chem. B 105 (2001) 2815.

[11] A. Patra, C.S. Friend, R. Kapoor, P.N. Prasad, Chem. Mater. 15 (2003) 3650.

[12] J. Premkumar, Chem. Mater. 16 (2004) 3980.

[13] J.D. Bryan, S.M. Heald, S.A. Chambers, D.R. Gamelin, J. Am. Chem. Soc. 126 (2004) 11640.

[14] P. V. Kamat, Chem. Rev. 93 (1993) 267.

[15] J. A. Bard, J. Phys. Chem. 86 (1982) 172.

[16] G. Burgeth, H. Kisch, Coord. Chem. Rev. 230 (2002) 40.

[17] A. Wood, M. Giersig, P. Mulvaney, J. Phys. Chem. B 105 (2001) 8810.

[18] M. Jakob, H. Levanon, P. V. Kamat, Nano Lett. 3 (2003) 353.

[19] V. Subramanian, E. E. Wolf, P. V. Kamat, J. Phys. Chem. B 107 (2003) 7479.

[20] M. Bideau, B. Claudel, L. Faure, M. Rachimoellah, Chem. Eng. Commun. 93 (1990) 167.

[21] K.I. Okamoto, Y. Yamamoto, H. Tanaka, M. Tanaka, A. Itaya, Bull. Chem. Soc. Jpn. 58 (1985) 2015.

[22] D. Hufschmidt, D. Bahnemmann, J.J. Testa, C.A. Emilio, M.I. Litter, J. Photochem. Photobiol. A: Chem. 148 (2002) 223.

[23] M. Abdulla-Al-Mamun, Y. Kusumoto, M. Muruganandham, Mater. Lett. 63 (2009) 2007.

[24] M. Abdulla-Al-Mamun and Y. Kusumoto, Chem. Lett. 38 (2009) 826.

[25] C. D. Wagner, W. M Riggs, L.E Davis, S.F Moulder, G.E. Mullenberg, Handbook of x-ray photoelectron spectroscopy (Perkin-Elmer corporation, Physical Electronics Division, New York, 1979).

[26] V. Subramanian, E. E. Wolf, P. V. Kamat, J. Am. Chem. Soc. 126 (2004) 4943.

[27] R. Cai, Y. Kubota, T. shuin, H. Sakai, K. Hashimoto, A. Fujishima, Cancer Research 52 (1992) 2346.

[28] J.R. Harbour, J. Tromp, M. L. Hair, Can. J. Chem. 63 (1985) 204.

[29] M. Fujihira, Y. Satoh, T. Osa, Nature, 293 (1981) 206.

[30] Amy L. Linsebigler, G Lu, Jr. John T. Yates, Chem. Rev. 95 (1995) 735.

[31] M. Abdulla-Al-Mamun, Y. Kusumoto, A. Mihata, M. S. Islam, B. Ahmmad, Photochem. Photobiol. Sci. 8 (2009) 1125

CHAPTER 13

SYNERGISTIC CELL-KILLING BY PHOTOCATALYTIC AND PLASMONIC PHOTOTHERMAL EFFECTS OF Ag@TiO_2 CORE-SHELL COMPOSITE NNANOCLUSTERS AGAINST HUMAN EPITHELIAL CARCINOMA (HeLa) CELLS

Abstract

The Ag metal core-TiO_2 shell (Ag@TiO_2) composite nanocluster with uniform size, shape and core-shell structures was successfully synthesized by a new simple citrate reduction method. The core-shell structure of Ag@TiO_2 nanocluster was characterized by using TEM, SEM, XPS, EDX, XRD, and photoluminescence spectra analysis. It was found that the Ag core is in metallic form which is covered by TiO_2 shell within 3-5 nm thickness and the core-shell particles size was about 30 nm. The photocatalytic and photothermal cell killing efficiency of colloidal Ag@TiO_2 core-shell nanocluster was evaluated against cancer (HeLa) cells under UV–vis irradiation. It was found that the Ag@TiO_2 nanocluster with an adequate Ag ratio to TiO_2 killed more malignant (HeLa) cells by 80% compared to TiO_2 nanoparticles alone. The comparative study of the cell viability using UV only, visible only and UV-visible light revealed that the synergy effect of photocatalytic hydroxyl radical formation and Ag-plasmonic photothermal generation plays a vital role for the cancer cell killing. Based on the obtained results, a plausible mechanism was also proposed. This work has already published in Applied Catalysis: A General, 2001, 398, 134-142.

13.1 Introduction

Metal nanoparticles such as Au and Ag play an important role on semiconductor to enhance the photocatalytic activity. They also exhibited the electric, magnetic, and optical properties [1-3] and were also widely exploited for use in photocatalytic degradation of organic contaminants in polluted air and waste water [4-6]. The doping of metal ions such as Pt^{4+}, Ir^{4+}, Rh^{3+}, Au^{3+}, Pd^{2+}, Co^{2+} and Ni^{2+} into TiO_2 directly influences the intrinsic properties of TiO_2 and extends its catalytic photoresponse into the visible region [7]. Metal nanoparticles deposited to TiO_2 nanostructures undergo Fermi level equilibration following the UV-excitation and enhance the efficiency of charge-transfer process [8,9]. Charge recombination or the grain boundary of heterogeneous semiconductor often limits the efficiency of light energy conversion. The semiconductor-metal composites system can suppress the charge recombination and enhance the energy conversion efficiency [10]. In the semiconductor-metal nanoclusters system metal nanoparticles are dispersed on oxide surfaces. The photogenered electrons of TiO_2 are capable to reduce the metal nanoparticles, depending on reactants and surrounding media. Corrosion or dissolution of the noble metal particles during the photocatalytic reaction is likely to limit the use of noble metals such as Ag and Au [11-13]. A better synthetic design can significantly improve the catalytic performance of metal-oxide composites. Hirakawa et al. [3] found that the metal core-TiO_2 outer shell semiconductor is a superior catalyst in terms of photocatalytic properties such as photoinduced charge separation, band gap excitation and charge equilibrium in the Fermi level as well as core-shell structures.

Generally Ag nanoparticles are chemically very reactive; it can be oxidized at direct contact with TiO_2 to produce silver oxide (Ag_2O). For this problem to prevent the oxidation we have been introduced the very simple new method to prepare $Ag@TiO_2$ by citrate reduction. The

citrate can cap the Ag nanoparticles and hydrolysis of titanium (IV) (triethanolaminato) isopropoxide can condense rapidly in boiling temperature on the Ag nanoparticles surface under N_2 purge and UV irradiation in solution to give the Ag metal core-TiO_2 shell structure.

Ag@TiO_2 has been successfully used to enhance the photocatalytic decomposition of organic compounds and photokilling of bacteria [14-16]. One of the transition noble metal of Au nanoparticles has also been successfully used for photothermal cancer (HeLa) cell killing in vitro experiment [17]. It is suggest that the photothermal toxicity due to the plasmonic absorption of Ag nanoparticles also strongly contributes to cytotoxicity on cancer cells. The photocatalytic cancer cell (HeLa) killing efficiency due to the synergistic effect of plasmon excited metal nanoparticles with excitation of electron-hole pairs in TiO_2 have never been reported to the best of our knowledge. In a preliminary communication we reported the ability of the Ag@TiO_2 nanocomposite clusters to kill cancer cells under UV-visible light irradiation [18]. Here we report the photocatalytic effect of Ag@TiO_2 on cancer (HeLa) cells at several TiO_2 concentrations and also at different molar ratios of Ag to TiO_2. We found that the photocatalytic cytotoxicity of Ag@TiO_2 required only one-fourth the irradiation time required by TiO_2 alone and that the killing efficiency of Ag@TiO_2 was more than three times higher than that of TiO_2 alone at the same concentration. The cancer cell killing efficiency factors that control the photocatalytic and plasmonic properties of core-shell nanostructures are also discussed.

13.2 Experimental

13.2.1 Chemicals and materials

Titanium (IV) (triethanolaminato)-isopropoxide ($N((CH_2)_2O)_3TiOCH(CH_3)_2$) (TTEAIP) (80 wt % solution in 2-propanol) was purchased from Aldrich. $AgNO_3$ (99.8%) and sodium citrate (99.0%) were purchased from Wako Pure Chemical Industries, Ltd. TiO_2 (Degusa, P25) was

used with a mainly anatase structure (ca. 80%) under the shape of non-porous polyhedral particles of ca. 20 nm mean size with surface area of 49.9 m^2/g.

13.2.2 Synthesis of Ag@TiO_2 Core-shell Nanocluster

The Ag@TiO_2 core-shell nanocluster was prepared from $AgNO_3$ salt and titanium (IV) (triethanolaminato)-isopropoxide (TTEAIP). $AgNO_3$ and TTEAIP were used as sources of Ag and TiO_2. Five different suspensions of Ag@TiO_2 nanoclusters were prepared by keeping the $AgNO_3$ concentration constant at 1mM while varying the TTEAIP concentration at 1,3,5,7 and 9 mM. These five Ag/TiO_2 suspensions gave [Ag]:[TiO_2] ratios of 1:1, 1:3, 1:5, 1:7 and 1:9. All concentrations are based on molar concentrations.

Ag@TiO_2 core-shell nanoclusters were prepared by adding 1 mM (1 M = 1 mol/dm^3) of $AgNO_3$ to the millipore distilled water under vigorous stirring at 60 °C constant temperature. TTEAIP of different molar concentrations and 2 ml of 1% sodium citrate were added to $AgNO_3$ solution. The solution was stirred for additional 15 min to allow complete core-shell formation. The temperature of the mixture was increased to boiling temperature under vigorous stirring. With continued heating of the solution, the color slowly changed from colorless to light brown. After 90 min, the color of the suspension turned from light to dark brown. After that, the sample suspension was cooled at room temperature. All solutions used were freshly prepared and kept stirring in a closed flask until the next step.

Next the solution was transferred to a conical flask with a rubber septum and the solution was purged with N_2 gas. Then the solution was irradiated with ultraviolet light (15 mW cm^{-2}) for at least 30 min to reduce any unreacted Ag^+ in solution to Ag°. Then the solution was centrifuged at 5000 rpm for 20 min. The precipitate nanocluster was washed two times with millipore water and one time with ethanol to remove the remaining citrate solution and minimize the water

content. After the supernatant was removed, clusters were collected and sterilized in an autoclave. Then the composite nanoclusters were dispersed in 5 mL MEM (minimum essential medium) solution and stored at 4 °C.

13.2.3 TiO_2 Powder

TiO_2 powder was prepared by changing temperature in the TTEAIP gel between 350 and 400 ºC. A gel was obtained by evaporation of the TTEAIP solvent using an evaporator at 80 ºC, and was heated at 150 ºC for 60 min before undergoing firing in furnace. The TiO_2 powder was used for comparisons between Ag@TiO_2 and TiO_2 (TTEAIP at 350 ºC).

13.2.4 Instrumental analysis

Absorption spectra were recorded on a UV-visible spectrophotometer (Shimadzu Corporation, MPS-2000, Japan) using a 1 cm path-length quartz cuvette. The size and shape of the nanocluster is analyzed by a transmission electron microscope (TEM) using a JEOL, JEM-3010 VII, TEM operating at 300 kV. Samples for TEM were prepared by ultrasonically dispersing in absolute ethanol, then placing a drop of this suspension onto a carbon coated copper grid and then dried in air. The nanocluster surface was also analyzed by a field-emission scanning electron microscope (FE-SEM, Hitachi, S-4100H), X-ray photoelectron spectroscopy (XPS, Quantum-2000, Scanning ESCA-1000 microprobe with Magnesium α radiation, Shimadzu) and X-ray diffraction (XRD, PANalytical) analyzer. Prior to FE-SEM measurements, the sample solution was dropped on a glass plate and then dried in air for approximately one week. Then the glass plate containing sample was coated with platinum by using a magnetron sputter and placed in the SEM for the analysis with desired magnifications. The XRD patterns were recorded using a X'Pert PRO PANalytical diffractometer over the scanned angle from 10 ° to 100 ° at a scanning rate of 3 °

per minute. The X-ray photoelectron spectra were collected on an ESCA-1000 X-ray photoelectron spectrometer (XPS), using Mg Kα X-ray as the excitation source. The quantitative chemical composition of the $Ag@TiO_2$ composite nanocluster surface was also measured using an energy dispersive X-ray spectrometer EDX (Energy Dispersive using X-ray, Philips, XL 30CP, microscope working at 15 kV) attached to the cold field SEM. The confirmation of oxidative cell killing by formation of hydroxyl radicals (·OH) on the surface of UV-visible illuminated $Ag@TiO_2$ was detected by a photoluminescence (PL) technique (Shimazu, RF-5300PC) with terephthalic acid as a probe molecule.

13.2.5 Cell Culture and Cell Incubation with Colloidal Nanoclusters

Cell line and counting method

A typical cancer cell line, Human Cervix Epitheloid Carcinoma (HeLa), was used in this study. The cells were cultured in minimum essential medium (MEM, Sigma, eagle) plus 10% new born calf serum (NBS, Invitrogen Corporation, Gibco) at 37 °C under 5% CO_2. The cells were plated at a concentration of about $3x10^5$ in 60-mm Petri dishes and were allowed to grow for 3 days. The old culture medium was replaced with nanocluster colloidal solution and recultured for 24 hours in an incubator. The colloidal solution was removed, and washed with phosphate buffer saline (PBS, Invitrogen Corporation, Gibco). After the cells were cleaved by Trypsin-EDTA (Gibco) and cells were stained with trypan blue (Nacalai Tesquse, Inc., Kyoto, Japan). Then, the cells were counted under 10x in bright field microscope (Olympus, CKX41). The cell survival was determined as the percentage of the number of unstained (Live) cells against the control dish cells.

Light Irradiation of MEM Containing Colloidal Nanocluster on Cells

In photocatalytic experiments, a xenon lamp (Inotech, LX300F, Japan) was used. The light wavelength was 350-600 nm (Asahi Techno glass, V-B46 as a band pass filter) and passed through a heat cutoff filter. The light power was measured by using a spectroradiometer (model LS-100, EKO Instruments Co. Ltd.). The power of light was 35mW/cm^2 and irradiation time was 5 min for each dish. A table rotator was used for the Petri dish to ensure the homogeneous light irradiation on the cells. The medium of cells cultured for 3 days was replaced with colloidal nanocluster solution, and then the cells were incubated for 24 hours. One dish only was photoirradiated without nanocluster solution (light control dish) and other dishes were photoirradiated with different quantities of colloidal nanocluster solution. The colloidal solution was removed, and washed with phosphate buffer saline (PBS) and then stained with trypan blue to evaluate the cell viability. Dead cells accumulated the dye were stained with blue color while living cells have no color. The living cells were counted as the percentage against the control dish cells.

Cells Imaging Method

The images were taken using an inverted Olympus CKX41 microscope with a numerical light field condenser (N.A.0.3), which delivers a very narrow beam of white light from tungsten lamp on top of the sample. A 40x objective was used to collect only the scattered light from the samples. The light field pictures were taken using an Olympus digital camera (Model No. C-5060, wide Zoom).

13.3 Results and discussion

13.3.1 Synthesis and Characterizations of Ag@TiO_2 Core-shell Nanocluster

The citrate reduction method was used to obtain the silver nanoparticles from silver nitrate which yield uniform particles size with of titanium (IV) (triethanolaminato)-isopropoxide

(TTEAIP) in boiling temperature. It has been demonstrated that the colloidal Ag@TiO_2 suspension is very stable than the one pot synthesis of Ag@TiO_2 by the dimethylformaamide (DMF) reduction. It is important that the reduction rate of Ag^+ ion is faster than the rate of formation of a TiO_2 shell [3]. We optimized the several batch preparations and found that temperature is suitable at 60 °C for Ag@TiO_2 core-shell nanocluster formation. The Ag^+ ions were reduced by sodium citrate to form Ag nanoparticles and may quickly interact with the amine group of TTEAIP. The reduction rate of Ag^+ to Ag° and hydrolysis of TTEAIP were rapidly improved to make TiO_2 shell formation on Ag particles core with increasing temperature to boiling temperature. It is very important to care the Ag particles, because it can be oxidized when contacting the surface oxygen of TiO_2. But, in the presence of sodium citrate a silver colloidal nanoparticle were coated thickly and homogeneously and was protected against the oxidation [19, 20]. The suspension was then heated for another 1 h leading to color change to dark brown. We purged the N_2 gas into suspension and irradiated UV light to remove the any Ag^+ ions remaining in solution or any layer of oxide on the silver surface. The UV irradiation and N_2 purging enabled to make the TiO_2-saturated Ag@TiO_2 nanocluster suspension. Finally, the suspension was centrifuged to remove water from the Ag@TiO_2 core-shell nanocluster suspension.

The stability of Ag@TiO_2 core-shell structure was tested by suspending in the nitric acid at pH 2. The Ag cluster, stabilized by nitric acid, is readily dissolved in acidic solution (pH 2). The prepared Ag@TiO_2 colloidal nanoclusters remained stable in acid solution. The stability test in acidic solution asserts the argument that the TiO_2 shell around the Ag core is uniform and also it provides the protection against acid-induced corrosion.

13.3.1.1 UV-visible Absorption Spectra

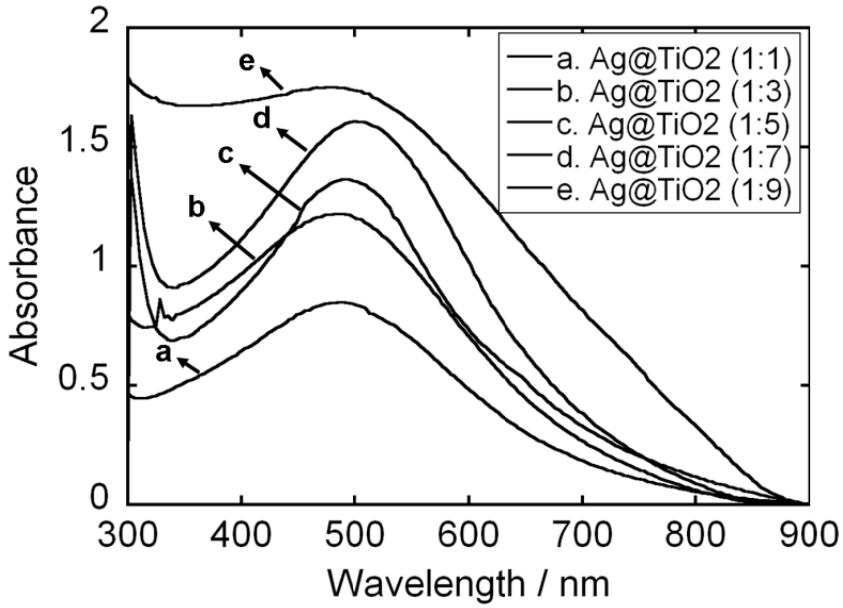

Fig. 13-1: Absorption spectra of Ag@TiO_2 various colloidal composite nanoclusters suspensions in water. The Ag: TiO_2 molar ratios were maintained at (a) 1:1, (b) 1:3, (c) 1:5, (d) 1:7 and (e) 1:9.

UV-visible absorption spectra of Ag@TiO_2 colloidal nanocluster suspensions with different TiO_2 contents as well as TTEAIP contents are shown in Fig. 13-1. Ag@TiO_2 shows the strong absorption in the visible region with plasmonic peaks. The presence of plasmonic peaks in curves shows that the Ag core is not oxidized, because the absence of any plasmonic peak in curves is associated with the oxidation of Ag nanoparticles [21]. This visible absorption arises from the surface plasmon band of Ag core and is strongly influenced by the oxide shell. At lower concentrations of TiO_2 shell, dampening and broadening of the surface plasmon bands (Fig.13-1, spectra a and b) were observed and at a higher concentration of TiO_2 shell the plasmon band of Ag core (Fig.13-1, spectrum e) was obscured. It is interesting to note that increase in the shell thickness is due to increase in the concentration of the precursor of TiO_2. We found the optimized shell thickness with uniform covering of Ag@TiO_2 at 1:5 and 1:7 molar ratios.

The $Ag@TiO_2$ catalyst exhibited strong absorption bands in the visible region and the maximum was found at about 500 nm. The TiO_2 lattice with some metal ions may introduces new energy levels in the band gap. The UV-visible diffuse reflectance spectroscopy was employed to estimate the band-gap energies of the prepared $Ag@TiO_2$ nanocomposites. Firstly, to establish the type of band-to-band transition in these synthesized particles, the absorption data were fitted to equations for direct band-gap transitions. The minimum wavelength required to promote an electron depends upon the band-gap energy Eg (in eV) of the photocatalyst and is given by $\lambda = 1240 / Eg$ where λ is the wavelength in nanometers [22]. The band gap excitation of $Ag@TiO_2$ at 2.50 eV undergoes charge separation in the redox process at the TiO_2 shell interface at about 500 nm.

13.3.1.2 TEM analysis

The $Ag@TiO_2$ core-shell structures were confirmed by transmission electron micrograph (TEM) images and are shown in Fig. 13-2. The milky colored spots represent Ag nanoparticles covered with a TiO_2 layer as shown in Fig. 13-2 (a). The TEM image shows that $Ag@TiO_2$ forms a well-dispersed core-shell structure. These core-shell composite nanoclusters are mostly spherical and overall diameters were 20-40 nm. The round dark structures of TiO_2 shell on the Ag core are evident and the shell is uniformly covered on the core (Fig. 13-2 b). All Ag core particles have an uniform thin capping of TiO_2 and the shell thickness is in the range of about 3-5 nm.

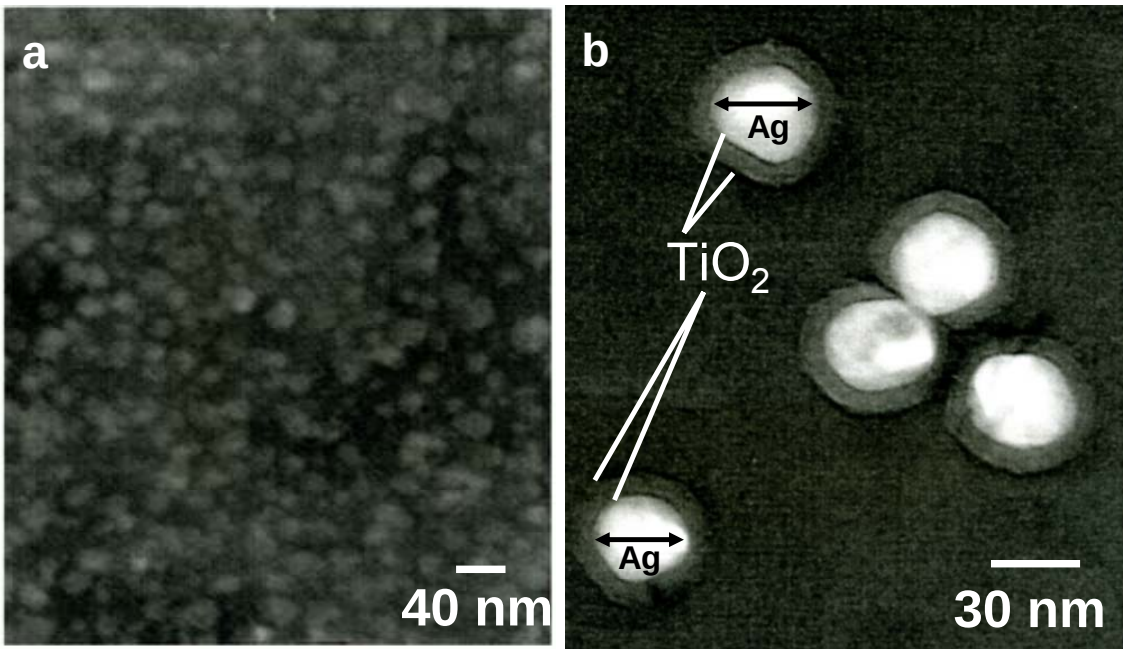

Fig. 13-2: Transmission electron micrograph of Ag@TiO_2 composite nanocluster. (a) Ag is uniformly covered by TiO_2 layer (milk spot). (b) Ag@TiO_2 showing the well crystalline nature of Ag metallic core and the uniform shell thickness of TiO_2. The Ag: TiO_2 molar ratio is 1:7 in (a) and (b).

13.3.1.3 SEM and XPS Analysis

The FE-SEM image of Ag@TiO_2 core-shell composite nanocluster (Fig. 13-3 (a)) shows that Ag was covered with TiO_2 nanocluster and the particles diameter is about 30 nm. The presence of metallic Ag core was confirmed by X-ray photocelectron spectroscopy (XPS) analysis. The peaks observed $3d_{3/2}$ and $3d_{5/2}$ at 373.9 and 367.9 eV were ascribed to metallic silver (Fig. 13-3 (b)). XPS analysis results of TiO_2 are shown in Fig. 13-3 (c). The peak located at 464.2 eV is assigned to Ti $2p_{1/2}$ and another one located at 458.5 eV to Ti $2p_{3/2}$. The splitting width between Ti $2p_{1/2}$ and Ti $2p_{3/2}$ is 5.7 eV, indicating a normal state of Ti^{4+} in as-prepared mesoporous TiO_2 [23].

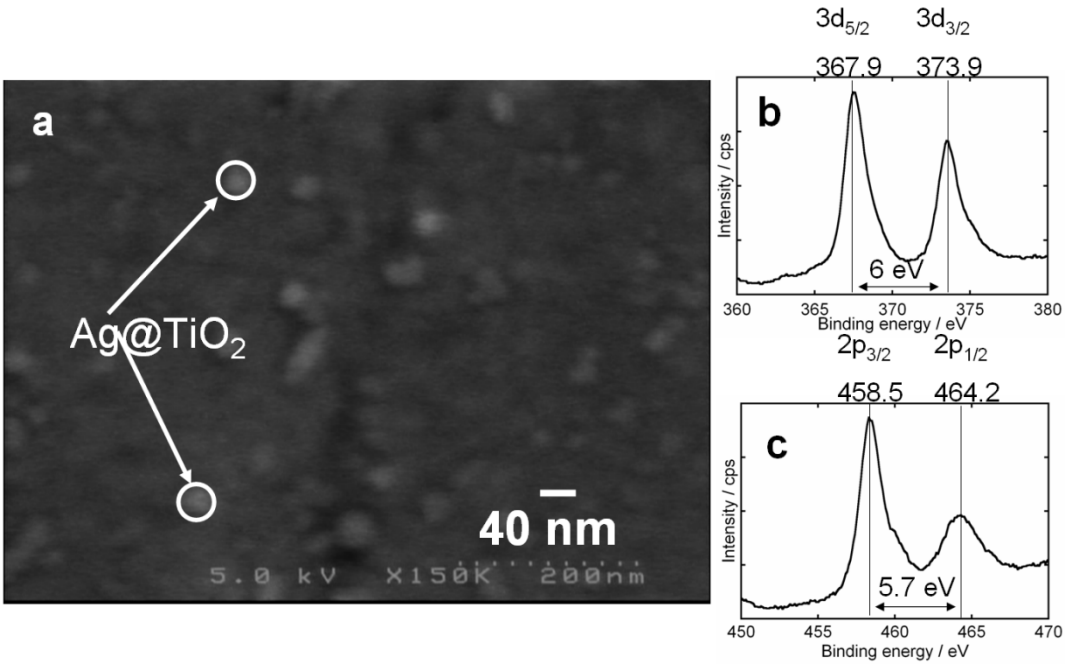

Fig. 13-3: (a) FE-SEM image of $Ag@TiO_2$ nanocluster morphology. The X-ray photoelectron spectroscopic scan survey in the region of (b) Ag 3d and (c) Ti 2p of the as-prepared $Ag@TiO_2$ nanoclusters. The Ag: TiO_2 molar ratio is 1:7.

The full-range survey of XPS spectra of naked TiO_2 (P25), naked TiO_2 (TTEAIP at 350 ºC) and $Ag@TiO_2$ is shown in Fig. 13-4. The naked TiO_2 (P25) and naked TiO_2 (TTEAIP at 350 ºC) samples contain Ti, O, and C elements, with sharp photoelectron peaks appearing at binding energies of 458 (Ti2p), 531 (O1s) and 285 eV (C1s), respectively. The carbon peak is attributed to the residual carbon from the sample and/or adventitious hydrocarbon from the XPS instrument itself. No residual nitrogen was detected in the $Ag@TiO_2$ sample, indicating that the complete reduction of the $AgNO_3$ precursor occurs during reduction and hydrolysis. It is clearly shown in Fig. 13-4 c that Ag $3d_{5/2}$ and Ag $3d_{3/2}$ have relatively intense signals with corresponding peaks at 367.9 and 373.9 eV, respectively. On the contrary, the $Ag@TiO_2$ samples contain not only Ti, O, and C, but also have the metallic Ag element, consistent with that observed in TiO_2-supported

metal catalysts. No peak corresponding to Ag_2O (367.8 eV) or AgO (367.4 eV) was observed, indicating that Ag species on TiO_2 nanostructures is of metallic nature [24, 25]. These results are also in good agreement with the XRD ones. The quantitative amounts of Ag, Ti, and O elements in Ag@TiO_2 nanocomposites (1:7 ratio) were characterized by XPS and their atomic percentage was 2.36, 16.00, and 52.86%; also mass percentage was 9.36, 28.09, and 31.00 %, respectively.

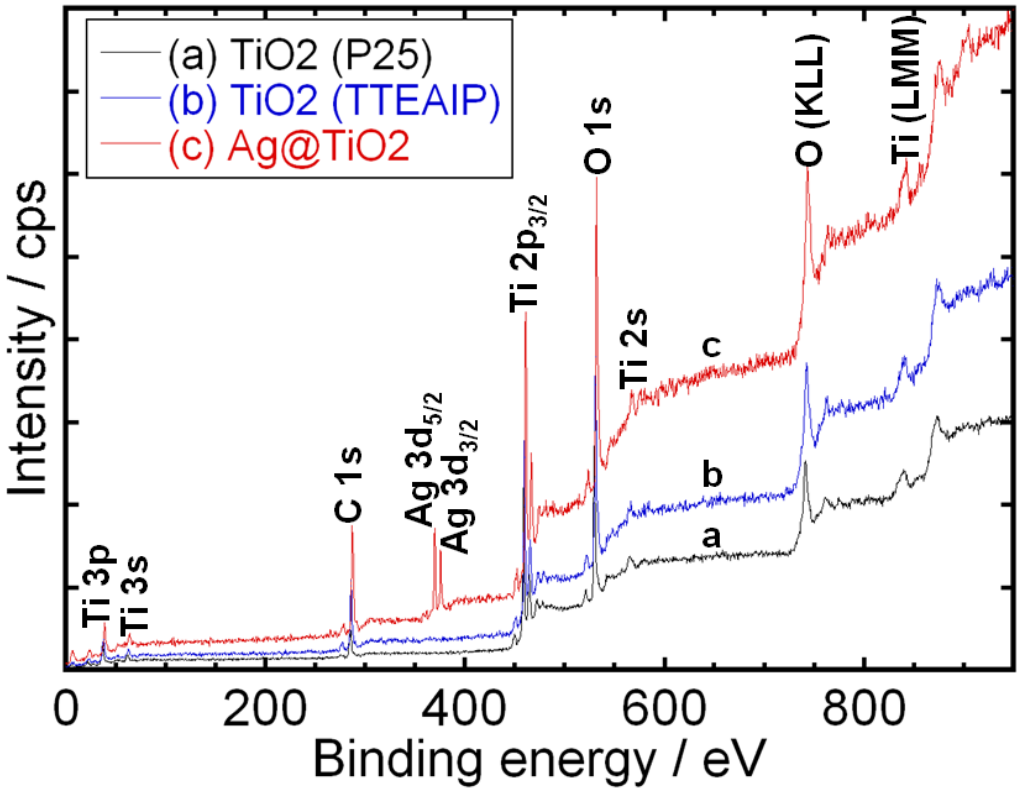

Fig. 13-4: XPS survey spectra of (a) naked TiO_2 (P25), (b) naked TiO_2 (TTEAIP at 350 ºC) and (c) Ag@TiO_2 core-shell nanocomposites.

13.3.1.4 EDX Analysis

EDX was employed to obtain the quantitative information on the amount and the distribution of silver and TiO_2 species in the sample. The EDX analyses show the presence of silver, titanium and oxygen as part of the composition of the material (Fig. 13-5(a and b)). Fig. 13-5(a) shows the TiO_2 uniformly covered on Ag nanoparticles and Fig. 13-5(b) shows the EDX spectrum of

$Ag@TiO_2$. It is clear that the molar ratio of Ag:Ti : O is 13.42 : 21.38 : 65.2, which is in agreement with stoichiometry of $Ag@TiO_2$ at a 1:7 molar ratio.

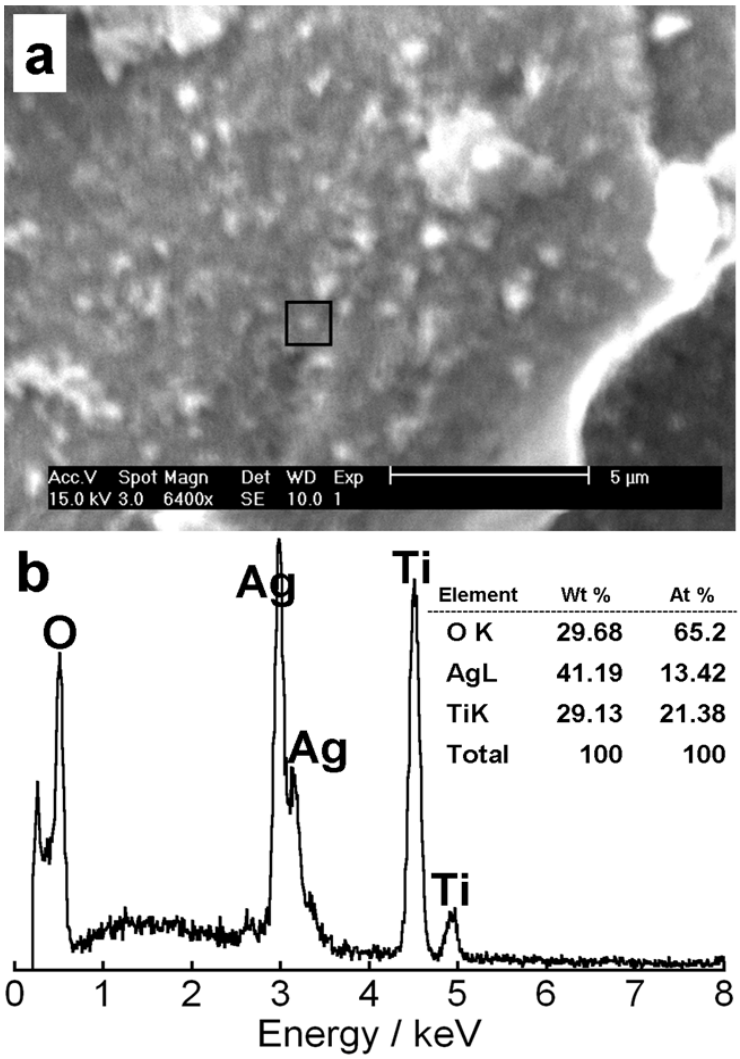

Fig. 13-5: EDX spectra of $Ag@TiO_2$. The strong Ag and Ti signals in the EDX spectrum indicate that Ag is metallic and Ti consists of mixed oxides. The Ag: TiO_2 molar ratio is 1:7 in (a) and (b).

13.3.1.5 XRD Analysis

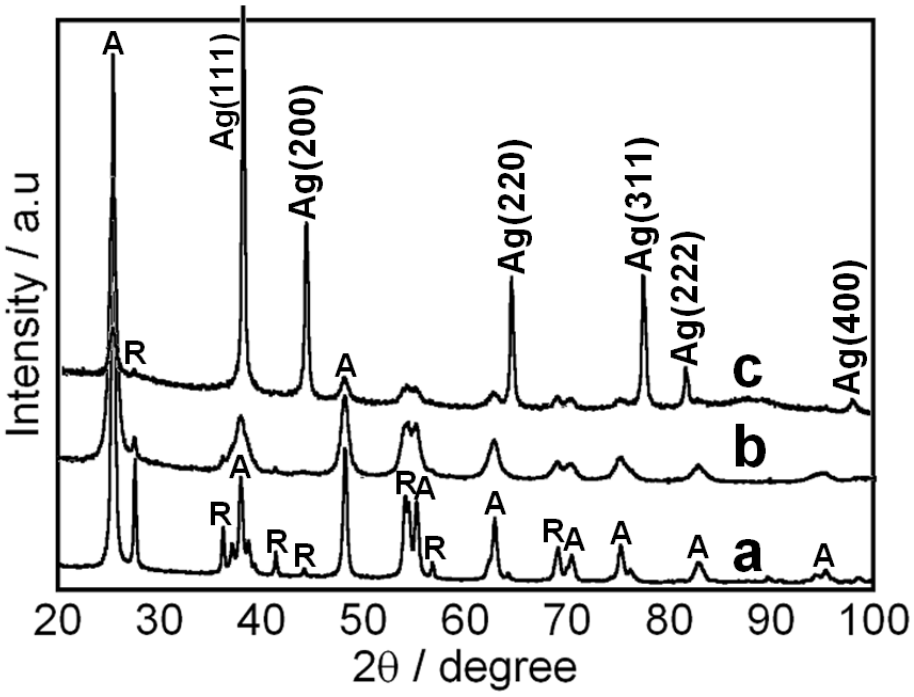

Fig. 13-6: X-ray diffraction patterns of (a) naked TiO_2 (P25), (b) naked TiO_2 (TTEAIP at 350 ºC), and (c) Ag@TiO_2 core-shell nanocomposites, confirming the formation of pure metallic-Ag@TiO_2 nanocomposites. A: anatase, R: rutile. The Ag:TiO_2 molar ratio is 1:7 in pattern (c).

The wide-angle X-ray diffraction (XRD) patterns of Ag@TiO_2, TiO_2 (TTEAIP at 350 ºC) and TiO_2 (P25) nanoclusters are shown in Fig. 13-6. Compared with the bare TiO_2, the Ag@TiO_2 nanoclusters exhibit new peaks at 38.09 (111), 44.28 (200), 64.42 (220), 77.36 (311), 81.54 (222) and 97.90º (400 plane) which belong to metallic silver, indicating that Ag is in metallic form (JCPDS, PDF, File No. 01-073-6859). No appearance of silver oxide-characteristic peak indicates that Ag° exists in the crystal lattices of TiO_2. It is very difficult to identify the shell TiO_2 in the XRD analysis because of relative intense Ag peaks. This may be due to the low amount of TiO_2 in the Ag@TiO_2 nanocluster which sparsely covered Ag nanoparticles. However, a typical anatase phase of TiO_2 intense peaks at 25.44, 38.30, 48.19, 55.27, and 62.80°

(JCPDS, PDF, File No. 01-071-1167) and very little typical rutile phase of TiO_2 weak peaks at 27.56, 36.23, 54.24 and 68.85° (JCPDS, PDF, File No. 01-076-0324) were observed.

13.3.2 Cancer Cell Killing Enhanced Using Ag@TiO_2 Core-Shell Nanocluster

In vitro experiments transmission electron microscopy (TEM) observation showed that the TiO_2 particles were adsorbed on the cell membrane and phagocytized into the cytoplasm during 24-h incubation with the cells [26]. There are many reports demonstrated that particles with nanoscale size smaller than 50 nm can easily enter into most cells, while those smaller than 20 nanometers can move out of blood vessels as they circulate through the body. The size of the blood vessel endothelium-wall porosity of normal cells is 10 nm while that of cancer cells is 10-100nm. The anatomical difference of the blood vessel and the nanoparticles in size and property is selective targeting of nanosized devices for cancer cells [27-30].

To investigate the cell viability, the cell dishes were treated and incubated with different amounts of Ag@TiO_2 colloidal nanocluster containing MEM solution (4, 8, 12, 16 and 20 μl) and another dish (control dish) was not treated with nanocluster solution.

The cells were stained by the trypan blue indicator; the dead cells accumulate the dye resulting in blue color, whereas the live cells have no color. The cell viability was determined as the percentage of the number of the unstained cells against that of the control dish cells. All the data are expressed as the mean of three-time separate culture. In the scale bar of Fig. 7 and 8, 100 means the number of living cells in the control dish in the absence of TiO_2 and Ag@TiO_2 nanocluster.

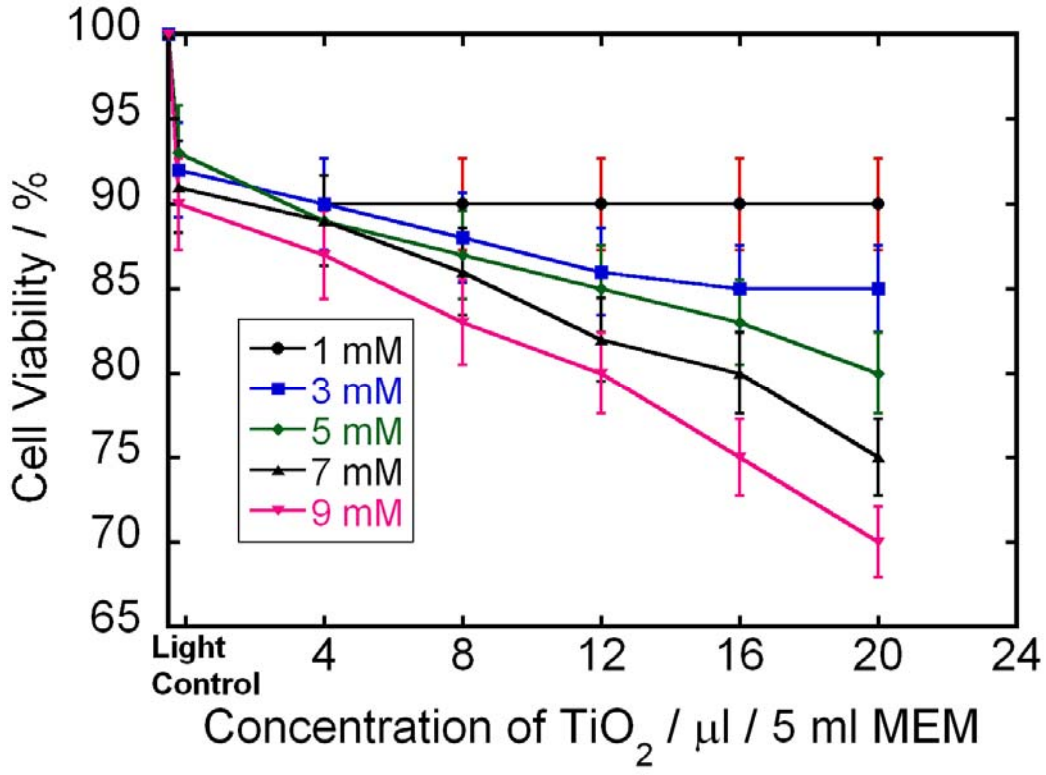

Fig. 13-7: Viability of HeLa cells incubated in MEM media containing 1, 3, 5, 7 and 9 mM TiO_2 nanoparticles. The 100% correspond to the control dish and the viability was calculated by the number of live cells against the control dish cells. Bars represent the region of measured 3 times data and the points represent the mean value from three measurements. Note the scale of ordinate (65~100%).

Fig. 13-7 shows the cell viability of HeLa cells treated with TiO_2-containing MEM solution under 24-h incubated condition. The viability under 10 min light irradiation without TiO_2 was 90-95 %. When TiO_2 was added, the HeLa cells were killed at higher TiO_2 concentrations as shown in Fig. 13-7. When the concentration of TiO_2 was 9 mM/5ml MEM in 20 µl treatments, maximum 30 % of the cells were killed after 10 min irradiation, whereas when the concentration of TiO_2 was 7, 5, 3 and 1 mM, maximum 25, 20, 15 and 10% of the cells were killed, respectively.

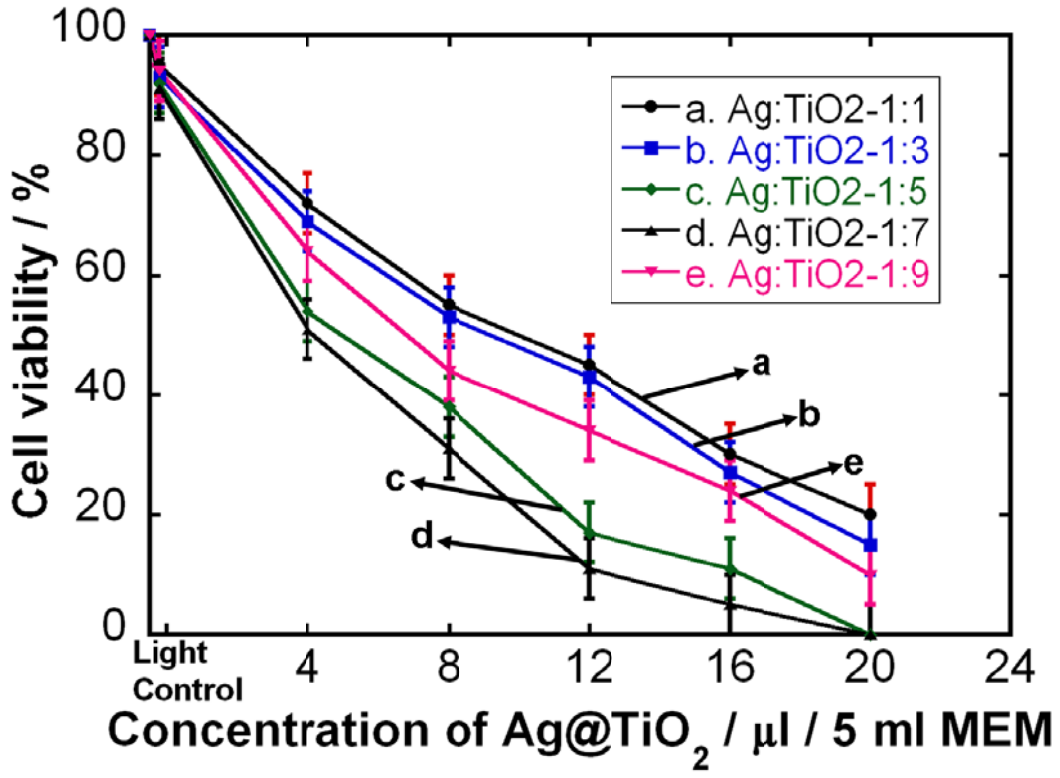

Fig. 13-8: Viability of HeLa cells incubated in MEM media containing Ag@TiO_2 core-shell nanoclusters with different Ag:TiO_2 ratios; (1mM) 1:1, (3mM) 1:3, (5 mM) 1:5, (7 mM) 1:7 and (9 mM) 1:9 with 5 min irradiation by Xe lamp. The concentration in parentheses stands for that of TiO_2. Also, see the caption to Figure 13-7.

Fig. 13-8 shows the viability of HeLa cells treated by Ag@TiO_2 under 24-h incubated condition. At a concentration of 20 µl of Ag@TiO_2 with molar ratios of 1:5 and 1:7 in 5 min light irradiation, 100% of the cells were killed rapidly, whereas at the same concentrations of TiO_2 (5 and 7 mM), maximum 20 and 25% cells were killed, respectively, as shown in Fig. 13-7. It is clear that the TiO_2 shell with the Ag core enhanced strikingly the cell killing efficiency compared with only TiO_2 treatment.

The cell killing effect of Ag@TiO_2 nanoclusters depends on the Ag:TiO_2 molar ratio. When the Ag:TiO_2 is 1:5 and 1:7, maximum100% of the cells were killed under 5 min irradiation and also when the ratio of Ag:TiO_2 was 1:1, 1:3 and 1:9, maximum 80, 85, and 90% of the cells were

killed, respectively. The photocatalytic activity depends on the TiO_2 shell thickness as well as the molar concentration. The increase in the shell thickness with the concentration of the precursor of TiO_2 (TTAEIP) was recognized from the TEM images. The photocatalytic activity of $Ag@TiO_2$ increased when the molar ratio increased from 1:1 to 1:7. However, further increase in the molar ratio decreased the photocatalytic activity. The lack of available charged TiO_2 shell surface at low TiO_2 concentrations (1:1 and 1:3 molar ratios) and significant dampening of the surface plasmon band due to the broad shell thickness of TiO_2 (1:9 molar ratio) may be treated as responsible for the decrease of photocatalytic activity against cancer (HeLa) cells.

Fig. 13-9 a and b shows microscopic images of HeLa cells after 24h incubation with medium-containing control dish cells and 10 min-irradiation light control dish cells. These two figures show that the cell morphological structure was mostly unchanged after 10 min irradiation. Fig. 13-9 c shows that the HeLa cells suffer photochemical and photothermal injury under 5 min light irradiation with $Ag@TiO_2$ for 24 h incubation. The dim white-red color shown in the cell images around the cell surface is due to the cell died at prolonged exposure of the cells in MEM solution outside the cell incubator. The white-red spots were shown in Fig. 13-9 c; the $Ag@TiO_2$ nanoclusters in the cytoplasm were gathered, forming larger aggregates. It can be concluded that the particles are taken up or in contact with the cells, because these white-red spots are not observed (Fig. 13-9 (a and b)) when nanoclusters are not present in the medium. Dead cells were also confirmed by the trypan blue indicator (Fig. 13-9 d).

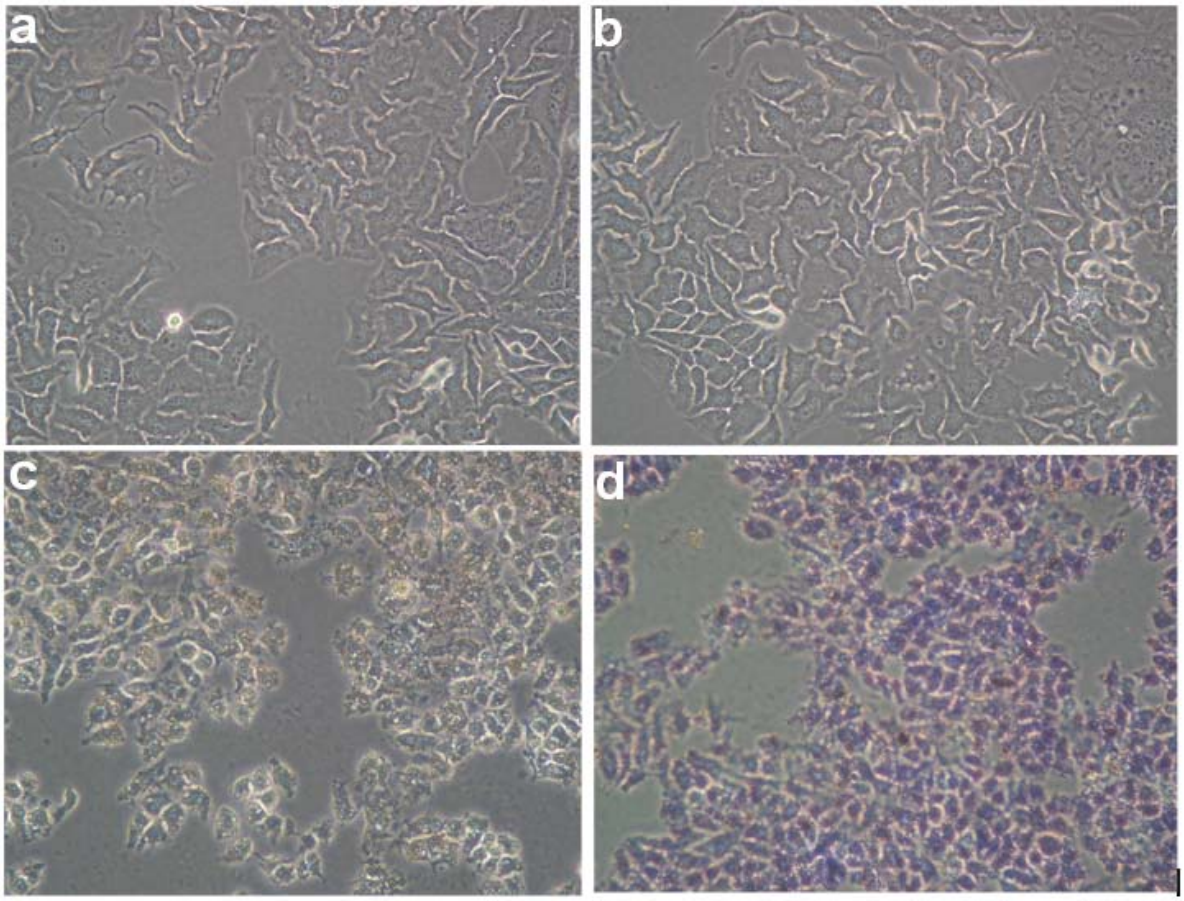

Fig.13-9: Microscopic images of HeLa cells. (a) with neither Ag@TiO_2 nanoclusters composites nor light, (b) after 10-min light irradiation without the nanocomposites, (c) after 5-min light irradiation with the nanocomposite, and (d) dead cells stained with trypan blue. Magnification: 200

It was reported that UV light penetration depth into the tissue is limited to a few fraction of a millimeter [31]. Although longer-time light irradiation is very painful and burns over the entire body, for the Ag@TiO_2 nanocluster-treated cancer cells, the irradiation time is very short with the low light power intensity. Low light power of intensity is very good for body. Although Ag@TiO_2 core-shell nanoclusters induced the cell death by photochemical and photothermal conversion, provided heat is insufficient to damage the neighboring normal cells.

13.3.2.1 Cancer Cell Killing Mechanism

UV light can excite an electron from a valance band to a conductance band in a TiO_2 semiconductor, leaving to hole in the valance band [32]. This electron-hole pair is in direct competition with trapping processes. The photocatalytic activity of TiO_2 will be enhanced by retarding the electron-hole recombination. The Ag core in $Ag@TiO_2$ enables to slow the electron–hole recombination on the surface of TiO_2 particles. As a result the trapped electron in conduction band and the trapped hole in valance band become free charge carriers in the conduction and valance bands.

But, interestingly in $Ag@TiO_2$ core-shell nanoclusters, the Ag core is able to charge electrons under UV irradiation and discharge them in the dark on demand. The electron charging and discharging depend on the two major factors: (i) the dielectric property of the medium and (ii) the density of electrons of the metal cluster. If the photoinduced excitation of $Ag@TiO_2$ is carried out in the presence of an electron acceptor such as thionine dye or oxygen, the photogenerated electrons are scavenged by the acceptor molecules [3].

Here we propose a plausible mechanism for the $Ag@TiO_2$ photocatalytic activity against cancer cells. The photoexcited electrons are penetrated or transferred quickly through TiO_2 shell into the Ag nanocore until the Fermi level charge equilibrium is attained between the shell and core systems (shown in Equation 1 and 2). After a favorable Fermi level (E_f =0.4 V vs NHE) is attained, electrons are facilitated to quickly transfer from excited TiO_2, initiating the redox reactions at the interface of TiO_2 shell and suspension (Fig. 13-10) [33].

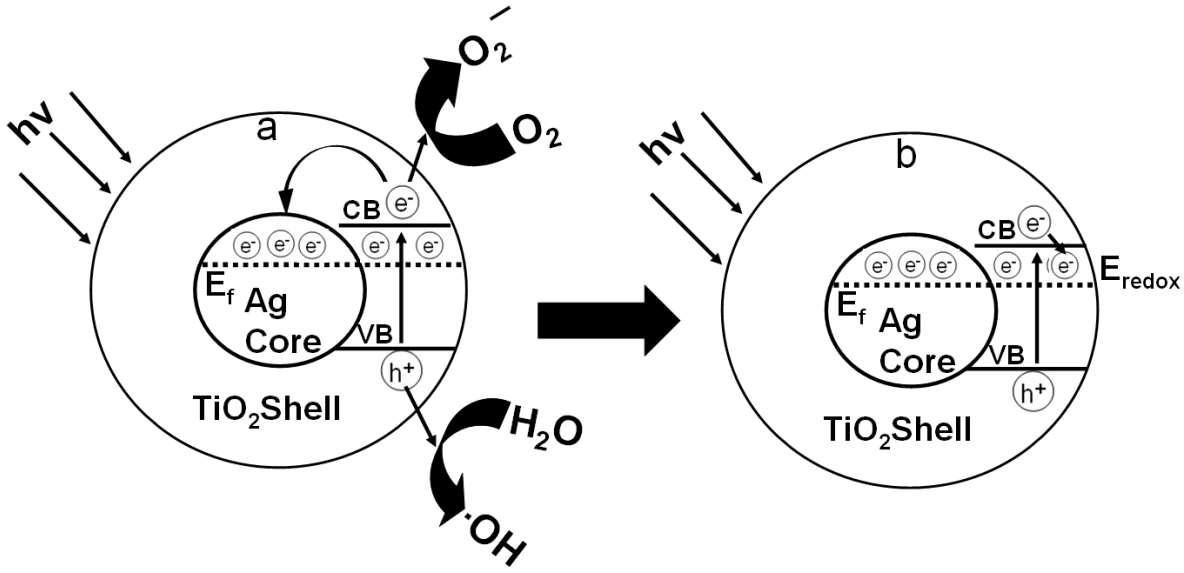

Fig. 13-10: Proposed mechanism for the interfacial charge separation of Ag@TiO_2 nanocluster under the UV-visible (350-600 nm) light irradiation.

The reactive oxygen species such as hydroxyl radicals and hydrogen peroxide are formed on the photoexcited Ag@TiO_2 nanocluster in MEM solution. The highly oxidizable hydroxyl and hydrogen peroxide species are expected to be toxic to the cells [33, 34].

$$(TiO_2)Ag + hv \rightarrow (TiO_2\ (e+h))\ Ag \qquad (1)$$

$$(TiO_2\ (e))Ag + O_2 \rightarrow (TiO_2)\ Ag + O_2{\cdot}^{-} \qquad (2)$$

$$TiO_2\,(h) + H_2O \rightarrow \cdot OH + H^+ \qquad (3)$$

$$O_2{\cdot}^{-} + H^+ \rightarrow HO_2\cdot \qquad (4)$$

$$2HO_2\cdot \rightarrow O_2 + H_2O_2 \qquad (5)$$

$$H_2O_2 + O_2^{-} \rightarrow \cdot OH + OH^{-} + O_2 \qquad (6)$$

It was reported that a photogenerated hole will react with a water molecule to form •OH, H_2O_2 and $O_2{\cdot}^{-}$ which can be expected to be toxic to cells as shown in reaction (3-6) [35, 36]. The photo-induced electrons transfer to the interfacial surface of excited TiO_2 and then to the Ag core until the Fermi level equilibrium will be attained [3]. Some of electrons can be transferred to the

TiO_2 surface and reduce the dissolved O_2 easily, because dissolved oxygen is also one of the good accepters of electrons as shown in Fig. 13-10 (left). The photo-generated holes on the TiO_2 surface can react with water to produce powerful oxidative radicals ·OH and HO_2· as shown in photocatalytic reaction mechanism (Equation 3 and 4) and Fig. 13-10 (left). The Ag core acts as a schottky barrier of TiO_2 excited electrons and protects the electron-hole recombination. As a result the photoinduced solid-liquid interfacial charge-transfer processes are promoted and the photocatalytic cell killing than TiO_2 alone is enhanced.

The oxidation by the photogenerated holes and oxidizing radicals at the semiconductor/metal interface is an important process. It can be a major factor in determining the overall photocatalytic efficiency of metal semiconductor nanocomposites. After excitation the electron migrates to the metal where it becomes trapped and the hole-electron recombination is suppressed. The hole is then free to diffuse to the semiconductor surface where oxidation of organic species can occur [37]. The metal is also important for the photocatalytic properties of the semiconductor by changing the distribution of electrons. For example, the metal and the n-type semiconductor have different Fermi level positions. The metal has a higher work function than the semiconductor. When the two species come in contact with the Fermi levels of the metal and the semiconductor, electrons are caused to flow to the metal from the semiconductor. The decrease in electron density within the semiconductor leads to an increase in the hydroxyl group acidity. This in turn affects the photocatalytic process on the semiconductor surface [37, 38].

13.3.2.2 Photoluminescence Detection of Hydroxyl Radical for Photocatalytic Cancer Cell Killing

The formation of hydroxyl radicals (·OH) on the surface of UV-visible irradiated Ag@TiO_2 is detected by a photoluminescence (PL) technique using terephthalic acid as a probe molecule.

Terephthalic acid reacts with hydroxyl radicals (•OH) to form highly fluorescent product, 2-hydroxyterephthalic acid during irradiation time. The intensity of the PL peak of 2-hydroxyterephtalic acid is in proportion to the amount of OH radicals produced in water.[40,41] This method relies on the PL signal at 425 nm of the hydroxylation of terephthalic acid with ·OH generated at the water/Ag@TiO_2 interface.

The experimental procedure of PL spectra was followed as given in supporting information. The PL spectra were compared between TiO_2 (P25) and Ag@TiO_2 (1:7 molar ratio) of the same concentration under the same UV-visible light irradiation. The PL spectra excited at 315 nm in terephthalic acid solution were measured every 10 min for TiO_2 and 5 min for Ag@TiO_2. Figure S1 shows the change of PL spectra from 5 x 10^{-4} M terephthalic acid solution in 2 x 10^{-3} M NaOH with irradiation time. As shown in Fig. S1 (as supporting data), gradual increase in the fluorescence at about 425 nm was observed by the irradiation of UV-visible light on the TiO_2 and Ag@TiO_2 solution. However, no PL increase was observed in the absence of UV-visible light for TiO_2 and Ag@TiO_2 samples. This suggests that the fluorescence is caused by chemical reactions of terephthalic acid with ·OH formed on the TiO_2 or Ag@TiO_2/water interface via photocatalytic reactions [40, 41].

For the comparative study of PL intensities of TiO_2 and Ag@TiO_2, it can be seen (Fig. S1) that the Ag@TiO_2 fluorescence intensity is much larger than TiO_2 alone. It can be concluded that the Ag core enhances highly effectively the photocatalytic activity. This result is also supported by the photocatalytic HeLa cell killing with Ag@TiO_2.

13.3.2.3 Synergistic Effect for Photocatalytic and Plasmonic Cancer Cell Killing

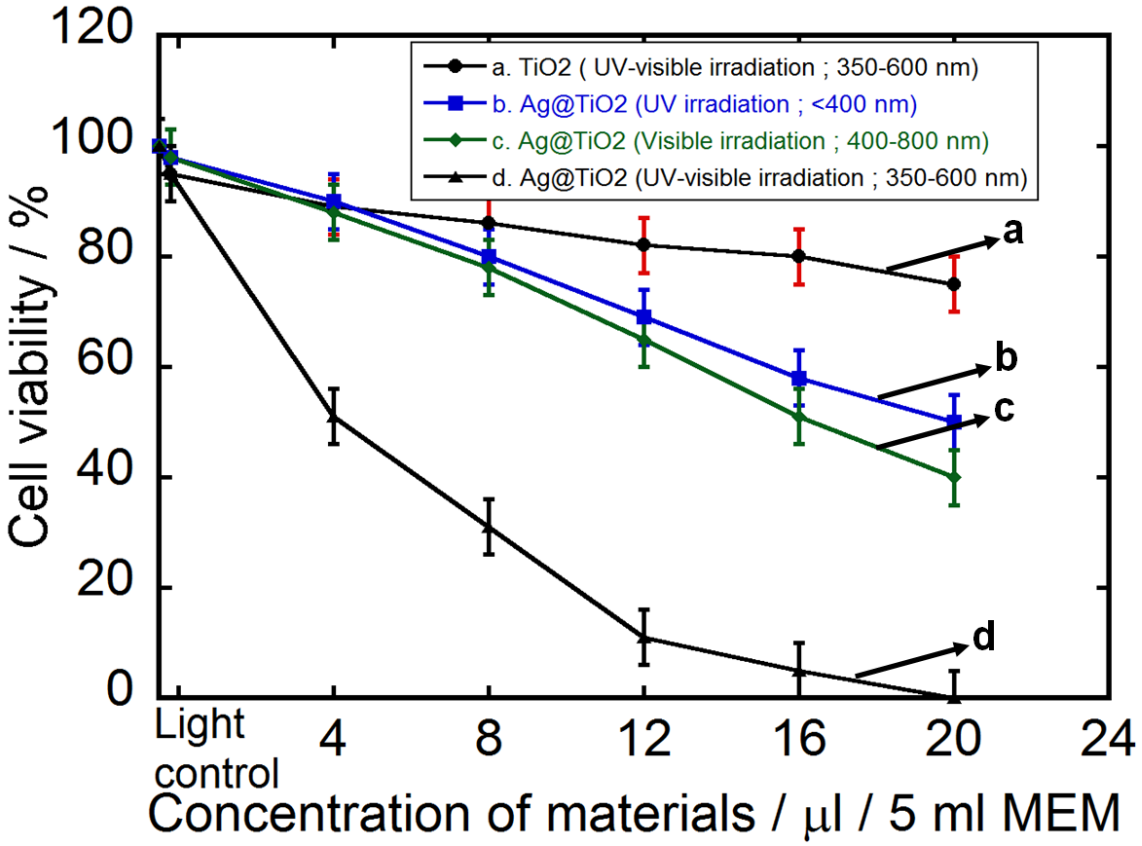

Fig. 13-11: Cell viability under 5-min UV, visible, and UV- visible light irradiation.

However, under dark conditions without light illumination, the cell killing effect does not change for every measurement using TiO_2 or $Ag@TiO_2$ core-shell nanoclusters. Illumination in the absence of TiO_2 or $Ag@TiO_2$ nanoclusters does not result in the photocatalytic cell killing of HeLa cells. Therefore, the presence of both UV-visible light irradiation and TiO_2 or $Ag@TiO_2$ nanoclusters is essential for the efficient cell killing. To compare the effect of UV and visible light in the cell killing activity of $Ag@TiO_2$ composite nanoclusters, only UV light (for TiO_2) or only visible light (for the Ag Plasmonic band) was used on the cells under 5 min light irradiation. The viability under 5-min light irradiation with 20 μl MEM containing the $Ag@TiO_2$ (1:7 molar

ratio) colloidal nanocluster was ca. 40 and ca. 50%, for visible and UV light, respectively, whereas that for only TiO_2 and $Ag@TiO_2$ under UV-visible light (350-600nm) was ca. 75 and ca. 0 %, respectively, as shown in Fig. 13-11. The experimental procedures are shown in supporting information in details. The data lead us to conclude that the synergistic effect based on the photocatalytic and plasmonic photothermal cancer cell killing plays a vital role in our cancer therapy.

13.4 Conclusions

We introduced the new simple method to prepare the $Ag@TiO_2$ core-shell composite nanoclusters. We probed that Ag is in metallic state and the TiO_2 shell uniformly cover around the core, determined by XPS, TEM and XRD analyses. We compared the photocatalytic and plasmonic photothermal activity of $Ag@TiO_2$ and TiO_2 (P25) against cancer (HeLa) cells for the first time to our best knowledge. The $Ag@TiO_2$ core-shell nanoclusters were found to increase the efficiency of interfacial charge-transfer and also the photocatalytic and plasmonic synergistic activity on cancer (HeLa) cell killing.

References

[1] K. Naoi, Y. Ohko, T. Tatsuma, J. Am. Chem. Soc. 126 (2004) 3664-3668.

[2] F. Aliev, M. Correa-Duarte, A. Mamedov, J. W. Ostrander, M. Giersig, L. M. Liz-Marza´n, N. Kotov, Adv. Mater. 11 (1999) 1006-1010.

[3] T. Hirakawa, P. V. Kamat, J. Am. Chem. Soc. 127 (2005) 3928-3934.

[4] P. V. Kamat, Chem. Rev. 93 (1993) 267-300.

[5] M. R. Hoffmann, S. T. Martin, W. Choi, D. W. Bahnemann, Chem. Rev. 95 (1995) 69-96.

[6] A. L. Linsebigler, G. Lu, J. T. Jr.Yates, Chem. Rev. 95 (1995) 735-758.

[7] L. Zang, W. Macyk, C. Lange, W. F. Maier, C. Antonius, D. Meissner, H. Kisch, Chem. Eur. J. 6 (2000) 379-384.

[8] M. Jakob, H. Levanon, P. V. Kamat, Nano Lett. 3 (2003) 353-358.

[9] V. Subramanian, E. E.Wolf, P. V. Kamat, J. Am. Chem. Soc. 126 (2004) 4943-4950.

[10] P. V. Kamat, J. Phys. Chem. B 106 (2002) 7729-7744.

[11] V. Subramanian, E. Wolf, P. V. Kamat, J. Phys. Chem. B 105 (2001) 11439-11446.

[12] V. Subramanian, E. E. Wolf, P. V. Kamat, Langmuir 19 (2003) 469-474.

[13] D. Lahiri, V. Subramanian, T. Shibata, E. E. Wolf, B. A. Bunker, P. V. Kamat, J. Appl. Phys. 93 (2003) 2575-2583.

[14] Mohammad R. Elahifard, S. Rahimnejad, S. Haghighi, R. Mohammad Gholami, J. Am. Chem. Soc. 129 (2007) 9552-9553.

[15] Y. Liu, X. Wang, F. Yang, X. Yang, Microporous and Mesoporous Mater. 114 (2008) 431-439.

[16] C. Hu, Y. Lan, J. Qu, X. Hu, A.Wang, J. Phys. Chem. B 110 (2006) 4066-4072.

[17] M. Abdulla-Al-Mamun, Y. Kusumoto, A. Mihata, M.S. Islam, B. Ahmmad, Photochem. Photobiol. Sci. 8 (2009) 1125-1129.

[18] M. Abdulla-Al-Mamun, Y. Kusumoto, M.S. Islam, Chem .Lett. 38 (2009) 980-981.

[19] C. J. Murphy, N. R. Jana, Adv. Mater. 14 (2002) 80-82.

[20] T. Ung, L. M. Liz-Marza´n, P. Mulvaney, Langmuir 14 (1998) 3740-3748.

[21] K.Awazu, M. Fujimaki, C. Rockstuhl, J.Tominaga, H. Murakami, Y. Ohki, N.Yoshida, T.Watanabe, J. Am. Chem. Soc. 130 (2008) 1676-1680.

[22] D.S. Bhatkhande, V.G. Pangarkar, A.A. Beenackers, J. Chem. Technol. Biotechnol. 77 (2001) 102.

[23] C. D. Wagner, W. M Riggs, L.E Davis, S.F Moulder, G.E. Mullenberg, in Handbook of x-ray photoelectron spectroscopy, ed. Perkin-Elmer corporation Physical Electronics Division, New York, 1979, pp. 82 & 68.

[24] E. Stathatos, P. Lianos, Langmuir 16 (2000) 2398-2400.

[25] T. Sano, N. Negishi, K. Uchino, J. Tanaka, S. Matsuzawa, K. Takeuchi, J. Photochem. Photobiol. A-Chem 160 (2003) 93-98.

[26] R. Cai, K. Hashimoto, K. Itoh, Y. Kubota, A. Fujishima, Bull. Chem. Soc. Jpn. 64 (1991) 1268-1273.

[27] Scott E. McNeil, J. Leukocyte Biol. 78 (2005) 585-594.

[28] N. Kohler, C. Sun, J. Wang, M. Zhang, Langmuir 21 (2005) 8858-8864.

[29] B. Devika Chithrani, Arezou A. Ghazani, C. W. Chan, Nano Letters, 6 (2006) 662-668.

[30] Y. Matsumura, H. Maeda, Cancer Research, 46 (1986) 6387-6392.

[31] L. J. Steven, R. W. David, M. R.Steven, Photochem. Photobiol. 45 (1987) 637-641.

[32] A. Fujishima, K. Honda, Nature 238 (1972) 37-38.

[33] M. Abdulla-Al-Mamun, Y. Kusumoto, B. Ahmmad, M.S. Islam, Top Catal 53 (2010) 571-577.

[34] R. Cai, Y. Kubota, T. shuin, H. Sakai, K. Hashimoto, A. Fujishima, Cancer Research 52 (1992) 2346-2348.

[35] C. D. Jaeger, A. J. Bard, J. Phys. Chem. 93 (1979) 3146-3152.

[36] R. Cai, Y. Kubota, T. Shuin, H. Sakai, K. Hashimoto, A. Fujishima, Chem. Lett. 3 (1992) 427-430.

[37] Amy L. Linsebigler, G. Lu, J. T. Jr. Yates, Chem. Rev. 95 (1995) 735-758.

[38] E. H. Rhoderick, R. H. Williams, Metal-Semiconductor Contacts, 2nd ed., Oxford University Press, New York, 1988.

[39] N. Jafiezic-Renault, P. Pichat, A, Foissy, R. Mercier, J. Phys. Chem. 90 (1986) 2733-2738.

[40] K. Ishibashi, A. Fujishima, T. Watanabe, K. Hashimoto, Electrochem.Commun. 2 (2000) 207-210.

[41] J. Yu, W. Wang, B. Cheng, B. Su, J. Phys. Chem. C 113 (2009) 6743-6750.

CHAPTER 14

ONE-STEP AND LARGE SCALE SYNTHESIS OF NONMETAL DOPED TiO_2 SUBMICROSPHERES AND THEIR PHOTOCATALYTIC ACTIVITY

Abstract

Without using an external precursor a simple and one-step method for the synthesis of C-doped TiO_2 submicrospheres has been developed via hydrolysis of titanium tetraisopropoxide in pure methanol followed by calcination under air at 500 ˚C. Also, with the addition of D-glucose and NH_4OH solution during the hydrolysis process, C- or N-doped and C, N co-doped TiO_2 sub microspheres can be prepared by the same method. The size of the submicrosphere was homogeneous ranging from 300 to 400 nm. The resulting sub microspheres were characterized by FE-SEM, TEM, XRD, XPS and UV–vis diffuse reflectance spectroscopy. The C- or N-doped and C, N co-doped submicrospheres showed obvious absorption in the wavelength up to around 650, 500 and 650 nm, respectively. The activity of the photocatalysts was evaluated by the hydroxyl radical formation under visible light irradiation. Finally, the mechanism of sphere formation is discussed. This work has already been published in Advanced Powder Technology, 2010, 21, 292-297.

14.1 Introduction

Among various semiconductors, TiO_2 has been considered to be the most promising photocatalyst for widespread environmental applications because of its biological and chemical inertness, strong oxidizing power, non-toxicity and long-term stability against photo and chemical corrosion [1]. However, due to its large band-gap of 3.2 eV, the anatage type of TiO_2

can show photoactivity only under UV light of wavelength <387 nm which accounts for merely ~5% of the solar photons, thereby hampering its wide usages. The doping to the TiO_2 photocatalyst with metal or nonmetal elements has currently been attracting intense interest as a promising way to extend the photoactive wavelength region to the visible light [2]. In 2002, Khan et al. first reported that carbon-doped TiO_2 was very active for photosplitting of water under visible light irradiation [3]. Asahi et al. reported the N-doped TiO_2 photocatalyst prepared by sputtering the TiO_2 target in an N2/Ar gas mixture and its application for the photodecomposition of methylene blue and gaseous acetaldehyde under visible light irradiation. They also showed that the substitutional doping of N was the most effective because its p state contributes to the band-gap narrowing by mixing with O 2p states [4]. Although TiO_2 can efficiently mineralize a great number of organic pollutants, the recovery of TiO_2 powder from treated water is still an obstacle to widely extending application as the photocatalyst particles particles must be filtered prior to the discharge of the treated water. To exclude the separation procedure, the immobilization of the TiO_2 photocatalysts on certain supporting materials such as glass, fiber or stainless steel has been frequently adopted as reviewed by Byrne et al. [5]. Unfortunately, a significant loss in the contact area between the immobilized photocatalyst and light limits its efficiency in the photocatalytic degradation of the organic substrates [6]. On the contrary, the TiO_2 powder in suspension systems enjoys an attractive advantage of good contact with light, thus leading to a relatively high quantum yield. Therefore, a possible practical alternative would be to maintain the supported catalyst in a suspension form. In a suspension system, the photocatalyst can be easily fluidized by air bubbling and settled by gravity after reactions. Micro-sized solid spherical TiO_2 photocatalysts have been synthesized by some researchers [7–9] as an ideal candidate for easy separation and recovery, since they can settle

down easily in aqueous suspension by gravity. The critical procedure in this method is that removal of the templates or the usage of two immiscible liquid phases results in the complication of the preparation, cracking of microsphere shells and limited applications. Recently, Nagamine et al. reported a simple method for preparing a TiO_2 microsphere. They sprayed water, by using a commercial nozzle with N_2 as the carrier gas, into an organic solution of titanium tetraisopropoxide (TTIP). The TiO_2 shell is formed via the hydrolysis of TTIP at the spherical interface between the water droplet and the organic solution [10]. Nagaoka et al. prepared the carbon/TiO_2 microsphere composite from the cellulose/TiO_2 microsphere composite. The size of microspheres was 25 lm and the microspheres had a low specific surface area of 0.70 m^2/g. The asprepared composite was applied for the photocatalytic decomposition of acetaldehyde under UV light irradiation [11]. To our best knowledge, C- and/or N-doped TiO_2 submicrosphere has not been reported so far. We, in this paper, report a simple method for the preparation of non-metal doped TiO_2 submicrospheres without using any special instrument or template. This method is one-step, economical and applicable in large scale industrial preparation. The as-prepared TiO_2 submicrospheres are photoactive in the visible region and have comparatively high surface areas.

14.2 Experimental

14.2.1 Preparation of doped TiO_2 submicrospheres

For the synthesis of C- and/or N-doped TiO_2 submicrostructures, the following general method was followed: 10 ml of TTIP (Wako, 99%) were dissolved in 20 ml of methanol (Wako, 99%) in a finely dried beaker. Then, 5 ml of doubly distilled water were added drop by drop to the solution under constant stirring. Immediately a white precipitate was formed which was dried for 12 h at 105 ˚C and then calcined from 300 to 700 ˚C for 3 h under air atmosphere. For the N-

doped TiO_2 submicrosphere, instead of water in above procedure, 5 ml of aqueous NH_4OH (1 M) solution was added to the TTIP–methanol solution. For the both carbon and nitrogen co-doped TiO_2, 5 ml aqueous D-glucose (1 M) was added (instead of water) to the TTIP–methanol solution and then 5 ml of aqueous NH_4OH solution was added, followed by stirring and drying.

14.2.2 Characterization of the submicrospheres

The UV–visible diffuse reflectance spectra of the doped TiO_2 submicrospheres were recorded using a multipurpose spectrophotometer (Shimadzu Corporation, MPS-2000) and BaSO4 as a reflectance standard. The size and surface condition of the submicrospheres were analyzed by a field-emission scanning electron microscope (FE-SEM) (Hitachi, S-4100H) and a transmission electron microscope (TEM) (JEOL, JEM-3010 VII, operating at 300 kV). Crystal structure identification was made by X-ray diffraction (XRD) using a PANalytical Advance X-ray diffractometer with CuKa radiation. Further, the existence and amount of dopants were measured by X-ray photoelectron spectroscopy (XPS) (Shimadzu, ESCA-1000) using MgKa X-ray as the excitation source and C1s (284.6 eV) as the reference line. Brunaur–Emmet–Teller (BET) surface areas (SBET) were determined using a Micrometritics (Bel sorp mini, Japan BEL) nitrogen adsorption apparatus. All the samples measured were degassed at 200 ˚C before the actual measurements. For the measurement of the active oxidative species (mainly corresponding to hydroxyl radicals (•OH) produced by TiO_2 submicrospheres), a fluorophotometer (Shimazu, RF-5300PC) was used.

14.2.3 Photocatalytic evaluation

The quantitative analysis of •OH radicals formation on the photocatalyst surface under visible light irradiation was performed by fluorescence technique using terephthalic acid, which readily reacted with •OH radicals to produce highly fluorescent product, 2-hydroxyterephthalic acid. The

fluorescence intensity of the peak attributed to 2-hydroxyterephtalic acid is known to be proportional to the amount of •OH radicals formed [12]. Sixty milligram of the prepared doped TiO_2 submicrospheres were added to 50 mL of $5x10^{-4}$ M terephthalic acid solution in 2 x 10^{-3} M NaOH, and then visible light irradiation to the solution was started.

A xenon lamp (Ushio, 500 W) was used as a visible light source with an UV cut-off filter. Sampling was performed in every 15 min. Solution after filtration through a 0.20-lm membrane filter was analyzed by a fluorescence spectrophotometer. The hydroxylation product of terephthalic acid, 2-hydroxyterephthalic acid, gave a peak at the wavelength of about 425 nm by the excitation with the wavelength of 315 nm.

14.3 Results and discussion

14.3.1 Characterization of the photocatalysts

Fig. 14-1a and b shows the SEM images of the C, N co-doped TiO_2 submicrospheres produced via the hydrothermal treatment of water without additives. The size of the submicrospheres ranges from 300 to 400 nm. Fig. 14-1c shows the TEM image of TiO_2 submicrospheres. It is seen from the SEM and TEM images that each submicrosphere is composed of aggregated TiO_2 nanoparticles of size ranging from 20 to 40 nm and the surfaces of the spheres are rough. The selected area electron diffraction (SAED) patterns (Fig. 14-1d) reveal the polycrystalline nature of the anatase and rutile phases for the TiO_2 submicrospheres. All other doped TiO_2 submicrospheres show the similar structural characteristics and thus the results are not shown here.

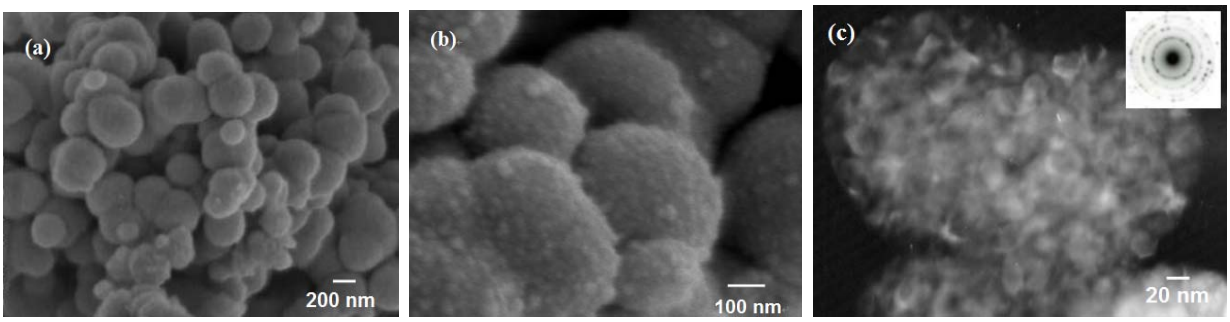

Fig. 14-1: SEM (a, b) and TEM (c) images of C, N co-doped TiO_2 submicrospheres.

The XRD patterns for the doped TiO_2 submicrospheres calcined at different temperatures are shown in Fig. 14-2. We can see that up to 500 ˚C the C-doped TiO_2 shows the pure anatase phase displaying no peaks attributed to the original material. But above 600 ˚C the rutile peaks increase. As the anatase phase is preferred for the photocatalytic application, all the doped-TiO_2 submicrosphere were calcined at 500 ˚C (the XRD spectrum of only C, N co-doped TiO_2 submicrospheres is shown in Fig. 14-2). Fig.14-3 shows nitrogen adsorption–desorption isotherms and a BJH pore size distribution (PSD) curve (inset) of the C, N co-doped TiO_2 submicrospheres. The TiO_2 submicrospheres exhibit a type-IV isotherm according to BDDT classification [13] with a H3 hysteresis loop in a higher pressure range from 0.5 to 0.9, suggesting the presence of some mesopores in the shell. The isothems with type-H3 hysteresis loops are reported for the aggregates of plate-like particles giving rise to slit-shaped pores [13].

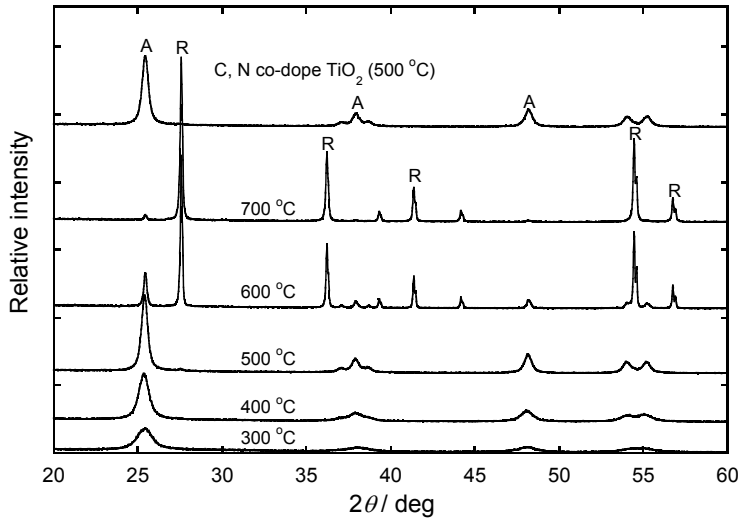

Fig.14-2: XRD patterns of C-doped TiO_2 submicrospheres calcined at different temperatures (300-700°C).

The corresponding PSD curve (inset) indicates some mesopores of an average size of ca. 10.5 nm present in the shell. The BET surface areas of the C- or N-doped and C, N co-doped TiO_2 submicrospheres were found to be ca. 15.5 and 16.9 m^2/g, respectively, whereas the surface area of TiO_2 was ca. 49 m^2/g. Although the particle sizes of submicrospheres are larger (about 15 times) than TiO_2 (P25), the mesopores in the shell might help somewhat to prevent a large decline in the surface area. The as-prepared C- or N-doped TiO_2 and C, N co-doped TiO_2 submicrospheres had grayish white, yellowish white and grayish brown color, respectively. The C-doped TiO_2 exhibited strong absorption (Fig. 12-4) in the UV region in the same way as the nondoped TiO_2 and a long tail in the visible region. Similarly the N doped TiO_2 submicrospheres exhibit strong absorption in the UV region and a weak absorption with a shoulder band around 450 nm. However, C, N co-doped submicrospheres exhibit comparatively strong absorption extending to around 650 nm. In case of the C-doped TiO_2 submicrospheres carbon may come from the alcohol. The reaction of TTIP with water is as follows:

$$TTIP + 2H_2O = TiO_2 + 4C_3H_7OH \quad (1)$$

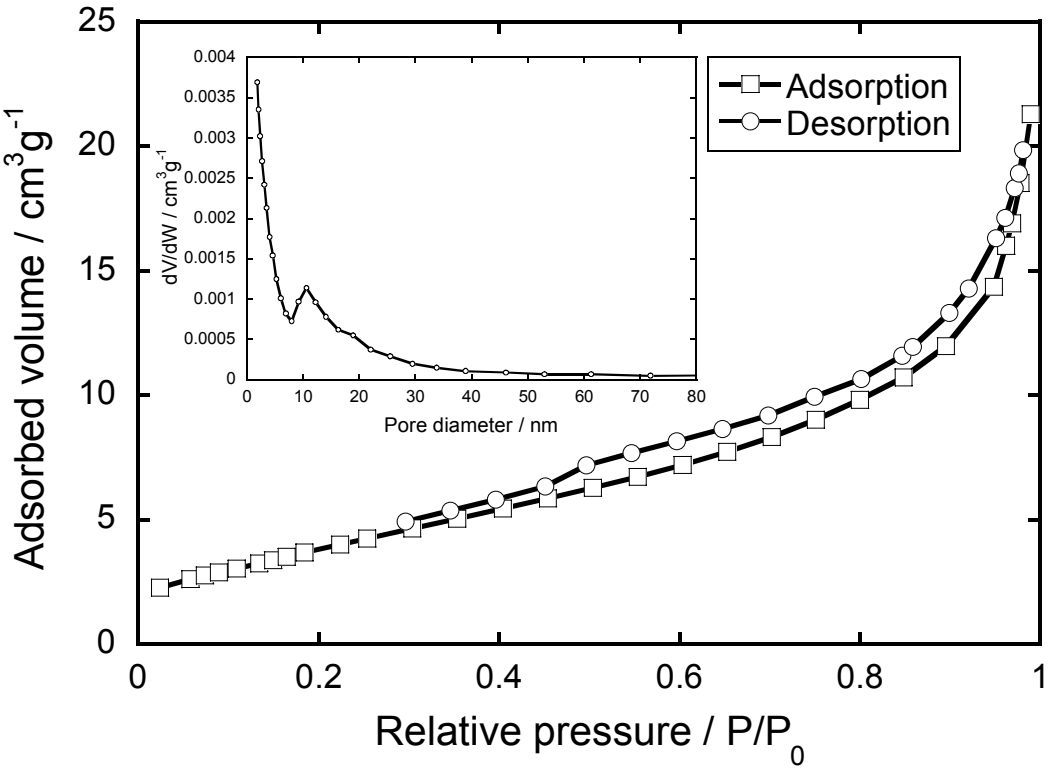

Fig. 14-3: Nitrogen adsorption-desorption isotherm and PSD curve (inset) of C, N co-doped TiO_2 submicrospheres.

Although almost all of the alcohol molecules in the system are evaporated during the drying process at 105 ˚C, we assume that some dissociated alcohol remained in the system by the chemical adsorption on the TiO_2 surface which becomes the source of carbon in the C-doped TiO_2. Thus an absorption edge is found at 650 nm for the C-doped TiO_2 submicrospheres. Interestingly, addition of NH_4OH (when attempting to prepare the C, N co-doped TiO_2) in the same system resulted in only the N-doped TiO_2, i.e., no absorption of C-doped TiO_2 is seen. Addition of nitrogen source (NH_4OH) increases the pH value of the system by ca. 1 which may

inhibit the dissociation process of alcohol and thus cannot remain in the system by the chemical adsorption. Thus, during drying at 105 ˚C all alcohol molecules are removed from the system. As a result no C-doping takes place and the absorption edge is found at around 500 nm which may be attributed only to the N-doped TiO_2 submicrospheres. However, C and N can be co-doped by adding D-glucose and NH_4OH solution during the hydrolysis process. In this case comparatively strong absorption is found due to the presence of co-doped carbon and nitrogen. Moreover, as shown later, the total amount of dopants is larger in the co-doped TiO_2 submicrospheres.

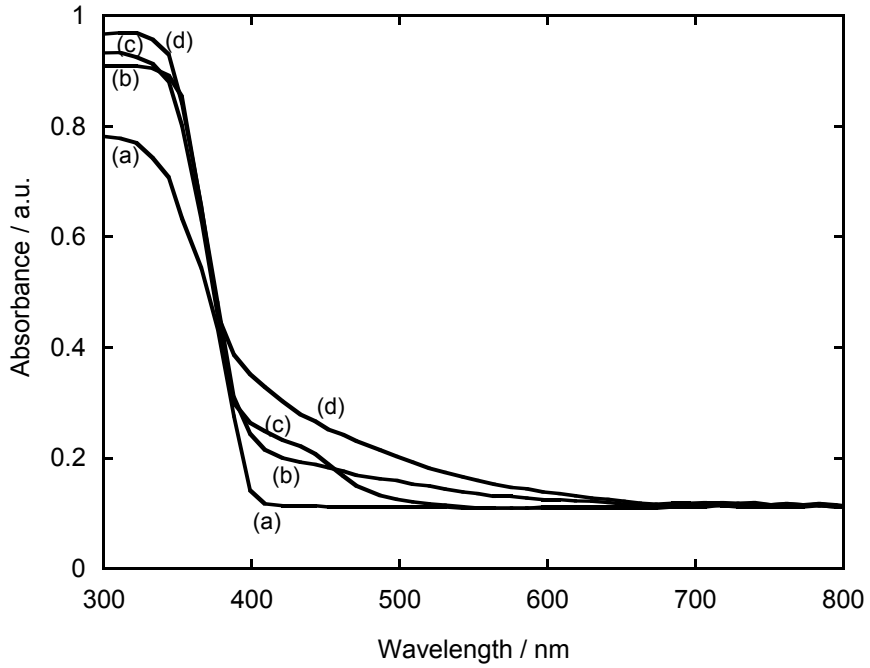

Fig. 14-4: UV–visible spectra of (a) bare TiO_2, (b) C-doped, (c) N-doped and (d) C, N codoped TiO_2 submicrospheres.

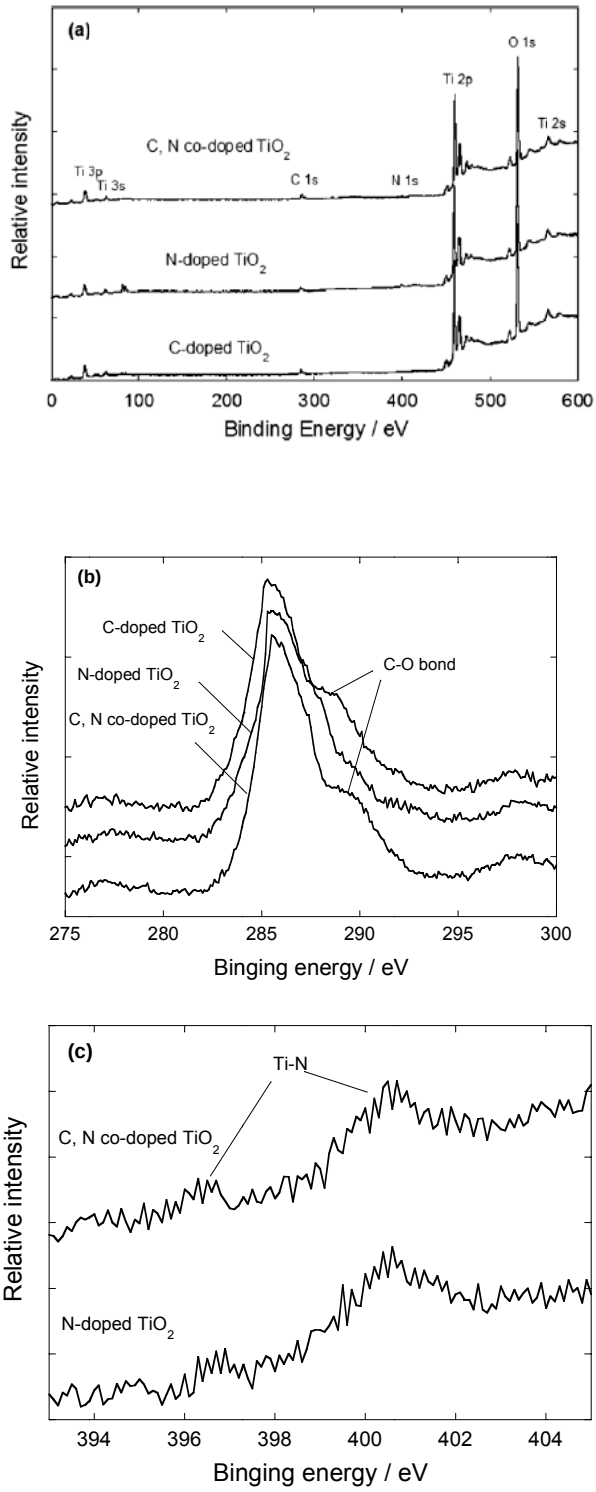

Fig. 14-5: XPS spectra of doped TiO_2 submicrospheres. (a) Survey spectrum, (b) C 1s and (c) N 1s curves for different samples.

The existence of dopants (i.e., C or N atoms implanted into TiO_2) in the as-prepared C–TiO_2 and N–TiO_2 particles was confirmed by XPS measurements. According to the XPS spectral analysis (Fig 14-5a) of the doped TiO_2 submicrospheres, the samples contain only Ti, O, C and N. The carbon peak in the N-doped TiO_2 (Fig. 14-5a) arises from the adventitious carbon as shown in Fig. 14-5b (see below). For all the samples the Ti 2p spectrum shows two peaks at 458.7 and 464.3 eV, corresponding to the Ti 2p3/2 and Ti 2p1/2 states of stoichiometric TiO_2, respectively. The O 1s spectrum also displays two peaks at 530.5 and 532.5 eV; the former is ascribed to lattice oxygen of TiO_2 whereas the latter is ascribed to surface-adsorbed oxygen species such as H_2O and CO_2 etc. [14]. To investigate the carbon states in the photocatalysts, we measured C 1s core level, as shown in Fig. 14-5b. A peak and a shoulder band at binding energy of 285.7 and 288.6 eV were observed for the C-doped TiO_2. The 285.7 eV peak arises from adventitious carbon containing compounds as contaminations [14], whereas the 288.6 eV shoulder band indicates the presence of C–O bonds. These data reveal that carbon atoms may substitute for some of the lattice titanium atoms and form Ti–O–C structure [15, 16]. This is different from the C-doped TiO_2 prepared by flame oxidation, in which carbon atoms partially substitute for some of the lattice oxygen atoms [3]. We can see that the N-doped TiO2 submicrospheres show no obvious shoulder for the C–O band but still it gives a peak for adventitious carbon. In Fig 5c, the peaks at around 400 eV and 397 eV in the N-dope TiO_2 are attributed to N 1s electron within different Ti–N bonding environments [17, 18]. These results indicate that the as-prepared samples are indeed the C-, N- and C, N co-doped TiO_2, which are in harmony with the above-mentioned appearance of the weak absorption shoulder in the visible region (Fig. 14-4). It is likely that during the heat treatment in air, $Ti(OH)_4$ (an intermediate product of Eq. (1)) is converted to TiO_2, but in the presence of carbon or nitrogen source, their

small amount is left in the crystal as doped C or N. It is reported that the doping of C or N would result in the formation of anion defects (oxygen vacancies), which would contribute to the weak absorption shoulder in the visible light region [19]. The carbon content in the C-doped TiO_2 in the present work was estimated by comparing the area of the 288.6 eV XPS peak, attributed to C–O bonds [15, 16, 20] of the C-doped TiO_2 and that of the 530.5 eV XPS peak, attributed to O 1s in the lattice oxygen of TiO_2. The sensitivity factors in XPS spectra for carbon and oxygen are 1.00 and 2.85, respectively, in our present work. Thus, the peak areas corrected with these sensitivity factors [21] showed that the carbon to oxygen atomic ratio in the present C-doped TiO_2 and C, N co-doped TiO_2 were about 0.7% and 0.6%, respectively. The similar method of measurement was applied to the N-doped TiO_2 and C, N co-doped TiO_2 samples (sensitivity factor was 1.77). The amount of N in the N-doped TiO_2 and C, N co-doped TiO_2 were found to be 0.9% and 0.85%, respectively. That means that the total amount of dopants in case of the C, N co-doped TiO_2 is ca. 1.45%.

14.3.2 Evaluation of the photocatalyst

The fluorescence emission spectrum (excitation at 315 nm) of terephthalic acid solution was measured every 15 min during illumination. It was found that the fluorescence intensity increases with increasing illumination time (data not shown). Consequently, we could conclude that *OH radicals formed at the C-doped TiO_2 interface were in proportional to the light illumination time obeying zero-order reaction rate kinetics. Based on the reports in radiation chemistry and sonochemistry, it was reasonable to assume that photogenerated O^{-}_2, HO_2^{*} and H_2O_2 did not interfere with the reaction between *OH and terephthalic acid [22]. Moreover, the generated spectrum had the identical shape and maximum wavelength with that of 2-hydroxyterephthalic

acid. These results suggested that fluorescent products formed using carbon-doped TiO_2 were due to the specific reaction between *OH radicals and terephthalic acid.

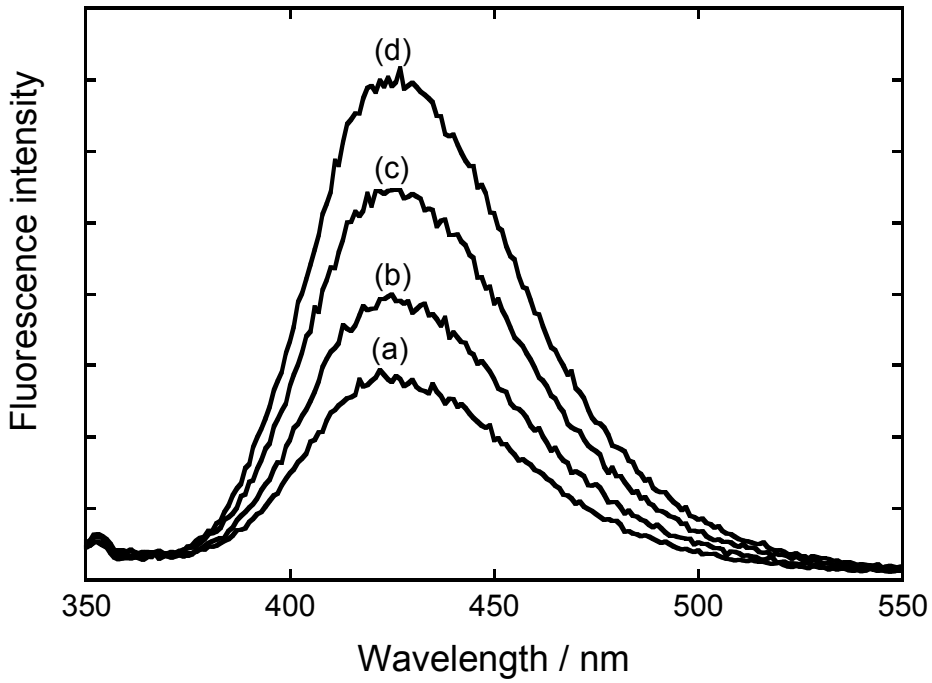

Fig. 14-6: Fluorescence spectra observed for (a) bare TiO_2, (b) C-doped, (c) N-doped and (d) C, N co-doped TiO_2 submicrospheres after 1 h of visible light irradiation.

Fig. 14-6 showed the plots of fluorescence intensity with various doped TiO_2 submicrospheres after 1 h of visible light irradiation (λ> 400 nm). We can see that C-doped TiO_2 shows comparatively lower efficiency due to weak absorption in the visible region. However, comparatively strong absorption is seen in case of N-doped TiO_2 showing relatively higher efficiency. As the absorption of C, N co-doped TiO_2 is relatively strong in the widespread wavelength; it shows the highest efficiency of hydroxyl radical formation. We expect that the amounts of dopants are controllable in our photocatalysts by changing the calcination time and the concentration of dopant precursor sources. Studies on the optimized activity by changing the amount of dopants in the TiO_2 submicrospheres are now in progress.

14.3.3 Mechanism of sphere formation

The spheres are formed via complicated processes involving the diffusion and reaction of several species [10] such as TTIP, titanium hydroxide and water. We consider a spherical water droplet surrounded by a methanol phase containing TTIP (see Fig 14-7). TTIP is transported into the water droplet only after being partially hydrolyzed at the water–methanol interface because of its low solubility to water. Titanium hydroxide yielded by partial hydrolysis is hydrophilic and diffuses toward the droplet center through the water–methanol interface. In the course of diffusion, titanium hydroxide undergoes the further hydrolysis and condensation, and is incorporated into the oxide shell, leading to the growth of shell. To confirm that for the formation of microspheres the hydrolysis reactions have to take place at the water–methanol interface, the order of the chemicals addition were changed. In the usual method, TTIP was first dissolved in methanol and then water was added for the formation of microspheres through the hydrolysis reaction. But in other experiment, first the hydrolysis reaction was performed by addition of the same amount of water and TTIP. After stirring well, methanol was added to this solution. Instead of submicrospheres, nanoparticles of TiO_2 were found. As the hydrolysis reaction takes place without a water–methanol interface in the later experiment, no microspheres were found. This result confirms that the sphere formation takes place via complicated processes involving the diffusion and reaction of several species at the water–methanol interface in the system.

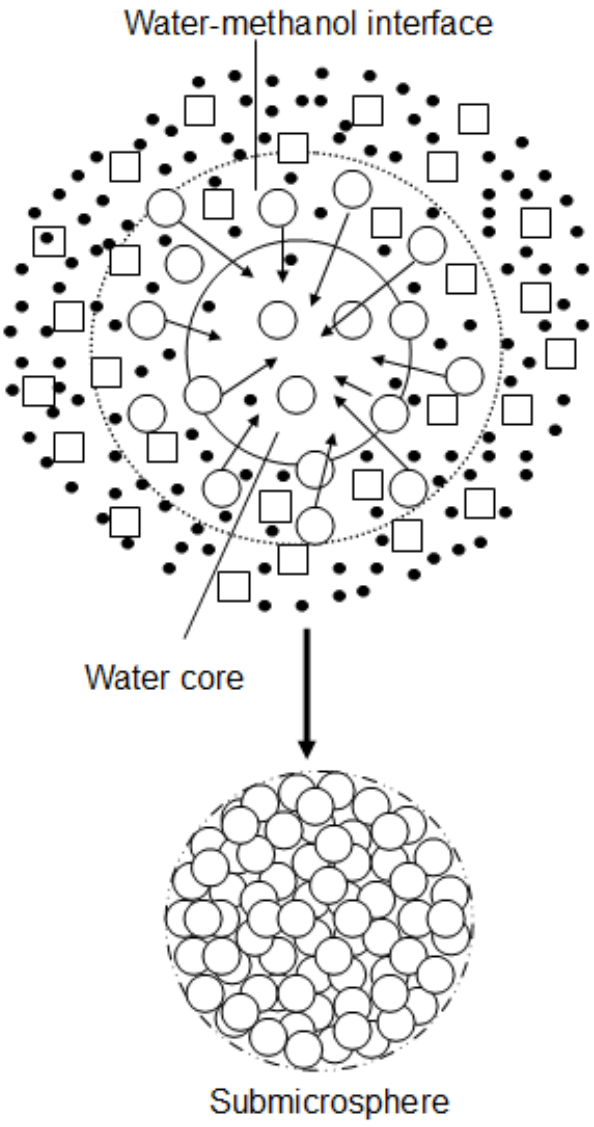

Fig. 14-7: Schematic illustration of the formation mechanism of TiO_2 submicrosphere. The square (□) and circle (○) stand for TTIP and titanium hydroxide, respectively, and the black dot (●) indicates the methanol molecules.

Usage of ethanol, instead of methanol, gave the similar TiO_2 submicrostructures. The amount of water to methanol was changed from 0.05 to 1 v/v and it was found that a volume ratio of 0.25:1 (water–methanol) is appropriate for finely crystallized submicrospheres. The shortage or

excess of water amount resulted in deformed submicrospheres or irregular sized aggregates of TiO_2 nanoparticles.

14.4 Conclusion

A simple method is developed for the preparation of the C- and/ or N-doped TiO_2 submicrospheres. The spheres are formed via complicated processes involving the diffusion and reaction of several species such as TTIP, titanium hydroxide and water. This method is one-step, economical and applicable on a large scale. The doped TiO_2 submicrospheres exhibit obvious absorption in the visible light range. The most important advantage these doped TiO_2 submicrospheres is that they are easy separable since they can settle down easily in aqueous suspension by gravity.

References

[1] J. Yu, W. Wang, B. Cheng, B.-L. Su, J. Phys. Chem. C 113 (2009) 6743–6750.

[2] E. Barborini, A.M. Conti, I. Kholmanov, P. Piseri, A. Podestà, P. Milani, C. Cepek, O. Sakho, R. Macovez, M. Sancrotti, Adv. Mater. 17 (2005) 1842–1846.

[3] S.U.M. Khan, M. Al-Shahry, W.B. Ingler Jr., Science 297 (2002) 2243–2245.

[4] R. Asahi, T. Morikawa, T. Ohwaki, K. Aoki, Y. Taga, Science 293 (2001) 269–271.

[5] J.A. Byrne, B.R. Eggins, N.M.D. Brown, B. McKinney, M. Rouse, Appl. Catal. B: Environ. 17 (1998) 25–36.

[6] A. Rachel, M. Subrahmanyam, P. Boule, Appl. Catal. B: Environ. 37 (2002) 301–308.

[7] P.F. Lee, X. Zhang, D.D. Sun, J. Du, J.O. Leckie, Colloids and Surfaces A: Physicochem. Eng. Aspects 324 (2008) 202–207.

[8] X.Z. Li, H. Liu, L.F. Cheng, H.J. Tong, Environ. Sci. Technol. 37 (2003) 3989–3994.

[9] S. Nagamine, A. Sugioka, H. Iwamoto, Y. Konishi, Powder Technol. 186 (2008) 168–175.

[10] S. Nagamine, A. Sugioka, Y. Konishi, Mater. Lett. 61 (2007) 444–447.

[11] S. Nagaoka, Y. Hamasaki, S. Ishihara, M. Nagata, K. Iio, C. Nagasawa, H. Ihara, J. Mol. Catal. A: Chem. 177 (2002) 255–263.

[12] K. Ishibashi, A. Fujishima, T. Watanabe, K. Hashimoto, Elctrochem. Commun. 2 (2000) 207–210.

[13] K.S.W. Sing, D.H. Everett, R.A.W. Haul, L. Moscou, R.A. Pierotti, J. Rouquerol, T. Siemieniewska, Pure Appl. Chem. 57 (1985) 603–619.

[14] H. Liu, A. Imanishi, Y. Nakato, J. Phys. Chem. C 111 (2007) 8603–8610.

[15] W. Ren, Z. Ai, F. Jia, L. Zhang, X. Fan, Z. Zou, Appl. Catal. B: Environ. 69 (2007) 138–144.

[16] Y. Wang, Y. Huang, W. Ho, L. Zhang, Z. Zou, S. Lee, J. Hazard Mater. 169 (2009) 77–87.

[17] X. Chen, Y. Lou, A.C.S. Samia, C. Burda, J.L. Gole, Adv. Funct. Mater. 15 (2005) 41–49.

[18] X. Chen, C. Burda, J. Phys. Chem. B 108 (2004) 15446–15449.

[19] J. Wang, S. Yin, M. Komatsu, Q. Zhang, F. Saito, T. Sato, Appl. Catal. B: Environ. 52 (2004) 11–21.

[20] E. Papirer, R. Lacroix, J.-B. Donnet, G. Nansé, P. Fioux, Carbon 33 (1995) 63–72.

[21] H. Irie, S. Washizuka, K. Hashimoto, Thin Solid Films 510 (2006) 21–25.

[22] H.M. Khan, M. Anwar, G. Ahmad, J. Radioanal. Nucl. Chem. Lett. 200 (1995) 521–527.

CHAPTER 15

SUMMARY OF THE DISSERTATION

The current PhD research is focused and aimed on syntheses of novel shaped magnetic nanomaterials, nanocomposites, nanophotocatalysts and their successful application on cancer cell killing under combined AC (alternating current) magnetic-field induction and photoirradiated conditions. In this thesis, we present a series of different novel experimental techniques for the synthesis of various magnetic, photocatalytic and photothermal nanoparticles with the aim of using them to cancer therapy. Accordingly, we successfully synthesized three famous forms of iron oxides like Fe_3O_4, γ-Fe_2O_3 and α-Fe_2O_3 and fabricated with TiO_2 photocatalyst to observe their cytotoxic effects in various aspects.

Because of our interest in the enhanced toxic effect of AC magnetic-field induction and photocatalytic reactions of several categories of magnetic nanoparticles produced by visible light irradiation, we studied the cancer cell killing effects under three distinct conditions, a) only AC magnetic-field induction, b) only photoirradiation and c) combined AC magnetic-field induction and photoirradiation conditions. We adopted HeLa cells as a model to investigate the thermal-photocatalytic cancer cell killing efficiency of as-synthesized nanomaterials. Furthermore, for the first time we assembled and used combined instrumentation modeling of AC magnetic-field and photoexcitation

Cancer costs billions of dollars and it caused about 13% of all human deaths world-wide. With the growth and aging of the population, prevention efforts are important to help reduce new cancer cases, human suffering, and economic costs. Our present research work has high impact for saving the life from cancer because cancer nanotechnology is a rapidly emerging field which holds great promise for revolutionizing cancer detection, diagnosis, treatment, and cure.

Furthermore, cancer nanotechnology holds the potential to ultimately improve access to cancer care worldwide including Japan.

Chapter 1 consists of a general feature introduction of the entire studies. At first, the basic facts about nanoparticle, nanoscience and nanotechnology and their application to cancer therapy, along with some facts about cancer was discussed. After that details about magnetic nanoparticles and hyperthermia are also described in this chapter. Finally, the aims and objectives of this study are illustarted.

Chapter 2 narrates about the preparation of distilled water, cell culture, instrument set up and details of the different experiments carried out.

Chapter 3 shows the synthesis of novel rose-type magnetic nanoplates. Rose-type magnetic nanoplates (RTMNPs) were synthesized by a simple hydrothermal decomposition method where $FeCl_2 \bullet 4H_2O$ was solely used as a precursor. The synthesized nanoplates were characterized using XRD, FE-SEM, UV-Vis absorption (reflectance) spectra and magnetic hysteresis loops. The resulting nanoplates were in the ranges of size 350–500 nm and width 60-70 nm with high crystallinity, purity (shown by XRD) and reproducibility. These iron oxide nanoplates have great potential in magnetic nanodevices and biomagnetic applications.

Chapter 4 deals with the synergistic effects of novel neck-structured α-Fe_2O_3 nanoparticles in cancer cell killing. Nanosized neck-structured α-Fe_2O_3 nanoparticles were prepared successfully from iron chloride tetrahydrate solely by the hydrothermal method. The FE-SEM and TEM studies revealed a unique necked structure with a particle size of ca. 50–60 nm. The synthesized nanomaterials showed the excellent colloid stability and magnetization ability. Finally, the as-prepared α-Fe_2O_3 nanoparticles suspensions showed almost 100% cancer cell killing by the significant temperature increment when an AC (alternating current) magnetic-field and photoirradiation were applied at a concentration of 80μg/mL MEM (minimum essential medium).

Chapter 5 illustrates the synthesis of Fe_3O_4@TiO_2 core-shell nanocomposites and their enhanced cytotoxicity. Fe_3O_4@TiO_2 core-shell nanocomposites were successfully prepared and characterized by FE-SEM, XRD, UV-Vis absorbance spectra, and EDX. The FE-SEM and EDX studies revealed core-shell structure with a particle size of ca. 40–50 nm. We adopted HeLa cells

as a model to investigate the thermal-photocatalytic cell killing efficiency of Fe_3O_4@TiO_2 using 150 μg/mL dose content for 10 min exposure time. We found neither only AC magnetic-field induction nor only photoirradiation condition could kill the cancer cells up to satisfactory level using Fe_3O_4@TiO_2 nanocomposites. Finally, the results revealed that almost 100% cancer cells were destructed by Fe_3O_4@TiO_2 nanocomposites whereas for bare Fe_3O_4 and bare TiO_2, 90% and 56% cancer cells were killed, respectively, under combined AC (alternating current) magnetic-field induction and UV-Vis photoirradiated conditions.

Chapter 6 deals with the formation of mixed α and γ-Fe_2O_3 nanoparticles and their application to cancer therapy. We synthesized mixed α and γ-Fe_2O_3 nanoparticles and investigated their toxic effects against HeLa cells under induced AC (alternating current) magnetic-fields and photoexcited conditions at room temperature. The findings revealed that the cell-killing percentage was increased with increasing dose for all types of treatments. Finally, 99% cancer cells were destructed at 1.2 mL dose when exposed to combined AC magnetic-field and photoexcited conditions (T_3) whereas 89 and 83 % of HeLa cells were killed under only AC magnetic-field induced (T_1) or only photoexcited (T_2) condition at the same dose.

Chapter 7 consists of synthesis of mixed α and γ-Fe_2O_3 nanoparticles and their synergistic toxic effect against HeLa cells. In this current study we synthesized mixed α and γ-Fe_2O_3 nanoparticles and their synergistic toxic effect against HeLa cells was investigated under AC (alternating current) magnetic-fields induction and photoirradiation conditions at room temperature. The experiment was designed to find out the cancer cell killing efficacy of as-synthesized bare γ-Fe_2O_3, bare α-Fe_2O_3 and mixed α and γ-Fe_2O_3 nanoparticles under combined AC magnetic-fields induction and photoirradiation conditions. The toxic effect of nanoparticles was obtained by counting the percentage of viable cells after all the treatments using a concentration of 150 μg/mL. The results revealed that the highest toxic effect was obtained using mixed α and γ-Fe_2O_3 nanoparticles under combined AC magnetic-field induction and photoirradiation conditions at a dose of 1.2 mL/ mL MEM (minimum essential medium), i.e., approximately 98% cancer cells were killed, whereas under only AC magnetic-field induction or only photoirradiation condition, only 89% and 66% cancel cells were destroyed using the same dose of same nanomaterials, respectively. We also noticed that 60% and 79% cancer cells were destroyed using bare α-Fe_2O_3 and bare γ-Fe_2O_3 nanoparticles, respectively, under combined AC magnetic-field induction and photoirradiation conditions using the same dose. To the best of our understanding, the

mechanism or reason for almost 100% HeLa cell killing under the combined condition can be ascribed to the combined or synergistic effect of AC magnetic-field induced hyperthermia and photocatalytic cytotoxicity.

Chapter 8 was designed to find out the cancer cell killing efficacy of as-synthesized neck-structured Fe_3O_4 and γ-Fe_2O_3 magnetic nanoparticles under AC magnetic-fields induction condition. Novel neck-structured Fe_3O_4 and γ-Fe_2O_3 magnetic nanoparticles were successfully prepared by a modified hydrothermal method. Ferrous chloride tetrahydrate was solely used as a precursor for the novel nanomaterials. The as-synthesized nanomaterials were characterized by using XRD, FE-SEM and TEM. Neck-structured particle morphology was observed for the first time in all of iron oxides with magnetic properties. The particle size observed was 50–60 nm. The synthesized nanomaterials showed excellent magnetization values when magnetic hysteresis loops were measured using a superconducting quantum interference device (SQUID) as well as excellent colloidal stability. Moreover, the as-prepared magnetic nanoparticles suspensions showed significant temperature increments and cancer (HeLa) cell destroying potentiality (91% and 95% for Fe_3O_4 and γ-Fe_2O_3, respectively) under an AC (alternating current) magnetic-field induction condition at room temperature using the concentration of 150 μg/mL.

Chapter 9 deals with the various impact of precursor and incubation time on the morphology of magnetic nanoparticles. We synthesized magnetite (Fe_3O_4) nanoparticles using precursor $FeCl_3$•$6H_2O$ or $FeCl_2$•$4H_2O$ with 5 or 8 mmol concentration and 3 or 5 h incubation time with the constant pH (7.5) by simple hydrothermal decomposition and then transferred them into maghemite (γ-Fe_2O_3) and hematite (α-Fe_2O_3). Precisely, the objectives of the study were to evaluate the influences of the precursor type, its concentration rate and incubation time on the morphology of the as-synthesized magnetic nanoparticles. Synthesized nanoparticles were characterized for XRD, FE-SEM, TEM, UV-Vis absorption (reflectance) spectra and magnetic hysteresis loops by superconducting quantum interference device (SQUID, Quantum Design MPMS-5) without any size sorting. In case of iron hexahydrate ($FeCl_3$•$6H_2O$) 5 mmol precursor concentration along with 5 h incubation period results in homogeneous spherical particles (standard). On the other hand same precursor but 8 mmol concentration and 3 h incubation period produced bigger particle size with heterogeneous spherical shape. In case of iron tetrahydrate ($FeCl_2$•$4H_2O$) almost neck-structured heterogeneous particles were obtained in all types of precursor concentrations and incubation period. Finally, our study revealed that in both

type of precursors, increased precursor concentration and decreased incubation period results in increased particles size.

Chapter 10 makes a comparison of as-prepared magnetic nanoparticles by co-precipitation and hydrothermal method. Magnetite (Fe_3O_4) nanoparticles were prepared by co-precipitation and hydrothermal methods and their phase transfer was done successfully to compare their performances in different aspects. Synthesized nanoparticles were characterized for XRD, FE-SEM, TEM, UV-Vis absorption (reflectance) spectra, magnetic hysteresis loops and AC magnetic field induced hyperthermia. The magnetic nanoparticles prepared by the co-precipitation method show superior performances in respect of heat dissipation capability, saturation of magnetization values and particle size when compared to those prepared by the hydrothermal method.

Chapter 11 deals with use of natural products (garlic) in cancer cell killing**.** Garlic (*Allium sativum*) is an herb that is used mainly as a food in many countries for its medicinal properties since ancient times. It enhances immune functions and has antibacterial, antifungal, antivirus and anticancer activities. Organosulfur compounds originating from garlic inhibit carcinogen activation. In this study we prepared aqueous garlic extract (AGE) and its *in vitro* application to cancer (HeLa) cell line was performed to observe the cancer cell killing efficacy. Different concentrations of AGE like 100, 200, 300, 400, and 500 μL per a 5-mL minimum essential medium solution were used for treatment. The results revealed that 95% cancer cells were destructed in a dose of 500 μL, whereas about 92, 87, 60, and 24% cancer cells were destructed in a dose of 400, 300, 200 or 100 μL of AGE, respectively.

Chapter 12 illustrates the synthesis of Cu-TiO_2 nanocomposites. The metallic Cu nanoparticles have been successfully deposited on the heterogeneous TiO_2 surface by the borohydride reduction of copper nitrate in water / CH_3CN mixture under Ar atmosphere. The synthesized Cu-TiO_2 nanocomposites show light absorption in the wide visible region and XPS studies show that Cu exists in metallic form. The catalytic activity of the Cu-TiO_2 nanocomposite was evaluated by the application to the photocatalytic cancer (HeLa) cell-killing under UV-visible light irradiation. The Cu-TiO_2 nanocomposite showed higher photocatalytic activity than commercial TiO_2 (P25) under the similar experimental conditions. Based on the observed results, a plausible mechanism was proposed.

Chapter 13 deals with the cytotoxic effects of core-shell structure of $Ag@TiO_2$ nanoclusters. The Ag metal core-TiO_2 shell ($Ag@TiO_2$) composite nanocluster with uniform size, shape and core-shell structures was successfully synthesized by a new simple citrate reduction method. The core-shell structure of $Ag@TiO_2$ nanocluster was characterized by using TEM, SEM, XPS, EDX, XRD, and photoluminescence spectra analysis. It was found that the Ag core is in metallic form which is covered by TiO_2 shell within 3-5 nm thickness and the core-shell particles size was about 30 nm. The photocatalytic and photothermal cell killing efficiency of colloidal $Ag@TiO_2$ core-shell nanoclusters was evaluated against cancer (HeLa) cells under UV–vis irradiation. It was found that the $Ag@TiO_2$ nanoclusters with an adequate Ag ratio to TiO_2 killed more malignant (HeLa) cells by 80% compared to TiO_2 nanoparticles alone. The comparative study of the cell viability using UV only, visible only and UV-visible light revealed that the synergy effect of photocatalytic hydroxyl radical formation and Ag-plasmonic photothermal generation plays a vital role for the cancer cell killing. Based on the obtained results, a plausible mechanism was also proposed.

Chapter 14 gives with the one-step synthesis of doped TiO_2 submicrospheres. Without using an external precursor a simple and one-step method for the synthesis of C-doped TiO_2 submicrospheres has been developed via hydrolysis of titanium tetraisopropoxide in pure methanol followed by calcination under air at 500 ˚C. Also, with the addition of D-glucose and NH_4OH solution during the hydrolysis process, C- or N-doped and C, N co-doped TiO_2 sub microspheres can be prepared by the same method. The size of the submicrosphere was homogeneous ranging from 300 to 400 nm. The resulting sub microspheres were characterized by FE-SEM, TEM, XRD, XPS and UV–vis diffuse reflectance spectroscopy. The C- or N-doped and C, N co-doped submicrospheres showed obvious absorption in the wavelength up to around 650, 500 and 650 nm, respectively. The activity of the photocatalysts was evaluated by the hydroxyl radical formation under visible light irradiation. Finally, the mechanism of sphere formation is discussed.

LIST OF PUBLICATIONS

The following publications have resulted from the studies undertaken for this degree:

1. **Md. Shariful Islam**, Yoshihumi Kusumoto, Md. Abdulla-Al-Mamun, Yuji Horie and Hirotaka Manaka, Enhancement of cumulative photoirradiated and AC magnetic-field induced cancer (HeLa) cell killing efficacy of mixed α and γ-Fe_2O_3 magnetic nanoparticles, ***New Journal of Chemistry***, 2012, **DOI:** 10.1039/C2NJ40029D.
2. **Md. Shariful Islam,** Yoshihumi Kusumoto, Md. Abdulla-Al-Mamun, **Novel rose-type magnetic (Fe_3O_4, γ-Fe_2O_3 and α-Fe_2O_3) nanoplates synthesized by simple hydrothermal decomposition,** *Materials Letters*, 66 (2011) 165-167.
3. **Md. Shariful Islam**, Yoshihumi Kusumoto, Md. Abdulla-Al-Mamun, and Yuji Horie, **Photocatalytic and AC Magnetic-field Induced Enhanced Cytotoxicity of Fe_3O_4@TiO_2 Core-shell Nanocomposites against HeLa Cells,** *Catalysis Communications***,** 16 (2011) 39–44.
4. **Md. Shariful Islam,** Yoshihumi Kusumoto, Md. Abdulla-Al-Mamun, and Yuji Horie, **Enhanced cancer cell (HeLa) killing efficiency of mixed alpha and gamma iron oxide superparamagnetic nanoparticles under combined AC (alternating current) magnetic fields and photoexcitation**, *IIUM Engineering Journal*,12(4) (**2011)** 67-72, ,(Special issue on Biotechnology).
5. **Md. Shariful Islam**, Yoshihumi Kusumoto, Md. Abdulla-Al-Mamun, and Yuji Horie, **Synergistic Cell-killing by Magnetic and Photoirradiation effects of Neck-structured α-Fe_2O_3 against Cancer (HeLa) Cells**, *Chemistry Letters*, 40 (**2011**) 773-775.
6. **M. S. Islam,** Y. Kusumoto, and M. Abdulla-Al- Mamun, **Cytotoxicity and Cancer (HeLa) Cell Killing Efficacy of Aqueous Garlic (*Allium sativum*) Extract,** *Journal of Scientific Research,* 3 (**2011**) 375-382.
7. **Md. Shariful Islam**, Yoshihumi Kusumoto, Md. Abdulla-Al-Mamun, andYuji Horie, **AC magnetic-field induced and photoexcited cancer cell (HeLa) killing efficacy of mixed α and γ-Fe_2O_3 superparamagnetic nanoparticles**, *Proceedings of the 2nd International Conference on Biotechnology Engineering, ICBioE'11, **Kuala Lumpur, Malaysia,*** May, 2011.

8. **Md. Shariful Islam1,** Junichi Kurawaki, Yoshihumi Kusumoto, Md. Abdulla-Al-Mamun, Md. Zobayer Bin Mukhlish, **Hydrothermal novel synthesis of neck-structured hyperthermia-suitable magnetic (Fe_3O_4, γ-Fe_2O_3 and α- Fe_2O_3) nanoparticles**, *Journal of Scientific Research,* 4(1) (2012) 99-107**.**
9. Md. Abdulla-Al-Mamun, Yoshihumi Kusumoto, Tohfatul Zannat, **Md. Shariful Islam, Synergistic cell-killing by photocatalytic and plasmonic photothermal effects of Ag@TiO2 core–shell composite nanoclusters against human epithelial carcinoma (HeLa) cells**, *Applied Catalysis A: General***,** 39 (**2011**) 134–142.
10. Md. Abdulla-Al-Mamun, Yoshihumi Kusumoto, Bashir Ahmmad, **Md. Shariful Islam, Photocatalytic Cancer (HeLa) Cell-Killing Enhanced with Cu–TiO2 Nanocomposite.** *Topics in Catalysis***,** 53 (**2010**) 571-577.
11. Bashir Ahmmad, Yoshihumi Kusumoto, **Md. Shariful Islam**, **One-step and large scale synthesis of non-metal doped TiO_2 submicrospheres and their Photocatalytic activity**, *Advanced Powder Technology***,** 21 (**2010**) 292–297.
12. Md. Abdulla-Al-Mamun, Yoshihumi Kusumoto, Tohfatul Zannat and **Md. Shariful Islam**, **Synergistic Enhanced Photocatalytic and Photothermal Cytotoxic Activity of Au@TiO_2 Nanopellets against Human Epithelial Carcinoma (HeLa) Cells**, *Physical Chemistry Chemical Physics*, 13 (**2011**) 21026-21034.
13. **Md. Shariful Islam**, Yoshihumi Kusumoto, Md. Abdulla-Al-Mamun, Hirotaka Manaka, Synthesis, Characterization and Application of Dumbbell-Shaped Magnetic (Fe_3O_4 and γ-Fe_2O_3) Nanoparticles against HeLa (Cancer) Cells, ***Current Nanoscience***, under review.
14. Md. Abdulla-Al-Mamun, Yoshihumi Kusumoto, and **Md. Shariful Islam**, Enhanced Photocatalytic Activity of Ag @ Fe-doped TiO_2 Core-Shell Composite Nanoclusters against Human Epithelial Carcinoma Cells, ***Journal of Materials Chemistry***, 2012, in press.
15. **Md. Shariful Islam**, Yoshihumi Kusumoto, Yuji Horie, Hirotaka Manaka, Md. Abdulla-Al-Mamun, **A comparative study on heat dissipation, morphological and magnetic properties of hyperthermia suitable nanoparticles prepared by co-precipitation and hydrothermal method**, *Bulletin of Materials Science,* under review.
16. Md. Abdulla-Al-Mamun, Yoshihumi Kusumoto, and **Md. Shariful Islam, Simple hydrothermal new synthesis of magnetic nano octahedron: Application to hyperthermia cancer cell killing,** *Canadian Journal of Chemistry***,** under review**.**

17. **Md. Shariful Islam**, Yoshihumi Kusumoto, Md. Abdulla-Al-Mamun , Hirotaka Manaka, Influences of precursor type, concentration and incubation time on the morphology of magnetic nanoparticles synthesized by hydrothermal decomposition, *Journal of Scientific Research,* under review.
18. **Md. Shariful Islam**, Yoshihumi Kusumoto and Alam Khan, **Cytotoxic effects of Lead (Pb) against Human Epithelial Carcinoma (HeLa) Cells**, *Toxicological Sciences, Communicated.*
19. **Md. Shariful Islam**, Yoshihumi Kusumoto, Md. Abdulla-Al-Mamun and Alam Khan, Arsenic induced cytotoxic effects against Human Epithelial Carcinoma (HeLa) Cells, *Turkish Journal of Chemistry, Communicated.*

CONFERENCE PRESENTATIONS

1. **17th -19th May, 2011, Kuala Lumpur, Malaysia,** The 2nd International Conference on Biotechnology Engineering, ICBioE'11**, <u>Oral Contribution</u>.**
2. **6th-8th September, 2011, Miyazaki**, Japan, Annual Meeting on Photochemistry 2011, **<u>Oral Contribution</u>.**
3. **14th -16th October, 2009, Akita, Japan,** The 12th Japan-Korea Symposium on Catalysis (JKSC 12 2009), **<u>Oral Contribution</u>.**
4. **6th-8th September, 2011, Miyazaki**, Japan, Annual Meeting on Photochemistry 2011, **<u>Poster Contribution</u>.**
5. **6th-8th September, 2011, Miyazaki**, Japan, Annual Meeting on Photochemistry 2011, **<u>Poster Contribution</u>.**
6. **6th-8th September, 2011, Miyazaki**, Japan, Annual Meeting on Photochemistry 2011, **<u>Poster Contribution.</u>**


The End